UNIVERSITY OF BIRMINGHAM

Vital Signs Monitoring using Doppler Radar and On-Body Antennas

by

Abubakar Tariq

Supervisor: Dr Hooshang Ghafouri-Shiraz

A Thesis submitted to the
University of Birmingham
for the degree of
DOCTOR OF PHILOSOPHY

SCHOOL OF ELECTRONIC, ELECTRICAL AND COMPUTER ENGINEERING
COLLEGE OF ENGINEERING AND PHYSICAL SCIENCE
University of Birmingham

August 2012

Abstract

The chest of a person moves due to the heart beating and the lungs expanding and contracting. So the chest movement contains information about the heart and breathing rates. This property is used to detect vital signs using Doppler radar and On-Body antennas. These methods can be accurate, cost-effective, portable, comfortable and low profile alternatives to present commercial heart and breathing rate monitoring devices. The 1st method employing Doppler Effect is non-contact. It detects both the heart and breathing rates using the modulated reflected signals from the chest of a person. A parametric study is conducted considering frequency, power and distance to determine the best parameters for maximum accuracy. A small population study is conducted considering 5 people to validate the accuracy and working of Doppler radar as a vital signs monitor. The 2nd method monitors the heart and breathing rates by sensing motion in the near field proximity of an antenna using the antenna's reflection coefficient. Simulation studies are conducted using CST chest models to verify the principle. An extensive parametric investigation considering frequency, antenna type, power, antenna location on body, body Position, and distances (between chest and antenna) is conducted to find parameters for maximum detection accuracy. A human population study considering 13 people is conducted to establish heart rate and heart rate variability (HRV) measurement feasibility. A signal processing study is also performed and the best algorithms are identified for accurate detection of vital signs. Besides this novel frequency and pattern reconfigurable antennas are proposed and designed for communications and/or vital signs monitoring purposes.

To my wonderful family

Acknowledgement

I was lucky to be given the chance to work with amazing people throughout my PhD at an accomplished institution.

My supervisor Dr. Hooshang Ghafouri-Shiraz was not only an amazing supervisor; he was a great mentor and friend. He guided me expertly not just in my PhD, but also in life issues. He has made me a better and more accomplished professional and person.

I had amazing colleagues including Moe Abbas, Deepak Shamvedi, M. A. Milani, Gaith Mansour, and Sampson Hu who made these years an amazing experience. I especially like to thank MohammadHossein Zoualfaghari for tolerating me these 4 years, helping me when I needed it and being a good friend. Despite my constant pestering of Dr. Yuriy Nechayev and Dr. Rijal Hammid, they always kept their doors open to me and guided me in my PhD.

My mother, father, sister, brother and fiancé have been amazing throughout my PhD, constantly pushing me on, believing in me even when I did not believe in myself, and being there for me whenever I needed them.

The whole Electronic, Electrical and Computer Engineering Department staff have been my family these past four years. I would like to thank Alan Yates, Dr. Peter Gardner, Professor Peter Hall, Dr. Paul Smith, Mary Winkles, Samantha McCauley, Andy Dunn, David Checketts, Robert Davies, Warren Hay, Dr. Steven Quigley for making me feel welcome and motivating me.

Even though the PhD years have sometime been extremely frustrating, not good for mental health (not a joke), they have been the best time of my life where I have learned so much not only technically but also worldly.

Table of Contents

Abstract ii

Publications xxix

1 Chapter 1 1

1.1 Motivation 1

1.1.1 Benefits of Doppler radar Vital Signs Monitoring 2

1.1.2 Benefits of On-Body Vital Signs Monitoring 3

1.1.3 Benefits of Frequency Reconfigurable antennas 4

1.1.4 Benefits of Pattern Reconfigurable antennas 4

1.2 Objectives 5

1.3 Challenges 6

1.4 Contributions 7

1.4.1 Effect of parameters on On-Body vital signs monitoring 7

1.4.2 Human Body measurements and Heart rate variability (HRV) study 7

1.4.3 Simulation study of On-Body vital signs monitoring 8

1.4.4 Effect of parameters on Doppler radar vital signs monitoring 8

1.4.5 Digital Signal Processing (DSP) 9

1.4.6 Frequency Agile Antennas 9

1.4.7 Pattern Agile Antennas 10

1.5 Thesis outline 10

1.6 References 12

2 Chapter 2 14

2.1 Introduction 14

2.2 Heart Motion 14
2.2.1 Electrical impulses of the heart 17
2.2.2 Surface Motion due to the Cardiac Cycle 18
2.3 Respiratory Motion 19
2.3.1 Surface Motion due to Respiration 20
2.4 Vital Signs 22
2.4.1 Pulse rate monitoring techniques: 22
2.4.2 Respiration rate monitoring techniques: 25
2.5 Summary 27
2.6 References 29
3 Chapter 3 32
3.1 Introduction 32
3.2 Literature Review 33
3.3 Principle and Mathematical Analysis 35
3.4 Setup and Methodology 38
3.4.1 Experimental equipment and Setup 38
3.4.2 Signal processing 41
3.4.3 Analysis Techniques 44
3.5 Effect of frequency 45
3.5.1 Experimental Setup 45
3.5.2 Results and Discussion 47
3.6 Effect of Distance 56
3.6.1 Experimental Setup 56
3.6.2 Results and Discussion 57

3.6.3 Respiration 60
3.7 Effect of power 61
3.7.1 Experimental Setup 61
3.7.2 Results and Discussion 62
3.7.3 Respiration 64
3.8 Human measurement results 66
3.8.1 Experimental setup 66
3.8.2 Results and Discussion 66
3.9 Conclusions 69
3.10 References 70
4 Chapter 4 73
4.1 Introduction 73
4.2 Principle 77
4.2.1 On-Body Vital Signs monitoring simulation study 77
4.2.2 CST Microwave studio 78
4.2.3 Multi-Layers Human Chest Model 78
4.2.4 Dielectric properties of chest 81
4.2.5 Chest Movement Models 82
4.2.6 Ultra-Wideband monopole antenna 83
4.2.7 Simulation Study considering effect of heart movement (only) 84
4.2.8 Simulation Study considering effect of chest movement 88
4.2.9 Antenna Comparison 93
4.2.10 Distance Effect 98
4.2.11 Conclusions from simulation study 99

4.3 Setup and Methodology 100
4.3.1 Experimental equipment and Setup 100
4.3.2 Signal processing 102
4.3.3 Human Subjects 104
4.3.4 Human Body Measurements 105
4.3.5 Analysis Techniques 106
4.4 Effect of frequency 107
4.4.1 Experimental Setup 107
4.4.2 Results and Discussion 109
4.5 Effect of antenna structure and polarization 116
4.5.1 Experimental Setup 116
4.5.2 Results and Discussion 122
4.6 Different power 128
4.6.1 Experimental Setup 128
4.6.2 Results and Discussion 129
4.6.3 Respiration 133
4.7 Antenna Location on body 134
4.7.1 Results and Discussions 135
4.8 Different distances 143
4.8.1 Experimental Setup 143
4.8.2 Results and Discussion 143
4.8.3 Respiration 149
4.9 Human body measurement results 151
4.9.1 Experimental setup 151

4.9.2 Results and Discussion 153
4.10 Heart rate Variability 163
4.10.1 Time domain measures of HRV 164
4.10.2 Experimental data 166
4.10.3 Results and Discussion 166
4.11 Conclusion 171
4.12 References 174
5 Chapter 5 179
5.1 Introduction 179
5.2 Antenna Filter Design 182
5.2.1 Switched Filter Design 182
5.2.2 Varactor Filter 186
5.3 Antenna Design 191
5.3.1 Wideband Antenna 191
5.3.2 Switched Monopole Antenna 192
5.3.3 Varactor Antenna 197
5.4 Radiation Pattern 200
5.5 Three modes antenna 206
5.6 Conclusions 217
5.7 References 218
6 Chapter 6 221
6.1 Introduction 221
6.2 Single Port Flower Vivaldi 228
6.2.1 Ideal Switch four way flower Vivaldi 230

6.2.2 Single Port Flower Vivaldi Antenna 237
6.3 Vital Signs Monitoring using single port flower Vivaldi antenna 248
6.3.1 Respiration 257
6.4 Conclusions 259
6.5 References 260
Chapter 7 262
Appendix A 274
Appendix B 274
B. Signal Processing 274
B.1 Fast Fourier Transform (FFT) 275
B.2 Autocorrelation 276
B.3 Wavelet Transform 277
B.3.1 Theory 277
B.3.2 Results and Discussions 279
B.4 Comparison of various signal processing techniques 287

List of Figures

Figure 2.1: Location of the heart in the rib cage. 15

Figure 2.2: Diagrammatic section of the heart. 16

Figure 2.3: Output of an electrocardiogram. 17

Figure 2.4: The thoracic wall and body cavities. 20

Figure 2.5: Diaphragm's role in breathing. 21

Figure 3.1: General experimental setup showing the VNA, chest belt and ECG monitor. 39

Figure 3.2: ECG electrodes placement on the left arm, right arm, and left leg. 40

Figure 3.3: Block diagrams showing the signal processing algorithm for calculating (a) heart rate from VNA signal, (b) heart rate from ECG device, (c) respiration rate from VNA signal, (d) respiration rate from MLT1132 piezo-resistive belt. 43

Figure 3.4: Bland-Altman plots for heart rate calculated using ECG device and Doppler radar at (a) 1 GHz, (b) 2.45 GHz, (c) 5.8 GHZ, (d) 7 GHz, (e) 9 GHz, (f) 10 GHz, (g) 11 GHz, (h) 12 GHz, (i) 13 GHz, (j) 15 GHz, and (k) 17 GHz. 49

Figure 3.5: ECG signal and filtered Doppler Radar heart rate plots at (a) 2.45 GHz, (b) 9 GHz, and (c) 17 GHz. 53

Figure 3.6: Heart rate [BPM] vs. Time for the ECG signal(blue) and Doppler Radar(red) at (a) 2.45 GHz, (b) 9 GHz, and (c) 17 GHz. 54

Figure 3.7: Breathing rate [Breaths per minute] vs. Time for the ECG signal and On-Body monitor for (a) 2.45 GHz, (b) 9 GHz and (b) 17 GHz, Breathing signal from On-Body Monitor and filtered MLT1132 Chest Belt for (c) 1 GHZ, (d) 9 GHz and (f) 17 GHz 56

Figure 3.8: Bland-Altman plots for heart rate calculated using ECG device and Doppler radar at (a) 50cm, (b) 1m, (c) 1.5m, (d) 2m, (e) 2.5m, and (f) 3m. 59

Figure 3.9: ECG signal and filtered Doppler Radar heart rate plots for (a) 2m and (b) 3m..... 59

Figure 3.10: Heart rate [BPM] vs. Time for the ECG signal (blue)and Doppler Radar(red) for (a) 2m and (b) 3m. 59

Figure 3.11: Breathing signal from Doppler radar and filtered MLT1132 Chest Belt waveform at 3m. 61

Figure 3.12: Bland-Altman plots for heart rate calculated using ECG device and Doppler radar at (a) 50cm, (b) 1m, (c) 1.5m, (d) 2m, (e) 2.5m, and (f) 3m. 63

Figure 3.13: ECG signal and filtered Doppler Radar heart rate plots for (a) -20 dBm and (b) -45 dBm. 64

Figure 3.14: Heart rate [BPM] vs. Time for the ECG signal and Doppler Radar for (a) -20 dBm and (b) -45 dBm. 64

Figure 3.15: Breathing signal from Doppler radar and filtered MLT1132 Chest Belt waveform at Doppler radar power of -45 dBm. 65

Figure 3.16: Difference in the Heart rate [BPM] between the ECG and Doppler Radar versus the SNR for all measurements. The Linear regression line (red) is also shown. The difference is taken to be the standard deviation of the difference from Bland-Altman Analysis. 68

Figure 4.1: Top view topology of Chest model in CST. Colour correspondence is same as fig (D=0.5 mm, S= 5mm, F= 5mm, M= 15mm, LD= 85mm, HD= 40mm to 55 mm, LW=275 mm, HW= 80mm). 79

Figure 4.2: Front view topology of Chest model in CST. Colour correspondence is same as fig 4.1 (D_1=150 mm, L_1= 50 mm, L_2= 100 mm). 80

Figure 4.3: Chest Model realized in CST Microwave Studio. 80

Figure 4.4: Topology of the Wideband monopole antenna. The dimensions are: A=44 mm, B=24 mm, G=0.5 mm, W_1= 5 mm, W_2= 6 mm, D=2 mm, W_3=17.5 mm and L= 25 mm. 83

Figure 4.5: Simulated S_{11} for the UWB monopole antenna. 84

Figure 4.6: Antenna reflection coefficient phase variations for various heart layer thicknesses at 2.45 GHz over 5 cycles. 85

Figure 4.7: Antenna reflection coefficient phase variations for various heart layer thicknesses at 5.8 GHz over 5 cycles. 86

Figure 4.8: Antenna reflection coefficient phase variations for various heart layer thicknesses at 9 GHz over 5 cycles. 87

Figure 4.9: Antenna reflection coefficient phase variations for various heart layer thicknesses at 2.45 GHz over 5 cycles (Inflated lungs). 88

Figure 4.10: Antenna reflection coefficient phase variations for various distances of the chest from the antenna at 2.45 GHz over 5 cycles. 90

Figure 4.11: Antenna reflection coefficient phase variations for various distances of the chest from the antenna at 5.8 GHz over 5 cycles. 90

Figure 4.12: Antenna reflection coefficient phase variations for various distances of the chest from the antenna at 9 GHz over 5 cycles. 91

Figure 4.13 (a): Antenna reflection coefficient phase variations for various distances of the chest from the antenna at 2.45 GHz over 5 cycles. 92

Figure 4.14: Topology of (a) Patch Antenna [8] (b) Loop Antenna [7] (c) Orientation of Antenna with respect to the chest. 95

Figure 4.15: Reflection coefficient with (a) antenna 1, (b) antenna 2, and (c) antenna 3 in free space, 2mm and 14mm away from chest model. 98

Figure 4.16: S_{21} characteristics of the cable used to connect the VNA with the antenna. 101
Figure 4.17: General experimental setup showing the VNA, chest belt and ECG monitor...102
Figure 4.18: Block diagrams showing the signal processing algorithm for calculating (a) heart rate from VNA signal, (b) heart rate from ECG device, (c) respiration rate from VNA signal, (d) respiration rate from MLT1132 piezoresistive belt. 103
Figure 4.19: Topology of the Wideband CPW antenna. The dimensions are: A=44 mm, B=24 mm, G=0.5 mm, W1= 5 mm, W2= 6 mm, D=2 mm, W3=17.5 mm and L= 25 mm.....108
Figure 4.20: Measured Reflection Coefficient of antenna shown in figure 4.19. 108
Figure 4.21: Bland-Altman plots for (a) 1 GHz, (b) 2.45 GHz, (c) 3.5 GHz, (d) 5.8 GHz, (e) 7 GHz, and (f) 9 GHz 111
Figure 4.22: ECG signal and filtered On-Body heart rate plots for (a) 1 GHz, (b) 2.45 GHz, (c) 3.5 GHz, (d) 5.8 GHz, (e) 7 GHz, and (f) 9 GHz.....112
Figure 4.23: Heart rate [BPM] vs. Time for the ECG signal and On-Body monitor for (a) 1 GHz, (b) 2.45 GHz, (c) 3.5 GHz, (d) 5.8 GHz, (e) 7 GHz, and (f) 9 GHz.....113
Figure 4.24: Breathing rate [Breaths per minute] vs. Time for the ECG signal and On-Body monitor for (a) 1 GHz, and (b) 9 GHz, Breathing signal from On-Body Monitor and filtered MLT1132 Chest Belt for (c) 1 GHz, and (d) 9 GHz 116
Figure 4.25: (a) Inverted F antenna (IFA) [8], (b) Coplanar waveguide 3d monopole antenna [7], (c) dipole antenna [7], (d) Loop antenna 1 [8], (e) Patch Antenna [8], (f) Loop Antenna 2 [7], (g) 3d Monopole Antenna[7], ...121
Figure 4.26: Bland-Altman plots for (a) IFA, (b) CPW3dM, (c) Dipole, (d) Loop1, (e) PatchR, (f) PatchG, (g) Loop2, (h) 3dM, and (i) CPWM 123
Figure 4.27: ECG signal and filtered On-Body heart rate plots for (a) IFA, (b) CPW3dM, (c) Dipole, (d) Loop1, (e) PatchR, (f) PatchG, (g) Loop2, (h) 3dM, and (i) CPWM 125

Figure 4.28: Heart rate [BPM] vs. Time for the ECG signal and On-Body monitor for (a) IFA, (b) CPW3dM, (c) Dipole, (d) Loop1, (e) PatchR, (f) PatchG, (g) Loop2, (h) 3dM, and (i) CPWM 126

Figure 4.29: Bland-Altman plots for (a) -10 dBm, (b) -20 dBm, (c) -30 dBm, and (d) -45 dBm. 131

Figure 4.30: ECG signal and filtered On-Body heart rate plots for (a) -10 dBm, (b) -20 dBm, (c) -30 dBm, and (d) -45 dBm. 132

Figure 4.31: Heart rate [BPM] vs. Time for the ECG signal (blue) and On-Body monitor (red) for (a) -10 dBm, (b) -20 dBm, (c) -30 dBm, and (d) -45 dBm. 132

Figure 4.32: a) Breathing rate [Breaths per minute] vs. Time for the MLT1132 signal and On-Body monitor at -45 dBm, (b) Breathing signal from On-Body Monitor and filtered MLT1132 Chest Belt Input at -45 dBm. 134

Figure 4.33: Antenna Locations on Body: (a) (Pos. 1) Left Side, (b) (Pos. 2) Right Side, (c) (Pos. 3) Left Backside, (d) (Pos. 4) Left Abdomen, (e) (Pos. 5) Top Left Chest (f) (Pos.6) Front Left Chest. 135

Figure 4.34: Bland-Altman plots for (a) Position 1, (b) Position 2, (c) Position 3, (d) Position 4, (e) Position 5, (f) Position 6, and (g) Position 6 (direct on skin). The Positions can be found in figure 4.33. 138

Figure 4.35: ECG signal and filtered On-Body heart rate plots for (a) Position 1, (b) Position 2, (c) Position 3, (d) Position 4, (e) Position 5, (f) Position 6, and (g) Position 6 (direct on skin). The Positions can be found in figure 4.33. 140

Figure 4.36: Heart rate [BPM] vs. Time for the ECG signal and On-Body monitor for (a) Position 1, (b) Position 2, (c) Position 3, (d) Position 4, (e) Position 5, (f) Position 6, and (g) Position 6 (direct on skin). The Positions can be found in figure 4.33. 141

Figure 4.37: Respiration graph obtained from MLT1132 belt (red) and On-Body Monitor when antenna was attached to left abdomen (pos. 4) 142

Figure 4.38: Bland-Altman plots for heart rate calculated using ECG device and Doppler radar for different distances, (a) Directly on skin , (b) Directly on clothes, (c) 5 cm, (d) 10 cm and (e) 20 cm, (f) 50 cm and (g) 1 m. 145

Figure 4.39: ECG signal and filtered On-Body antenna heart rate plots for different distances, (a) Directly on skin , (b) Directly on clothes, (c) 5 cm, (d) 10 cm and (e) 20 cm, (f) 50 cm and (g) 1 m. 147

Figure 4.40: Heart rate [BPM] vs. Time for the ECG signal(blue) and On-Body antenna(red) for different distances, (a) Directly on skin , (b) Directly on clothes, (c) 5 cm, (d) 10 cm and (e) 20 cm, (f) 50 cm and (g) 1 m. 148

Figure 4.41: Breathing rate [Breaths per minute] vs. Time for the ECG signal and On-Body monitor when the antenna is (a) directly on the clothes, (b) 5cm away from chest and (c) 1m away from chest. Breathing signal from On-Body Monitor and filtered MLT1132 Chest Belt when the antenna is (d) directly on the clothes, (e) 5cm away from chest and (f) 1m away from chest. 151

Figure 4.42: Difference in the Heart rate[BPM] between the ECG and On-Body monitor versus the SNR for all measurements in sitting(red) and supine(blue) position. The Linear regression lines are also shown. 156

Figure 4.43: (a) Breathing rate [Breaths per minute] vs time [sec] calculated for MLT1132 Chest Belt (red) and On-Body Monitor (Blue) ,(b) On-Body respiration signal (blue) vs. MLT1132 chest belt respiration signal for subject 5(from 4.4.3) sitting. 161

Figure 4.44: (a) Breathing rate [Breaths per minute] vs time [sec] calculated for MLT1132 Chest Belt (red) and On-Body Monitor (Blue) ,(b) On-Body respiration signal (blue) vs. MLT1132 chest belt respiration signal for subject 1(from 4.4.3) supine. 162

Figure 4.45: (a) Breathing rate [Breaths per minute] vs time [sec] calculated for MLT1132 Chest Belt (red) and On-Body Monitor (Blue) ,(b) On-Body respiration signal (blue) vs. MLT1132 chest belt respiration signal for subject 4(from 4.4.3) sitting. 162

Figure 4.46: (a) Breathing rate [Breaths per minute] vs. time [sec] calculated for MLT1132 Chest Belt (red) and On-Body Monitor (Blue) ,(b) On-Body respiration signal (blue) vs. MLT1132 chest belt respiration signal for subject 4(from 4.4.3) supine. 162

Figure 4.47: Peak detection results in a 15 second duration for subject 4 (from section 4.3.3) in sitting position. 167

Figure 4.48: Peak detection results in a 15 second duration for subject 3 (from section 4.3.3) in supine position. 167

Figure 4.49: Histograms with 8 msec bins for subject 3 (a) sitting (from ECG) (b) sitting (from On-Body), (c) supine (from ECG), (d) sitting (from On-Body). Also shown are the max bins count and the maximum bin centres. (x-axis is in ms) 168

Figure 4.50: Histograms with 8 msec bins for subject 4 (a) sitting (from ECG) (b) sitting (from On-Body), (c) supine (from ECG), (d) sitting (from On-Body). Also shown are the max bins count and the maximum bin centres. (x-axis is in ms) 169

Figure B.1: On-Body Vital Signs signal from (a) subject A, and (b) subject B. 275

Figure B.10: 3d plot of wavelet coefficients for the filtered time domain On-Body signals (from Fig. B.2) for subject (a) A and (b) B. 283

Figure 5.1: Topology of CPW switched Filter. G_1= 0.5 mm, G_2=1 mm, D=8 mm, W_1=2 mm, W_2=2 mm, C=3.35 mm, G=0.5 mm, W=3 mm. 183

Figure 5.2: S-Parameter simulation results of CPW switched filter shown in Fig. 5.1 with S_3 on resulting in $\lambda_g/4$ resonators of length 18.35 mm and 9 mm. 184

Figure 5.3: Electric Field Distribution at (a) 3.56 GHz and (b) 6.698 GHz clearly showing larger and smaller $\lambda_g/4$ resonators. 185

Figure 5.4: Simulation results of (a) S_{21} and (b) S_{11} of the filter shown in Fig. 5.1 for different switch combinations. Resonant frequencies of 3.63 GHz, 4.95 GHz and 6.18 GHz are achieved in (b). 186

Figure 5.5: Topology of CPW varactor Filter, the dimensions are W_1=2.1 mm, W_2=7 mm, W_3=3 mm, L_1=4 mm, G_1=1 mm. CPW dimensions same as Fig. 5.1. 187

Figure 5.6: Simulation results of S-parameters of CPW filter shown in Fig. 5.5 without using varactor diode. 187

Figure 5.7: Normalized voltage wave in the short circuit slotline at the fundamental frequency and 1st Harmonic. 188

Figure 5.8: Simulation results of reflection coefficient of short circuit slotline with varactor at position B (Null point of 1st Harmonic, see Fig.5.7) for different values of capacitors. 189

Figure 5.9: Simulation results of S_{21} for the short circuit slotline with varactor at position A(see Fig.5.7) for different values of capacitors. 190

Figure 5.10: Simulation results of reflection coefficient of short circuit slotline with varactor at position A(see Fig.5.7) for different values of capacitors. Resonant frequencies vary from 2.57 GHz to 5.54 GHz. 190

Figure 5.11: Measured and simulated results of the reflection coefficient for antenna shown in Fig. 4.4. 191

Figure 5.12: Switched monopole antenna along with biasing circuit, the lumped element connecting with the bias lines are the RF chokes (inductors), the lumped elements connecting cut portions of copper are DC blockers (capacitors), the rest are diode switches. 192
Figure 5.13: Wideband measured and simulated results of reflection coefficient when switch combination 1 is ON. 193
Figure 5.14: (a) Narrowband measured and simulated results of reflection coefficient when switch combination 2 is ON. Measured resonance at 4.45 GHz. 193
Figure 5.15: The reflection coefficient measured results for all switch combinations. 196
Figure 5.16: Simulation results of reflection coefficients for switch combination 3 when ideal copper strip is used as ON state diode and open circuit for OFF state diode, when actual diode parameters obtained from Infenion are used for ON state diode and open circuit for OFF state diode, when actual diode parameters obtained from Infenion are used for both ON and OFF state diode. 197
Figure 5.17: Varactor monopole antenna along with biasing circuit, the lumped element connecting with the bias lines are the RF chokes (inductors), the lumped elements connecting cut portions of copper are DC blockers (capacitors), the lumped element at the entrance of the slot are switches and along the slot are varactors. 198
Figure 5.18: (a) Measured, (b) Simulation results of reflection coefficients of varactor monopole showing both wideband and narrowband modes for different capacitor values. .. 199
Figure 5.19: Vivaldi tapered slot antenna using varactor filter described in section 5.2.2. ... 200
Figure 5.20: Simulated reflection coefficient of tapered slot Vivaldi antenna using varactor filter described in section 5.2.2 200

Figure 5.21: Measured radiation patterns in (a) e-plane and (b) h-plane at 3.6 GHz for wideband antenna with no ring slots, wideband antenna with ring slots blocked and narrow band antenna with ring slots not blocked. 202

Figure 5.22: Measured and Simulated radiation patterns at 3 GHz and 4.45 GHz for the switched monopole antenna..... 204

Figure 5.23: Measured and Simulated radiation patterns at 2.88 GHz and 4.62 GHz for the varactor monopole antenna..... 205

Figure 5.24: Topology of CPW Filter. G_1= 1mm, G=0.5mm, W_1=2mm, W=3mm, D_1= 6.25mm, D=14.5mm, S=9mm..... 206

Figure 5.25: CPW filter with two $\lambda/4$ unequal resonators from entry point X..... 207

Figure 5.26: S-parameters for filter in fig. 5.25. 207

Figure 5.27: (a) Electric field strength at 2.159 GHz, (b) Surface current density at 2.159 GHz, (c) Electric field strength at 3.251 GHz, and (d) Surface current density at 3.251 GHz for filter in fig. 5.24 with switch combination S_1 on. 209

Figure 5.28: $\lambda/2$ resonator formed when filter of fig. 5.24 has switch combination S_1 and S_5 ON. 210

Figure 5.29: S_{11} parameter results for wideband CPW antenna (from section 5.3.1) integrated with the filter shown in Fig. 5.28. 211

Figure 5.30: (a) Electric field (b) Surface current density at 2.828 GHz when switch combination S_1 is on for filter in fig. 5.24 on a CPW antenna 212

Figure 5.31: Simulated and Measured notch band modes for 3 mode antenna. The measured notches occur at 2.7 GHz, 3.2 GHz and 3.6 GHz..... 213

Figure 5.32: Simulated and Measured pass band modes for 3 mode antenna. The measured resonant pass band frequencies are at 2.9 GHz, 3.7 GHz and 4.7 GHz. 214

Figure 5.33: Simulated and Measured wide band mode for 3 mode antenna. The antenna has measured reflection coefficient below -10 dB from 2.8 – 6 GHz, and a measured reflection coefficient below – 6 dB from 2.6 – 6 GHz. 214

Figure 5.34: Measured Reflection coefficient results for 3 mode antenna considering notch-band, pass-band and wideband modes.....215

Figure 5.35: Measured and Simulated radiation patterns at 2.89 GHz and 4.635 GHz respectively.....216

Figure 5.36: Measured gain results for boresight for notch and wideband modes.....217

Figure 6.1: Schematic of reconfigurable antenna with CPW-to-slotline transition and a pair of Vivaldi shaped radiating slots [2].....222

Figure 6.2: Wideband circular antenna array [3].....223

Figure 6.3: Schematic diagram of metallic cubic cavity [4].....224

Figure 6.4: (a) Top and side views and (b) perspective view of the printed star antenna [5].225

Figure 6.5: Spiral antenna with monolithically integrated RF- MEMS, U=1.58mm [6]. 226

Figure 6.6: Concept of proposed pattern reconfiguration antenna [7]. 227

Figure 6.7: Topology of feed structure of antenna. (W_1=4.2 mm, L_1=46.67 mm, L_2=21 mm. W_2=2.5 mm, W_3=0.5 mm, W_4=1.5 mm, W_5=0.4 mm, G_1=1.25 mm, G_2=0.25 mm).....228

Figure 6.8: Topology of the ground structure of antenna. (G=1.5 mm, P_1=15.2 m, P_2=30.2 mm, R= 38.9 mm, U=80mm, N=7.5 mm, O=4mm) 229

Figure 6.9: Electric Field Intensity at 6 GHz for Switch Combination S1-S2-S3.....230

Figure 6.10: Electric Field Intensity at 6 GHz for Switch Combination S4-S1-S2. 230

Figure 6.11: Reflection coefficient of ideal switch flower Vivaldi with S4-S1-S2 ON.....231

Figure 6.12: Radiation pattern (H-plane) of ideal switch flower vivaldi with S4-S1-S2 ON at (a) 3.5 GHz, (b) 4.75 GHz, and (c) 6 GHz 232
Figure 6.13: Radiation pattern (E-plane) of ideal switch flower vivaldi with S4-S1-S2 ON at (a) 3.5 GHz, (b) 4.75 GHz, and (c) 6 GHz 233
Figure 6.14: Reflection coefficient of ideal switch flower Vivaldi with S1-S2-S3 ON..... 234
Figure 6.15: Radiation pattern (H-plane) of ideal switch flower vivaldi with S1-S2-S3 ON at (a) 3.5 GHz, (b) 4.75 GHz, and (c) 6 GHz 235
Figure 6.16: Radiation pattern (E-plane) of ideal switch flower vivaldi with S1-S2-S3 ON at (a) 3.5 GHz, (b) 4.75 GHz, and (c) 6 GHz 236
Figure 6. 17: Gain of ideal switch flower Vivaldi for two switch combinations (S1,S2 & S3 : S4,S1 & S2) 237
Figure 6.18: Single feed flower Vivaldi along with biasing circuit, the lumped element connecting with the bias lines are the RF chokes (inductors), the lumped elements connecting cut portions of copper are DC blockers (capacitors), the lumped element in the center are diodes. 238
Figure 6.19: Reflection coefficient of single port flower Vivaldi antenna for switch combination 1. 240
Figure 6.20: Reflection coefficient of single port flower Vivaldi antenna for switch combination 2. 240
Figure 6.21: Reflection coefficient of single port flower Vivaldi antenna for switch combination 3. 241
Figure 6.22: Reflection coefficient of single port flower Vivaldi antenna for switch combination 4. 241

Figure 6.23: Radiation pattern (H-plane) of single port flower vivaldi with switch combination 1at (a) 3.5 GHz, (b) 4.75 GHz, and (c) 6 GHz 242
Figure 6.24: Radiation pattern (E-plane) of single port flower vivaldi with switch combination 1at (a) 3.5 GHz, (b) 4.75 GHz, and (c) 6 GHz 243
Figure 6.25: Radiation pattern (H-plane) of single port flower vivaldi with switch combination 3at (a) 3.5 GHz, (b) 4.75 GHz, and (c) 6 GHz 244
Figure 6.26: Radiation pattern (E-plane) of single port flower vivaldi with switch combination 3at (a) 3.5 GHz, (b) 4.75 GHz, and (c) 6 GHz 245
Figure 6.27: Radiation pattern (H-plane) of single port flower vivaldi with all switch combinations at (a) 3.5 GHz, (b) 4.75 GHz, and (c) 6 GHz.....247
Figure 6.28: Gain of ideal switch flower Vivaldi for all switch combinations 248
Figure 6.29: Experimental Configurations: (a) Person directly in front of max antenna gain, (b) Person at a 45^0 angle from max antenna gain, (c) Person in the direction of max antenna gain but with transmitted signal passing directly through the receiving antenna, (d) Person at 90^0 from maximum antenna gain, (e) Person at 180^0 from maximum antenna gain.....251
Figure 6.30: Bland-Altman plots for heart rate calculated using ECG device and Doppler radar for experimental configurations from fig 6.29. (a) 1st configuration, (b) 2nd configuration, (c) 3rd configuration, (d) 4th configuration and (e) 5th configuration. 254
Figure 6.31: ECG signal and filtered Doppler Radar heart rate plots for experimental configurations from fig 6.29. (a) 1st configuration, (b) 2nd configuration, (c) 3rd configuration, (d) 4th configuration and (e) 5th configuration. 255
Figure 6.32: Heart rate [BPM] vs. Time for the ECG signal (blue) and Doppler radar (red) for experimental configurations from fig 6.29. (a) 1st configuration, (b) 2nd configuration, (c) 3rd configuration, (d) 4th configuration and (e) 5th configuration. 256

Figure 6.33: Breathing rate [Breaths per minute] vs. Time for the ECG signal and Doppler radar monitor configuration (a) 1, (b) 3 and (c) 5. Breathing signal from Doppler radar and filtered MLT1132 Chest Belt for configuration (d) 1, (e) 3 and (f) 5. These configurations can be found in Fig. 6.29.....259

List of Tables

Table 3.1 Constant Parameters for effect of frequency experiments 46

Table 3.2(a): Statistical Analysis of heart rate from ECG and Doppler Radar at various frequencies (1-10 GHz). 47

Table 3.3: Statistical Analysis of Respiration rate from Chest Belt MLT1132D and Doppler radar at 2.45 GHz, 9 GHz, and 17 GHz. 55

Table 3.4: Constant parameters for distance variation measurements 57

Table 3.5: Statistical Analysis of heart rate from ECG and Doppler Radar at various frequencies for different distances. 58

Table 3.6: Statistical Analysis of Respiration rate from Chest Belt MLT1132 and Doppler radar at 1 m and 3 m. 60

Table 3.7: Constant parameters for power variation measurements 61

Table 3.8: Statistical Analysis of heart rate from ECG and Doppler Radar at various frequencies for different powers. 62

Table 3.9: Statistical Analysis of Respiration rate from Chest Belt MLT1132D and Doppler radar at -10 dBm and -45 dBm 65

Table 3.10: VNA parameters for Human measurement experiments 66

Table 3.11: Statistical analysis for Heart Rate obtained by using Doppler radar and ECG device for different subjects. 67

Table 4.1: Dielectric Parameters of the body tissues at 2.45 GHz 81

Table 4.2: Dielectric Parameters of the body tissues at 5.8 GHz 81

Table 4.3: Dielectric Parameters of the body tissues at 9 GHz 82

Table 4.4: Reflection coefficient phase and magnitude variations for various heart layer thicknesses at 2.45 GHz. 85

Table 4.5: Reflection coefficient phase and magnitude variations for various heart layer thicknesses at 5.8 GHz. 86

Table 4.6: Reflection coefficient phase and magnitude variations for various heart layer thicknesses at 9 GHz. 86

Table 4.7: Reflection coefficient phase and magnitude variations for various heart layer thicknesses at 2.45 GHz (Inflated lungs). 87

Table 4.8: Reflection coefficient phase and magnitude variations for various distances of the chest from the antenna at 2.45 GHz, 5.8 GHz and 9 GHz. 89

Table 4.9: Reflection coefficient phase and magnitude variations for various distances of the chest from the antenna at 2.45 GHz, 5.8 GHz and 9 GHz. 92

Table 4.10: Reflection coefficient phase and resonant frequencies for various distances of the chest from four antennas at 2.45 GHz. 97

Table 4.11: Reflection coefficient phase and resonant frequencies for various distances between chest and antenna at 2.45 GHz. 99

Table 4.12: Human Body Measurements (Gender = Gen, Height = Ht, Wight = Wt, Body Mass Index = BMI, Chest Circumference = CC, Waist Circumference = WC, Chest Depth = CD, Chest Width = CW) (Inhalation = i, Exhalation = e) 104

Table 4.13: BMI Body Type Classification [15] 105

Table 4.14: Constant Parameters for effect of frequency experiments 109

Table 4.15: Statistical analysis of heart rate from ECG and On-Body antenna at various frequencies. All BA results are in BPM. 110

Table 4.16: Statistical analysis of breathing rate from MLT1132 chest belt and On-Body antenna at various frequencies. 115
Table 4.17: Statistical analysis of heart rate from ECG and On-Body Monitor for tested antennas. 122
Table 4.18: Statistical analysis of heart rate from ECG and On-Body antenna for different powers. 130
Table 4.19: Statistical analysis of breathing rate from MLT1132D and On-Body antenna for -10 dBm and -45 dBm power. 133
Table 4.20: Statistical analysis of heart rate from ECG and On-Body antenna for different antenna locations on the body. (antenna locations can be found in Figure 4.33) 137
Table 4.21: Respiration rate statistical considering breathing signal from MLT1132D chest belt and On-Body monitor for different antenna positions on body (Positions can be seen in fig. 4.33). 142
Table 4.22: Statistical Analysis of heart rate from ECG and On-Body antenna for different distances between antenna and chest 144
Table 4.23: Statistical analysis of breathing rate from MLT1132 chest belt and On-Body antenna at various distances. 150
Table 4.24: Statistical analysis of heart rate calculated from ECG and On-Body monitor for different subjects in sitting position. 153
Table 4.25: Statistical analysis of heart rate calculated from ECG and On-Body monitor for different subjects in supine position. 154
Table 4.26: SNR/accuracy (within 3 BPM) correlation (Pearson correlation coefficient r and the p-value) with body measurements (from 4.3.3) for sitting and supine positions. A p-value less than 0.05 means a significant correlation is present. 158

Table 4.27: Respiration rate statistical analysis for different subjects in sitting position. (Numbers correspond to 4.4.3 subject numbers). Average does not include subject 8. 160

Table 4.28: Respiration rate statistical analysis for different subjects in supine position. (Numbers correspond to 4.4.3 subject numbers). Average does not include subject 6. 160

Table 4.29: HRV assessment in the sitting position (Numbers correspond to 4.4.3 subject numbers) 170

Table 4.30: HRV assessment in the supine position (Numbers correspond to 4.4.3 subject numbers) 171

Table 6.1: Switch Combinations vs. Antenna Radiation Emission 239

Table 6.2: Switch Combination vs. -6dB and -10dB Bandwidths 239

Table 6.3: Statistical Analysis of heart rate from ECG and Doppler Radar for different experimental considerations (from fig. 6.29) 253

Table 6.4: Statistical analysis of breathing rate from MLT1132 chest belt and Doppler Radar for different experimental configurations (from fig. 6.29) 258

Publications

Journal Publications

Tariq, A.; Ghafouri-Shiraz, H.; , "Frequency-Reconfigurable Monopole Antennas," *Antennas and Propagation, IEEE Transactions on*, vol.60, no.1, pp.44-50, Jan. 2012

Tariq, A.; Ghafouri-Shiraz, H.; , "Noncontact heart rate monitoring using Doppler radar and continuous wavelet transform," *Microwave and Optical Technology Letters*, vol. 53, issue 8, pp.1793–1797, May 2011.

Conference Publications

Tariq, A.; Ghafouri-Shiraz, H.; , "On-body antenna for vital signs and heart rate variability monitoring," *Antennas and Propagation Conference (LAPC), 2011 Loughborough* , vol., no., pp.1-4, 14-15 Nov. 2011

Tariq, A.; Hamid, M.R.; Ghafouri-Shiraz, H.; , "Reconfigurable monopole antennas," *Antennas and Propagation (EUCAP), Proceedings of the 5th European Conference on* , vol., no., pp.2160-2164, 11-15 April 2011

Tariq, A.; Ghafouri-Shiraz, H.; , "Vital signs detection using Doppler radar and continuous wavelet Transform," *Antennas and Propagation (EUCAP), Proceedings of the 5th European Conference on* , vol., no., pp.285-288, 11-15 April 2011

Tariq, A.; Shiraz, H.G.; , "Reconfigurable Monopole antenna using varactors," *UK URSI Festival of Radio Science*, University of Leicester, 12 Jan 2011

Tariq, A.; Shiraz, H.G.; , "Doppler radar vital signs monitoring using wavelet transform," *Antennas and Propagation Conference (LAPC), 2010 Loughborough* , vol., no., pp.293-296, 8-9 Nov. 2010

Publications to be submitted

Tariq, A.; Ghafouri-Shiraz, H.; , "A feasibility study on On-Body antenna vital signs and Heart rate variability monitoring," *Antennas and Propagation, IEEE Transactions on.*

Tariq, A.; Ghafouri-Shiraz, H.; , "A parametric study of On-Body vital signs monitoring," *Antennas and Propagation, IEEE Transactions on*

Tariq, A.; Ghafouri-Shiraz, H.; , "Pattern reconfigurable flower Vivaldi antenna," *Antennas and Propagation, IEEE Transactions on*

Tariq, A.; Ghafouri-Shiraz, H.; , " Frequency Reconfigurable Coplanar Waveguide (CPW) monopole antenna with notch-band, pass-band and wideband modes," *Antennas and Propagation, IEEE Letter on*

1 Chapter 1

Introduction

1.1 Motivation

Cardiovascular diseases are responsible for 17.1 million deaths annually according to the world health organization (WHO) [1]. Chronic lung disease affects one in 7 people in the United Kingdom [2]. This combined with an ageing population has resulted in the rise of long term health care costs. There is a need for monitoring non-critical patients in their homes rather than hospitals to reduce costs which requires cost effective and reliable home healthcare devices. Vital signs (especially breathing rate and heart rate) monitoring is one of the key features for these devices. The present methods for heart rate monitoring include Electrocardiography (ECG) and plethysmography, both of which are uncomfortable, require constant contact and are usually expensive. The techniques for breathing rate monitoring include capnography and spirometery which involve breathing into tubes. Piezoresistive belts, in which a belt is placed around the chest for detecting its expansions and contractions, are also used for respiration measurement. All these methods are uncomfortable, require constant contact (inhibiting movement) and are expensive. Alternative devices should be non-invasive, more comfortable, cost effective, portable, reliable and accurate. Non invasiveness is especially important in case of infants, burnt victims, patients irritated by wires, belts, tubes etc. Long term healthcare monitoring devices such as sleep monitors or Heart Rate Variability (HRV) detectors (which involve 24-hour measurements) have a special demand for

comfortable and non-intrusive devices. Furthermore, there is also an interest in detecting the heart rate of commercial truck drivers, to determine the possibility of drug use and lack of sleep. Also for airport security, casinos and automatic teller machines there is a desire to screen unusual heart and physiological activity. Other applications include continuous monitoring of soldiers, firemen and police officers in dangerous and life threatening circumstances. All the above mentioned reasons have seen a surge of research in this area.

1.1.1 Benefits of Doppler radar Vital Signs Monitoring

Microwave Doppler radar is an extremely promising tool for monitoring the heart and breathing rate of patients with heart related illnesses, lung disorders, diabetes etc. As stated before the continuously attached and invasive nature of commercial vital sign monitors is off-putting to many patients. Doppler radar can be used to monitor vital signs in a completely non-invasive way and this will greatly improve the quality of care and mobility for such patients. Long term monitoring will especially become more feasible. This makes Doppler radar ideal for sleep monitoring applications. One of the extraordinary features of Doppler radar vital signs monitoring is that as the Doppler radar measures the mechanical movement of the heart, diseases that affect the mechanical movement of the heart but are not apparent in the electrical activity of the heart can be diagnosed. The Doppler radar can measure heart rate up to a distance of 2m, thus it can be used as surveillance equipment to detect people behind walls. It can be used to observe abnormal heart rates while questioning suspects. Long route truck driver heart rates can be tracked to detect signs of inability to drive properly for long periods of time. The heart rate of miners, police officers, firemen, and other security personnel can be monitored to determine their functioning ability under pressure and

threatening situations. Other applications include detecting people trapped under rubble or on the battlefield for signs of life [3].

A lot of research has been conducted on Doppler radar vital signs monitoring [3-9] which will be discussed in chapter 3. In this thesis the gaps found in the present research body have been filled.

1.1.2 Benefits of On-Body Vital Signs Monitoring

On-Body vital signs monitoring involves the monitoring of heart rate using antennas placed on the chest of a patient. These antennas can be attached directly on the body or on clothes seamlessly, and this makes them more comfortable and less invasive as compared to most commercial devices available. The best part of On-Body vital signs monitoring is that the communication system already present on the body for On-Body communication purposes can with a few modifications be used for vital signs monitoring. On-Body antenna monitoring is much more accurate and requires significantly less power than Doppler radars. The On-Body vital sign monitors can be placed permanently on the body or on the clothes worn by miners and security personal along with a transmitter unit. In this way the heart and breathing rate of these personnel can be continuously monitored and in the case of any disasters their situation can be assessed in a more informed manner. The other potential applications for this method are the same as those of Doppler radar vital signs monitoring. Minimal research [10-11] has been conducted on this exciting topic and this thesis will attempt to explore the feasibility of On-Body vital sign monitoring and find out the best parameters (frequency, power, antenna type, etc.) for accurate operation.

1.1.3 Benefits of Frequency Reconfigurable antennas

Recent years have seen rapid advancement in wireless communication technologies. Communication devices are now expected to be able to handle a wide range of standards and frequencies (e.g. GSM, UMTS, WiFi, PCS, Bluetooth). Designing separate antennas for each standard is very inefficient and has resulted in increased investigation of frequency reconfigurable antennas. Frequency reconfigurable antennas offer a number of advantages over wideband antennas with filters and multiple narrowband antennas [12]:

1) Compact Size

2) Similar Radiation Pattern across operating band

3) Efficient use of electromagnetic spectrum

4) Reduced effect of co-site interference and jamming.

Software defined radios and cognitive radios have a special demand of frequency reconfigurable antennas that have a wideband mode which scans the spectrum for availability and then switches to that particular narrowband frequency. [13-14]

Considering the advantages and uses of frequency reconfigurable antennas, significant research has been reported on it which is discussed in chapter 5. This thesis will introduce novel ways of achieving frequency reconfigurable operation.

1.1.4 Benefits of Pattern Reconfigurable antennas

Radiation pattern reconfigurable antennas provide the following significant advantages over conventional antennas [15]:

1) Avoid noisy environments.

2) Avoid electronic jamming.

3) Improve system gain and security.

4) Conserve energy by focussing on the intended direction.

5) Increase number of subscribers.

Pattern reconfigurable antennas can also be used for vital sign monitors. They can be used to target the chest of the desired person only and in the process reduce clutter and noise from the environment compared to an omni directional antenna. They can also be used to find out the directional location of the person and that information can lead to the transmission of the Doppler radar continuous waves in the correct direction. Due to its advantages over omni-directional antennas in certain applications, pattern reconfigurable antennas have been studied in detail and the discussion of this research can be found in chapter 6. In this thesis novel antenna designs for pattern reconfigurable operation are proposed.

1.2 Objectives

The aims and objectives of this project are to:

- Find out the effect of frequency, power, and antenna type on the accuracy of Doppler radar vital signs monitoring.
- Find out the effect of frequency, power, antenna type, polarization, body type, body position, antenna distance (from chest), signal processing techniques and antenna position (on body) on the accuracy of On-body vital signs monitoring. This will also include experiments on many people to verify accuracy of technique.
- Analyze the results obtained using proven statistical analysis techniques (such as Bland-Altman plots), SNR, linear regression, etc. and make conclusions.
- Investigate the feasibility of detecting Heart Rate Variability (HRV) using On-Body Vital signs monitoring technique.

- Develop CST Microwave studio heart, lung and chest movement models. Determine the effect of movement of these models on the reflection coefficient phase of an antenna attached parallel to the chest.
- Examine and develop novel techniques, to achieve frequency agility operation of wideband antennas, for use in cognitive radio. The antennas designed should have wideband, narrow band and notch band capability.
- Examine and develop novel techniques, to achieve radiation pattern reconfigurable operation of wideband antennas, for diversity purposes and vital signs monitoring.

1.3 Challenges

The most significant challenges in completing the project were:

- Developing novel ideas for original research.
- Respiratory and ECG module hardware setup and programming.
- Vector Network analyzer programming.
- Designing suitable antennas for vital signs monitoring.
- Measuring results from all devices (Respiratory module and ECG module) and VNA simultaneously for comparison.
- Statistical analysis.
- Digital Signal Processing (DSP) including filter design, spectral analysis, and fundamental frequency extraction.
- Delay times for CST Microwave studio simulations.
- Novel pattern and frequency reconfigurable antenna designs.

1.4 Contributions

1.4.1 Effect of parameters on On-Body vital signs monitoring

The heart and breathing rate were monitored considering the following parameters:

- Frequency (1-9 GHz)
- Antenna type (9 antennas)
- Power (-10 dBm to -45 dBm)
- Antenna location on body (7 locations)
- Body Position (2 positions)
- Distances (0 to 1 m)

These experiments were carried out for the first time in literature for the aforementioned parameters. Frequency variation has been studied briefly in literature but over a much smaller range and a different frequency band.

After statistical analysis conclusions were drawn on the best possible parameters for efficient operation. The reasons for improvement, worsening or indifference of results to the parameter changes were also discussed. These results can be found in chapter 4.

1.4.2 Human Body measurements and Heart rate variability (HRV) study

Measurements were carried on 13 people with different body types to confirm the accuracy and feasibility of the On-Body antenna vital signs monitoring technique.

HRV studies were also performed in the sitting and supine states on many subjects to determine the feasibility of HRV monitoring for On-Body antenna vital signs monitoring technique.

Both these studies have not been performed before in literature. These results can be found in chapter 4.

1.4.3 Simulation study of On-Body vital signs monitoring

A comprehensive simulation study was undertaken to investigate the effect on reflection coefficient phase of an antenna attached parallel to the moving chest of a person. This study included determining the effect on accuracy of monitoring for different:

1) Frequency

2) Distance (between chest and antenna)

3) Antenna ground size

The antenna was either considered to be stationary and the body moving or it was considered that the chest and antenna were stationary and only the heart was beating (moving) inside the chest. This type of study using CST Microwave studio has been conducted for the first time for On-Body vital signs monitoring. These results can be found in chapter 4.

1.4.4 Effect of parameters on Doppler radar vital signs monitoring

The heart and breathing rate accuracy were monitored for the following parameters:

- Frequency (1-17 GHz)
- Antenna type (Omni directional and Directional)
- Power (-10 dBm to -45 dBm)
- Distance (50 cm to 3m)

Certain frequencies have been studied in literature but with different antennas, people, equipment and conditions. This study used similar conditions, system, antennas and a much wider frequency range to establish the effect of frequency on the accuracy of the vital signs monitoring. A distance study has been done up to 2 m but not 3m. A power study was

conducted in [5] but in apnoea state which does not consider the effect breathing will have on heart rate monitoring at lower frequencies.

Conclusions were drawn on the best possible parameters for efficient and accurate operation of Doppler radar for vital signs monitoring. The reasons for improvement, worsening or indifference of results to the parameter changes were also discussed. These results are studied in chapter 3.

1.4.5 Digital Signal Processing (DSP)

Digital signal processing techniques were proposed to extract the desired data from the collected noisy signals. This included filter design, spectral analysis and fundamental frequency extraction techniques.

The novel aspects were the use of:

1) Wavelet signal processing to extract the heart rate.

2) Continuous Wavelet Transform (CWT) spectral analysis to obtain unique insights into the heart signal obtained from On-Body antenna vital signs monitoring.

The CWT resulted in excellent time and frequency resolution of the heart signal. The different DSP methods were compared to determine the most robust and accurate method for vital signs monitoring. DSP is studied in chapter 4.

1.4.6 Frequency Agile Antennas

Novel frequency agile coplanar waveguide (CPW) filters were designed that can be integrated with any CPW antenna to achieve frequency reconfigurability. One filter using switches achieved narrow band, notch band and wide band operations. A second filter using varactors gave a continuous narrow band mode of operation for wide frequency range. This varactor

filter could achieve both a narrowband and wideband operation. Both the filter designs could be applied to tapered slot antennas as well. Frequency agile antennas are discussed in chapter 5.

1.4.7 Pattern Agile Antennas

Novel pattern reconfigurable antennas were proposed and designed based on the Vivaldi structure. The antenna used a single port with 4 switches to achieve 4 quadrant pattern reconfigurable operation. These antennas were also shown to be useful in measuring heart rate of patients in any direction (along the 4 quadrants), while reducing the effect of clutter from the environment compared to an omni-directional antenna. They could potentially detect the location of a person as well. Pattern reconfigurable antennas are discussed in chapter 6.

1.5 Thesis outline

In Chapter 2 the physiological activities behind the circulatory and respiratory systems are discussed. The effect of these activities on surface chest movement is studied. Also, a brief description of the various methods used for heart rate and respiratory rate monitoring is provided.

Chapter 3 covers Doppler radar vital signs monitoring theory. In this chapter the feasibility of Doppler radar vital signs monitoring is investigated by conducting a study on several people. Mathematical analysis validating the use of Vector Network Analyzer (VNA) as a Doppler radar is presented. A parametric study is conducted to determine the best frequency, power and distance for accurate operation of Doppler radar.

In chapter 4 On-Body vital signs monitoring is investigated. In this chapter it is demonstrated that the reflection coefficient phase of a single antenna, attached parallel to a person's chest, is capable of monitoring the heart rate and the breathing rate of a person with excellent

accuracy. The effect of moving heart and chest models on the reflection coefficient phase of an antenna held parallel to the chest is investigated using simulations in CST Microwave Studio 2012. The effect of frequency, power, antenna type, body type, antenna distance, position of the antenna on the chest, etc. is investigated by performing experiments varying these parameters. A study involving 13 people in the supine and sitting state is conducted to determine the feasibility of monitoring vital signs using On-Body antennas. The feasibility of heart rate variability (HRV) calculation which involves variation in beat-to-beat intervals of heart is also examined. At the end of this chapter an analysis of the different DSP techniques used is also presented.

In chapter 5 frequency reconfigurable antennas are designed. A novel Coplanar Waveguide (CPW) band-pass filter using short circuit slotlines and varactor diodes is introduced. This band-pass filter when integrated with a CPW wideband antenna produces frequency agility with a wideband mode and a continuous narrowband mode. The design of another CPW filter based on a square ring resonator with switches is also shown and applied to a wideband antenna making it reconfigurable. Complete working and design principles along with simulated S-parameter results of the filters are presented. The simulated and measured reflection coefficient, radiation patterns and gain characteristics of the antennas incorporating the filters are also shown. A novel antenna having stop-band, narrow-band and wide-band modes is also proposed and designed.

In chapter 6 novel pattern reconfigurable antennas based on the Vivaldi structure are investigated, designed and tested. A novel single port antenna in which switches are used to switch between 4 radiation patterns is introduced. The radiation pattern, reflection coefficient and gain of this antenna are measured. The experimental and simulation results are presented and compared.

At the end there are conclusions and suggestions for future work in chapter 7.

1.6 References

[1] (http://www.who.int/cardiovascular_diseases/en/ ,2011)

[2] (http://www.lunguk.org/media-and-campaigning/media-centre/lung-stats-and-facts/factsaboutrespiratorydisease.htm , 2011)

[3] Byung-Kwon Park; Lubecke, V.; Boric-Lubecke, O.; Host-Madsen, A.; , "Cardiopulmonary Signal Sensing from Subject Wearing Body Armor," *Engineering in Medicine and Biology Society, 2007. EMBS 2007. 29th Annual International Conference of the IEEE* , vol., no., pp.366-369, 22-26 Aug. 2007

[4] D. Droitcour, O. Boric-Lubecke, V. M. Lubecke, J. Lin, G. T. A. Kovacs, "Range Correlation and I/Q Performance Benefits in Single-Chip Silicon Doppler Radars for Noncontact Cardiopulmonary Monitoring," *IEEE Transactions on Microwave Theory and Techniques*, Vol. 52, No. 3, , pp. 838- 848, March 2004.

[5] D. Obeid, S. Sadek, G. Zaharia and G.E Zein, "Multi-Tunable Microwave System for Touchless Heartbeat Detection and Heart rate variability Extraction," *Microwave and Optical Technology Letters*, vol.52, no.1, pp.192-198, Jan 2010.

[6] Massagram, W.; Lubecke, V.M.; Host-Madsen, A.; Boric-Lubecke, O.; , "Assessment of Heart Rate Variability and Respiratory Sinus Arrhythmia via Doppler Radar," *Microwave Theory and Techniques, IEEE Transactions on* , vol.57, no.10, pp.2542-2549, Oct 2009.

[7] Tariq, A.; Ghafouri-Shiraz, H. , "Noncontact heart rate monitoring using Doppler radar and continuous wavelet transform," *Microwave and Optical Technology Letters*, vol. 53, issue 8, pp.1793–1797, May 2011.

[8] Tariq, A.; Ghafouri-Shiraz, H.; , "Vital signs detection using Doppler radar and continuous wavelet Transform," *Antennas and Propagation (EUCAP), Proceedings of the 5th European Conference on* , vol., no., pp.285-288, 11-15 April 2011

[9] A.D. Droitcour, "Non-contact measurement of heart and respiration rates with single chip microwave Doppler radar," *Ph.D. Dissertation, Stanford University*, USA, July 2006.

[10] Serra, A.A.; Nepa, P.; Manara, G.; Corsini, G.; Volakis, J.L.; , "A Single On-Body Antenna as a Sensor for Cardiopulmonary Monitoring," *Antennas and Wireless Propagation Letters, IEEE* , vol.9, no., pp.930-933, 2010

[11] Tariq, A.; Ghafouri-Shiraz, H.; , "On-body antenna for vital signs and heart rate variability monitoring," *Antennas and Propagation Conference (LAPC), 2011 Loughborough* , vol., no., pp.1-4, 14-15 Nov. 2011

[12] Peroulis, D., K. Sarabandi, and P. B. K. Katehi, “Design of reconfigurable slot antennas,” *IEEE Transactions on Antennas and Propagation*, Vol. 53, 645–654, 2005.

[13] S.-H. Oh, J. T. Aberle, S. Anantharaman, K. Arai, H. L. Chong, and S.C. Koay, “Electronically tunable antenna pair and novel RF front-endarchitecture for software-defined radios,” *EURASIP J. Appl. Signal Processing*, vol. 2005, pp. 2701–2707, 2005.

[14] S. Yang, C. Zhang, H. K. Pan, A. E. Fathy, and V. K. Nair, “Frequency reconfigurable antennas for multiradio wireless platforms,” *IEEE Microwave Mag*., vol. 10, no. 1, pp. 66–83, Feb. 2009.

[15] Dong Jiawei; Li Yongxiang; Zhang Biao; , "A Survey on Radiation Pattern Reconfigurable Antennas," *Wireless Communications, Networking and Mobile Computing (WiCOM), 2011 7th International Conference on* , vol., no., pp.1-4, 23-25 Sept. 2011

2 Chapter 2

Heart and Respiratory Motion

Abstract— In this chapter the physiological activities behind the circulatory and respiratory systems are discussed. The effect of these activities on surface chest movement is studied. Also, a brief description of the various methods used for heart rate and respiratory rate monitoring is provided.

2.1 Introduction

Our goal in this thesis is to determine the heart rate and the breathing rate by measuring the chest movement (caused by the heart beats and lungs movement) with Doppler radar and On-Body antennas. In this chapter we will study the motion of the heart and lungs along with its effect on the chest. Heart Motion is discussed in section 2.2. In this section the effect of heart movement on the chest is also analyzed. Section 2.3 discusses the respiratory system motion and its effect on the chest. In section 2.4, vital signs and their usual monitoring techniques are presented. Finally there are conclusions in section 2.5.

2.2 Heart Motion

Blood is driven to tissues throughout the body by an involuntary muscle called the heart. The heart pumps blood through the tissues by rhythmic contractions. The periodic contractions are responsible for generating the pressure that drives the blood flow. This contraction results in

motion of the heart within the chest. When the heart strikes the chest during this motion a measurable displacement occurs at the skin surface [1].

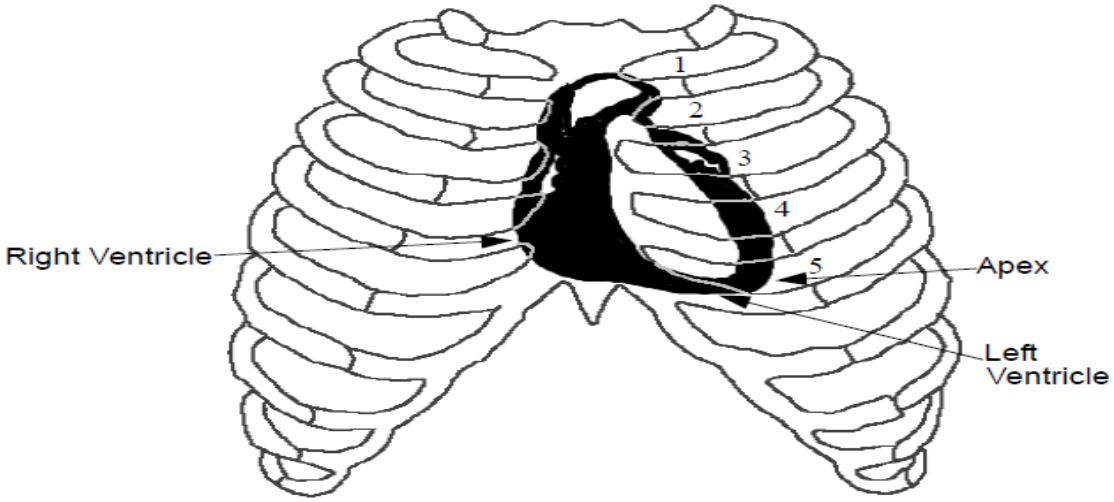

Figure 2.1: Location of the heart in the rib cage.

Lying in the middle of the thorax, the heart is covered by the lungs and covered by the sternum. The cartilages of the third, fourth, and fifth ribs also cover the front of the heart as shown in fig. 2.1 [2]. Two thirds of the heart is located on the left of the midline. The lowest superficial part of the heart is the apex. The heart is directed downward, forward and to the left. The motion of the apex could be felt at the fourth or fifth intercostal space, near the left mid-clavicular line [3]. The intercostal spaces are indicated in fig. 2.1 by the numbers 1-5.

Each side of the heart is responsible for providing blood to different parts of the body. The left side pumps blood to the organs and tissues, while the right side pumps blood to the lungs. Figure 2.2 [4] shows a diagrammatic section of the heart. Blood from peipheral tissues enters the right atrium from the vena cava. The tricuspid valve opens to allow blood from the right atrium to enter the right ventricle. The contracting of the right ventricle causes the pulmonary valve to open. This results in blood from the top of the right ventricle to enter the lungs through the pulmonary atery. In the lungs carbon dioxide is removed from the blood and

oxygen is introduced. This blood then re-enters the heart through two pulmonary veins into the left atrium and back of the heart. The mitral valve opens to allow the blood from the left atrium to enter the left ventricle. The contracting of the left ventricle opens the aortic valve and causes the blood to exit from the top of the heart into the aorta. From then on the blood is delivered to various tissues in the body through a system of arteries. This provides the tissues with nutrients and oxygen, and removes the waste products. This process is repeated periodically as our heart beat [5]. The heart rate is the number of processes (heartbeats) per unit of time, typically expressed as beats per minute.

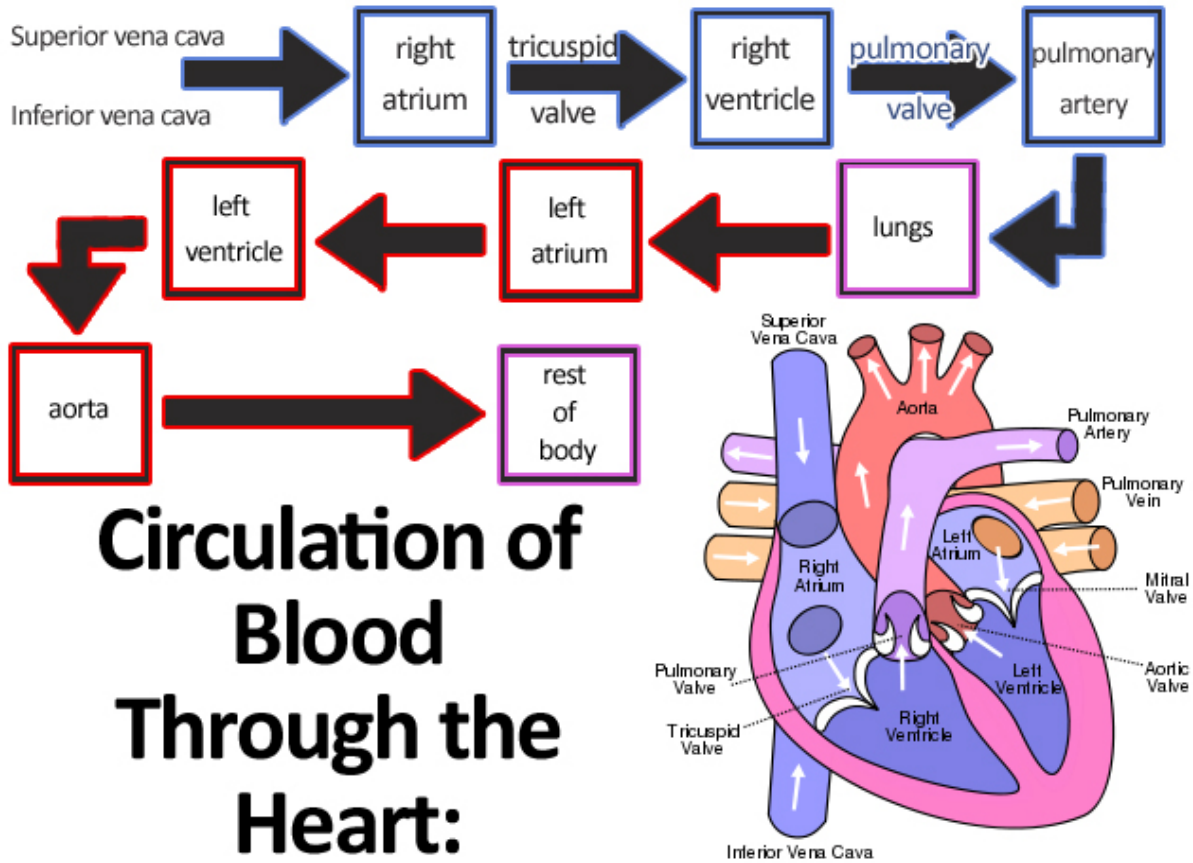

Figure 2.2: Diagrammatic section of the heart.

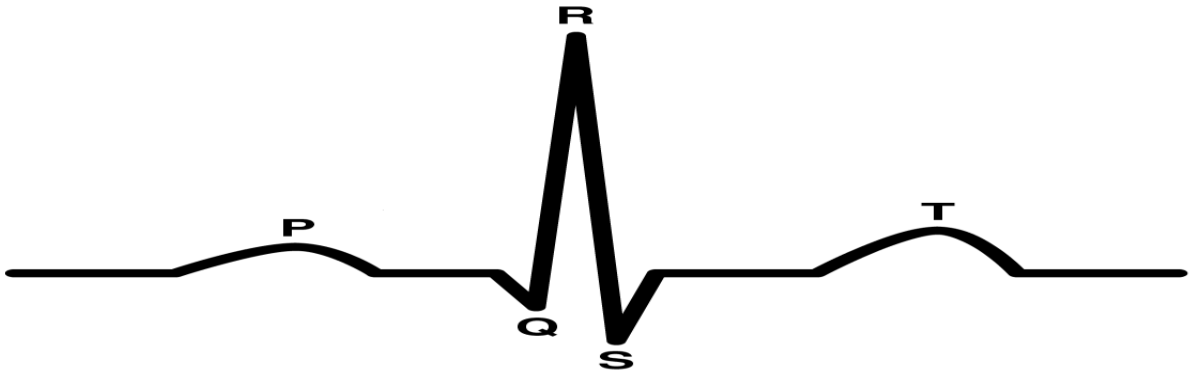

Figure 2.3: Output of an electrocardiogram.

2.2.1 Electrical impulses of the heart

The right atrium of the heart contains the pacemaker cells. These cells are directly responsible for the control of the heart rate. They generate the electrical impulses that synchronize the heart beating. These impulses cause both atria to contract simultaneously. After the atria both the ventricles contract simultaneously. The electrocardiogram (ECG) measures the electrical changes (voltage) on the skin caused by changes in membrane potential across cells in the heart. It measures this by mounting electrodes on the chest and limbs of the human subject. The waveforms that are seen in the electrocardiogram of Figure 2.3 are generated by the atria and ventricles. The atrial depolarization is represented by the P wave. This triggers artia contraction. The ventricular depolarization is represented by the QRS complex. This triggers ventricles contraction. The ventricular repolarisation is represented by the T wave. The atrial repolarisation is not visible in the ECG since it overlaps the QRS complex. Changing the placement of the electrodes on the body leads to the varying of the shapes and sizes of the P and T waves and the QRS complex. This is caused because different locations of the electrodes detect information about different areas of the heart.

2.2.2 Surface Motion due to the Cardiac Cycle

The depolarization of the heart as discussed in the previous section triggers atrial and ventricular contractions. This depolarization and polarization form a cycle of contractions. These contractions are responsible for the heart displacement and movements of the ribs and tissues near the heart. Particularly, the ribs and tissues move due to the changes in the shape and volume of the heart. These movements also cause the chest to move. The non-contact Doppler radar cardio-respiratory monitor and the On-Body vital signs monitor both can detect these chest movements and monitor the heartbeats.

The largest movement of the chest is caused by the contraction and relaxation of the left ventricle. During a state of the heart called isovolumetric contraction, the heart partially rotates counter clockwise and this results in the front of left ventricle hitting the chest. [6]. The contracting of the left ventricle causes the heart to become more circular resulting in bigger diameter of the heart that adds a push to the chest wall. The chest will pulse outward due to the left ventricular motion and then retract during ventricular ejection [7].The chest pulsing outwards due to left ventricular motion is called the point of maximal impulse (PMI). It is usually obvious, for any healthy patient, as a single outward motion but may not be visible for many patients over 50 years of age. It is also claimed that this outward motion might be weakened or unnoticeable for obese, muscular, and elderly patients [6]. Although there are some other motions in the left region of the chest, they are not as noticeable as the PMI. Furthermore, the motion of the right ventricle in healthy subjects is not detectable at all. That is why PMI is considered as the most significant heart action that causes chest displacement.

The position of the human subject, i.e. sitting, lying or standing up, affects the amount of the chest wall motion. The position of the subject is an important factor to be considered when measuring the displacement of the chest wall [6]. In addition, the physiological differences between people (age, body shape, and masculinity) influence the amount of motion at the skin surface for every individual. For example, the amount of chest movement due to heartbeats is affected by the age because the speed and intensity of the motion of the heart varies with age [6]. The maximum chest displacement detected was 1.2 mm by [7], and the maximum displacement using non-contact sensors has an average of 0.6 mm [1].

2.3 Respiratory Motion

During the respiration cycle carbon dioxide is removed from the lungs and oxygen is replenished. Contracting of muscles during respiration changes the thorax volume. This change causes pressure difference between thorax and the external environment resulting in air movement to and from the lungs (from areas of high pressure to areas of low pressure). The movement of the chest due to thorax volume change is quite significant. The non-contact Doppler radar cardio-respiratory monitor and the On-Body vital signs monitor can detect these movements and monitor the respiration rate.

Breathing is controlled subconsciously at the base of the brain. It continues when we sleep or when we are unconscious. Even though breathing is an automatic process, people can still control it. People can voluntarily hold their breath or control it whenever they want to speak, sing, etc. Normally, the brain monitors the blood and senses the amount of oxygen and carbon dioxide. When the amount of carbon dioxide increases, it stimulates the body to breathe more

deeply and often. In contrast, when the concentration of carbon dioxide is low, the body breathes less deeply and often .The healthy adult inhales and exhales, on average, about 15 times per minute [8].

2.3.1 Surface Motion due to Respiration

When we breathe, muscles contract and cause the chest wall to move outward. These muscles are shown in Fig. 2.4 and include the diaphragm, the intercostal muscles (the muscles between the ribs), the neck muscles, and the abdomen muscles. The diaphragm is the most important muscle. It is a sheet muscle that separates the abdomen from the chest cavity. It is located in the base of the sternum and binds to the lower side of the rib cage, and the spine.

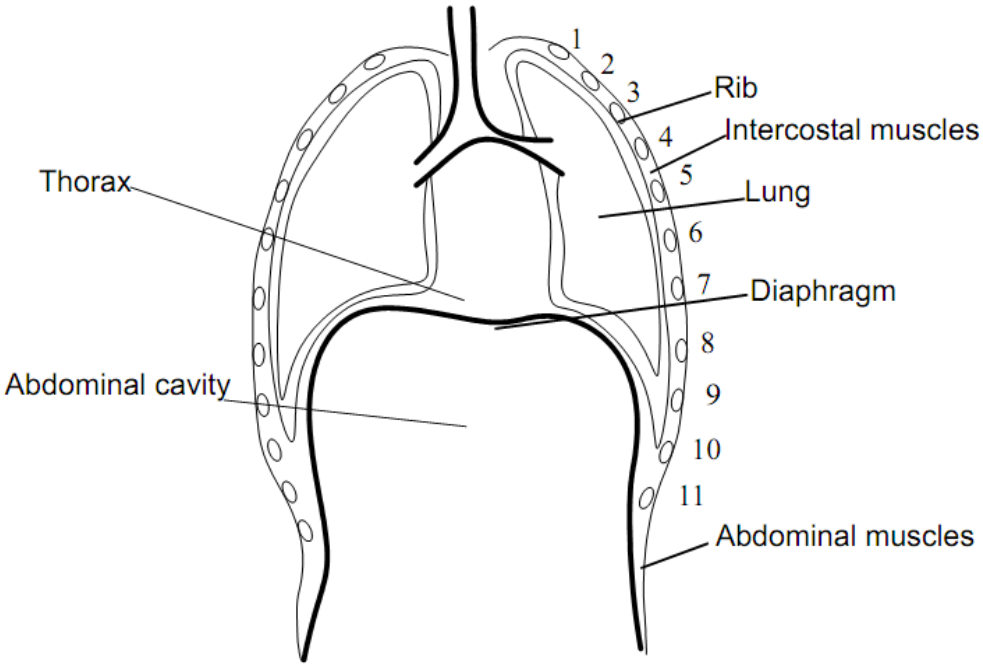

Figure 2.4: The thoracic wall and body cavities.[9]

Figure 2.5 shows the motion of the diaphragm during inhalation and exhalation. When the diaphragm contracts, it moves lower which enlarges the thorax and pushes the abdominal

viscera towards the abdominal wall. When the abdominal wall is stretched beyond a certain limit further contraction of the diaphragm causes the lower ribs to elevate. These movements lead to the reduction of thoracic pressure [10].

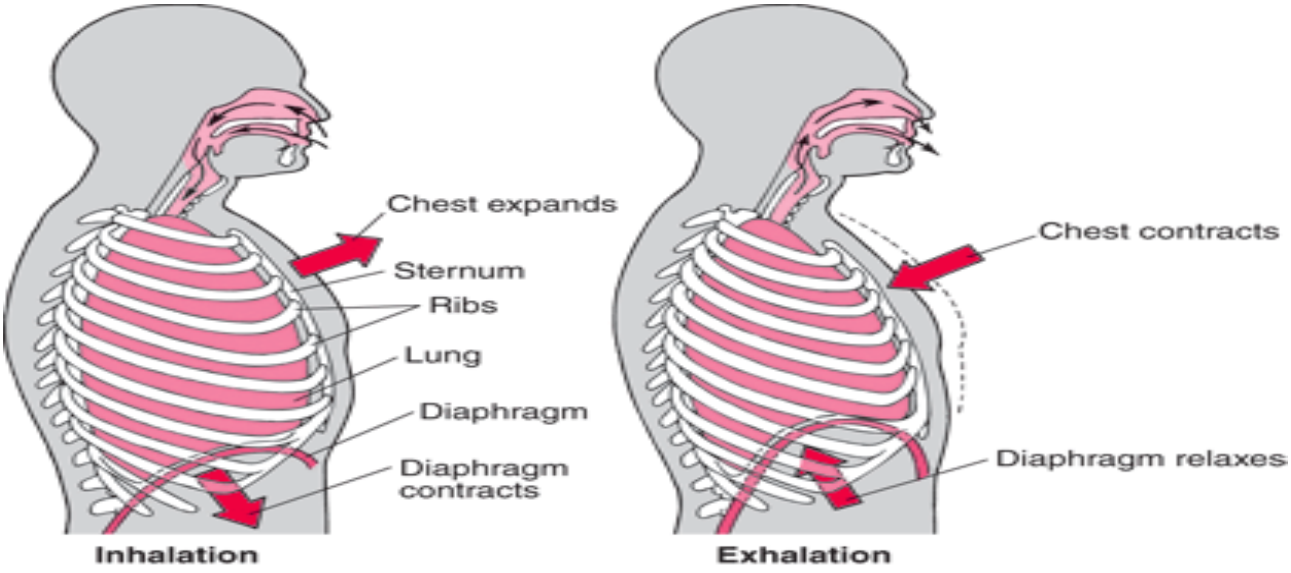

Figure 2.5: Diaphragm's role in breathing. [8]

The external intercostal muscles also contract with the diaphragm and pull the ribs upward and outward further increasing the thorax volume and decreasing the thoracic pressure. Air enters the lungs from the external environment in order to equalize the pressure. This is called inhalation, and it is noticeable by the expansion of the lungs. Exhalation occurs when the diaphragm relaxes and moves back up. The lungs and chest, which were stretched during inhalation, expel air out of the lungs. This is usually passive and occurs because of the elasticity of the lungs and chest wall, so no effort is needed to breathe out. Nevertheless, sometimes the abdominal muscles contract and push the relaxed diaphragm against the lungs, which causes the air to be pushed out. This usually occurs during energetic exercises[8]. The contraction of the abdominal muscles also causes the depression of the lower ribs and the

contraction of the internal intercostal muscles. The major movement of the surface of the chest is caused by the abdominal and the ribs movement as described. In general, the expansion of the chest due to breathing is between 4 and 12 mm [11]. Nevertheless, this expansion depends on the human subject physiology and how much air he inhales.

2.4 Vital Signs

Vital signs are physiological measurements recorded to assess the basic body functions. In most cases vital signs include the following four measurements [12]:

1. Pulse rate (or Heart Rate)
2. Respiration rate (Breathing Rate)
3. Blood pressure
4. Body temperature

Vital signs are generally recorded in clinical and emergency situations to determine what illnesses a person may have. The onset of certain physiological conditions can be determined by changes in vital signs. Vital signs are also used for general health monitoring during exercise. In this thesis alternate techniques for heart and breathing rate measurements are studied, so the focus is on pulse and respiration rate monitoring methods.

2.4.1 Pulse rate monitoring techniques:

Pulse rate is representative of the heart rate and rhythm. The heart rate in adults is normally between 50 and 90 beats per minutes [12]. Some people have heart rates slightly outside of this range, but a heart rate that is radically outside this range is an indicator of cardiac abnormalities. [12].

The most common method for measuring the heart rate is by using the electrocardiogram (ECG). The 3-lead electrocardiogram is usually employed for basic heart rate and rhythm monitoring, but 5 or 12 lead electrocardiograms provide more information. As the leads are placed on different points [13], various electrical depolarization paths can be monitored leading to the diagnosis of various illnesses. These illnesses include hypertrophy, ischemia, or necrosis, i.e. ECG is the gold standard of heart rate monitoring devices but has several disadvantages. Electrodes need to be attached to the person's skin via cables. These cables restrict movement and the electrodes themselves can cause irritation to the skin of certain patients especially burnt victims. Loose electrode connections can also bring about unwanted motion artefacts on the ECG signals. Moreover, since the voltage detected by the ECG is under 12mV if the skin of the patient is unclean or has a lot of hair (blocking electrical contact between skin and electrode) the results obtained can be incorrect.

Besides ECG, pulse oximeters which are attached to finger tips can also be used to measure pulse rates. Pulse oximeter monitors the oxygen saturation of the patient's blood. The monitored signal changes according to the heart rate as the arterial blood vessels it measures expand and contract with each heart beat.

Polar straps (electric chest straps) [14] are also used to monitor heart rate during exercises. They produce a pulse when an R-wave is encountered and using the timings of the generated pulses, the pulse rate is calculated. In this way they measure a bipolar electrocardiogram. It does not provide a true electro cardiogram and is inaccurate if skin under the strap is not moistened properly.

The heart rate can also be monitored either by measuring chest movement due to heart or by measuring the motion due to arterial pulses. Mechanocardiography involves the measurement of the mechanical movement of the chest due to heart.

Apexcardiography [15,16] uses a transducer to measure the chest movement at the apex compared to the rest of the chest. Positioning the device requires extreme care and is not reliable for repeatability.

The kinetocardiogram [15,16] measures the chest movement at the apex relative to a fixed point in space rather the rest of the chest. It is similar to the apexcardiogram in operation.

A displacement cardiograph [17] consists of a tuned circuit oscillator coil that is placed 5-15mm from the chest of a patient. Any change in the environment of the coil due to the vibratory motion of the chest causes a change in the frequency of oscillation of the coil which is compared with a reference frequency to produce a voltage. This voltage corresponds to the chest movement. The field of the coil can penetrate the chest tissue and thus the actual heart motion itself can be measured. The final result consists of the super imposing of both chest and heart motion. It is more sensitive compared to the apexcardiogram and kinectocardiogram.

The laser displacement method measures the heart rate by reflecting a laser beam off the chest wall and measuring the displacement. As the laser cannot penetrate clothing, this technique needs the patient to be unclothed.

The ballistocardiograph [18] measures the heart rate by attaching an accelerometer to the patient's chest. It requires the device to be attached to a moving part of the chest.

In this thesis Doppler radar and On-body antennas are used to monitor the heart rate. Doppler radar can operate through clothing and can also measure the heart and breathing rate simultaneously. The heart rate is extracted using filtering.

The On-body antenna method monitors the heart rate by detecting motion in the proximity of an antenna attached parallel to the chest. Chest movements are modulated on the reflection coefficient phase of the antenna and using signal processing the heart rate can be extracted. It

can also operate through clothing and measures both the heart and breathing rate simultaneously. The antenna has to be attached to the chest or kept up to 20mm away from the chest to monitor the heart rate while the breathing rate can be monitored up to 1m away from the chest.

Doppler radar can work up to 2 m away from the chest and is the only technique that can work through clothing and measure both heart and breathing rates simultaneously from a distance. On-Body Antenna technique can also work through clothing, measure both heart and breathing rates, but requires contact or needs to be just 20mm away for heart and 1m away for breathing rate measurements. It requires minimal equipment and is more accurate than Doppler radar.

2.4.2 Respiration rate monitoring techniques:

The normal respiration rate in adults is 16 to 24 breaths per minute [12]. It can go down to 8 breaths per minute for very healthy people, but a respiratory rate out of this range is usually an indicator of respiratory system problems. Breathing rate, pattern, effort, and volume of respiration together can provide a clear picture of respiratory physiology.

Respiration can be measured by:

1) Measurement of air-flow

2) Measurement of chest movement or effort due to respiration

3) Oxygen Saturation Measurement

Direct air-flow measurement is achieved by using face masks. Face masks change the normal breathing pattern of the subject but can detect total gas volume during inhalation and exhalation. Capnography and thermocouple can indirectly measure the airflow and disturb the

normal breathing pattern much less as compared to face masks. They however cannot detect the volume of air flow.

Thermocouples [19] measure the respiration rate by detecting the temperature in front of the mouth or nose. Inhaled air is cool while exhaled air is warm. The difference between the two with time gives an indication of respiration rate. Capnography [19] involves an infrared analyzer placed in front of the mouth. This analyzer can detect the difference between the CO_2 levels of exhaled and inhaled air. It is frequently used in sleep laboratories.

Pulse oximetry [20] devices measure the oxygen saturation of blood. They are incapable of measuring respiration rate or flow but can measure respiratory disturbances.

Surface measurement of breathing rate can be done in two ways: either by detecting the linear displacement of the thorax or the abdomen, or determining the circumference or area of the thorax region.

Plethysmography involves the measurement of change in volume of various organs or parts of the body. These measurements give rise to respiration waveforms from which the rate can be calculated. Plethysmographs cannot measure exact respiratory volume.

They usually include:

1) inductance plethysmograpy

2) Impedance plethysmography

3) Strain Gauges

4) Piezoelectric strain gauge

In respiratory inductance plethysmograpy[21], wire coils attached to elastic bands surround the chest. The expansion and contraction of the chest due to breathing changes the inductance of the coils and gives an indication of the respiration rate.

In Impedance plethysmography[21], electrodes are attached on the subject's skin. During respiration, chest movement causes the impedance between the electrodes to alter which is measured. This alteration directly corresponds to the respiration waveform.

Strain gauges [22] measure the expansion and contraction of the chest or abdomen and can translate this into respiration waveform.

Piezoelectric resistive belts produce a voltage when stretched due to the chest or abdomen movement during respiration.

Linear displacement of the thorax or abdomen can be detected using a laser sensor. A laser sensor targets a point on the chest and measures the time it takes for the laser to reflect back to determine the distance. This distance when plotted over time gives the respiration wave. The advantage of laser sensor is that no resistance to breathing is imposed but the target person cannot be clothed as the laser cannot penetrate clothing. Multiple lasers to target multiple points are proposed so that the volume of respiration can be modelled as well.

Doppler radar can detect the respiration rate with clothing and does not impose any breathing restriction. Similarly On-Body antenna monitoring does not impose any restrictions as the antenna is attached using tape, a clip on, i.e. or is kept up to 1 m away from the chest. It can work through clothing and is extremely accurate.

2.5 Summary

The heart is the muscle that provides blood to various parts of the body through blood vessels. The respiratory system removes air filled with carbon dioxide from the lungs and replaces it with air filled with oxygen. Together the heart rate and the breathing rate constitute the vital signs and provide invaluable knowledge regarding the health status of a person.

The movement of the left ventricle of the heart within the chest is the primary cause of movement of the chest due to heart beats. The chest movement due to heart is about 0.6 mm [1]. The contraction of the diaphragm during inhalation causes air to flow into the lungs and pushes the abdomen and ribs outward. This causes the expansion of the chest due to respiration which is between 4 and 12mm [11]. The chest movements due to heart beating and breathing can be detected using Doppler radar and On-Body antenna vital signs monitoring techniques.

The normal heart rate is between 50 and 90 beats per minute [12]. The 12 lead ECG is the most accurate method of monitoring the heart rate. Other methods include pulse oximetry devices and polar straps. Mechancardiography measures the heart rate by detecting movement of chest due to heart beats. In addition to this, direct heart movement measurements and arterial pulse movements can also provide information about heart rate. These methods include apexcardiography, kinetocardiography, displacement cardiography, laser displacement sensors, and ballistocardiographs.

The normal respiration rate is between 16 to 24 breaths per minute [12]. Respiration rate can be measured by considering air flow, chest movement due to respiration or oxygen saturation of blood. Face masks provide direct respiration rate measurement but inhibit normal breathing. Capnography measures CO_2 levels while thermocouples measure temperature levels outside the mouth to determine respiration rate. Pulse oximetry can determine respiratory disturbances rather than respiratory rate. Respiration rate can also be calculated by determining the thorax volume or circumference change during breathing. The methods normally used for these measurements include inductance plethysmograpy, impedance plethysmography, strain gauges, piezoelectric transducer belts and laser displacement sensors.

The usefulness of the Doppler radar stems from the fact that it can monitor both the heart and breathing rate simultaneously up to a distance of 1 m with clothes. It does not inhibit movement and is non-invasive. Its accuracy and reliability will be discussed in chapter 3.

The On-Body vital signs monitors can also detect both the heart and breathing rate simultaneously. It can be attached to clothes, skin or be kept up to 20mm away from the target chest for heart rate measurements and 1 mm away for breathing rate measurements. It does not inhibit movement and is also non invasive. It is much more accurate and reliable than the Doppler radar monitor as will be seen in chapter 4.

2.6 References

[1] A.D. Droitcour, "Non-contact measurement of heart and respiration rates with single chip microwave Doppler radar," *Ph.D. Dissertation, Stanford University, USA*, July 2006.

[2] Flint, Practical Treatise on the Diagnosis, Pathology, and Treatment of Diseases of the Heart, Philadelphia: Blanchard Lea, 1859.

[3] Schlant, R. C., Silverman, M.E., and Roberts, W. C. (1990). The Heart, Arteries, and Veins. San Francisco: McGraw Hill. pp. 14-35.

[4] [http://en.wikipedia.org/wiki/Heart, Accessed 10 may 2011]

[5] A. Vander, J. Sherman, and D. Luciano, Human Physiology: The Mechanisms of Body Function, Seventh Edition, San Francisco: McGraw Hill, 1998

[6] E. Braunwald and J. K. Perlkoff, "Physical examination of the heart and circulation," in Heart Disease: A Textbook of Cardiovascular Medicine, (E. Braunwald, D. P. Zipes, and P. Libby, Eds.), New York: W. B. Saunders Company, 2001, pp.45-81.

[7] P. M. S. Gillam, A. A. Deliyannis, and J. P. D. Mounsey, "The left parasternal impulse," British Heart Journal, vol. 26, pp. 726-736, 1964.

[8] The Merck Manual Home Health Handbook, 2011. Control of Breathing [online] (Updated August 2006) Available at:http://www.merckmanuals.com/home/print/sec04/ch036/ch036e.html [Accessed 8 August 2011].

[9] D. G. Osmond, "Functional anatomy of the chest wall," in The Thorax, (C. Russo, Ed.), New York: Marcel Dekker, Inc., 1995, pp. 413-444.

[10] J. R. Rodarte and F. R. Shardonofsky, "Respiratory system mechanics," in Textbook of Respiratory Medicine, 3rd ed., (J. F. Murray and J. A. Nadell, Eds.), New York: W.B. Saunders Company, 2000, pp. 91-117.

[11] D. Obeid, S. Sadek, G. Zaharia and G.E Zein, "Multi-Tunable Microwave System for Touchless Heartbeat Detection and Heart rate variability Extraction," *Microwave and Optical Technology Letters*, vol.52, no.1, pp.192-198, Jan 2010.

[12] D. L. Gorgas, "Vital signs and patient monitoring techniques," in Clinical Procedures in Emergency Medicine: 4th ed., (J. R. Roberts and J. R. Hedges, Eds.), Philadelphia,: Saunders, 2004, pp. 3-28.

[13] L. Goldberger, Clinical Electrocardiography: A Simplified Approach, Chicago: Mosby, 1999.

[14] M. Scanlon, "Acoustic monitoring of first responder's physiology for health and performance surveillance," *Proceedings of the SPIE*, vol. 4708, pp. 342-353, 2002.

[15] W. H. Bancroft Jr. and E. E. Eddleman Jr., “Methods and physical characteristics of the kinetocardiographic and apexcardiographic systems for recording low-frequency precordial motion,” *American Heart Journal*, vol. 73, no. 6, pp.756-764, 1967.

[16] E. Braunwald and J. K. Perlkoff, “Physical examination of the heart and circulation,” in Heart Disease: A Textbook of Cardiovascular Medicine, (E. Braunwald, D. P. Zipes, and P. Libby, Eds.), New York: W. B. Saunders Company, 2001, pp.45-81.

[17] T. R. Fenton and R. Vas, “Measuring characteristics of the displacement cardiograph,” *Medical and Biological Engineering*, vol. 11, no. 5, pp. 552-558, 1973.

[18] P. Mounsey, “Precordial ballistocardiography,” *British Heart Journal*, vol. 19, pp. 259-271, 1957.

[19] B. A. Phillips, M. I. Anstead, and D. J. Gottlieb, “Monitoring sleep and breathing: methodology; Part I: Monitoring breathing,” *Clinics in Chest Medicine*, vol. 19, no. 1, pp. 203- 212, 1998.

[20] G. Ramachandran, M. Singh, "Three-dimensional reconstruction of cardiac displacement patterns on the chest wall during the P, QRS, and T-segments of the ECG by laser speckle interferometry," *Medical and Biological Engineering and Computing*, vol. 27, no. 5, pp. 525-530, 1989.

[21] H. R. Gribbin, “Using body surface movements to study breathing,” *Journal of Medical Engineering and Technology*, vol. 7, no. 5, pp. 217-223, 1983.

[22] P. J. Fadel, S. M. Barman, S. W. Phillips, and G. L. Gebber, “Fractal fluctuations in human respiration,” *Journal of Applied Physiology*, vol. 97, pp. 2056-2064, 2004.

3 Chapter 3

Vital signs Monitoring using Doppler Radar

Abstract: In this chapter the feasibility of Doppler radar vital signs monitoring is investigated by conducting a study on several people. Mathematical analysis validating the use of Vector Network Analyzer (VNA) as a Doppler radar is presented. A parametric study is conducted to determine the best frequency, power and distance for accurate operation of Doppler radar.

3.1 Introduction

As stated in section 1.1 the current methods for heart and breathing rate monitoring are either expensive or uncomfortable, or both. There is a need for alternative methods that are non-invasive, more comfortable, cheap, portable, reliable and robust. The above mentioned reasons have resulted in a surge of research in this area [1-12].

In this chapter we will use a non-contact Doppler radar to detect vital signs of a person and investigate the effect of frequency, power and distance on the accuracy of Doppler radar vital signs monitoring. A study involving several people will also be conducted to verify its accuracy and working across a variety of body types. All these experiments will give an idea of the ideal design considerations for a practical device.

The objective of this research is to establish whether this technique is capable of detecting the vital signs of a person in a controlled environment. If it is capable with suitable accuracy, then this method may replace the already existing apparatus such as ECG and plethysmography

devices for heart rate monitoring; capnography, spirometery and piezoresistive belts for breathing rate monitoring. Other objectives included finding out the best parameters (frequency, power etc.), so that a prototype considering those parameters can be designed in the future.

In section 3.2, a mathematical analysis validating the use of Vector Network Analyzer (VNA) as a Doppler radar is presented. Furthermore the general experimental setup is established. Sections 3.3, 3.4, and 3.5 contain the results and discussions of the effect of frequency, power, and distance on the accuracy of Doppler radar vital signs measurement. Section 3.6 presents the experimental results and discussions of the Doppler radar study on several people. Finally in Section 3.8 there are conclusions.

3.2 Literature Review

Microwave Doppler radar is a promising tool for monitoring the heart and breathing rate of patients with heart related illnesses, lung disorders, diabetes etc. ECG improves the quality of care for burn victims and infants. Non-invasive monitoring devices do not require physical wires, allowing freedom of movement for patients so that their daily routine is not affected. Along with the above mentioned uses Doppler radar has been used for detecting people under rubble or on the battlefield even with armor [3].

A 0.25 μm silicon chip with a 2.4 GHz Doppler radar was used in Ref. [4] to measure the vital signs. With a direct conversion transceiver accuracy within 3 beats per minute (of reference device) of 40% to 100% was achievable. It was found out that the limiting factor was the occurrence of null points. Null points are caused when the sinusoidal signal has got zero magnitude making phase difference calculation impossible. This was remedied using a quadrature (I/Q) receiver that ensured that if one channel was at null point the other channel

would be at optimum point. This resulted in an accuracy always greater than 80%. Besides this the range correlation effect was also tested experimentally. D. Obeid [5] used VNA as a tunable Doppler radar with frequency as the tuned parameter. It was demonstrated that in apnea state, as the frequency increases the variation of the phase due to chest motion increases. A smoothing algorithm based on Newton's binomial was shown to improve the performance of the Doppler radar system employed. A transceiver operating in the Ka band with low power (12.5 μW) double sideband signal transmission was used to eliminate the null point problem in [6]. The null points were removed by ensuring a proper frequency separation. This system gave accuracy above 80%. Indirect-conversion receiver improved the detection accuracy and Signal-to-Noise ratio (SNR) by lowering the dc offset and 1/f noise. The Ka-band improved the sensitivity of the Doppler radar to minute movements due to shorter wavelengths. Heart rate variability and Respiratory Sinus Arrhythmia was calculated in [7] using Doppler radar for a population comprising of 12 human subjects in both the supine and sitting position. The radar system was comprised of a direct conversion quadrature transceiver which employed linear demodulation. It was observed that in the supine position much better agreement was obtained between the radar system and reference ECG device. Human cardiopulmonary radar crossection (RCS) was measured in [8] using a Doppler radar. The noise and clutter in the received signal were removed by using a center estimation algorithm with dc-cancellation.

Theoretical SNR considering the residual phase noise, baseband 1/f noise and additive white Gaussian noise (AWGN) was calculated in [9]. This theoretical model was justified using experimental analysis conducted on 22 people. It was observed that improving the SNR resulted in improved accuracy. A parametric study was conducted by the author considering the distance between radar and the person under test and frequency of the Doppler radar

system [10, 11]. It was found that decreasing distance and increasing frequency in the UWB range resulted in improved accuracy. Besides this Wavelet based signal processing techniques were used to provide unique insights into the signal and detect vital signs accurately.

A detailed examination of the theoretical, mathematical and experimental analysis along with realistic uses and limitations of the Doppler radar for heart beat detection can be found in [12].

There are some gaps in the literature concerning the effect of frequency and power. Previous studies have either involved different systems (antennas, chips, VNAs) or been conducted in the apnea state (no breathing). It has been endeavored to fill those gaps by this extensive study. The next section contains a mathematical overview of the system used.

3.3 Principle and Mathematical Analysis

The human chest moves on average approximately 0.2mm to 0.5mm because of the heart beating and 8mm to 12mm because of the respiration cycle [5]. These movements form a quasi periodic motion. According to Doppler theory, when a surface has zero net velocity but a time varying position, a wave reflected from it will have its phase modulated proportionally to that time varying position [4]. Hence, when the continuous wave (CW) from the Voltage Network Analyzer (VNA) at a certain frequency is incident upon the chest it is reflected with the quasi periodic motion modulated on it. The reflected signal in its base band form contains information about the chest motion from which heart and breathing rate can be extracted using signal processing.

A CW signal *T(t)* with an amplitude A and a carrier frequency *f* is transmitted from a VNA. It is given by:

$$T(t) = A\cos(2\pi ft + \phi(t)) \tag{3.1}$$

where t is the elapsed time and $\phi(t)$ is the phase noise introduced by the VNA. This wave travels towards the target chest at a distance d and after reflection contains the chest movement $x(t)$ modulated on it. The total distance travelled by the wave is equal to $2d$. This results in the signal received at the receiver antenna of the VNA to be given by:

$$R(t) \approx \cos(2\pi ft - \frac{2\pi}{\lambda}(2x(t) + 2d) + \phi(t - \frac{2d}{c}) + \theta_x)$$

$$R(t) \approx \cos(2\pi ft - \frac{4\pi x(t)}{\lambda} - \frac{4\pi d}{\lambda} + \phi(t - \frac{2d}{c}) + \theta_x) \quad (3.2)$$

where λ is the carrier wavelength and $\phi(t - \frac{2d}{c})$ is the phase noise after time shift and θ_x is the constant phase shift due to the reflection at the body surface. In the case of VNA this returned signal is down-converted to an IF ($f_{IF} = f_{RF} - f_{LO}$) depending on the value set by the user. This results in a down-converted signal given by:

$$R_{IF}(t) \approx \cos(2\pi f_{IF} t - \frac{4\pi x(t)}{\lambda} - \frac{4\pi d}{\lambda} + \theta_o + \theta_x + \phi(t) - \phi(t - \frac{2d}{c}))$$

$$R_{IF}(t) \approx \cos(2\pi f_{IF} t - \frac{4\pi x(t)}{\lambda} + \theta + \Delta\phi(t)) \quad (3.3)$$

where $\theta = (\frac{4\pi d}{\lambda} + \theta_o + \theta_x)$ and depends on the distance from the target, θ_o depends on the phase shift introduced by the distance between mixer and the antenna among other factors [4]. $\Delta\phi(t) = \phi(t) - \phi(t - \frac{2d}{c})$ is equal to the residual phase noise.

After this the IF signal is digitized and this is given by [13,14]:

$$R_{IF}(n\Delta t) \approx \cos(2\pi f_{IF} n\Delta t - \frac{4\pi x(n\Delta t)}{\lambda} + \theta + \Delta\phi(n\Delta t)), n = 1,2,3,4..... \quad (3.4)$$

where n represents a point on the digital signal $R_{IF}(n\Delta t)$. The $R_{IF}(n\Delta t)$ signal is then demodulated using I/Q demodulation. The signal is divided into two parts for I/Q demodulation, one is down-converted to baseband without any phase shift and the other is down-converted after passing through a 90^0 phase shift. Any phase shifting combination such as [45^0 ,-45^0] , [0^0 , 90^0], etc. can be used as long as the phase shift between the two baseband signals is 90^0. This creates the following two baseband signals:

$$B_I(n) \approx \cos(\frac{4\pi x(n)}{\lambda} + \theta + \Delta\phi(n)), n = 1,2,3,4..... \quad (3.5)$$

$$B_Q(n) \approx \sin(\frac{4\pi x(n)}{\lambda} + \theta + \Delta\phi(n)), n = 1,2,3,4..... \quad (3.6)$$

From the I/Q demodulated signals, the phase can be extracted using small angle approximation, arctangent demodulation, principal component combining etc. [12]. In the VNA used (HP 8722D) arctangent demodulation is used. The phase can be extracted using arctangent demodulation by using the following equation:

$$\Delta\theta = \arctan(\frac{B_Q(n)}{B_I(n)}) = \arctan\left[\frac{\sin(\frac{4\pi x(n)}{\lambda} + \theta + \Delta\phi(n))}{\cos(\frac{4\pi x(n)}{\lambda} + \theta + \Delta\phi(n))}\right] = \frac{4\pi x(n)}{\lambda} + \theta + \Delta\phi(n) \quad (3.7)$$

If the residual phase noise can be neglected the final output is directly proportional to the chest motion $x(n)$:

$$\Delta\theta \propto \frac{4\pi x(n)}{\lambda} \quad (3.8)$$

From equation 3.8 the heart and breathing rate can be extracted.

Accurate demodulation of quadrature outputs is necessary for correct measurement of vital signs. One of the major hurdles for accurate demodulation is the presence of large DC offsets. The DC offsets act as a linear transform on the I and Q components in equation 3.7.

This equation thus becomes:

$$\Delta\theta = \arctan\left[\frac{V_Q + \sin(\frac{4\pi x(n)}{\lambda} + \theta + \Delta\phi(n))}{V_I + \cos(\frac{4\pi x(n)}{\lambda} + \theta + \Delta\phi(n))}\right] \tag{3.8}$$

where V_I and V_Q are the DC offsets. The DC offsets are present because of finite port to port isolation of the VNA as well as because of clutter reflections. Details of how to remove DC offsets and residual phase noise can be found in [4] and [12].

3.4 Setup and Methodology

In section 3.4.1 the equipment used for Doppler radar vital signs monitoring will be introduced. The signal processing techniques used to analyze the collected data will be described in 3.4.2. Then the different methods used for the statistical analysis of collected data will be presented in section 3.4.3.

3.4.1 Experimental equipment and Setup

Fig. 3.1 shows the experimental setup of the employed Doppler radar system for vital signs monitoring. The basic components comprising the Doppler radar vital signs monitor include HP 8722D or R&S ZVA67 vector network analyzer (VNA) and two horn antennas. The phase noise is less than -35 dBc for HP8722D VNA at the frequencies used. The noise level for R&S ZVA67 is less than -118dbm at the frequencies used. These values were extracted from the relevant datasheets. The horn antenna model was WBH1-18S and its datasheet is placed in

Appendix A. The main aim was to determine the best parameters including frequency, power, etc. for the most accurate operation of the Doppler radar as a vital signs monitor. The VNA presented the obvious choice to perform this study as a wide range of these parameters is provided by a VNA and they can be varied very easily. The VNA was programmed using Microsoft Visual basic and it was connected to a Laptop using a GPIB-to-USB converter. The antennas were 20 cm apart and were directed towards the chest of the person under test.

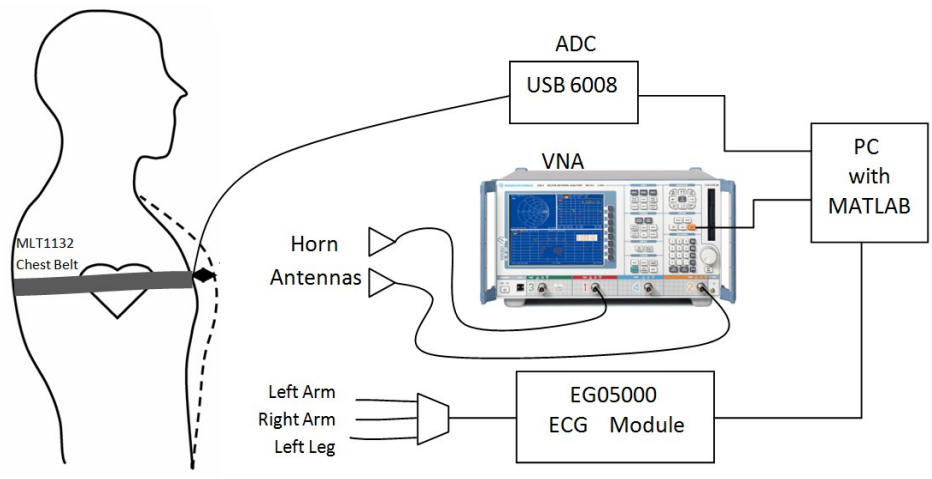

Figure 3.1: General experimental setup showing the VNA, chest belt and ECG monitor.

ECG module EG05000 from Medlab was used as a reference device for heart rate measurement. It has built in isolation, filtering and amplification. Three electrodes were used and were placed at the ends of the left arm, right arm and left leg as shown in Figure 3.2. Electrodes used were commercially available MLA1010B Disposable Ag/AgCl ECG Electrodes. The EG05000 communicated with the PC through a USB connection and it was programmed in C programming language.

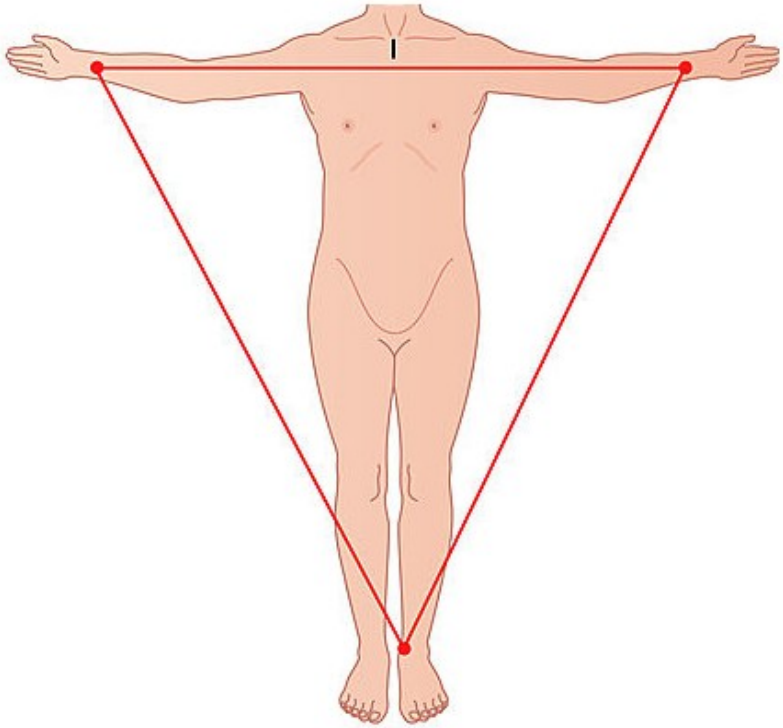

Figure 3.2: ECG electrodes placement on the left arm, right arm, and left leg.

MLT1132 Respiratory Belt Transducer from AD-Instruments was used as reference for breathing rate measurement. The belt was placed either on the chest or the abdomen depending on where maximum displacement due to breathing was observed. The analog signal from the belt was converted into a digital signal and input into the PC through a USB using 12-Bit, 10 kS/s NI-USB 6008 device.

The person under test was wearing normal clothing. He/She was then told to sit down on a chair with the antenna pointed towards his/her chest at different distances. He/She was asked to refrain from moving or talking for the duration of the experiment. The position of the person was adjusted by considering whether the breathing signal was visible on the VNA when the person was breathing normally, and whether the heart signal was visible on the VNA when the person was in apnea state. For the actual experimental measurements, he/she was told to breathe normally for the duration of 5 minutes. All of the experiments were

performed in normal lab environment. Normal lab comprised of equipment with various dielectrics scattered throughout the lab, but only the person conducting the experiment and the person being experimented on were allowed in the lab.

3.4.2 Signal processing

A comprehensive analysis of the signal processing regime chosen (including the filters, window length and spectrum analysis algorithm) can be found in appendix B. The Digital Signal Processing (DSP) techniques employed here were used for noise removal and extraction of the breathing and heart rates from the signals obtained via the VNA, ECG, and chest belt. For the VNA vital signs detection, the first step involved separating the heart and breathing signal. To achieve this the signal obtained from the VNA was passed first through a Butterworth 6^{th} order highpass filter with cutoff at 0.7 Hz after which it was passed through a Butterworth 8^{th} order lowpass filter with cut off at 5 Hz. The orders of the filters were chosen by considering the most accurate results obtained from the analysis of collected data. After filtering, over a 10 second window the heart rate was calculated using Fast Fourier Transform (FFT). The peak spectral power in the range from 0.7-2 Hz was chosen as the Heart rate frequency. The cutoff values were chosen based on the average maximum and minimum heart rates. A 10 second window was found the most adequate to accurately detect the heart rate, even though it was detectable in smaller and larger windows. Then this 10 second window is moved forward by one second and the same procedure is applied. This continues up to the end of the signal obtained from the VNA. FFT was chosen after the data analysis results for autocorrelation, FFT and continuous wavelet transform algorithms revealed it to be the most accurate. The ECG rate was found by using peak detection to find the R points (as discussed in section 2.2.1.). After this the mean of the inverted time differences between the R points for

a 10 second window gave the heart rate for that window. For both ECG and Doppler radar heart rate estimation, the heart rate was calculated every second by moving a 10-second window forward by one second and then averaging over the previous 8 windows. The reason for averaging over 8 windows was because that was the normal averaging procedure seen in commercial devices.

The respiration rate detection from the Doppler radar involved finding the peak spectral power of the Fast Fourier transform of a 15 second VNA signal window in the 0.1 to 0.6 Hz frequency range without filtering. This window is then moved forward by one second and the same procedure is applied again.

The respiration rate from the MLT 1132 Chest belt was calculated by first passing the signal from the chest belt through an 8^{th} order low pass filer with a cut off at 0.9 Hz. From the filtered signal, the peak spectral power in the 0.1-0.6 Hz range was detected. This 15 sec window is then moved forward by one second and same procedure followed again. Both the respiration rates (from the chest belt and Doppler radar) are averaged over previous 8 windows. The reason for choosing a 15 second window for the respiration signal case was that it has a lower frequency than heart signal and this requires a larger window for accurate capturing of required information. The maximum and minimum cut off rates for breathing rate were based on the maximum and minimum average breathing rates. The cut off frequency and the order of the low pass filter was based on the best results of the data analysis. The reason for averaging over 8 windows was because that was the normal averaging procedure seen in commercial devices.

The block diagram of all these signal processing algorithms is shown in Figure 3.3.

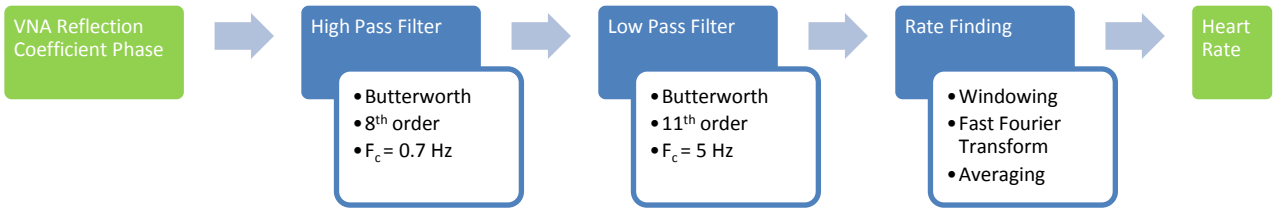

(a)

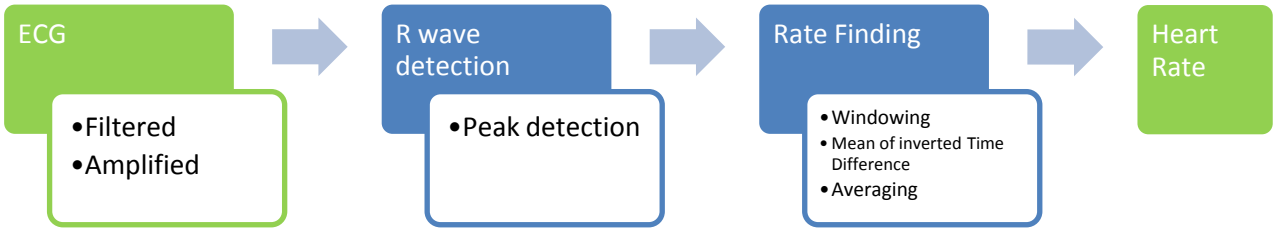

(b)

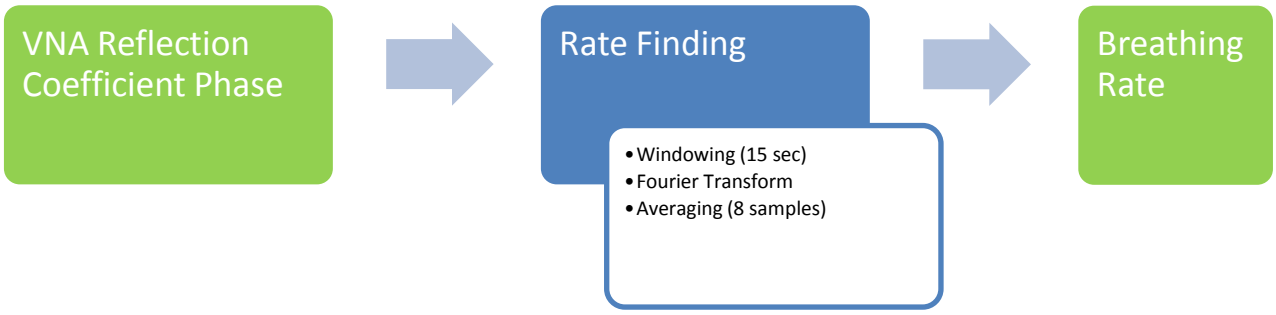

(c)

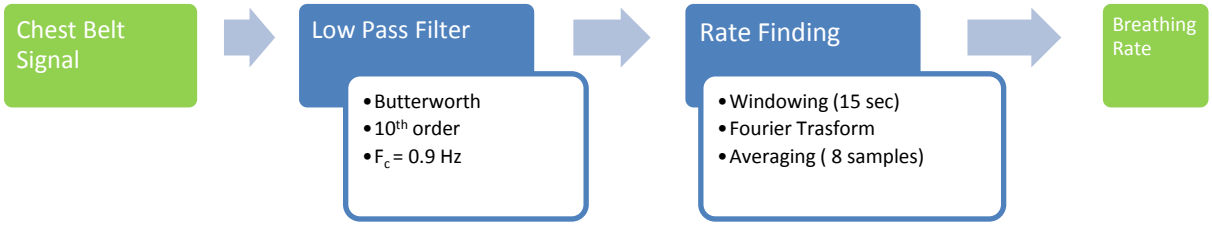

(d)

Figure 3.3: Block diagrams showing the signal processing algorithm for calculating (a) heart rate from VNA signal, (b) heart rate from ECG device, (c) respiration rate from VNA signal, (d) respiration rate from MLT1132 piezo-resistive belt.

3.4.3 Analysis Techniques

Replacing an old medical data measuring technique with a new one requires analysis methods that show the extent to which the two techniques agree with each other in order to determine the suitability of replacement. Correlation coefficients are not considered a reliable indicator in this case as the results can be misleading [15]. In the results and discussion sections of this chapter, first the accuracy within 5 BPM of the reference will be used to give an indication of suitability. Furthermore a popular clinical measurement comparison technique called Bland Altman analysis and Signal to Noise ratio will be used.

Bland Altman Analysis (BA)

This comparison method plots the difference between the "gold standard" reference method and the new proposed method against their mean [15]. It states that the "gold standard" should not be considered completely error free and thus the difference can give more useful information as the data are spread out giving a better picture of the bias and the variations of the measurements [15-16]. If the difference between the two compared results is within a defined set of limits then the gold standard can be replaced with the new proposed method.

The lack of agreement between the two methods can be summarized by estimating the mean of the difference d and the standard deviation of the difference sd. Also supposing the difference distribution to be Gaussian, 95 % of the differences would lie within $d - 2sd$ and $d + 2sd$. These limits are called the 95 % confidence intervals [15-16].

Signal-to-Noise Ratio

An SNR definition similar to [9] was used. In it the SNR was calculated using the power spectrum density of the Doppler radar. One such power spectrum is shown in fig. 3.3 (e). The

average heart beat for one minute of the total duration (5 minutes) of the signal from the reference device was considered to be the average (here it is 1.523 Hz x 60= 91.38 BPM). Any power within 10 BPM (0.17 Hz) of this average in the power spectrum density of the radar signal for the same 1 minute was considered to be the signal power. Power outside this range from 40 to 132 BPM (0.67 Hz-2.2 Hz) was considered noise power. This was done for the other 4 one minute durations of the signal as well. The average over the five SNR results was taken to be the final SNR.

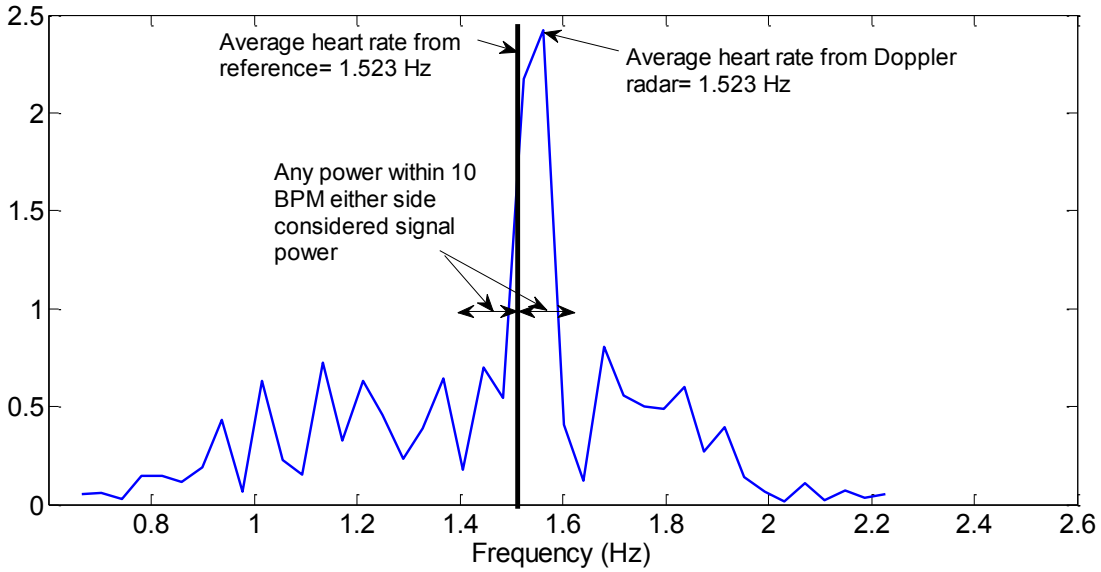

Figure 3.3 (e) Doppler radar power spectrum showing signal power definition.

3.5 Effect of frequency

3.5.1 Experimental Setup

The basic experimental setup described in section 3.4.1 will be used here. For the purpose of determining the effect of frequency on the Doppler radar vital signs detection accuracy, the frequency was varied using a VNA and the horn antennas were at a distance of 1m from the

target chest of a healthy 24 year old male. The parameters and states which were kept constant are given in Table 3.1.

Table 3.1 Constant Parameters for effect of frequency experiments

Power	**-10 dBm**
Duration	5 minutes
Sampling Rate	30 samples/sec
Body Position	Sitting
Antenna	Horn

Three 5 minute measurements were taken for the following frequencies: 1 GHz, 3.5 GHz, 5.8 GHz, 7 GHz, 9 GHz, 10 GHz, 11 GHz, 12 GHz, 13 GHz, 15 GHz, and 17 GHz. Two measurements which showed least signs of movement after visual inspection were chosen to be analyzed. Besides this the EG05000 and the MLT1132D as described in section 3.4.1 were used to measure the heart and breathing rate, respectively. The MLT1132D chest belt was used to measure the respiration rate for the Doppler radar vital signs measurements at 2.45 GHz, 9 GHz and 17 GHz only. This was because respiration rate detection was working with almost 100% accuracy for all of the frequencies and the introduction of the belt caused people to breathe more heavily and unnaturally to get a noticeable correct breathing signal for the belt. This unnatural and forced movement can cause an error in all vital sign detections from the Doppler radar and thus was avoided for most of the measurements.

3.5.2 Results and Discussion

3.5.2.1 Heart Rate

Table 3.2 shows the SNR, Accuracy, average ECG Heart rate, average Doppler radar heart rate; Bland-Altman (BA) mean difference, standard deviation and the 95 % confidence intervals of the heart rate detected using the Doppler radar monitoring method and the reference ECG device for the tested frequencies.

Table 3.2(a): Statistical Analysis of heart rate from ECG and Doppler Radar at various frequencies (1-10 GHz). All BA results are in BPM.

Frequency (GHz)	**1**	**2.45**	**5.8**	**7**	**9**	**10**
SNR	0.4304	0.5538	0.5361	0.6792	0.7584	0.6235
Accuracy (%) (within 5)	45.1	43.4	65	71.8	84.9	66.1
ECG Heart Rate(BPM)	58.6	61.3	60.1	60.9	61.3	72.7
On-Body Heart Rate (BPM)	64.9	62.4	66.3	61.4	61.2	69.2
Mean Diff (BA) (d)	-6.3309	-1.0568	-6.1732	-0.5132	0.1347	3.4299
Standard Deviation (BA) (s_d)	10.7087	10.1363	11.8821	5.9817	3.8626	6.4409
d +1.96 s_d (BA)	14.6581	18.8104	17.1157	11.2110	7.7055	16.0540
d -1.96 s_d (BA)	-27.3200	-20.9240	-29.4621	-12.2374	-7.4361	-9.1942

Table 3.2 (b) Statistical Analysis of heart rate from ECG and Doppler Radar at various frequencies (11-17 GHz). All BA results are in BPM.

Frequency (GHz)	**11**	**12**	**13**	**15**	**17**
SNR	0.5571	0.5411	0.4163	0.5115	0.6556
Accuracy (%) (within 5)	48.3	42.5	32.8	52.9	65.8
ECG Heart Rate(BPM)	67.4	68.8	59.9	66.3	65.7
On-Body Heart Rate (BPM)	66.1	69.4	68.7	67.9	66.5
Mean Diff (BA) (d)	1.3729	-0.6567	-8.7300	-1.6179	-0.7815
Standard Deviation (BA) (s_d)	8.8917	9.5431	7.5195	9.6639	7.3556
d +1.96 s_d (BA)	18.8006	18.0478	6.0083	17.3232	13.6355
d -1.96 s_d (BA)	-16.0548	-19.3611	-23.4683	-20.5591	-15.1985

Figure 3.4 shows the Bland-Altman plots for the tested frequencies.

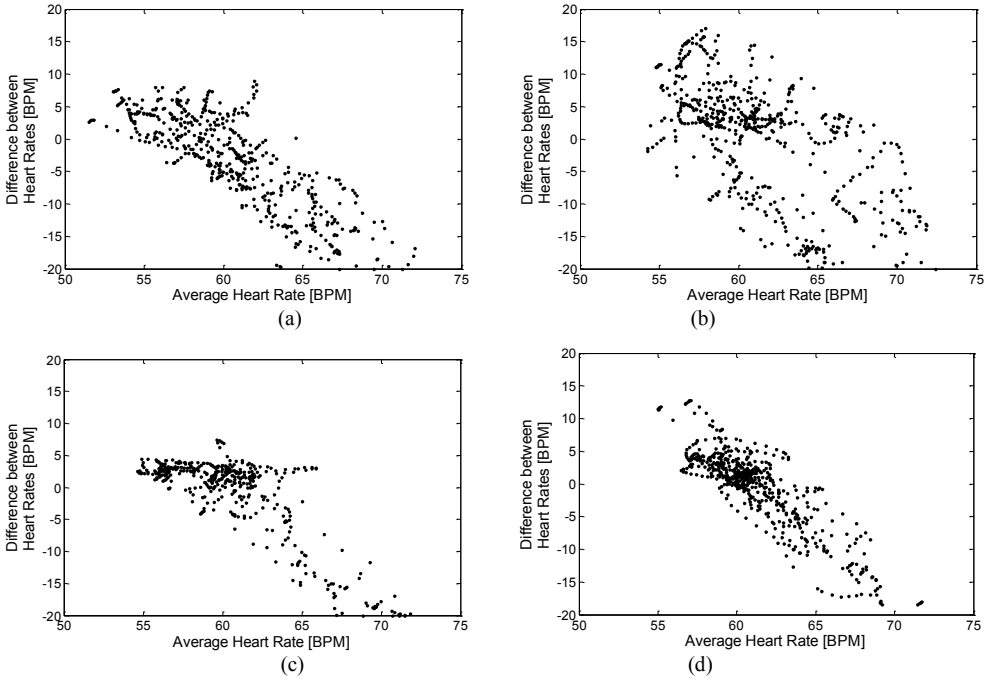

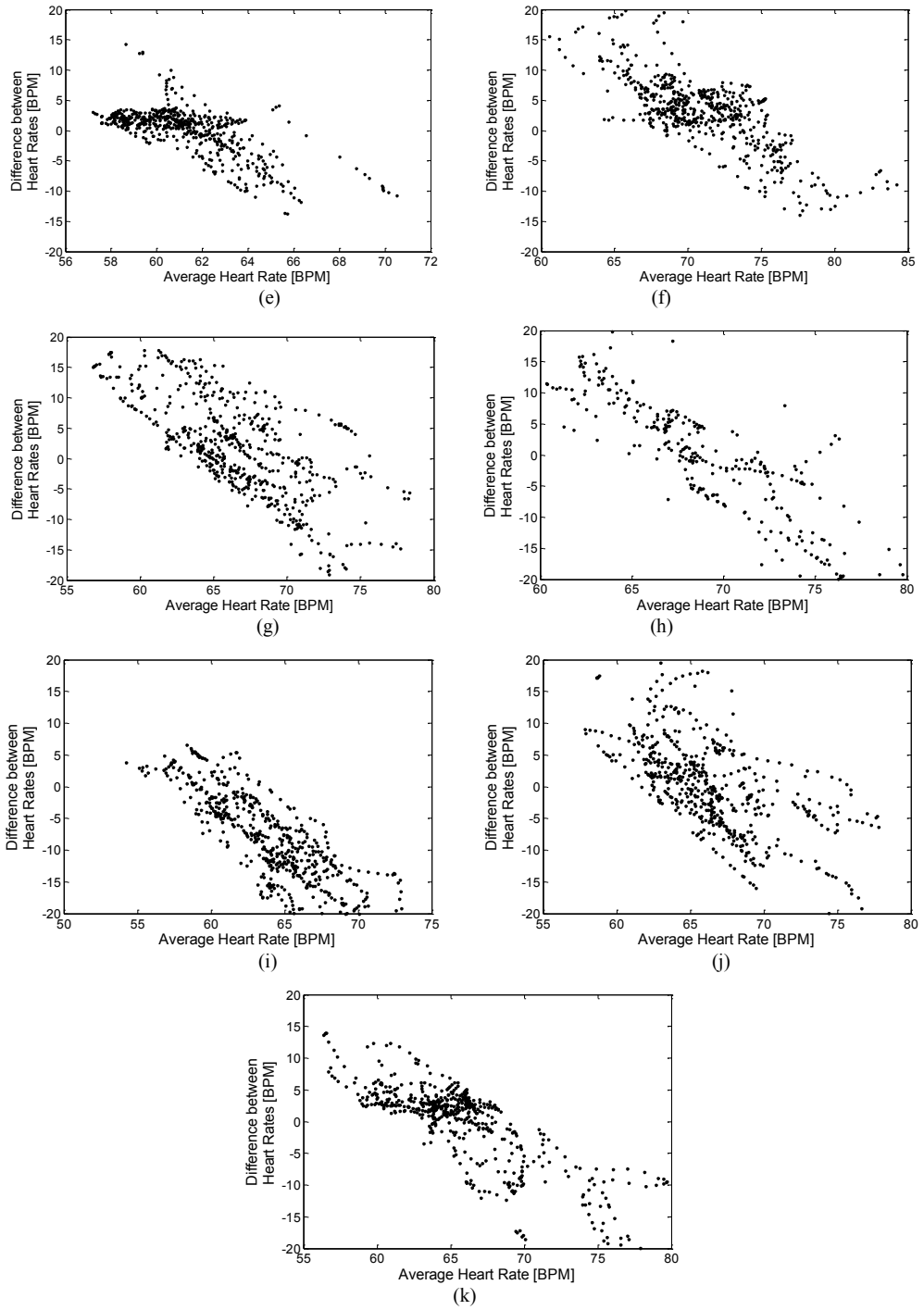

Figure 3.4: Bland-Altman plots for heart rate calculated using ECG device and Doppler radar at (a) 1 GHz, (b) 2.45 GHz, (c) 5.8 GHZ, (d) 7 GHz, (e) 9 GHz, (f) 10 GHz, (g) 11 GHz, (h) 12 GHz, (i) 13 GHz, (j) 15 GHz, and (k) 17 GHz.

As can be seen from Table 3.2, the SNR and accuracy all increase up to 9 GHz with the max values of 0.7584 and 84.9% , respectively after which they start decreasing again and

remain almost similar from 10 GHz to 17 GHz. The reason for the improvement from 1 GHz to 9 GHz lies in Equation 3.8. As the frequency increases, the variation in the phase increases due to chest movements. This increased sensitivity to minute movements results in improved accuracy as the phase variation due to chest movements overpowers the noise. Also as the frequency increases the directivity and gain of the antenna increases and the radiation beam becomes narrower and concentrated on the chest, if the target chest is right in front as it is in this case. This increased directivity and reduced 3dB beam width also results in less sensitivity to noise from the surrounding environment. As the frequency goes on increasing the accuracy keeps on getting better up to a certain optimum frequency (for this system), after which the harmonic interference and inter-modulation interference start to have a negative impact on detection accuracy. This is especially true for the cases where the harmonics of the breathing rate are close to the heart rate. The accuracy is also more negatively affected in the case of close heart and breathing rates. Harmonics result from the non-linear property of the cosine transfer function. The non-linear nature of the cosine transfer function is due to the non-linear system (mixer, oscillator, low noise amplifiers, etc.) that produces it. The final cosine baseband function of equation 3.4 when expanded into its Fourier series form, results in harmonics of both the heart and the breathing signals. If the harmonics of the breathing frequency are near the heart beating frequency, detection accuracy of heart beating frequency is reduced. This is the harmonic interference. To down convert the returned high frequency signal (from the Doppler radar) into baseband, it has to be passed through a mixer. The mixer down converts the returned signal by multiplying it with the local oscillator signal. This multiplication gives rise to various cross products. If these cross products are near the heart beating and breathing frequencies, they cause interference. This is called the intermodulation interference. The observation of increasing frequency beyond a certain optimum frequency

resulting in reduced accuracy was also reported in [17]. But in [17] and [6] even up to a frequency of 26 GHz, the heart rate was accurately detectable. Here the extra noise in the system (due to the coaxial cables and connectors used) had an effect on accuracy. Furthermore, the increased sensitivity after 9 GHz makes the antenna more sensitive to unwanted motion artifacts as well. It is vulnerable to minute unwanted motion artifacts producing spikes especially in the case the chest had extra fat or non-uniform chest motion. By non-uniform motion the author is referring to the fact that not all areas of the chest illuminated by the transmitted signal move the same amount, this causes unwanted peaks and troughs in some cases in the signal. This was found to be especially prevalent in the case of high frequencies. Also in some cases the chest expanded due to breathing in and the abdomen contracted leading to further unwanted artifacts in the returned signal. All these resulted in reduced accuracy after 9 GHz. This trend of accuracy, SNR and frequency can be seen in all the Bland-Altman results as well, where the mean difference and standard deviation of difference for 9 GHz was the best of all the frequencies at 0.1347 BPM and 3.8626 BPM respectively. Advanced signal processing techniques involving harmonic cancellation can lead to an improved accuracy and is proposed as future work. The results obtained here were verified by using a wideband Vivaldi antenna and R&S ZVA67 VNA with different connections. The noise level for R&S ZVA67 is less than -118dbm at the frequencies used. The tapered slotline Vivaldi antenna used had a gain of 5.3 dB at 3 GHz, 5.6 dB at 6 GHz and 7.14 dB at 9 GHz. For this setup again 9 GHz was found to be the ideal frequency.

Figure 3.5 shows the ECG graph and the filtered VNA heart graph for a 30 second duration of one 5 min input for 2.45 GHz, 9 GHz and 17 GHz. The 30 second windows were chosen after visual inspection to reflect the state of the signal throughout the measurement. It is observed in fig. 3.5 that the filtered Doppler radar heart wave at 9 GHz has the most clearly visible

peaks of the three. Figure 3.6 shows the BPM versus time graph of one five minute measurement for 2.45 GHz, 9 GHz and 17 GHz. From fig. 3.6 it is clear that the BPM results for the 9 GHz measurements follow the results of the reference ECG most closely of the three frequencies shown.

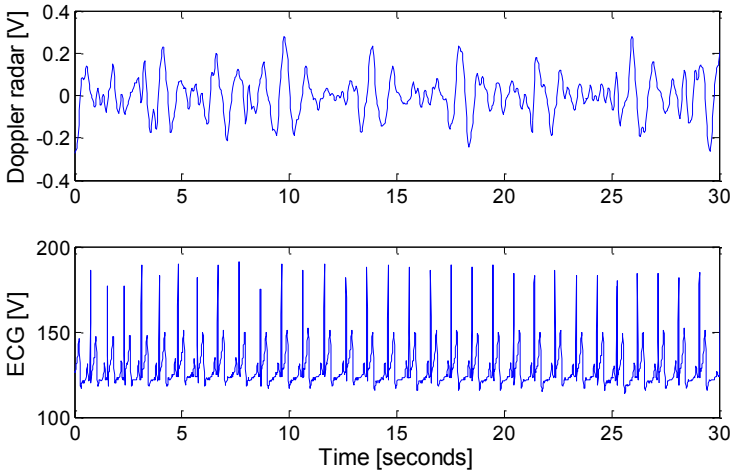

(a)

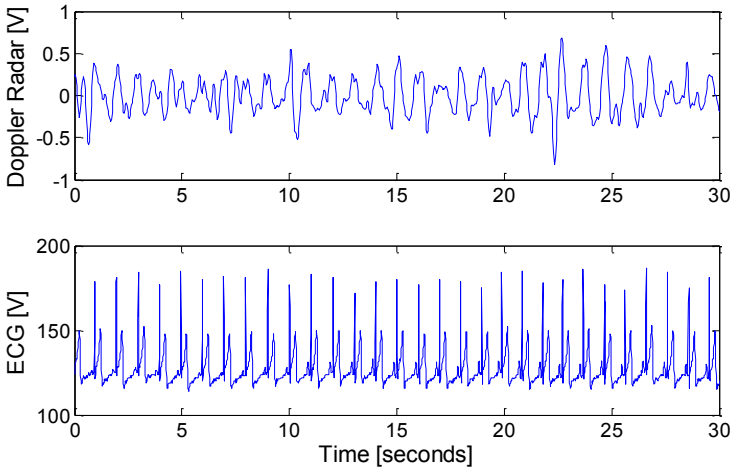

(b)

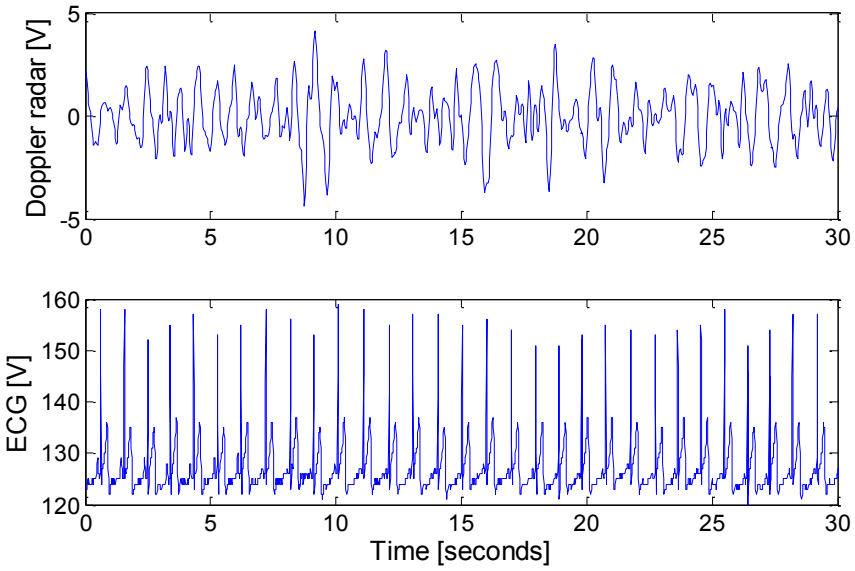

(c)

Figure 3.5: ECG signal and filtered Doppler Radar heart rate plots at (a) 2.45 GHz, (b) 9 GHz, and (c) 17 GHz.

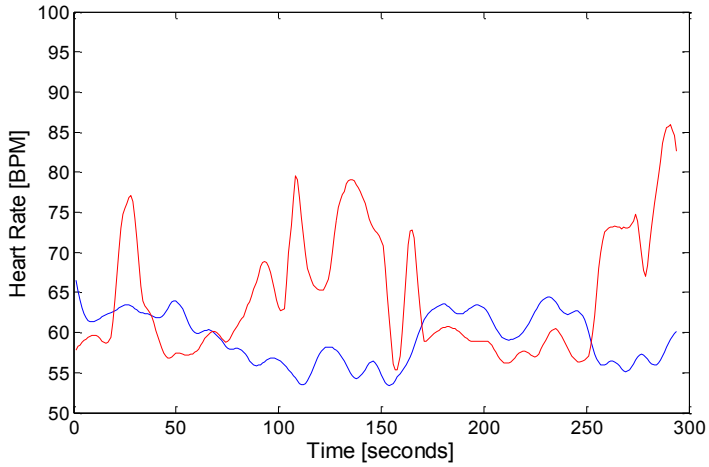

(a)

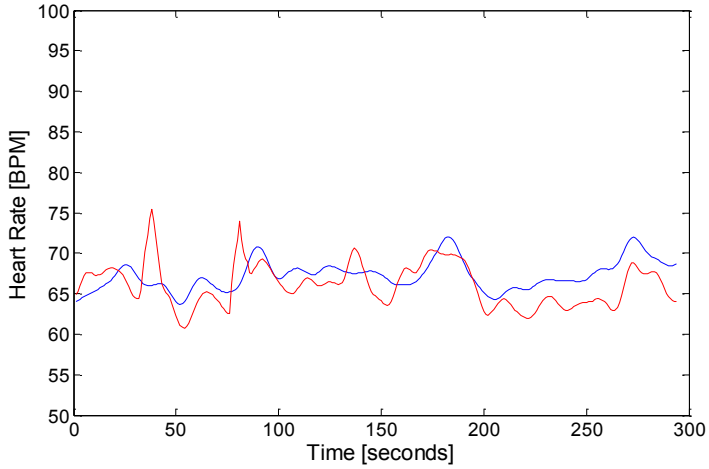

(b)

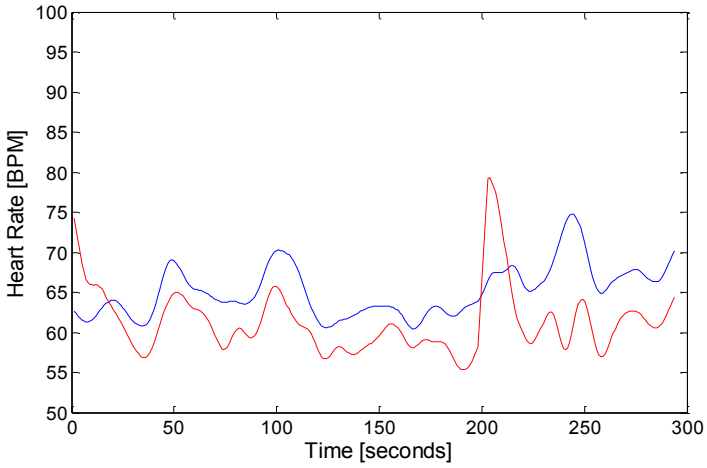

(c)

Figure 3.6: Heart rate [BPM] vs. Time for the ECG signal(blue) and Doppler Radar(red) at (a) 2.45 GHz, (b) 9 GHz, and (c) 17 GHz.

3.5.2.2 Respiration

Table 3.3 shows the accuracy within 1,2,3,4 and 5 breaths, average breathing rate from chest belt and Doppler radar, Bland-Altman analysis results for the breathing rate extracted using the Doppler radar and MLT1132 chest belt for 2.45 GHz, 9GHz, and 17 GHz. These frequencies were chosen as they lie at the extremities and middle of the frequencies tested. It is observed that the frequency does not have any significant effect on the accuracy of the respiration monitoring. Accuracy of 100% within 3 BPM for all frequencies is achieved. The Bland -Altman analysis shows similar results with the worst 95% confidence intervals being a very respectable (1.6324, -2.3410) at 9 GHz. The respiration results further enhance the argument that at higher frequencies the decreased heart rate accuracy is because of increased harmonic and intermodulation interference at higher frequencies. At lower frequencies the chest variation in equation 3.8 due to heart motion is not enough to overcome overall noise level of the system or is too minute to be detectable by the system used. However, the chest

variation due to respiration movement is significant. It overcomes the noise level of the system for accurate extraction of respiration rate.

Figure 3.7 shows the Breathing rate in breaths per minute and a 50 second window of the breathing signals, from the Doppler radar and the chest Belt at 2.45 GHz, 9 GHz and 17 GHz. Good agreement between the respiration results from the belt and the Doppler monitor is observed. At higher frequencies higher phase variation is also observed as predicted by equation 3.8. In short the respiration rate is detectable at all frequencies used but for the heart rate detection there is an ideal frequency (9 GHz) for the system used.

Table 3.3: Statistical Analysis of Respiration rate (breaths per minute) from Chest Belt MLT1132D and Doppler radar at 2.45 GHz, 9 GHz, and 17 GHz.

Frequency	**Accuracy within**					**MLT1132 Belt Breathing Rate (breaths per minute)**	**Doppler Breathing Rate (breaths per minute)**
	±1(%)	±2(%)	±3(%)	±4(%)	±5(%)		
2.45 GHz	81.3	100	100	100	100	13.1	13.1
9 GHz	74.8	89.7	100	100	100	13.2	13.6
17 GHz	100	100	100	100	100	20.6	20.5

Frequency	Bland Altman (breaths per minute)			
	Mean Difference	Standard Deviation	d +1.96 s_d (BA)	d -1.96 s_d (BA)
2.45 GHz	-0.0146	0.7729	1.5002	-1.5295
9 GHz	-0.3543	1.0136	1.6324	-2.3410
17 GHz	0.0553	0.4243	0.8870	-0.7764

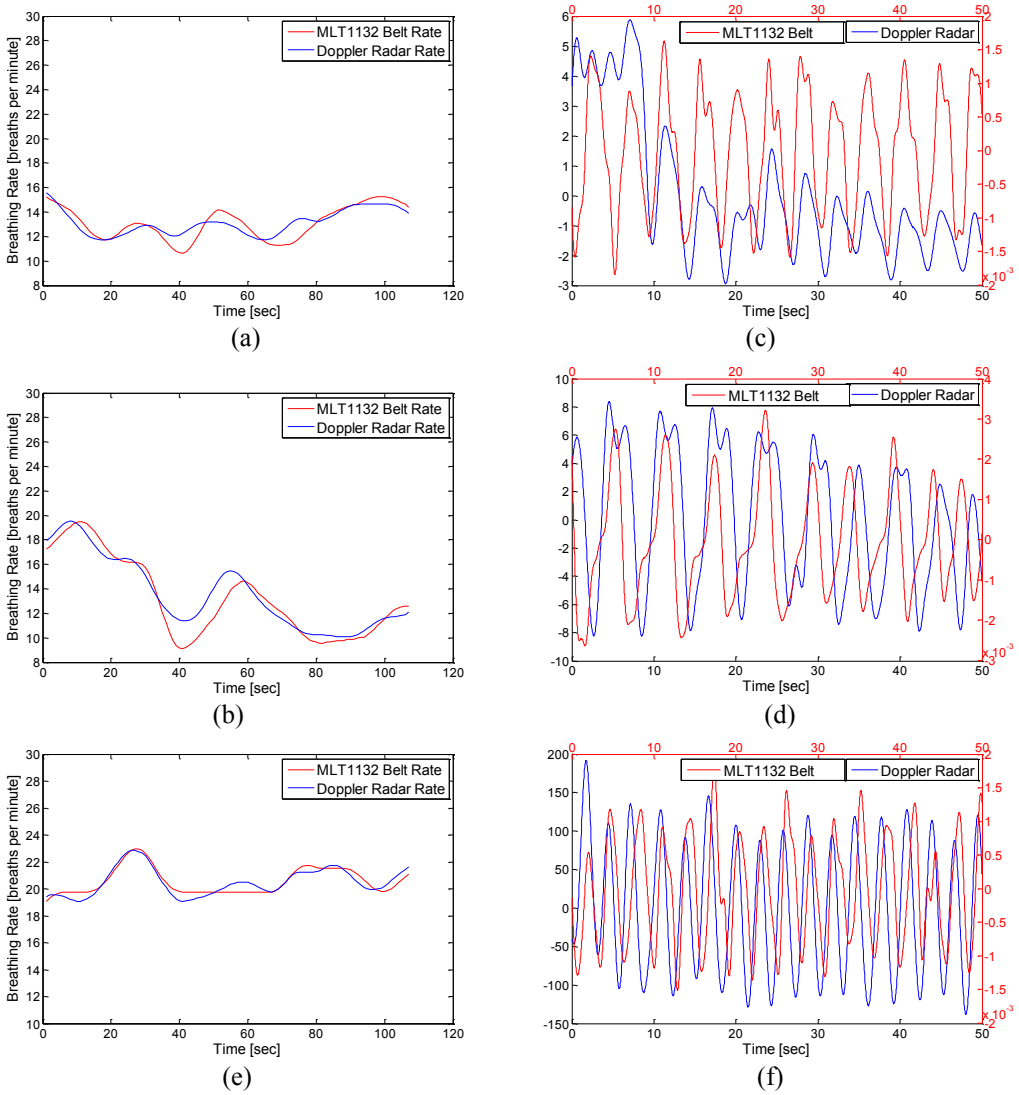

Figure 3.7: Breathing rate [Breaths per minute] vs. Time for the ECG signal and On-Body monitor for (a) 2.45 GHz, (b) 9 GHz and (b) 17 GHz, Breathing signal from On-Body Monitor and filtered MLT1132 Chest Belt for (c) 1 GHZ, (d) 9 GHz and (f) 17 GHz

3.6 Effect of Distance

3.6.1 Experimental Setup

For the purpose of determining the effect of distance between the Doppler radar antennas and the human subject's chest, the distance was varied from 50 cm to 3m in steps of 50 cm while keeping other parameters constant and using the same experimental setup as described in

3.4.1. The subject was again asked to sit on a chair and refrain from any sort of movements. The parameters which were kept constant are shown in table 3.4:

Table 3.4: Constant parameters for distance variation measurements

Power	**-10 dBm**
Duration	5 minutes
Sampling Rate	30 samples/sec
Body Position	Sitting
Frequency	9 GHz

Similarly as in the previous section three measurements were taken of 5 minutes each, of which 2 motion artifact free ones were chosen for analysis. The subject was a 24 year old healthy male. Besides this the EG05000 as described in section 3.4.1 was used to measure the heart rate. For the respiration 2 one minute readings were done at 3m with the MLT1132 chest belt, and were chosen for analysis.

3.6.2 Results and Discussion

Table 3.5 shows the SNR, accuracy, average ECG Heart rate, average Doppler heart rate, and Bland-Altman analysis results for the tested distances. Figure 3.8 shows the Bland-Altman plots for the different distances. From the results in table 3.5 it can be clearly seen that up to 2m the accuracy and the SNR are good after which the accuracy falls dramatically. The accuracy is around 80% for distances up to 2m and is 88.8% at 2m. The Bland-Altman analysis also shows less difference between the two methods up to 2m.

Figure 3.9 shows the ECG graph along with the filtered Doppler heart graph at 2m and 3m. The 1m counterpart for figures 3.9 can be found in section 3.5.2.1. In these figures the extent of degradation from 1m to 3m is clearly seen. The Doppler radar heart signal is excessively noisy and its peaks are not well defined at 3m. Figure 3.10 shows the BPM versus time graph for five minute duration of the signals for 2m and 3m. The 1m counterpart for figures 3.10 can be found in section 3.5.2.1.The BPM for 2m Doppler results follow the reference very well

but for 3m the results are far apart. It was expected that the accuracy of detection will decrease with increasing distance. More free space losses occur as the signal has to travel longer distances. The clutter from the environment increases as well due to diverging antenna radiation. This diverging antenna radiation pattern also results in less focus on the chest. These are the major causes of reduction in accuracy.

Table 3.5: Statistical Analysis of heart rate from ECG and Doppler Radar at various frequencies for different distances. All BA results are in BPM.

Distance (m)	**50cm**	**1m**	**1.5m**	**2m**	**2.5m**	**3m**
SNR	0.7679	0.7584	0.7987	0.8077	0.7075	0.8072
Accuracy (%) (within 5)	79.6	83.7	79.4	88.8	55.6	35.4
ECG Heart Rate(BPM)	65.0	62.9	67	65.5	65.7	67.6
On-Body Heart Rate (BPM)	66.1	61.9	66.8	64.9	61.4	60.2
Mean Diff (BA)	-1.0607	0.7219	0.1495	0.5826	4.2837	7.3823
Standard Deviation(s_d)	6.7801	4.7248	5.6453	4.3750	5.3679	4.8697
d +1.96 s_d (BA)	12.2283	9.9826	11.2144	9.1576	14.8048	16.9269
d -1.96 s_d (BA)	-14.3496	-8.5387	-10.9153	-7.9923	-6.2374	-2.1623

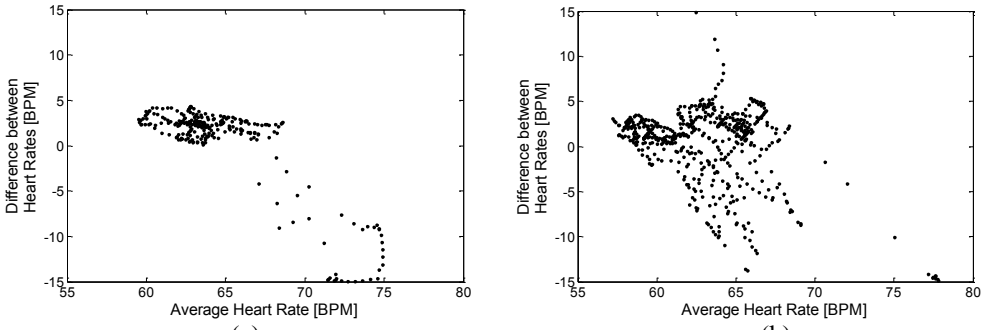

(a) (b)

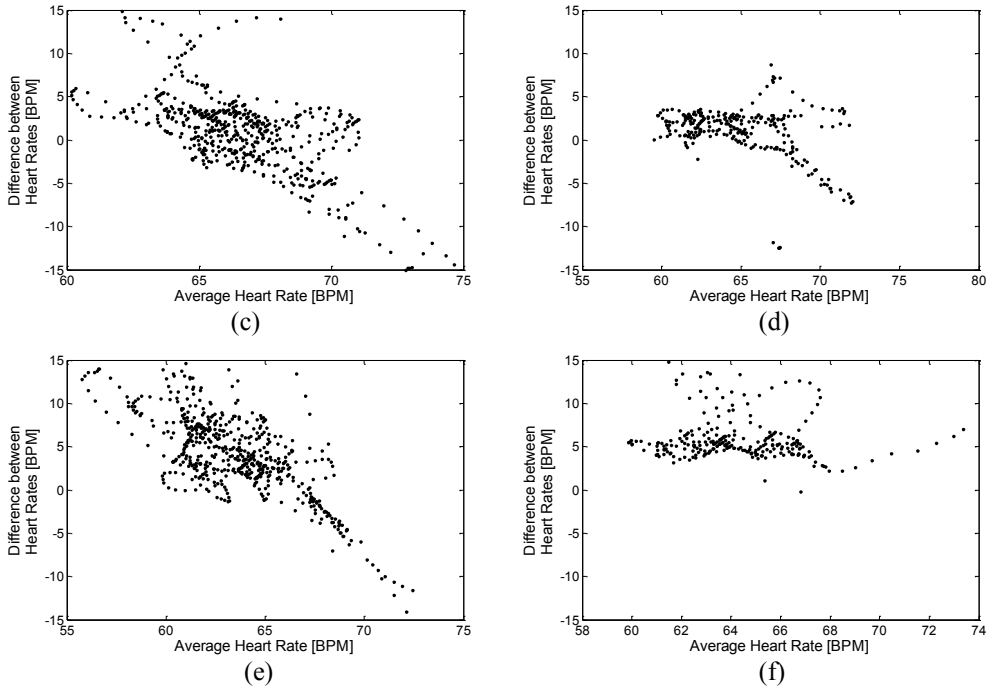

Figure 3.8: Bland-Altman plots for heart rate calculated using ECG device and Doppler radar at (a) 50cm, (b) 1m, (c) 1.5m, (d) 2m, (e) 2.5m, and (f) 3m.

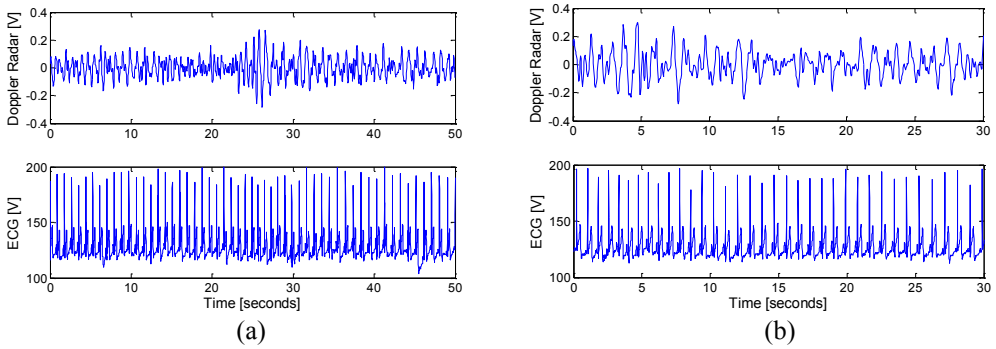

Figure 3.9: ECG signal and filtered Doppler Radar heart rate plots for (a) 2m and (b) 3m.

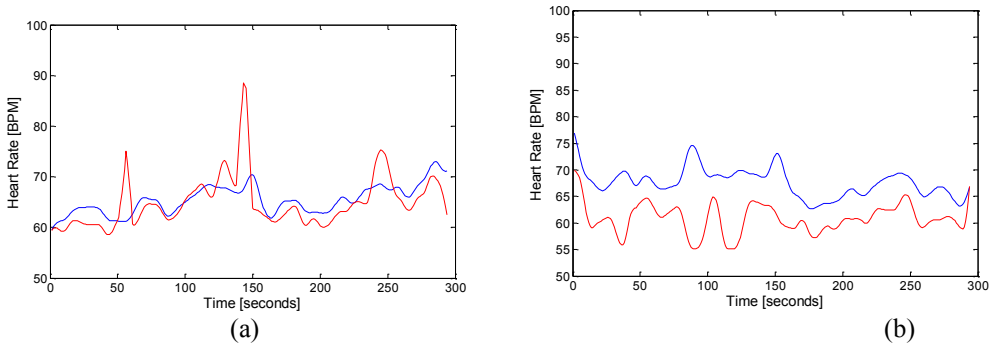

Figure 3.10: Heart rate [BPM] vs. Time for the ECG signal (blue)and Doppler Radar(red) for (a) 2m and (b) 3m.

3.6.3 Respiration

The respiration analysis including accuracy within 1, 2, 3, 4, 5 breaths per minute, average breathing rate from the Doppler radar and MLT1132 piezo-resistive chest belt, Bland Altman Parameters (Mean difference, Standard deviation of the difference, 95 % confidence intervals) for 1m and 3m is shown in table 3.6. Even at 3m the respiration rate detected from Doppler radar shows an accuracy of 88.6 % within 5 beats. Similarly the 95 % confidence interval for the Bland-Altman analysis at 3m is between 5.6072 and -2.2962. As the respiration signal is a very strong signal as compared to the heart signal it is not affected as much as the heart signal by free space losses, clutter and noise from the environment which increase as the distance increases. It is also not drowned under a powerful signal as the heart signal is drowned under the respiration signal. Both these factors ensure that the respiration rate is detectable with considerable accuracy even at 3m distance. Figure 3.11 shows the respiration signal obtained from the Doppler radar and the filtered MLT1132 chest belt signal at 3m. Both of them show excellent similarity. The errors that occurred for the respiration were more to do with the subject's unwanted movements rather than the effect of the distance. If no unwanted motion artefacts occur 100 % accuracy is possible.

Table 3.6: Statistical Analysis of Respiration rate from Chest Belt MLT1132 and Doppler radar at 1 m and 3 m.

Distance	**Accuracy**					**MLT1132 Belt Breathing Rate (breaths per minute)**	**Doppler Breathing Rate (breaths per minute)**
	±1(%)	±2(%)	±3(%)	±4(%)	±5(%)		
1m	74.8	89.7	100	100	100	13.2	13.6
3m	65.7	68.6	77.1	80	88.6	13.9	15.5

Distance	Bland Altman (breaths per minute)			
	Mean Difference	Standard Deviation	d +1.96 s_d (BA)	d -1.96 s_d (BA)
1m	-0.3543	1.0136	1.6324	-2.3410
3m	1.6555	2.0162	5.6072	-2.2962

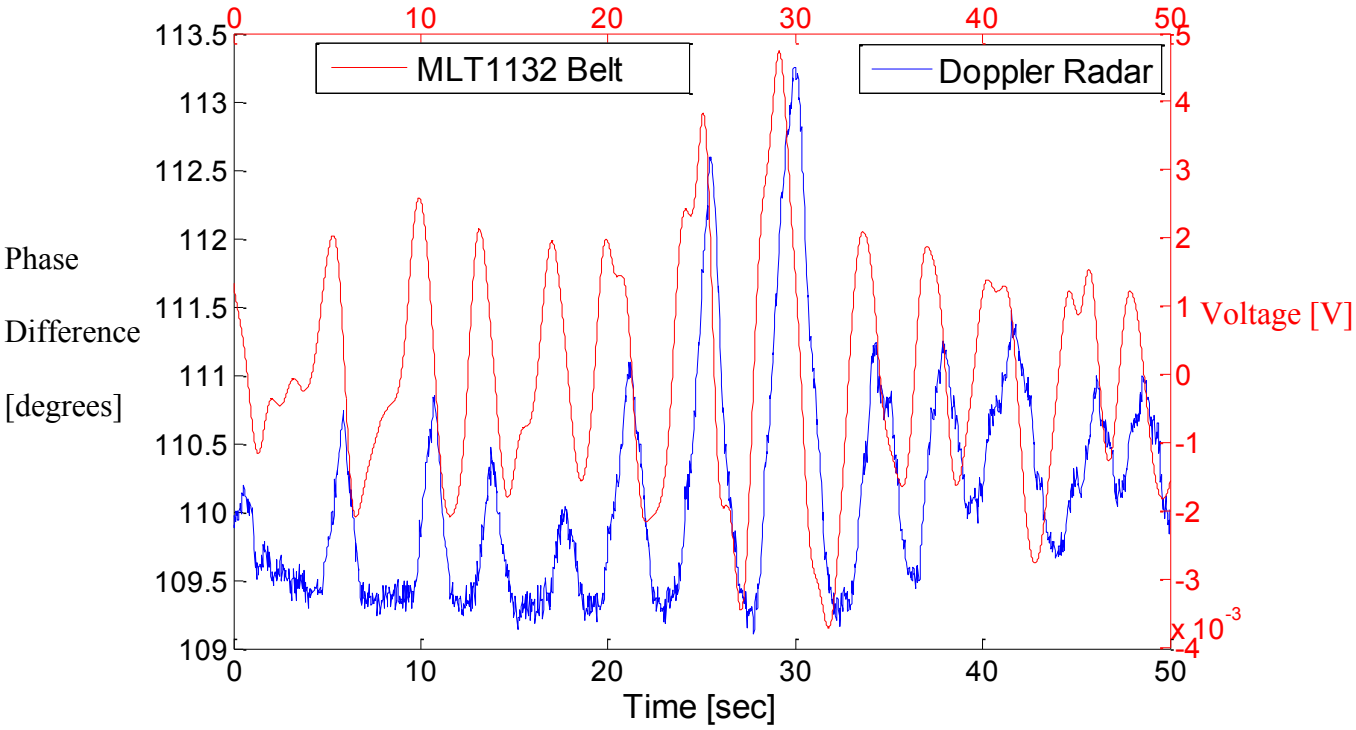

Figure 3.11: Breathing signal from Doppler radar and filtered MLT1132 Chest Belt waveform at 3m.

3.7 Effect of power

3.7.1 Experimental Setup

For the purpose of determining the effect of power, it was varied from -10 dBm to -45 dBm using the VNA while keeping the other parameters constant and using the same experimental setup as described in 3.4.1. The subject, a 24 year old healthy male, was asked to sit on a chair and refrain from any sort of movement. The parameters which were kept constant were:

Table 3.7: Constant parameters for power variation measurements

Frequency	**9 GHz**
Duration	5 minutes
Sampling Rate	30 samples/sec
Distance	1 m
Position	Sitting

Three 5 minutes measurements were taken for the following powers: -10 dBm, -20 dBm, -30 dBm, -45 dBm. Two measurements which showed least signs of movement after visual inspection were chosen to be analysed. Besides this the EG05000 and the MLT1132D as described in section 3.4.1 were used to measure the heart and breathing rate respectively. MLT1132D was attached to the chest for 2 one min measurements at -45 dBm.

3.7.2 Results and Discussion

Table 3.8 shows the SNR, accuracy, average ECG Heart rate and average Doppler heart rate, Bland-Altman (BA) mean difference, standard deviation and the 95 % confidence intervals for the tested powers. Figure 3.12 contains the Bland-Altman plots for the powers examined.

Table 3.8: Statistical Analysis of heart rate from ECG and Doppler Radar at various frequencies for different powers. All BA results are in BPM.

Distance (m)	**-10dBm**	**-20dBm**	**-30dBm**	**-45dBm**
SNR	0.7584	0.8357	0.6833	0.6057
Accuracy (%) (within 5)	83.7	87.4	49.5	34.2
ECG Heart Rate(BPM)	62.9	65.3	66.4	69
On-Body Heart Rate (BPM)	61.9	64	64	65.4
Mean Diff (BA)	0.7219	1.2606	2.3309	3.5790
Standard Deviation (BA)	4.7248	3.6566	8.0538	8.0577
d +1.96 s_d (BA)	9.9826	8.4276	18.1164	19.3720
d -1.96 s_d (BA)	-8.5387	-5.9064	-13.4546	-12.2141

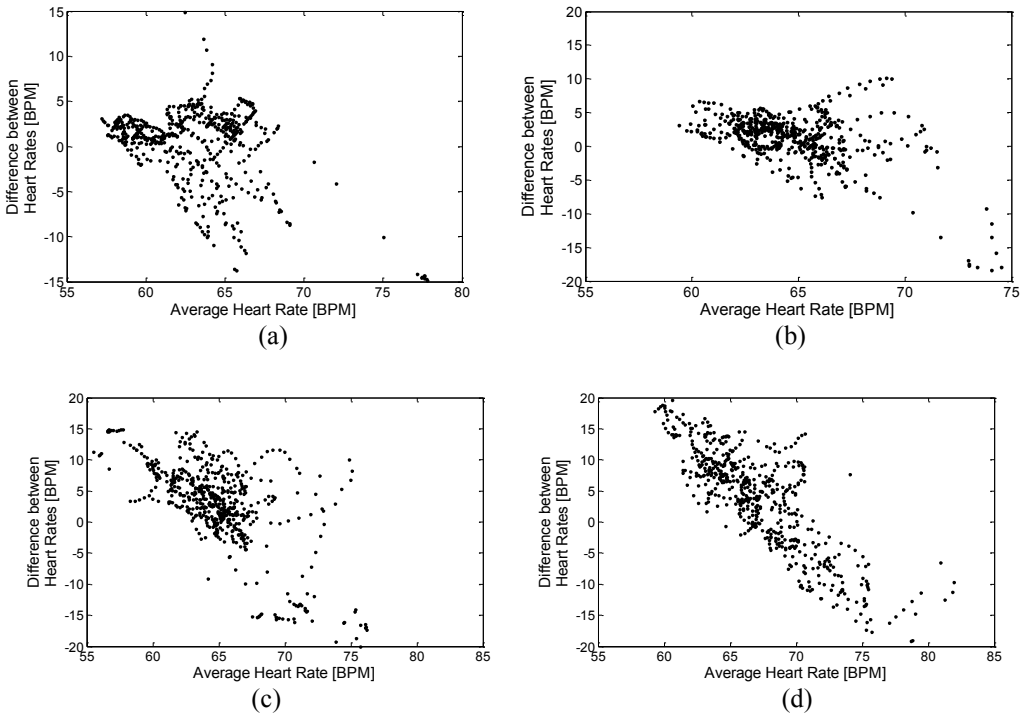

Figure 3.12: Bland-Altman plots for heart rate calculated using ECG device and Doppler radar at (a) 50cm, (b) 1m, (c) 1.5m, (d) 2m, (e) 2.5m, and (f) 3m.

It is observed that up to -20 dBm the results have accuracy well above 80%. After which it starts dropping rapidly. The SNR and the Bland-Altman results follow a similar trend with the 95% confidence intervals going beyond 10 and -10 for powers below -20 dBm. Figure 3.13 shows the ECG heart graph along with the corresponding Doppler radar heart graph for -20 dBm and -45 dBm. Figure 3.14 shows the BPM calculated using Doppler radar and ECG for a 5 minute measurement at -20 dBm and -45 dBm. The -10 dBm counterpart for figures 3.13 and 3.14 can be found in section 3.5.2.1. From figures 3.5(b) and 3.13 the observation of less prevalence of noise and better defined heart beat peaks up to -20 dBm is made. Similarly in figures 3.6 (b) and 3.14 the BPM for ECG and Doppler radar show the trend of following each other well up to a power of -20 dBm. At -45 dBm the Doppler radar BPM graph of figure 3.14 (b) shows very erratic results. These results point to the creation of a device which can operate accurately with power as low as -20 dBm.

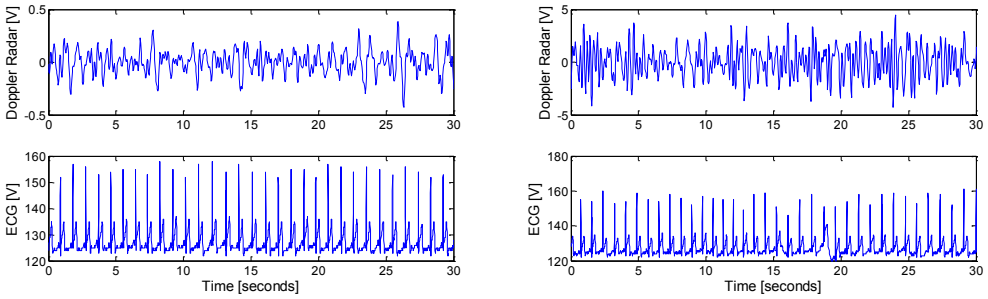

Figure 3.13: ECG signal and filtered Doppler Radar heart rate plots for (a) -20 dBm and (b) -45 dBm.

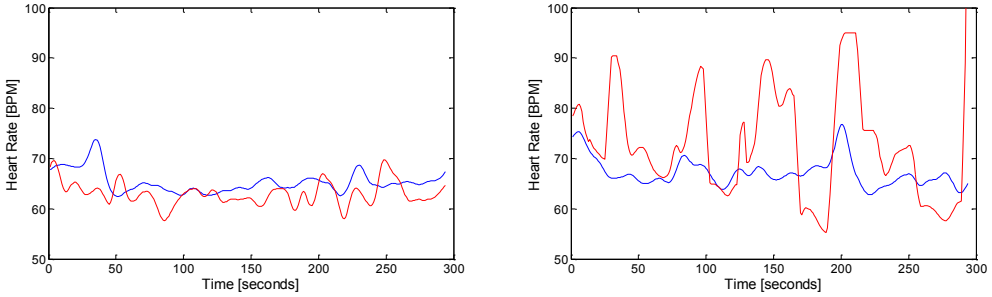

Figure 3.14: Heart rate [BPM] vs. Time for the ECG signal and Doppler Radar for (a) -20 dBm and (b) -45 dBm.

3.7.3 Respiration

Table 3.9 shows the respiration rate analysis results including accuracy within 1, 2, 3, 4, 5 breaths, average breathing rate calculated from the Doppler radar and MLT1132 piezoresistive chest belt, Bland Altman Parameters (Mean difference, Standard deviation of the difference, 95 % confidence intervals) at -10 dBm and -45 dBm. Even at -45 dBm the respiration rate is detectable with an accuracy of 97.1 % within 5 breaths. The 95% Bland-Altman confidence interval is between 5.1583 and -1.7378. The respiration rate is not affected as heavily as the heart rate in terms of accuracy as the respiration signal is a much more powerful signal and is not drowned out by a more dominant signal with more power as the heart signal is. It is less affected by noise as well because its power level is much higher than the noise power level. All these reasons result in accurate detection of breathing rate even at powers as low as -45 dBm.

Table 3.9: Statistical Analysis of Respiration rate from Chest Belt MLT1132D and Doppler radar at -10 dBm and -45 dBm

Power	**Accuracy**					**MLT1132 Belt Breathing Rate (breaths per minute)**	**Doppler Breathing Rate (breaths per minute)**
	±1(%)	±2(%)	±3(%)	±4(%)	±5(%)		
-10 dBm	74.8	89.7	100	100	100	13.2	13.6
-45 dBm	58.8	64.7	73.5	82.4	97.1	13.5	15.2

Power	Bland Altman (breaths per minute)			
	Mean Difference	Standard Deviation	d +1.96 s_d (BA)	d -1.96 s_d (BA)
-10 dBm	-0.3543	1.0136	1.6324	-2.3410
-45 dBm	1.7103	1.7592	5.1583	-1.7378

Figure 3.15 shows the Doppler radar and filtered MLT1132 chest belt respiration signals obtained with the radar operating at -45 dBm. It can be seen that both follow similar patterns but the Doppler radar respiration signal has a lot of noise associated with it. This is expected due to the low power, however with filtering this noise can be removed if necessary.

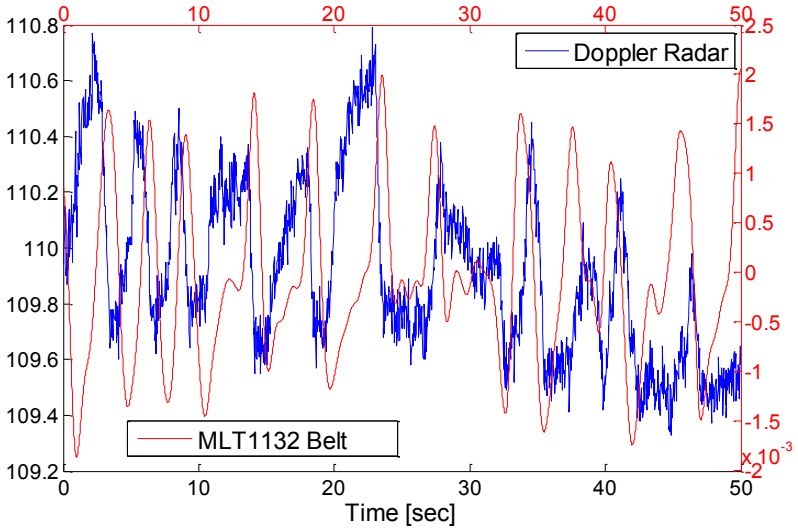

Figure 3.15: Breathing signal from Doppler radar and filtered MLT1132 Chest Belt waveform at Doppler radar power of -45 dBm.

3.8 Human measurement results

3.8.1 Experimental setup

In this section the results of experiments carried out on 6 people using the Doppler radar will be shown. In these experiments, the basic experimental setup described in section 3.4.1 was employed. The antenna used was the horn antenna, with the subject at a distance of 1m from the antenna. The subject was asked to sit on a chair and refrain from any sort of movements. The frequency and power of operation were 9 GHz and -10 dBm respectively. The summary of the parameters used can be found in Table 3.10.

Table 3.10: VNA parameters for Human measurement experiments

Frequency	9 GHz
Power	-10 dBm
Duration	5 minutes
Sampling Rate	30 samples/sec
Antenna	Horn

Three readings of five minutes each were taken out of which two best were chosen for analysis. Besides this the EG05000 as described in section 3.4.1 was used to provide the reference heart rate. All these experiments were performed in normal lab environment with the subjects wearing their own clothes. If the subject was wearing a jacket or sweater he/she was asked to remove it, so all the experiments were conducted on thin layer clothes.

3.8.2 Results and Discussion

3.8.2.1 Heart Rate calculation

The Bland-Altman Mean Difference, Standard Deviation of Difference and 95 % confidence intervals along with the Average Heart rates, accuracy within 5 BPM, and SNR for Doppler radar experiments were calculated and are shown in Table 3.11.

The mean difference and the standard deviation of differences for all the results were 2.2586 BPM and 4.2396 BPM respectively, while the 95% confidence intervals were 10.5681 BPM and -6.0510 BPM. The mean accuracy within 5 BPM is 79.4 %. The average SNR is 0.6. These values indicate that the Doppler radar was able to successfully detect the heart rate of people in the sitting position with reasonable accuracy. So it is feasible to use the Doppler radar for applications that require accuracy within 5 BPM. But if an application requires more exact monitoring (accuracy within 1 beat), like in an ambulance or an operation room or for the measurement of metabolic rate then it is not suitable. This accuracy can be improved by using improved signal processing techniques and a system with less overall noise.

Table 3.11: Statistical analysis for Heart Rate obtained by using Doppler radar and ECG device for different subjects.

No	Bland Altman (BPM)		Limits of Agreement (BPM)		Avg. HR [BPM]		Accuracy within 5 BPM	SNR
	Mean	Standard Deviation (StD)	Mean+1.96 StD	Mean-1.96 StD	Onbody	ECG		
1	0.7219	4.7248	9.9826	-8.5387	61.9	62.9	83.7	0.7584
2	1.2574	4.6584	10.3878	-7.8730	58.9	60.2	90.6	0.4705
3	2.2876	8.5045	18.9564	-14.3811	72.6	74.9	47.6	0.5513
4	4.1463	2.5746	9.1925	-0.8999	57.2	61.3	76.9	0.6677
5	1.3851	3.2271	7.7102	-4.9401	70.3	71.7	90.5	0.4820
6	3.7530	1.7479	7.1789	0.3271	73.7	77.4	87.1	0.9635
mean	2.2586	4.2396	10.5681	-6.0510	65.8	68.1	79.4	0.6
StD	1.4089	2.3919	4.2962	5.4286	7.3	7.5	16.4	0.2

The standard deviation of the difference between the HR of the ECG and Doppler radar was plotted versus the SNR for all measurements done in this chapter and is shown in figure 3.16. A trend of higher SNR leading to smaller error (difference) was observed and is also clear in the linear regression plot (red line in fig. 3.16). At low SNR's as expected the error in BPM is generally higher but even at a SNR of -8.237 dB, difference of 1.735 was achieved for one

measurement. The general trend however suggests better accuracy with increased SNR. The SNR can be improved by using equipment with lower residual phase noise, base band noise and RF additive white Gaussian noise [12]. It can also be improved by increasing the signal power and decreasing the distance between the Doppler antennas and the subject's chest. Using a frequency which maximizes sensitivity while limiting intermodulation and harmonic interference can also improve SNR [17]. Better signal processing also improves SNR and thus accuracy. Even at low SNR with advanced signal processing techniques (especially spectral estimation methods), accurate detection is still possible and is proposed as future work.

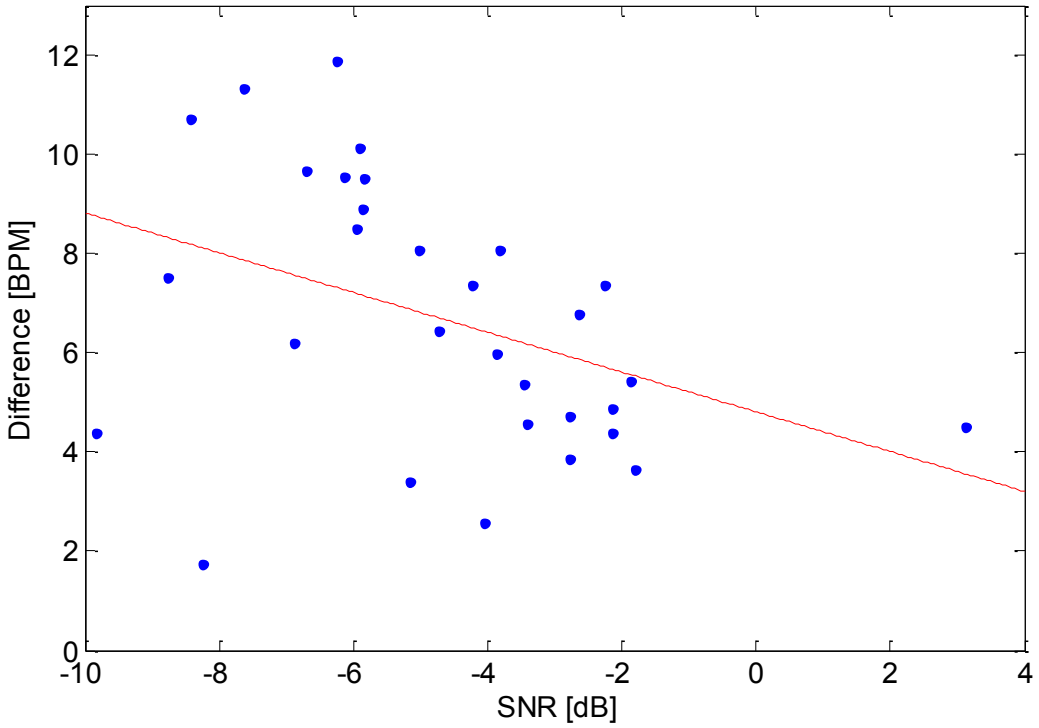

Figure 3.16: Difference in the Heart rate [BPM] between the ECG and Doppler Radar versus the SNR for all measurements. The Linear regression line (red) is also shown. The difference is taken to be the standard deviation of the difference from Bland-Altman Analysis.

Some of the subjects were moving quite frequently and this contributed considerably to decreasing the accuracy especially for subject 3. No unwanted motion artefacts removing

signal processing was employed. Sudden movements can be filtered out but not continuous movements. So antenna diversity techniques [19] and better signal processing can improve the accuracy in cases in which the subject moves excessively and consistently.

3.9 Conclusions

The Doppler radar was found to be effective in measuring the heart rates of people within 5 BPM (accuracy 79.4%). This can be used to determine whether a person's heart beat is normal or not. However it was not suitable for very accurate measurements (within 1 BPM) and for such applications ECG or a plethysmograph are more suitable at this stage of the research. It was found that a certain ideal frequency exists for detecting vital signs with the most accuracy which strikes a balance between improved sensitivity and acceptable inter-modulation and harmonic interference. This frequency was found to be 9 GHz for the system used but it may vary between systems considering good accuracy has been obtained at Ka band [6]. The factors affecting the ideal frequency in the experiments in this chapter are overall system noise. At higher frequencies especially above 9 GHz the system (cables, antenna, VNA) had higher noise levels and the antenna's radiation pattern characteristics were very erratic. The non- uniform motion of the chest as explained in section 3.5.2.1 also has an effect. It was found that up to 2m good accuracy for heart rate detection can be obtained. Although 1m was the point up to which consistently reliable accuracy could be achieved. Power as low as -20 dBm was found to give good accuracy (87.4%) and this points to the creation of low power devices. For the respiration rate it was found that all frequencies were suitable because the sensitivity of the radar was high enough for low frequencies as the respiration signal is quite strong, and it was excellent for high frequencies as it is not affected by any intermodulation or harmonic interferences being the dominant signal. Even at power

as low as -45 dBm and distance as far as 3m the respiration rate was still detectable with accuracy of 97.1% and 88.6% within 5 breaths per minute.

One of the major hurdles was the unwanted motion artefacts. Antenna Diversity[19] or improved signal processing techniques are proposed to remove such unwanted movements. Advanced signal processing techniques, including de-noising algorithms to improve SNR and better spectral estimation techniques can play a big part in improving the overall accuracy of the system. Wavelet signal processing techniques which include wavelet based filtering and spectral estimation techniques [18] are gaining a lot of popularity for detecting weak bio signals and should help improve the performance of the system.

The effect of various parameters on the accuracy of Doppler radar vital signs monitoring has been studied and suitable parameters to achieve good accuracy have been proposed. Using the proposed parameters experiments have been conducted on 6 people, which demonstrate the possibility of using Doppler radar as a viable vital signs monitoring alternative to the methods already present. Besides this methods to improve the overall system performance have been proposed.

3.10 References

[1] (http://www.who.int/cardiovascular_diseases/en/ ,2011)

[2] (http://www.lunguk.org/media-and-campaigning/media-centre/lung-stats-and-facts/factsaboutrespiratorydisease.htm , 2011)

[3] Byung-Kwon Park; Lubecke, V.; Boric-Lubecke, O.; Host-Madsen, A.; , "Cardiopulmonary Signal Sensing from Subject Wearing Body Armor," *Engineering in Medicine and Biology Society, 2007. EMBS 2007. 29th Annual International Conference of the IEEE* , vol., no., pp.366-369, 22-26 Aug. 2007

[4] D. Droitcour, O. Boric-Lubecke, V. M. Lubecke, J. Lin, G. T. A. Kovacs, “Range Correlation and I/Q Performance Benefits in Single-Chip Silicon Doppler Radars for Noncontact Cardiopulmonary Monitoring,” *IEEE Transactions on Microwave Theory and Techniques*, Vol. 52, No. 3, , pp. 838- 848, March 2004.

[5] D. Obeid, S. Sadek, G. Zaharia and G.E Zein, “Multi-Tunable Microwave System for Touchless Heartbeat Detection and Heart rate variability Extraction,” *Microwave and Optical Technology Letters*, vol.52, no.1, pp.192-198, Jan 2010.

[6] Y. Xiao, J. Lin, O. Boric- Lubecke and V.M. Lubecke,” Frequency-tuning technique for remote detection of heartbeat and respiration using low-power double-sideband transmission in the Ka-band,” *IEEE Trans. On Microwave Theory and Technique*, vol.54, no.5, pp.2023-2032, May 2006.

[7] Massagram, W.; Lubecke, V.M.; Host-Madsen, A.; Boric-Lubecke, O.; , "Assessment of Heart Rate Variability and Respiratory Sinus Arrhythmia via Doppler Radar," *Microwave Theory and Techniques, IEEE Transactions on* , vol.57, no.10, pp.2542-2549, Oct 2009.

[8] Kiriazi, J.E.; Boric-Lubecke, O.; Lubecke, V.M.; , "Considerations in measuring vital signs cross section with Doppler radar," *Radio and Wireless Symposium (RWS)*, 2011 IEEE , vol., no., pp.426-429, 16-19 Jan. 2011

[9] Droitcour, A.D.; Boric-Lubecke, O.; Kovacs, G.T.A.; , "Signal-to-Noise Ratio in Doppler Radar System for Heart and Respiratory Rate Measurements," *Microwave Theory and Techniques, IEEE Transactions on* , vol.57, no.10, pp.2498-2507, Oct. 2009

[10] Tariq, A.; Ghafouri-Shiraz, H. , “Noncontact heart rate monitoring using Doppler radar and continuous wavelet transform,” *Microwave and Optical Technology Letters*, vol. 53, issue 8, pp.1793–1797, May 2011.

[11] Tariq, A.; Ghafouri-Shiraz, H.; , "Vital signs detection using Doppler radar and continuous wavelet Transform," *Antennas and Propagation (EUCAP), Proceedings of the 5th European Conference* on , vol., no., pp.285-288, 11-15 April 2011

[12] A.D. Droitcour, “Non-contact measurement of heart and respiration rates with single chip microwave Doppler radar,” *Ph.D. Dissertation, Stanford University, USA*, July 2006.

[13] Hiebel, M., Fundamental of Vector Network Analysis, 4th ed. Germany:Rhode & Shwarz, 2008.

[14] Changzhan Gu; Jiang Long; Jiangtao Huangfu; Qiao, S.; Cui, W.Z.; Ma, W.; Lixin Ran; , "An instruments-built Doppler radar for sensing vital signs," *Antennas, Propagation and EM Theory, 2008. ISAPE 2008. 8th International Symposium on* , vol., no., pp.1398-1401, 2-5 Nov. 2008

[15] J. M. Bland and D. G. Altman, “Measuring agreement in method comparison studies,” *Statistical Methods in Medical Research*, vol. 8, pp. 135-160, 1999.

[16] J. M. Bland and D. G. Altman, “Statistical methods for assessing agreement between two methods of clinical measurement,” *Lancet*, vol. 1, no. 8476, pp. 307-310, 1986.

[17] C. Li, Y. Xiao, J. Lin, “Optimal carrier frequency of Non-contact Vital Sign Detectors,” *IEEE Radio and Wireless Symposium*, 2007, pp.281-284, 9-11 Jan 2007.

[18] Causevic, E.; Morley, R.E.; Wickerhauser, M.V.; Jacquin, A.E.; , "Fast wavelet estimation of weak biosignals," *Biomedical Engineering, IEEE Transactions on* , vol.52, no.6, pp.1021-1032, June 2005

[19] Fletcher, R.; Jing Han; , "Low-cost differential front-end for Doppler radar vital sign monitoring," *Microwave Symposium Digest, 2009. MTT '09. IEEE MTT-S International* , vol., no., pp.1325-1328, 7-12 June 2009

4 Chapter 4

On-Body Vital Signs Measurement

Abstract: In this chapter we will demonstrate that the reflection coefficient phase of a single antenna attached parallel to a person's chest is capable of monitoring the heart rate and the breathing rate of that person with excellent accuracy. First heart and chest motion is modelled in CST microwave studio. The effect of these moving chest models on the reflection coefficient phase of an antenna held parallel to the chest is simulated. The effect of frequency, power, antenna type, body type, antenna distance (from chest), position of the antenna on the chest, etc. will be investigated by performing experiments varying these parameters. A study involving 13 people in the supine and sitting state is conducted to determine the feasibility of monitoring vital signs using On-Body antennas for different body types. The feasibility of heart rate variability (HRV) calculation which involves variation in beat-to-beat intervals of heart will also be examined. Several signal processing techniques are analyzed to determine the most accurate one for On-Body vital signs monitoring.

4.1 Introduction

On-Body communication involves communication between various devices on the body, using the surface of the body as the propagation channel. It has been touted as a very popular option for applications in medical diagnostics and real time patient monitoring [1]. Further applications include personal entertainment, future infantry soldier, sports training, police, firemen, military and security agencies, extension to personal mobile communications etc. As stated in previous chapters, devices that can be used for constant health care by a non-specialized user at home or devices that can be used in a controlled environment by medical professionals are a growing area of research [2-5]. Considering the popularity of both On-Body communications and home health care devices, in this chapter the feasibility of vital signs monitoring using an antenna already attached to the body for communication purposes is also examined. The beauty of this method is that a transmitter antenna already attached to the body (for On-Body communication purposes) with slight modifications can be utilized to perform vital signs measurement rather than connecting an extra sensor. Uncomfortable strap

belts and electrodes can be replaced by a single compact device. During training exercises these home friendly devices can serve as a non-intrusive method of monitoring.

Alternate wearable devices for vital signs monitoring have received a lot of interest in literature due to their extensive uses. Among wearable devices, in [2] a complete system called iCalm was designed to be a user friendly system that can be operated without a medical professional or a clinical environment. The user had the ability to turn the system on or off as he pleased and it was ideal for long term monitoring applications. The system had its own radio module for data transfer along with a photoplethysmograph and an electrodermal activity sensor. It could measure electrodermal activity, temperature, motor activity, and plethsmography. In [3], a wearable zero net energy biosensor was produced that used the chest movement to not only sense the respiration rate but also harvest energy to power an ultra low power microcontroller with low data rate wireless link. The biosensor consisted of the following components: (1) a garment with a fabric integrated respiratory effort sensor, (2) a module that stores, filters and extracts physiological data, (3) a low power, low data rate short range wireless link. The required data was processed, extracted and then stored for a while after which it was transferred via a wireless link to a personal communications device. It used a miniature rotator permanent magnet DC generator. This method proved to be successful in measuring the respiration rate with reasonable accuracy and sending it over a wireless link using the movement of the chest to harvest power. In [4] an antenna connected parallel to the chest was demonstrated to be a possible method to detect heart beat and breathing rate. This was a preliminary study in which the antenna type and frequency were not optimized; only the concept was introduced. Three frequencies (370 MHz, 900 MHz and 1.5 GHz) in the UHF band were used and it was found out that at lower frequencies, better sensitivity was achieved. The respiration spectral component and its harmonics were easier to

remove at lower frequencies which made it easier to detect heart rate. Popular noise removal techniques such as median filtering and Savitzky-Golay filtering were employed which improved the detection accuracy. Results were shown for 60 second samples of a sitting person breathing normally and in the apnea state. In [5] a wearable Doppler radar was designed using microstrip elements at 2.45 GHz. It was used to monitor heart activity without the need of electrical contact or optical access to the patient's skin. The feasibility of the device for monitoring heart signal was validated, and it was shown that it has the potential to be a replacement for ECG in situations requiring non-invasiveness. It was envisioned in [5] that such a device can be used in security and disaster relief, and may be embedded in clothes, beds, and chairs. P.S. Hall and Yang Hao [6] have performed a detailed analysis of the On-body communication theory including antenna design. The current state of the art systems are discussed and future applications including medical, personal entertainment, law enforcement and military applications are presented. In Reference [7], the wave propagation On-Body along with the effect of different polarization states is investigated. The effect on the near and far field behavior of the antenna in the proximity of the body is also discussed. Based on these studies novel antennas are designed which significantly increase the path gain. In Reference [8], simulation and experimental parametric studies are performed to address the effect of the human body on various narrowband and ultra wide band antennas. This study aimed to find the best narrow band and ultra wideband antennas for robust and power-efficient communication operation on the human body. Novel antennas are designed with which experiments are conducted on several individuals. The effect of subject specificity of the On-Body radio propagation channels is also investigated for both narrow band and wideband systems.

Minimal research has been conducted on the effect of frequency on On-Body vital signs monitoring using a single antenna. No research as far as the author knows has been conducted on the effect of antenna type, power, antenna position on body, body type, and distance of antenna from chest. A lot of gaps in On-Body vital signs monitoring research have been filled by this study. In [4] only the heart beat average rate in a 60 sec sample was calculated. In this work that idea is extended to determine whether it is possible to detect the heart rate over shorter intervals. The feasibility of HRV using this technique has also not been investigated before and will be examined for the first time. The respiration signal obtained from this technique is compared to the reference signal from a piezorestive chest belt for different parameters (frequency, power etc.) and excellent similarity is achieved between them.

One of the key objectives of this research is to establish whether this technique is capable of detecting the vital signs of a person in a controlled environment. If it is capable with suitable accuracy, then this method may replace already present apparatus such as ECG and plethysmography devices for heart rate monitoring; capnography, spirometery and piezoresistive belts for breathing rate monitoring. Other objectives included finding out the best parameters (frequency, power, antenna etc.), so that a prototype considering those parameters can be designed in the future. Furthermore the possibility of using this method for long term monitoring applications such as heart and HRV monitoring during sleep was also examined. To achieve this, experiments were conducted for five minute intervals on 13 people. From this the effect of body type on accuracy was determined as well.

In section 4.2 there is some background and theory. In it this technique is verified using a simple chest model with an antenna in CST. Section 4.3 establishes the general experimental setup. From then on the corresponding sections (4.4, 4.5, 4.6, 4.7, 4.8 and 4.9) contain the results and discussions of the effect of various parameters (frequency, antenna type, power,

antenna position on body, different distances, and body type) on the accuracy of On-Body vital signs measurement. In section 4.10 the feasibility of heart rate variability (HRV) measurement is established.

4.2 Principle

In the author's previous work [9] an antenna connected parallel to the chest of a person sitting still was successful in measuring the heart rate accurately with considerable accuracy. The human chest moves due to breathing and heart beating. The reflection coefficient phase (RCP) of an antenna is affected by the human chest movement when the chest occupies the antenna near field. This is due to the fact that the relative dielectric constant changes in the antenna near field. As a result of this the information of heart and breathing cycle is modulated on the reflection coefficient phase. The heart and breathing rate can then be extracted using signal processing techniques. In order to verify these observations moving heart and chest models were simulated using CST Microwave studio design environment.

4.2.1 On-Body Vital Signs monitoring simulation study

Although some research has been conducted on determining the possibility of using a single On-Body antenna as a vital signs detector [4][9], there has been no computer simulation study to ideally study the effect of the chest motion on the On-Body antenna's reflection coefficient. In this section, three-dimensional layer based models of the human skin, fat, muscle, heart and lungs were designed to represent the chest in CST microwave studio. The models were designed considering conductivity, permittivity, μ, density and thermal conductivity. The simulations were carried out with respect to different frequencies, lung models (inflated and non-inflated), heart and chest movement conditions, antennas, distances, etc.

4.2.2 CST Microwave studio

CST MICROWAVE STUDIO is a software package used for electromagnetic analysis and design in the high frequency range. CST MICROWAVE STUDIO uses the Finite Integration Technique (FIT) for modelling. In this method complex structures at high frequencies can be simulated feasibly as the numerical effort required for complex problems increases more slowly compared to other electromagnetic computational methods. CST time domain solver uses proprietary technologies such as the Perfect Boundary Approximation (PBA), Thin Sheet Technique (TST), and multilevel subgridding scheme. These technologies improve memory efficiency and performance of CST time domain solver compared to conformal methods while maintaining the accuracy. Nowadays many applications use FIT modelling such as ultralow-frequency geophysics, radar signature technology, antennas, wireless communications devices, digital interconnects, biomedical imaging/treatment, photonic, nanoplasmonics, etc. For these reasons, CST MICROWAVE STUDIO has been chosen as the simulator to model an On-Body antenna mounted on a three dimensional chest model.

4.2.3 Multi-Layers Human Chest Model

A three-dimensional simplified chest model was developed considering several major layers in the human body. The layers included the skin, fat, muscles, heart, and lungs. Figures 4.1 and 4.2 show the top and front view of the layers combined in order to form one object which represents the human chest. Figures 4.1 and 4.2 also show the various dimensions of each layer as suggested by [10]. The heart is surrounded by the lungs and considering that it was modeled to be a cavity in the lungs as shown in fig. 4.1. All the layers were modeled as

rectangular boxes. These boxes were matched to average male chest dimensions. The simulated structure was 20 cm long and 30 cm wide. In order to obtain a more accurate model, the skin, fat and muscle layers were extended on the sides, as shown in fig 4.1. The antenna is also shown parallel to the chest. The antenna's position was chosen to be exactly on top of the heart as that is the position it was attached in the practical experiments (see fig. 4.2). A thin vacuum layer D of 2 mm thickness was assumed between the antenna surface and the skin. Slight variation of this thin layer did not have an effect on the trend followed by the simulation results. Fig 4.3 shows the realization of this model in CST Microwave studio.

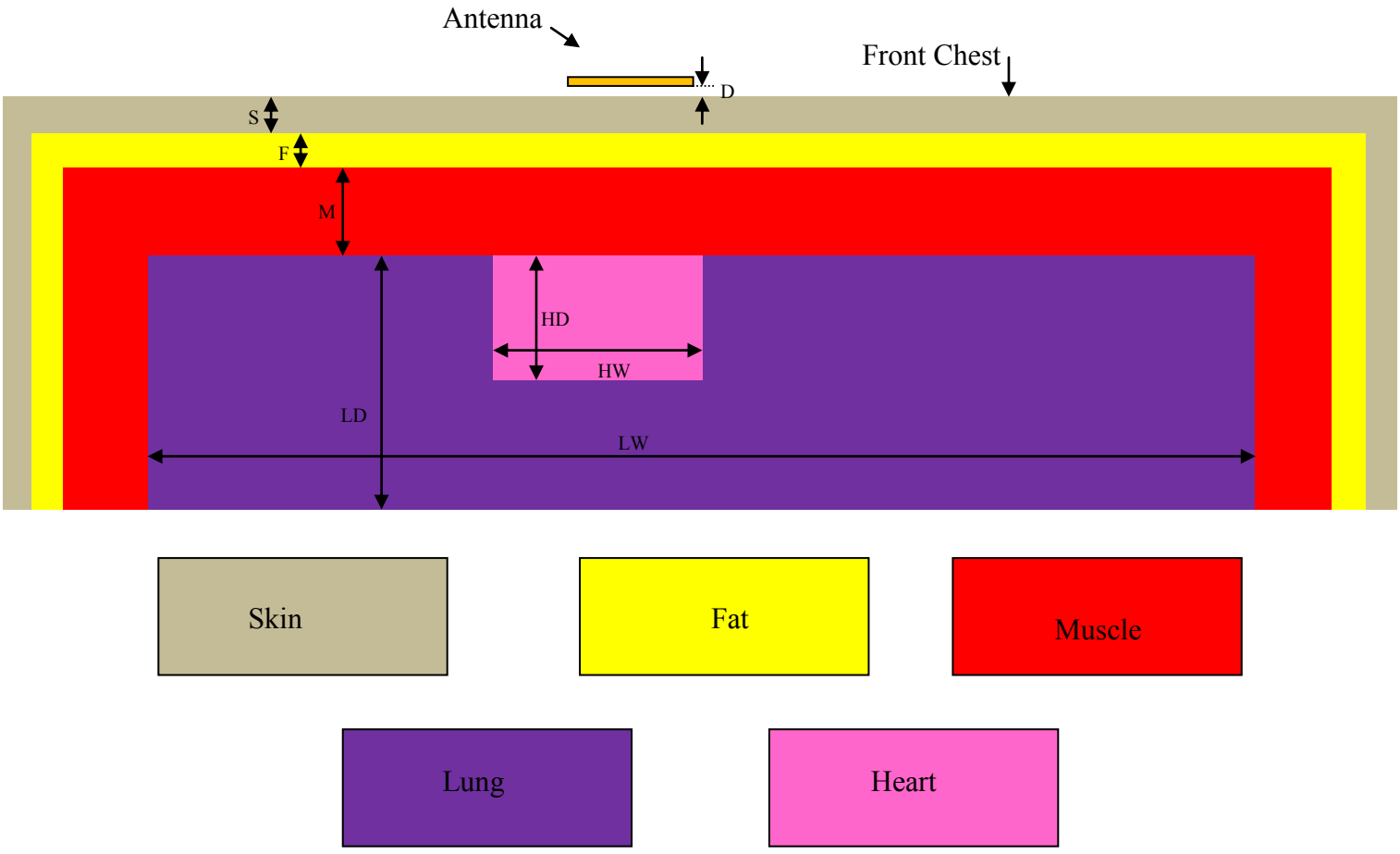

Figure 4.1: Top view topology of Chest model in CST. Colour correspondence is same as fig (D=0.5 mm, S= 5mm, F= 5mm, M= 15mm, LD= 85mm, HD= 40mm to 55 mm, LW=275 mm, HW= 80mm).

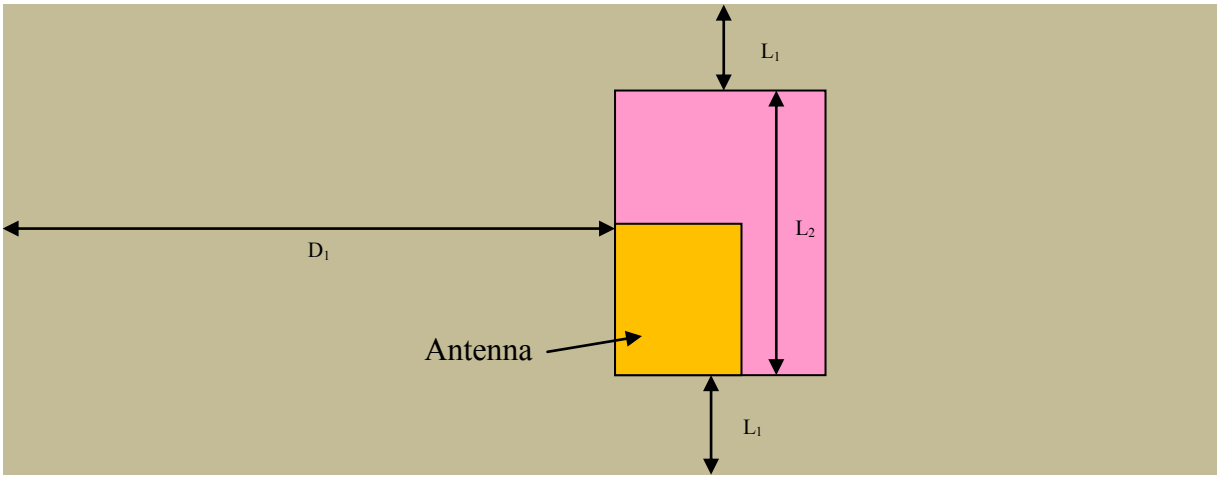

Figure 4.2: Front view topology of Chest model in CST. Colour correspondence is same as fig 4.1 (D_1=150 mm, L_1= 50 mm, L_2= 100 mm).

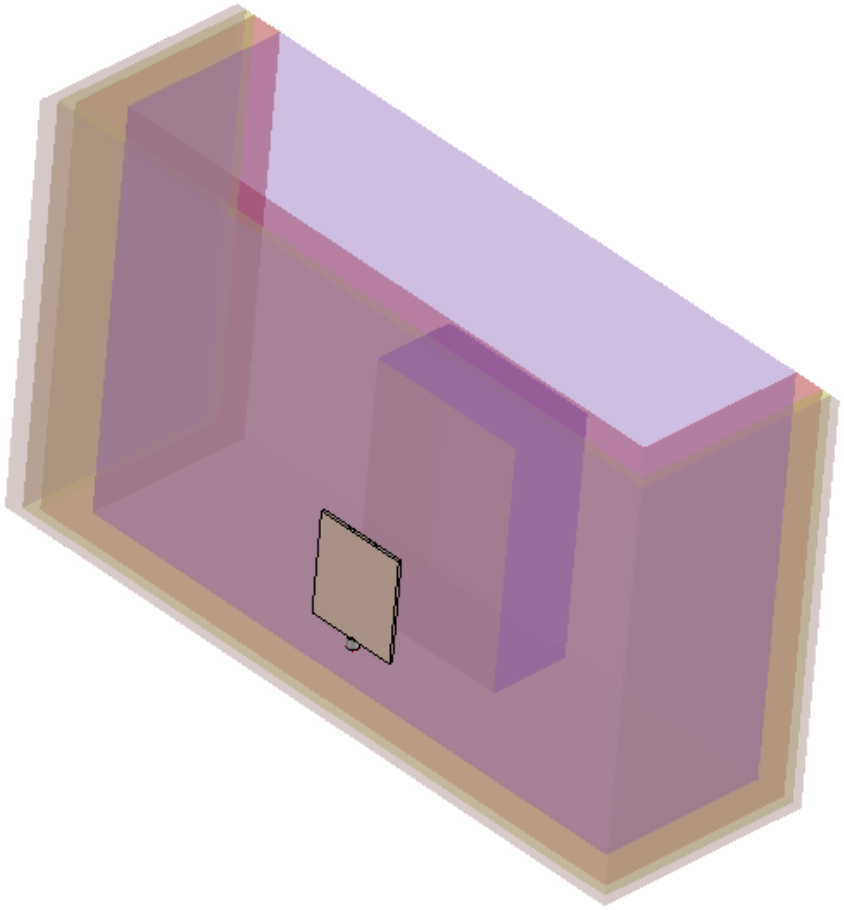

Figure 4.3: Chest Model realized in CST Microwave Studio.

4.2.4 Dielectric properties of chest

The dielectric parameters of the tissues were computed according to the model described by [11]. As these parameters change with frequency, three different sets of parameters were compiled at 2.45 GHz, 5.8 GHz and 9 GHz, and are shown in tables 4.1, 4.2 and 4.3. These parameters define the electrical properties of the dielectric layers that represent various tissues of a human chest.

Table 4.1: Dielectric Parameters of the body tissues at 2.45 GHz

Body Tissue	Permittivity	Conductivity (s/m)	Permeability	Density (Kg/m^3)	Thermal Conductivity (w/m.k)
Skin	38.007	1.464	1	1100	0.293
Fat	5.2801	0.104	1	1100	0.201
Muscles	52.729	1.739	1	1040	0.46
Lungs	48.380	1.682	1	1040	0.5
Heart	54.814	2.256	1	1020	0.624

Table 4.2: Dielectric Parameters of the body tissues at 5.8 GHz

Body Tissue	Permittivity	Conductivity (s/m)	Permeability	Density (Kg/m^3)	Thermal Conductivity (w/m.k)
Skin	35.114	3.717	1	1100	0.293
Fat	4.955	0.293	1	1100	0.201
Muscles	48.485	4.962	1	1040	0.46
Lungs	43.75	4.821	1	1040	0.5
Heart	48.949	5.862	1	1020	0.624

Table 4.3: Dielectric Parameters of the body tissues at 9 GHz

Body Tissue	Permittivity	Conductivity (s/m)	Permeability	Density (Kg/m^3)	Thermal Conductivity (w/m.k)
Skin	32.25	6.895	1	1100	0.293
Fat	4.680	0.514	1	1100	0.201
Muscles	44.126	9.192	1	1040	0.46
Lungs	39.306	8.796	1	1040	0.5
Heart	43.79	10.35	1	1020	0.624

4.2.5 Chest Movement Models

In order to perform the simulation study several chest movement models were considered. In one case only the heart was moving inside the chest and all the other layers including antenna were stationary. The heart layer thickness varies between 40 and 55mm during the cardiac activity [9]. This case was simulated to determine whether the motion of the heart inside the chest was capable of causing a change in the reflection coefficient of an antenna connected parallel to the chest. Several cardiac cycles were modeled considering the fact that the heart varied first from 40mm to 55mm and then again came back to 40 mm. This process continues.

The second case involved the entire chest moving while the antenna position was kept constant. The chest moves 0.2 to 0.5mm due to heart beats and between 8 to 12mm due to breathing [11]. These two conditions were modeled separately with the antenna at an initial distance of 2 mm away from the chest.

Cardiac cycles were modeled with the chest moving from 2 mm to 2.5 mm away from the antenna and then coming back to 2 mm. This process was continued. The breathing cycle was

modeled with the chest moving 2mm to 14mm away from the antenna and then coming back to 2mm. This process continues.

In real life the chest and the antenna move relative to each other and this ultimately results in the heart and breathing rate to be modulated on to the reflection coefficient of the antenna. But modeling this relative motion was beyond the scope of this work and here just the principle of On-Body vital signs monitoring will be established.

4.2.6 Ultra-Wideband monopole antenna

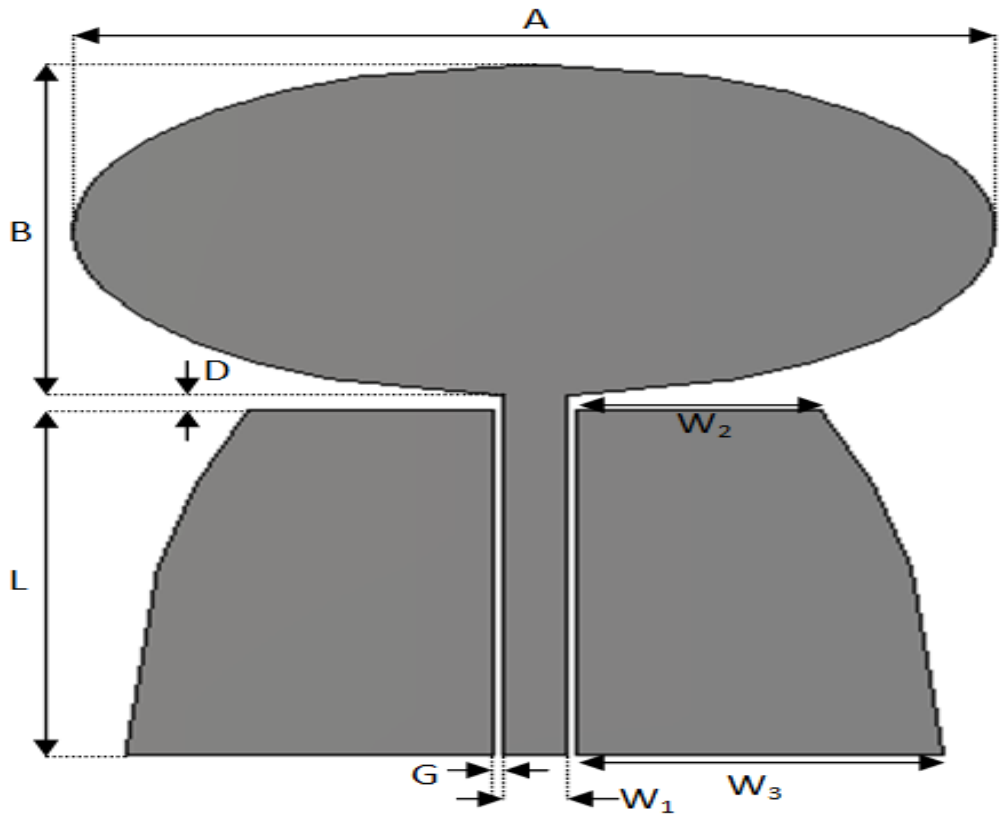

Figure 4.4: Topology of the Wideband monopole antenna. The dimensions are: A=44 mm, B=24 mm, G=0.5 mm, W_1= 5 mm, W_2= 6 mm, D=2 mm, W_3=17.5 mm and L= 25 mm.

To study the effect of frequency, a wideband monopole antenna was used to carry out simulations and observe the effect of the chest wall motion on the reflection coefficient of that

antenna. The topology of the Ultra-Wideband (UWB) monopole antenna used for this study is shown in fig. 4.4.

Since the aims of the simulations were to demonstrate the working of On-Body vital signs monitoring technique and to study the effect of frequency on the accuracy of the heart and breathing rate detection, a wide band monopole antenna was chosen. Its simulated reflection coefficient is shown in fig. 4.5. The figure also shows the three frequencies at which the simulations will be run and the reflection coefficient magnitude in dB at those positions. This antenna was designed on TLC-30-0620-CL1 substrate.

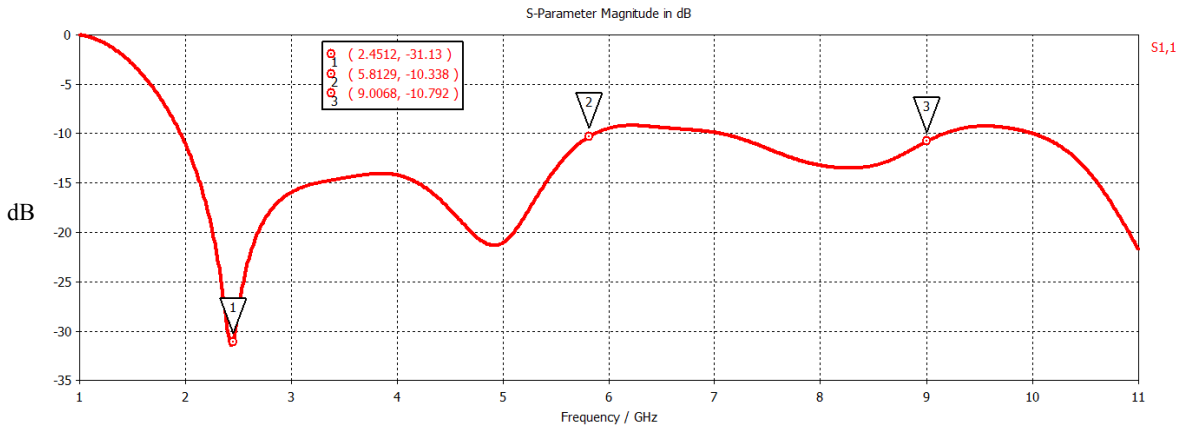

Figure 4.5: Simulated S_{11} for the UWB monopole antenna.

4.2.7 Simulation Study considering effect of heart movement (only)

In this section the simulated reflection coefficient results for the antenna in fig. 4.4 considering only heart movement (while the chest and antenna are stationary (see fig. 4.1)) are presented. Due to the immense processing time required for these simulations only three heart layer thicknesses (40, 47.5, and 55mm) were chosen for 5.8 GHz and 9 GHz. Four heart layer thicknesses (40, 45, 50, and 55mm) were chosen for 2.45 GHz. One cardiac cycle was defined as the heart thickness starting from 55mm to 40mm and then again returning back to 55mm. This was continued for five cycles. During the cardiac cycle, the phase variation due to the heart layer thickness variation is considered linear. The phase variations obtained at

2.45 GHz, 5.8 GHz and 9 GHz are shown in tables 4.4, 4.5 and 4.6 respectively. MATLAB was used to draw the phase variation graph over several cardiac cycles. The cardiac cycles for 2.45 GHz, 5.8 GHz and 9 GHz are shown in figures 4.6, 4.7 and 4.8 respectively. It is observed that the variation in the reflection coefficient caused by the movement of the heart alone inside the chest is negligible for all the frequencies used. Hence it can be safely assumed that just the heart beating inside the chest is not a major factor in modulating the reflection coefficient phase of the antenna attached parallel to chest in experimental results. In real experiments there are extra noise factors (ports, connectors, co-axial cable, clutter from the environment, non-planar and non-linear nature of heart movement), which would further diminish the effect just heart movements have on the reflection coefficient of the antenna.

Table 4.4: Reflection coefficient phase and magnitude variations for various heart layer thicknesses at 2.45 GHz.

Heart Layer Thickness (mm)	Reflection Coefficient Phase (degrees)	Reflection Coefficient Magnitude (dB)
55	185.89748	-16.316834
50	185.89512	-16.316519
45	185.89491	-16.31658
40	185.89412	-16.3165

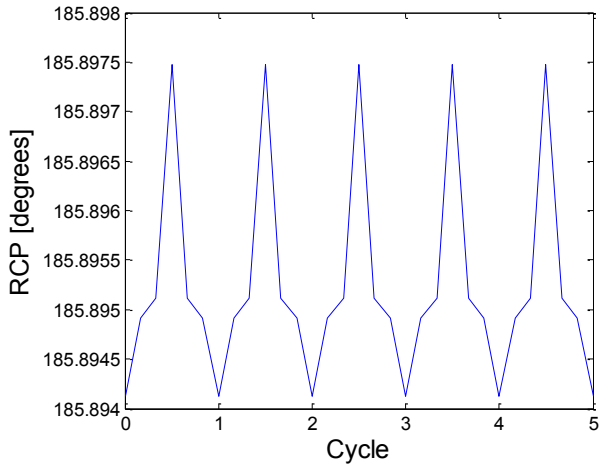

Figure 4.6: Antenna reflection coefficient phase variations for various heart layer thicknesses at 2.45 GHz over 5 cycles.

Table 4.5: Reflection coefficient phase and magnitude variations for various heart layer thicknesses at 5.8 GHz.

Heart Layer Thickness (mm)	Reflection Coefficient Phase (degrees)	Reflection Coefficient Magnitude (dB)
55	132.3107	-9.5335081
57.5	132.31078	-9.5335052
40	132.31467	-9.5332363

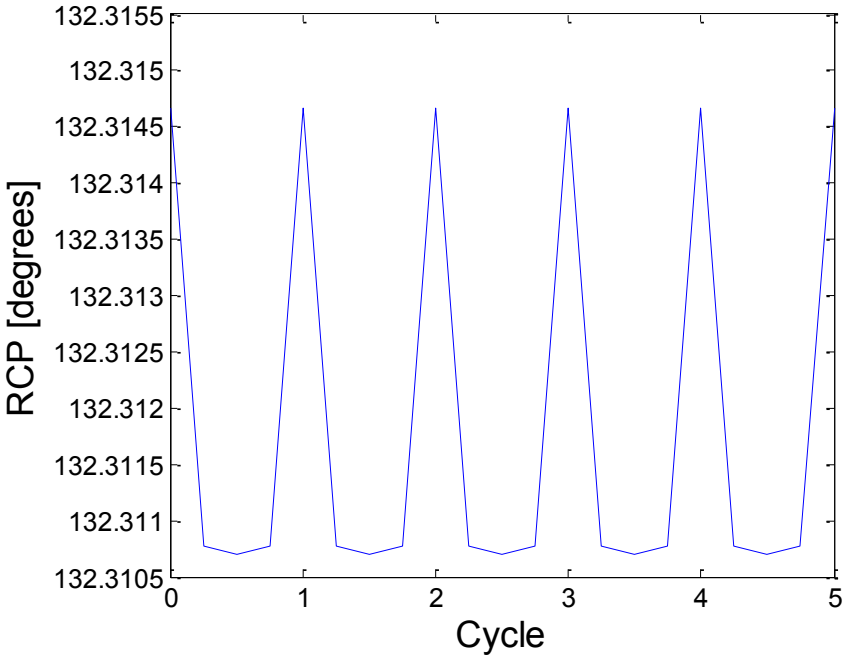

Figure 4.7: Antenna reflection coefficient phase variations for various heart layer thicknesses at 5.8 GHz over 5 cycles.

Table 4.6: Reflection coefficient phase and magnitude variations for various heart layer thicknesses at 9 GHz.

Heart Layer Thickness (mm)	Reflection Coefficient Phase (degrees)	Reflection Coefficient Magnitude (dB)
55	-142.3917	-11.972759
57.5	-142.3917	-11.97274
40	-142.39171	-11.972759

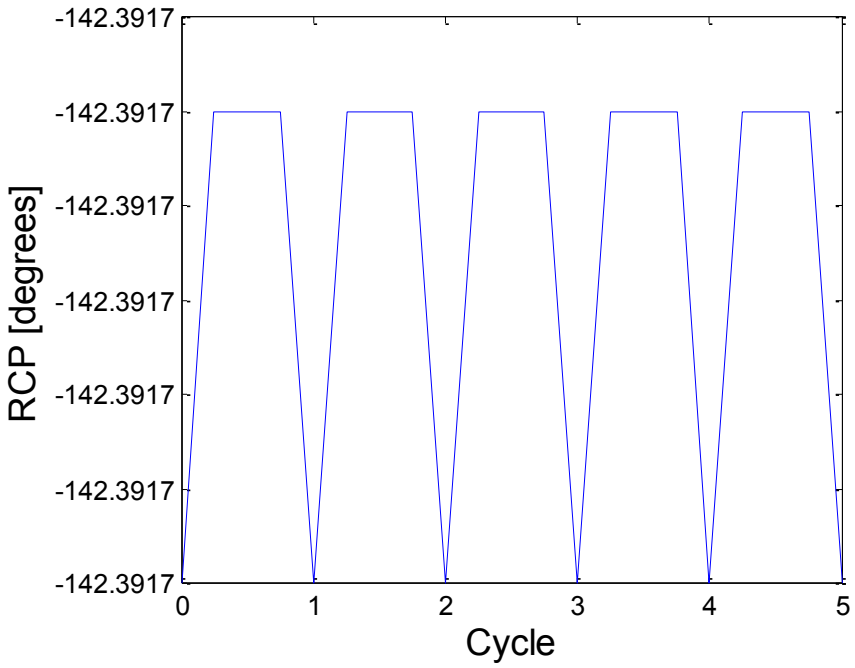

Figure 4.8: Antenna reflection coefficient phase variations for various heart layer thicknesses at 9 GHz over 5 cycles.

These simulations were conducted considering the lungs to be deflated. When the lungs are inflated their conductivity and permittivity changes (permittivity= 20.477, conductivity= 0.80416 at 2.45 GHz). The phase variations and the corresponding 5 cycle graph at 2.45 GHz are shown in table 4.7 and figure 4.9 respectively.

Table 4.7: Reflection coefficient phase and magnitude variations for various heart layer thicknesses at 2.45 GHz (Inflated lungs).

Heart Layer Thickness (mm)	Reflection Coefficient Phase (degrees)	Reflection Coefficient Magnitude (dB)
55	186.59171	-15.361991
50	186.58956	-15.36146
45	186.59161	-15.36274
40	186.59298	-15.360272

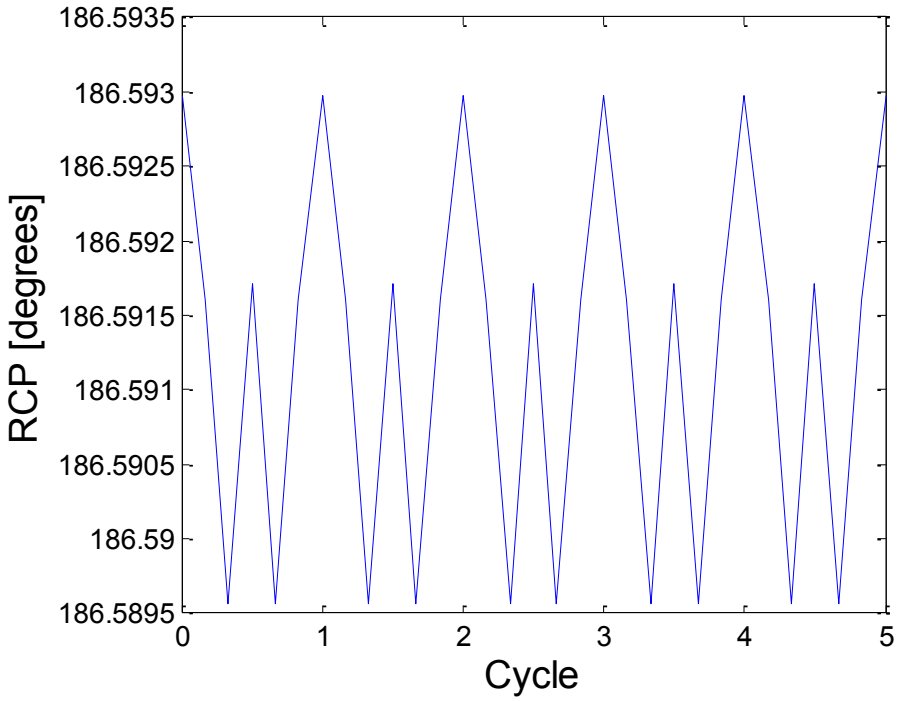

Figure 4.9: Antenna reflection coefficient phase variations for various heart layer thicknesses at 2.45 GHz over 5 cycles (Inflated lungs).

It is clear that the state of the lungs (inflated or deflated) has negligible effect on the extent of reflection coefficient phase variation between the various thicknesses of the heart. So the general trend of the antenna phase variation not being affected much by just heart movement still holds. An interesting result here is that the inflated and deflated lung results are different from each other by about 0.7 degrees. So the electrical property changes of the lungs during deflation and inflation have a direct effect on the antenna reflection coefficient phase even though the lung thickness is kept constant.

4.2.8 Simulation Study considering effect of chest movement

In this section simulations were carried out considering the antenna to be stationary and the whole chest moving. The heart thickness was taken constant at 47.5 mm. Two cases were

considered, one for the cardiac cycle and the other for the respiratory cycle. The antenna is kept 2 mm away from the chest.

Cardiac Cycle

For the cardiac cycle the chest moves 0.2 to 0.5mm due to heart beats [12]. Due to immense processing times, three points (0mm, 0.25mm, 0.5 mm) in this cycle were chosen for simulation. During the cardiac cycle, the phase variation due to the chest movement is considered linear. The phase variations obtained at 2.45 GHz, 5.8 GHz and 9 GHz are shown in table 4.8. MATLAB was used to draw the phase variation graph over several cardiac cycles. The cardiac cycles for 2.45 GHz, 5.8 GHz and 9 GHz are shown in figures 4.10, 4.11 and 4.12 respectively. The highest phase variations are observed for 5.8 GHz. At 2.45 GHz the least variations are observed. These variations nonetheless are significantly more compared to the case when only the heart is moving. This shows that even a minute movement of the chest brings about a measurable change in the reflection coefficient phase of an antenna attached parallel to it.

Table 4.8: Reflection coefficient phase and magnitude variations for various distances of the chest from the antenna at 2.45 GHz, 5.8 GHz and 9 GHz.

Frequency (GHz)	**2.45 GHz**		**5.8 GHz**		**9 GHz**	
D (mm)	Reflection Coefficient Phase (degrees)	Reflection Coefficient Magnitude (dB)	Reflection Coefficient Phase (degrees)	Reflection Coefficient Magnitude (dB)	Reflection Coefficient Phase (degrees)	Reflection Coefficient Magnitude (dB)
0	186.37696	-14.60	137.40397	-9.55	-135.15611	-12.143
0.25	186.2654	-15.53	140.1383	-10.04	-136.98341	-11.550
0.5	185.89234	-16.32	133.50453	-11.47	-137.34504	-11.523

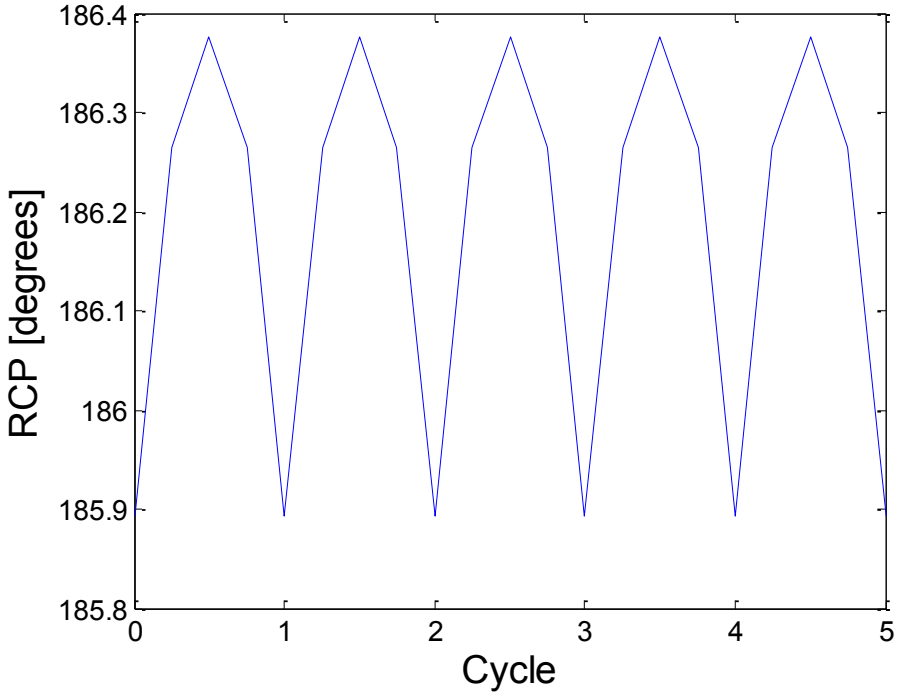

Figure 4.10: Antenna reflection coefficient phase variations for various distances of the chest from the antenna at 2.45 GHz over 5 cycles.

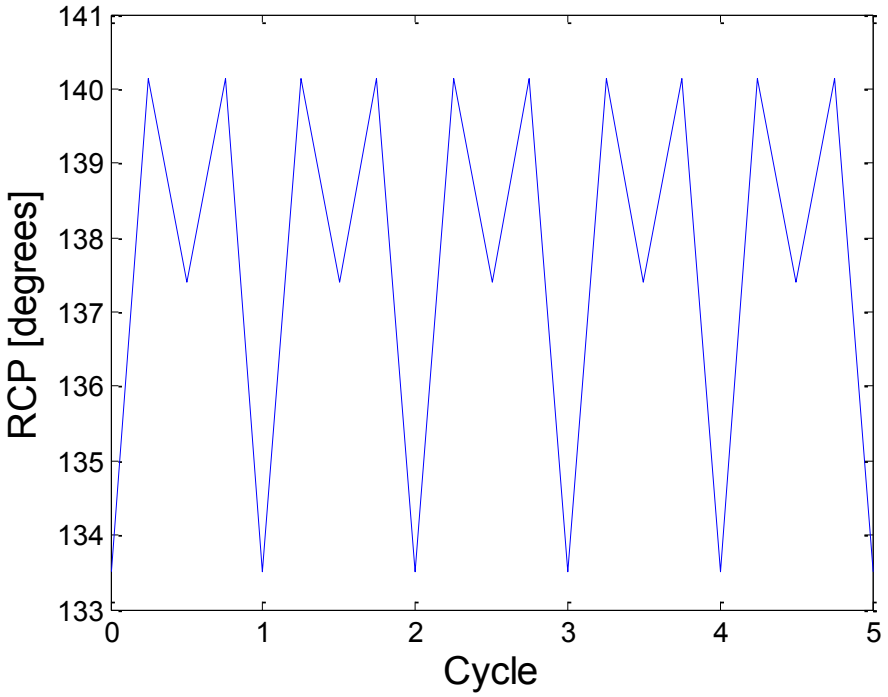

Figure 4.11: Antenna reflection coefficient phase variations for various distances of the chest from the antenna at 5.8 GHz over 5 cycles.

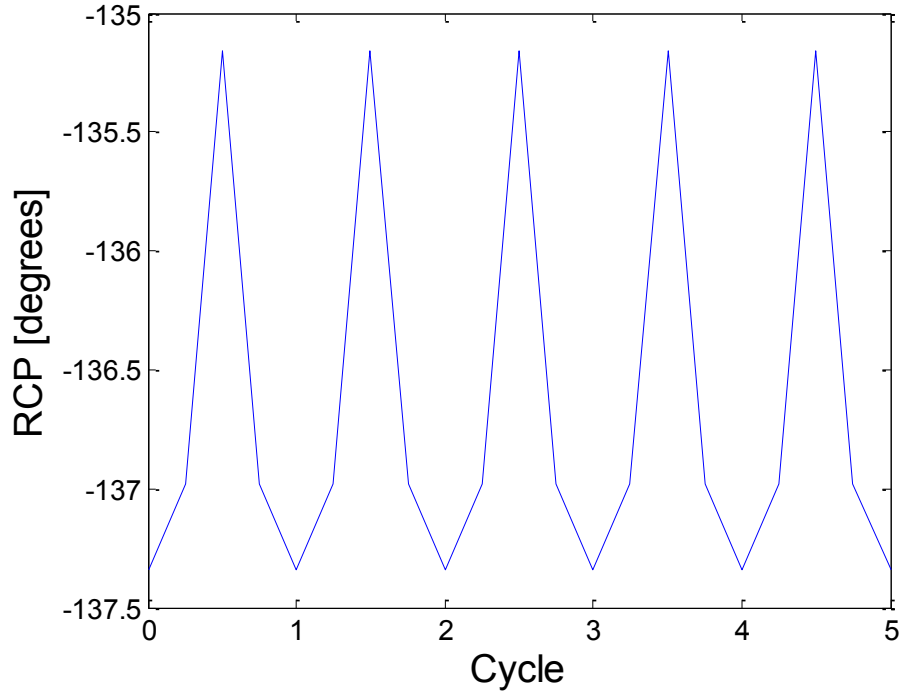

Figure 4.12: Antenna reflection coefficient phase variations for various distances of the chest from the antenna at 9 GHz over 5 cycles.

Respiratory cycle

For the respiratory cycle the chest moves 8 mm to 12mm due to the lungs expanding and contracting and the antenna position is kept constant [12]. Due to immense processing times, only three points (0mm, 6mm and 12mm) of the respiration cycle were chosen for simulation. The phase variation due to chest movement is considered linear. The phase variations obtained at 2.45 GHz, 5.8 GHz and 9 GHz are shown in table 4.9. MATLAB was used to draw the phase variation graph over several respiration cycles. The respiratory cycles for 2.45 GHz, 5.8 GHz and 9 GHz are shown in figures 4.13 (a), (b) and (c) respectively. From Table 4.9 it is clear that as the frequency increases the variation in phase decreases. This was repeated for another monopole wideband antenna with similar results. These simulations point to the use of lower frequencies for better sensitivity of the antenna to chest movements.

Table 4.9: Reflection coefficient phase and magnitude variations for various distances of the chest from the antenna at 2.45 GHz, 5.8 GHz and 9 GHz.

Frequency (GHz)	**2.45 GHz**		**5.8 GHz**		**9 GHz**	
D (mm)	Reflection Coefficient Phase (degrees)	Reflection Coefficient Magnitude (dB)	Reflection Coefficient Phase (degrees)	Reflection Coefficient Magnitude (dB)	Reflection Coefficient Phase (degrees)	Reflection Coefficient Magnitude (dB)
0	185.89234	-4.5195371	137.40397	-9.5512642	-128.65165	-12.266731
6	149.33972	-4.4933059	170.52136	-11.227219	-130.17037	-10.599232
12	130.1608	-16.316773	185.6994	-8.685951	-134.95588	-10.511072

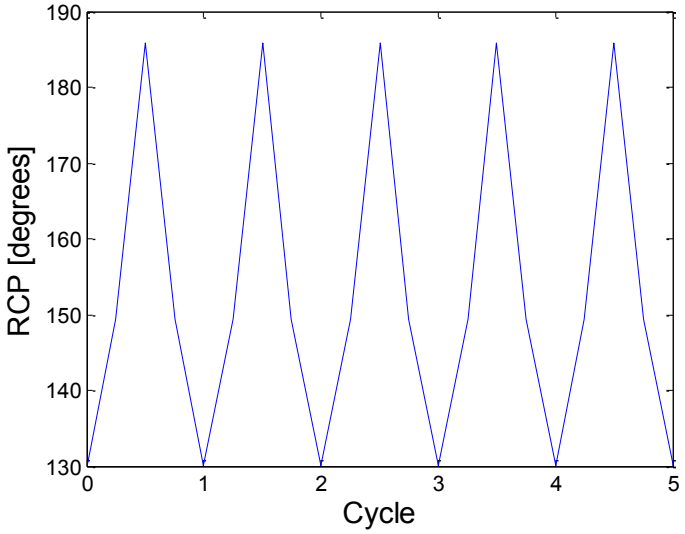

Figure 4.13 (a): Antenna reflection coefficient phase variations for various distances of the chest from the antenna at 2.45 GHz over 5 cycles.

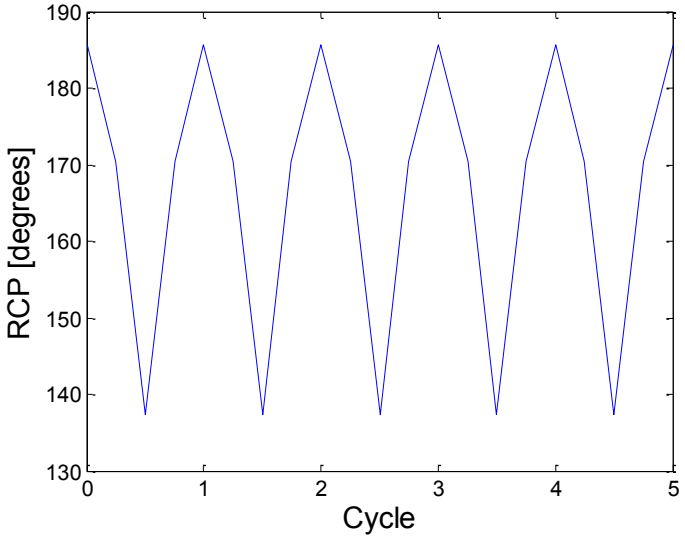

Figure 4.13 (b): Antenna reflection coefficient phase variations for various distances of the chest from the antenna at 5.8 GHz over 5 cycles.

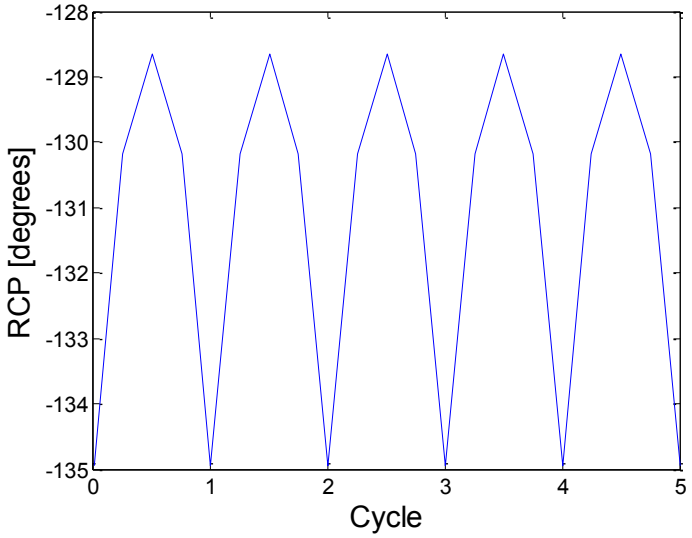

Figure 4.13 (c): Antenna reflection coefficient phase variations for various distances of the chest from the antenna at 9 GHz over 5 cycles.

4.2.9 Antenna Comparison

In this section four antennas will be used to perform the respiration cycle simulations to determine the effect of antenna type on the reflection coefficient phase sensitivity. The antennas were chosen based on the best experimental results from section 4.5. The four antennas are:

1) Patch antenna (shown in figure 4.14(a)) with its ground towards the chest.

2) Patch antenna with its radiating patch towards the chest.

3) Loop antenna (shown in figure 4.14(b))

4) Monopole antenna (from Figure 4.4) (more detail in section 4.2.6)

Figure 4.14 (c) shows the orientation of these antennas with respect to the chest. Only the respiration cycle was considered because here only the extent of phase variation achievable was sought. The antenna was again 2mm away from the chest. The chest was then moved a farther 0mm to 12mm from the antenna. Only two extreme distances (0mm and 12mm) were

considered as only the phase variation extent was to be determined. Antennas 1-3 are specifically designed to operate at 2.45 GHz, while antenna 4 is a wideband antenna. The phase and resonant frequency variations for all of these antennas are shown in table 4.10. Figures 4.15 (a), (b) and (c) show the reflection coefficient magnitude of antennas 1, 2 and 3.

In free space, antennas 1-3 resonate at 2.45 GHz.

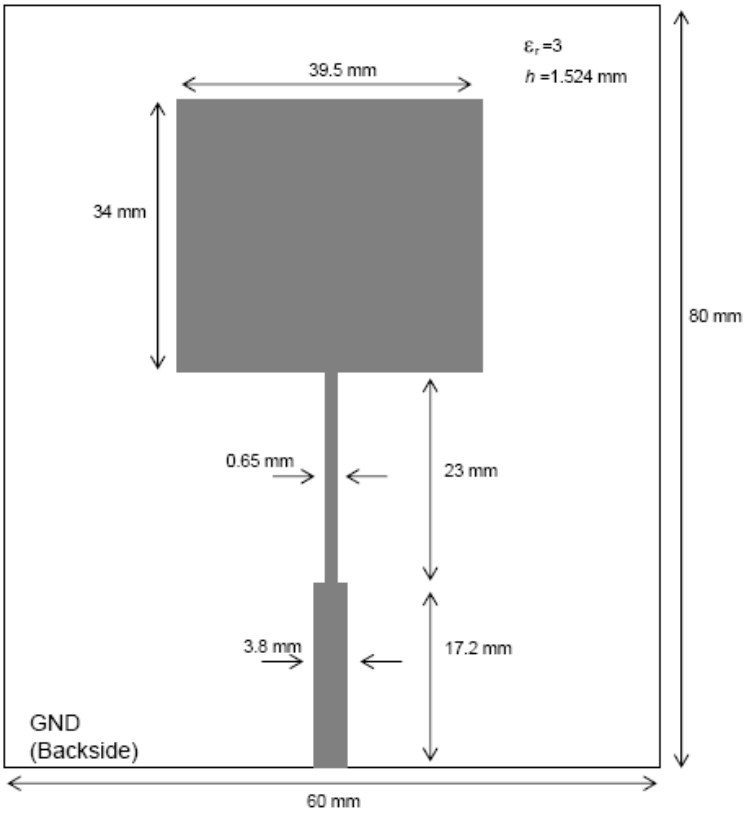

(a)

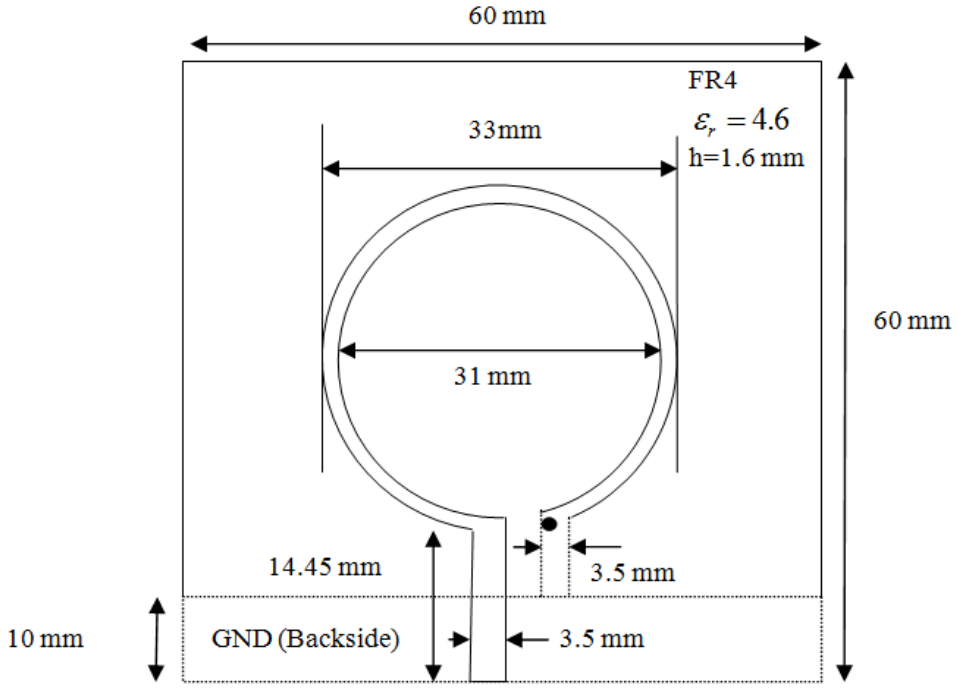

(b)

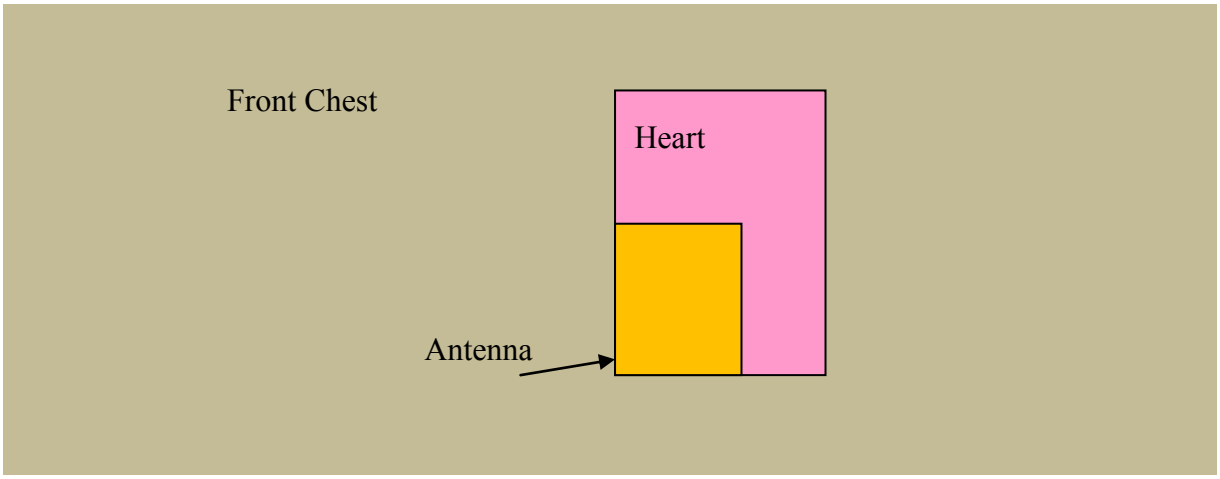

(c)

Figure 4.14: Topology of (a) Patch Antenna [8] (b) Loop Antenna [7] (c) Orientation of Antenna with respect to the chest.

It is clear from table 4.10 that reflection coefficient phase variation is higher for the loop and monopole antennas, while it is lower for the patch antenna with radiating element facing the chest, and it is lowest for the patch antenna with ground facing the chest. The reason for these results is that the bigger the ground plane, the less effect the chest presence and movement have on the antenna. The loop antenna and monopole antenna have minimal ground planes while the patch antenna has a significant size ground plane. The patch antenna with ground plane towards the chest gets shielded from the effect of the chest while the patch antenna with radiating patch towards chest does not get shielded but still has less phase variation compared to antenna 3 and 4 due to its large ground plane. We see that the S_{11} characteristics for antenna 2 when it is 2mm away from the chest model are much deteriorated. This is due to the fact that the radiating element of the patch antenna (for antenna 2) is facing the chest and is very close to it. Although at 14 mm away from the chest the S_{11} characteristics are just shifted from its resonant frequency. The resonant frequency changes from 2.162 dB to 2.4 dB for antenna 3 when the chest is 2mm and 14mm away from the antenna. So the resonant frequency varies heavily for the loop antenna (antenna 3) and patch antenna with radiating element facing the chest (antenna 2). For the loop antenna it is because of no ground plane while the patch with radiating element towards the chest does not get shielded from the chest as the ground plane is not facing the chest.

Table 4.10: Reflection coefficient phase and resonant frequencies for various distances of the chest from four antennas at 2.45 GHz.

Antenna Type	**Antenna 1**		**Antenna 2**		**Antenna 3**		**Antenna 4**
Distance (mm)	Resonant Frequency (dB)	Reflection coefficient Phase at 2.45 GHz (degrees)	Resonant Frequency (dB)	Reflection coefficient Phase at 2.45 GHz (degrees)	Resonant Frequency (dB)	Reflection coefficient Phase at 2.45 GHz (degrees)	Reflection coefficient Phase at 2.45 GHz (degrees)
2	2.426	137.9088	2.48 (only -6dB)	138.1928	2.162	24.43120	185.8923
14	2.424	137.8975	2.157	145.71004	2.4	57.79657	130.1608

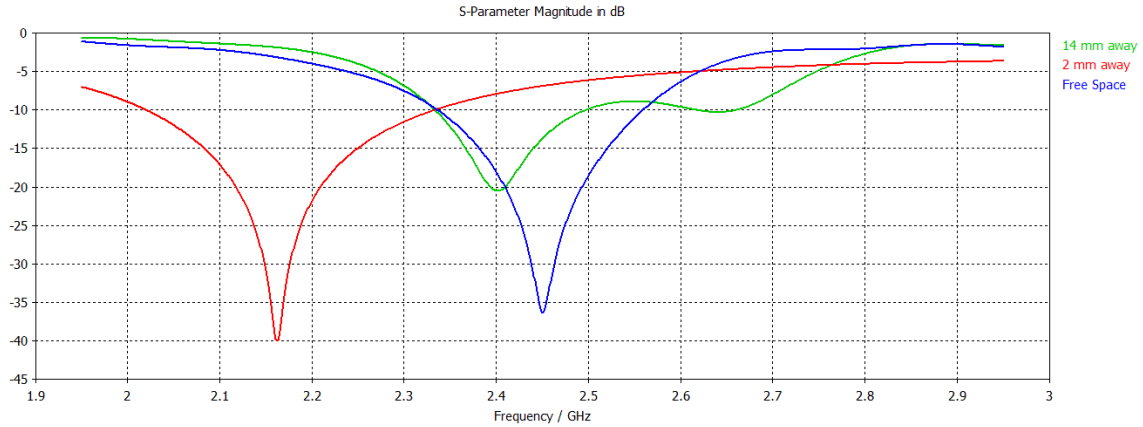

(a)

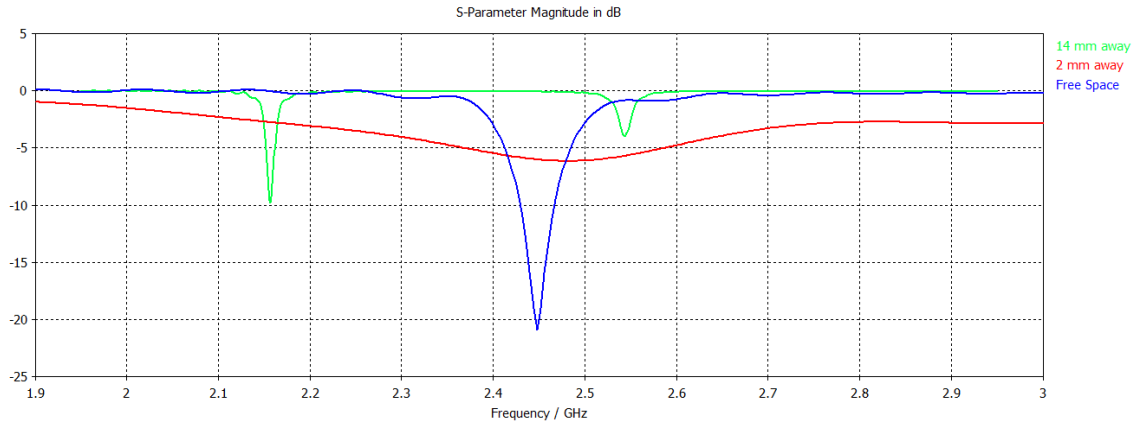

(b)

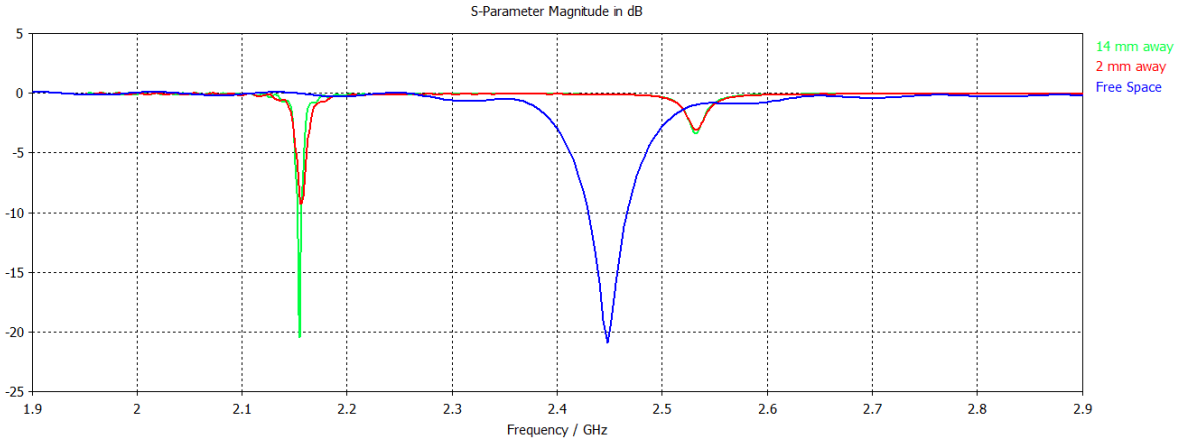

(c)

Figure 4.15: Reflection coefficient with (a) antenna 1, (b) antenna 2, and (c) antenna 3 in free space, 2mm and 14mm away from chest model.

4.2.10 Distance Effect

The effect of increasing the distance between the antenna and chest on the reflection coefficient phase of the antenna was examined in this study. The patch antenna with radiating element facing the chest was used to perform the study. The antenna position was kept constant while the chest first moved from 0mm to 12 mm when it was 2mm from the antenna. For the second case, chest was moved from 0mm to 12 mm when it was 200mm away from antenna. Only the extremes (0mm and 12mm) were simulated. The phase variations and the resonant frequencies achieved are shown in Table 4.11.

It is clear from Table 4.11 that when the distance between the antenna and chest was increased the reflection coefficient phase of the antenna was less sensitive to the movement of the chest.

Table 4.11: Reflection coefficient phase and resonant frequencies for various distances between chest and antenna at 2.45 GHz.

Total distance between chest and antenna (mm)	Resonant Frequency (dB)	Reflection coefficient Phase at 2.45 GHz (degrees)
2 mm	2.48 GHz (but only – 6 dB)	145.71004
14 mm	2.157 GHz	138.19286
200 mm	2.154 GHz	137.91482
212 mm	2.154 GHz	137.94547

4.2.11 Conclusions from simulation study

It was shown that the reflection coefficient phase variation obtained for an antenna attached parallel to the chest was mainly due to the chest movement relative to the antenna. Even though the antenna was kept stationary in these experiments and real life does not follow this scenario, the principle was still established. It was also shown that antennas with minimal grounds were the most sensitive to chest movements. Increasing the distance between the chest and the antenna had the effect of decreasing the sensitivity of the antenna reflection coefficient phase to chest movements. The 3-D model developed here represents a rough description of the complex biological human chest. The results obtained showed that the on-body technique holds promise for the measurement of vital signs. To prove the ability and accuracy of the On-Body vital signs monitoring technique, actual experiments were performed on human subjects, the results of which are presented in the following sections.

4.3 Setup and Methodology

In this section the equipment used for On-Body vital signs monitoring will be introduced. The signal processing techniques used to analyze the data will be described in 4.3.1. Section 4.3.2 will discuss the population used. The different measurements used to describe the body type and shape will be presented. Then the different methods used for the analysis of collected data will be presented in section 4.3.3.

4.3.1 Experimental equipment and Setup

The basic components comprising the On-Body vital signs monitor include HP 8722D vector network analyzer (VNA), R&S ZVA67 VNA and an antenna. VNA noise contributions are quantified in section 3.4.1. The S_{21} characteristics of the cable used to connect the VNA with the antenna are shown in fig. 4.16. The aim was to determine the best parameters including frequency, power, etc. for the most accurate operation of On-Body vital signs monitor. For such a study, the VNA presented the obvious choice as a wide range of these parameters is provided by a VNA. The VNA was programmed using Microsoft Visual basic and it was connected to the Laptop using a GPIB-to-USB converter. The antenna was attached parallel to the chest with the help of a tape and a belt if needed. The antenna used for experiments in which the frequency was varied was a CPW monopole antenna or a monopole antenna with truncated ground. These antennas were designed to be wideband and Omni directional.

The ECG device EG05000 from medlab was used as reference for heart rate. It has built in isolation, filtering and amplification. Three electrodes were used and were placed at the ends of the left arm, right arm and left leg. Electrodes used were commercially available MLA1010B Disposable Ag/AgCl ECG Electrodes. The EG05000 could communicate with the PC through a USB connection and its programming was in C programming language.

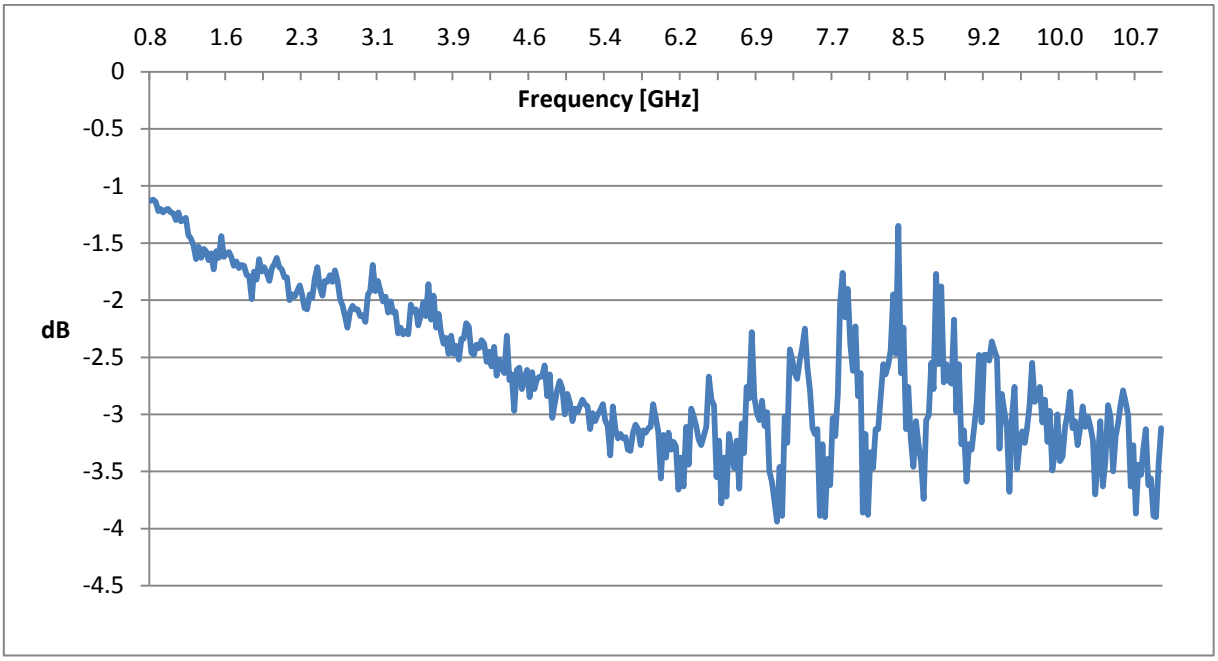

Figure 4.16: S_{21} characteristics of the cable used to connect the VNA with the antenna.

MLT1132 Respiratory Belt Transducer from ADInstruments was used as reference for breathing rate. The belt was placed either on the chest or the abdomen depending on where maximum displacement due to breathing was observed. The analogue signal from the belt was converted into a digital signal and input into the PC through a USB using 12-Bit, 10 kS/s NI-USB 6008. The general setup including all these components is shown in Figure 4.17.

The subject was wearing normal clothing. If the subject was wearing a jacket or a sweater, etc., he/she was asked to remove it so that the experiments can be performed on shirts and not be affected by the uneven nature of such clothing. The subject was seated with the antenna attached parallel to the chest and refrain from moving or talking for the duration of the experiment. For the supine position experiment subject lay down flat on the ground over a sheet with arms on the sides.

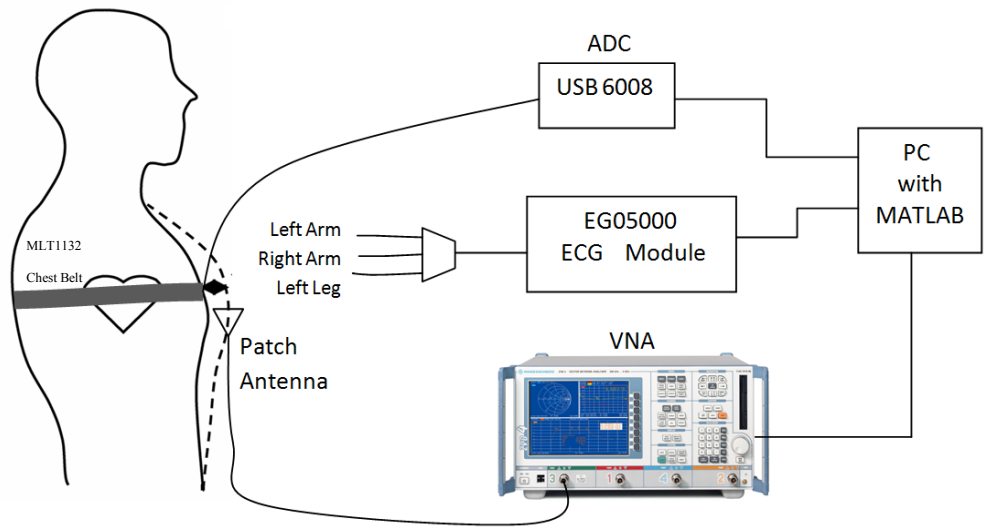

Figure 4.17: General experimental setup showing the VNA, chest belt and ECG monitor.

Before starting the experiment the antenna was attached with tape on the person's chest after adjusting its position. The position was adjusted by considering whether the breathing signal was visible on the VNA when the person was breathing normally, and whether the heart signal was visible on the VNA when the person was in apnea state. For the actual experimental measurements, he/she was instructed to breathe normally for the duration of 5 minutes. All of the experiments were performed in normal lab environment.

4.3.2 Signal processing

The signal processing techniques employed for the experiments in this chapter are exactly the same as described in section 3.4.2 with the exception that the order of the high and low pass Butterworth filters is 8 and 11 rather than 6 and 8. The orders of the filters were chosen by hit and trial method based on best results. A detailed study of the choice of digital signal processing algorithm can be found in Appendix B.

The summary of the various signal processing algorithms used for extracting vital signs in the form of block diagrams can be seen in figure 4.18.

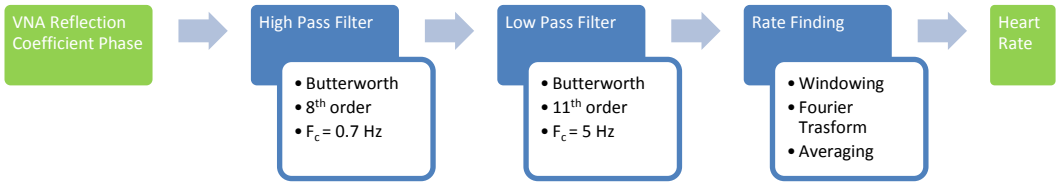

(a)

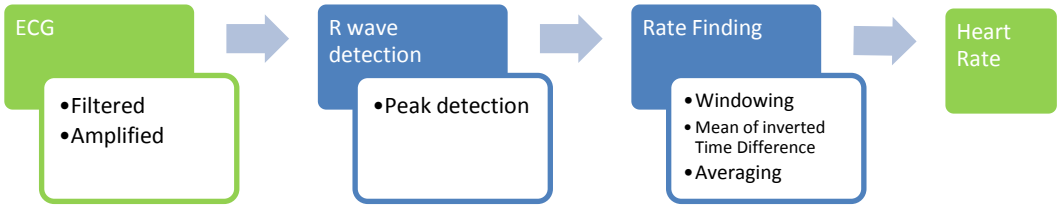

(b)

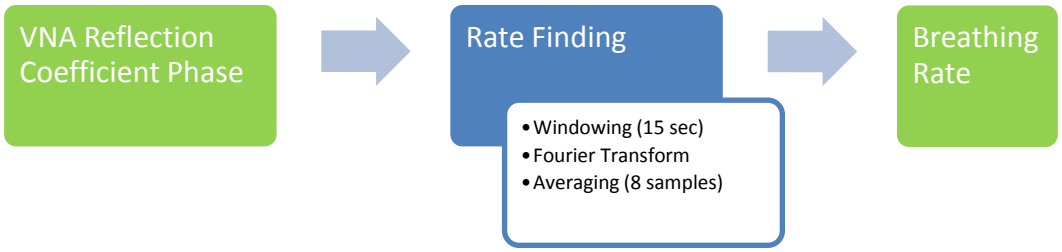

(c)

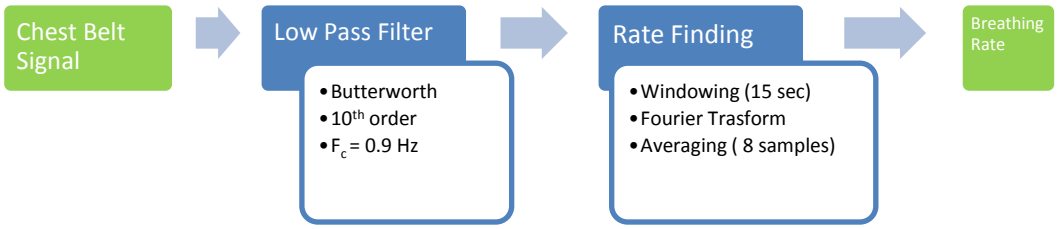

(d)

Figure 4.18: Block diagrams showing the signal processing algorithm for calculating (a) heart rate from VNA signal, (b) heart rate from ECG device, (c) respiration rate from VNA signal, (d) respiration rate from MLT1132 piezoresistive belt.

4.3.3 Human Subjects

Experiments were conducted on 13 people in total (2 female and 11 male). The average age of the population tested was 23.8 with a standard deviation of 8.2. The average BMI of the population was 24.5 with a standard deviation of 3.7. The other measurements are shown in Table 4.12. Section 4.3.4 describes how these measurements were obtained. It was made sure that none of the people experimented upon had any heart or lung diseases or a pacemaker. In the case of the females it was also made sure none of them were pregnant.

Table 4.12: Human Body Measurements (Gender = Gen, Height = Ht, Wight = Wt, Body Mass Index = BMI, Chest Circumference = CC, Waist Circumference = WC, Chest Depth = CD, Chest Width = CW) (Inhalation = i, Exhalation = e)

No	Age	Gen	Ht [cm]	Wt [kg]	BMI [Kg/m^2]	CCi [cm]	CCe [cm]	WCi [cm]	WCe [cm]	CDi [cm]	CDe [cm]	CWi [cm]	CWe [cm]
1	26	M	186.5	70	20.1	92.5	87.5	80	83.5	19	16.9	29.3	27.7
2	30	M	167.9	85	30.2	109	107.5	103	98	24.2	22.9	32.5	32
3	24	M	173.7	74.1	24.6	92.5	92.1	82	81.7	23.7	21.7	30.7	28.2
4	33	M	179.95	83.8	25.9	101.4	95	89.4	86.3	23.5	21.7	30	27.6
5	26	M	171.5	65	22.1	98.5	93.2	82.1	79.3	21	20.6	30.8	28.7
6	30	M	175.25	78	25.4	96	93.9	83.1	81.4	20.3	18.8	27.9	26.3
7	24	M	164	68.6	25.5	100	96.4	86.5	84.5	21.1	20	28.4	27.5
8	24	M	184.5	86.7	25.5	109.5	100.5	95	93.5	26	22.2	35.6	33.8
9	19	F	172.8	53.4	17.9	76	70	66.6	68.4	19.7	17.5	24.9	22.9
10	24	M	168.6	82.6	29.1	101	99.4	103.1	98.5	24.5	23.3	31.4	29
11	26	M	170.9	80	27.4	101.2	97.5	94.5	92	23.7	22.7	30.7	28.5
12	26	M	175	78	25.5	104.5	100.5	93.6	95.5	21.7	20.5	33.2	20.5
13	19	F	166	53.2	19.3	86	81	67.5	69.5	19.3	17	25.7	23.6
Avg	23.8		173.6	73.7	24.5	97.8	93.4	86.6	85.5	22.1	20.4	30.1	27.4
StdD	8.2		6.8	11.2	3.7	9.1	9.6	11.5	9.8	2.2	2.3	2.9	3.6

4.3.4 Human Body Measurements

The measurement parameters chosen here were based on whether they would have an effect on the detection accuracy results if they were changed. Also similar parameters were used in a study on Doppler radar vital signs monitoring results over a 20 people sample population in [12]. Details of how these parameters are measured can be found in [12].

Body mass index

The BMI is a heuristic proxy for human body fat which is based on an individual's height and weight. It is measured by dividing a subject's body weight by the square of his/her height.

$$BMI = \frac{Weight}{Height^2}$$

It has been adopted by most as the common method to represent a body type although it does not account for the difference between a moderately obese person and a muscular person, nor does it consider the composition change with age. Its performance has shown to be improved by using different powers for different genders and age but here the normally used power of two will be employed [13][14]. Different categories of classification of BMI include [15]:

Table 4.13: BMI Body Type Classification [15]

Category	BMI Range
Underweight	<18.5
Normal	18.5-24.99
Overweight	25-29.99
Obese	≥30

4.3.5 Analysis Techniques

Replacing an old medical data measuring technique with a new one requires analysis methods which show the extent to which the two techniques agree with each other in order to determine the suitability of replacement. Correlation coefficients are not considered a reliable indicator in this case as the results can be misleading [16]. In the results and discussion sections of this chapter, first the accuracy within 5 BPM of the reference will be used to give an indication of suitability. Furthermore a popular clinical measurement comparison technique called Bland Altman analysis and Signal to Noise ratio will be used. The Bland Altman analysis and SNR is already described in section 3.4.3.

Correlation Coefficient

The correlation coefficient will be used to determine whether there is any relationship between the measured human body parameters and the detection accuracy as well as the SNR of the measured results. Pearson correlation coefficient is a measure of the strength of association between two given variables (X and Y) and is calculated by [19]:

$$r = \frac{\sum_{i=1}^{n}(X_i - \overline{X})(Y_i - \overline{Y})}{(n-1)s_x s_y}$$

Where s_x and s_y are the standard deviations of X and Y, and n is the size of X and Y. The Pearson correlation coefficient, r, can have a value between 1 and -1 depending on whether there is a directly proportional or inversely proportional relationship between the two variables. A value of 0 means no correlation is present. The closer it is to ±1, more perfectly linear the relationship is. The p-value is used to test the hypothesis of no correlation. It gives the probability of getting the observed correlation by a random chance. For example if the p

value is 0.05, there is only a 5% chance of getting the observed correlation randomly. Usually a value of p below or equal to 0.05 means the correlation value is significant. The p-value can be calculated by the following formula:

$$\rho = \frac{\mathrm{cov}(X,Y)}{s_x s_y} = \frac{E[(X-\mu_Y)(Y-\mu_Y)]}{s_x s_y}$$

where E is the expected value. So p-value is the covariance divided by the product of the standard deviations. Further details of this calculation can be found in [19].

Linear Regression Analysis

Linear Regression models the relationship between variables using linear functions. It can be used as a predicting model to forecast data or it can be used to quantify the strength of the relationship between two variables [20]. The coefficient of determination R^2 is used to determine how well the model fits the real data points. A value equal to 1 indicates that the linear model explains all the variation of the dependent variable, a value of 0.6 indicates that 60 % of the variation is explained by the model [20]. In a linear model fitted by least squares it is equal to the square of the Pearson correlation coefficient r .

4.4 Effect of frequency

4.4.1 Experimental Setup

The basic setup as described in section 4.3.1 will be used here. For the purpose of determining the effect of frequency, the frequency was varied using a VNA and a wideband CPW planar monopole antenna was chosen to be attached parallel to the front left chest of subject 1(from 4.3.3). This antenna was designed to be as small as possible, not have a ground plane and operate over a wideband. The topology and reflection coefficient of the antenna are shown in figure 4.19 and 4.20 respectively. The reflection coefficient magnitude at the

measured frequencies of 1 GHz, 2.45 GHz, 3.5 GHz, 5.8 GHz, 7 GHz, and 9 GHz is -3.97 dB, -6.16 dB, -11.62 dB, -8.49 dB, -11.70 dB, and -16.33 dB respectively. The design of this antenna is discussed further in section 5.3.1.

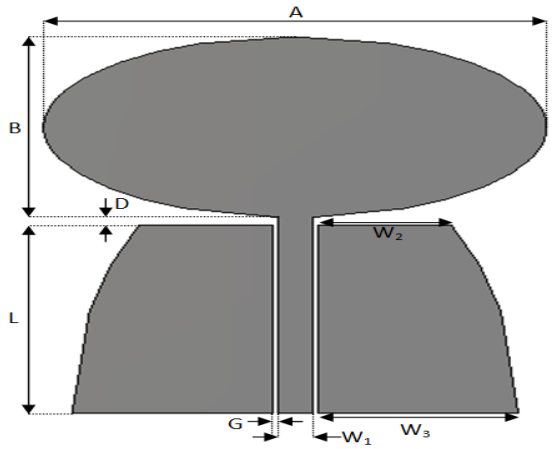

Figure 4.19: Topology of the Wideband CPW antenna. The dimensions are: A=44 mm, B=24 mm, G=0.5 mm, W1= 5 mm, W2= 6 mm, D=2 mm, W3=17.5 mm and L= 25 mm.

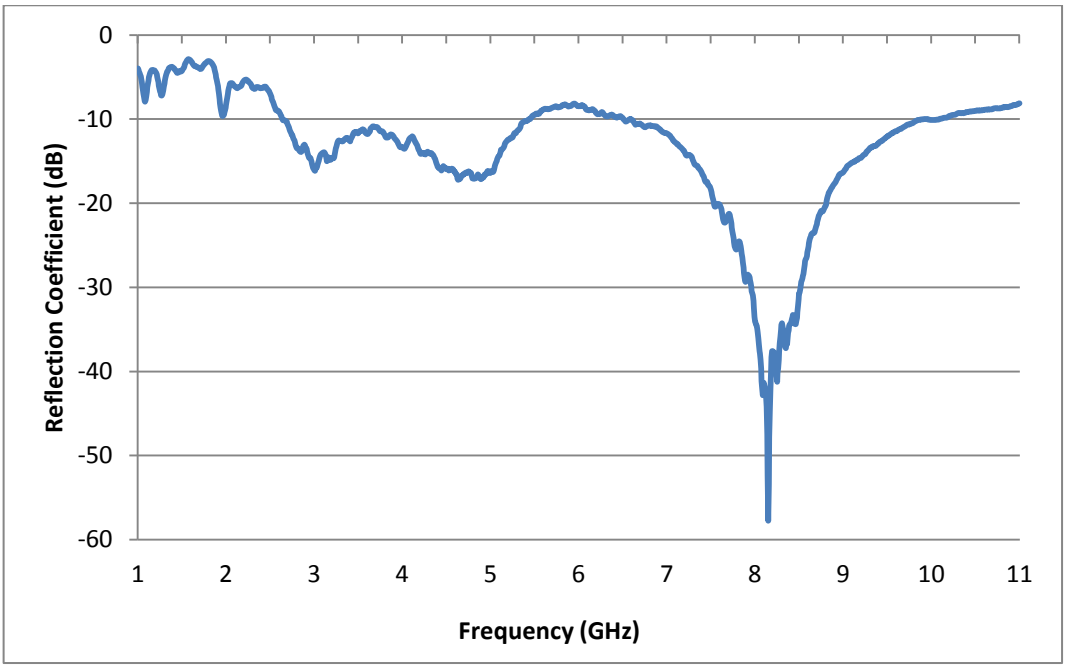

Figure 4.20: Measured Reflection Coefficient of antenna shown in figure 4.19.

For this study, the subject was asked to sit on a chair and remain still. The antenna was attached to his clothes using tape. The parameters and states which were kept constant are shown in Table 4.14.

Table 4.14: Constant Parameters for effect of frequency experiments

Power	-10 dBm
Duration	5 minutes
Sampling Rate	30 samples/sec
Body Position	Sitting
Antenna	CPW Planar Monopole Antenna

Three 5 minutes measurements were taken for the following frequencies: 1 GHz, 2.45 GHz, 3.5 GHz, 5.8 GHz, 7 GHz, and 9 GHz. Two measurements which showed least signs of movement after visual inspection were chosen to be analysed. Besides this the EG05000 and the MLT1132D as described in section 4.3.1 were used to measure the heart and breathing rate respectively. The MLT1132D was used only in one of the measurements to record the breathing signal as the introduction of the belt caused people to breathe more heavily and unnaturally to get a noticeable correct breathing signal for the belt. This unnatural and forced movement can cause an error in all vital sign detections and thus was avoided for the other two measurements.

4.4.2 Results and Discussion

4.4.2.1 Heart Rate

Table 4.15 shows the SNR, Accuracy, ECG Heart rate, On-Body heart rate, Bland-Altman mean difference, standard deviation and the 95 % confidence intervals of the heart rate detected using the On-Body monitoring method for the tested frequencies. Figure 4.21 shows the Bland-Altman plot for the tested frequencies. From the table a trend of decreasing detection accuracy with increasing frequency is observed. The Bland-Altman plots also show

more bias (increasing divergence from the zero difference line) with increasing frequency, which is reflected in the various Bland-Altman (BA) analysis values in Table 4.15. The accuracy percentages, SNRs and Bland-Altman plots all show the trend of decreasing performance with increasing frequency. The accuracy within 1 beat drops below 80% at 5.8 GHz and is only 33.5% at 9 GHz while maximum accuracy within 1 beat of 95.9% is achieved at 1 GHz. Accuracy within 5 BPM is around 90 % even at 7 GHz.

Table 4.15: Statistical analysis of heart rate from ECG and On-Body antenna at various frequencies. All BA results are in BPM.

Frequency (GHz)	**1**	**2.45**	**3.5**	**5.8**	**7**	**9**
SNR	1.4364	1.0077	1.3509	0.7631	0.7961	0.6978
Accuracy (%) (within 1 BPM)	95.9	87.8	91	77.7	63.3	33.5
Accuracy (%) (within 2 BPM)	98.47	93.7	99.66	84.78	78.4	42.52
Accuracy (%) (within 3 BPM)	98.8	95.1	100	86.7	83.8	47.6
Accuracy (%) (within 4 BPM)	99.1	95.6	100	88.4	87.9	50.2
Accuracy (%) (within 5 BPM)	99.7	96.1	100	89.3	90.8	53.9
ECG Heart Rate(BPM)	76.6	71.7	75.1	80.2	74.82	79.2
On-Body Heart Rate (BPM)	76.4	72	74.8	79.1	74.5	75.4
Mean Diff (BA)	0.2052	-0.2969	0.2025	1.0698	0.3283	3.8106
Standard Deviation (BA)	0.6964	3.2386	0.5797	4.8127	3.6427	8.0428
d +1.96 s_d (BA)	1.57	6.05	1.34	10.5	7.47	19.57
d -1.96 s_d (BA)	-1.16	-6.65	-0.93	-8.36	-6.81	-11.95

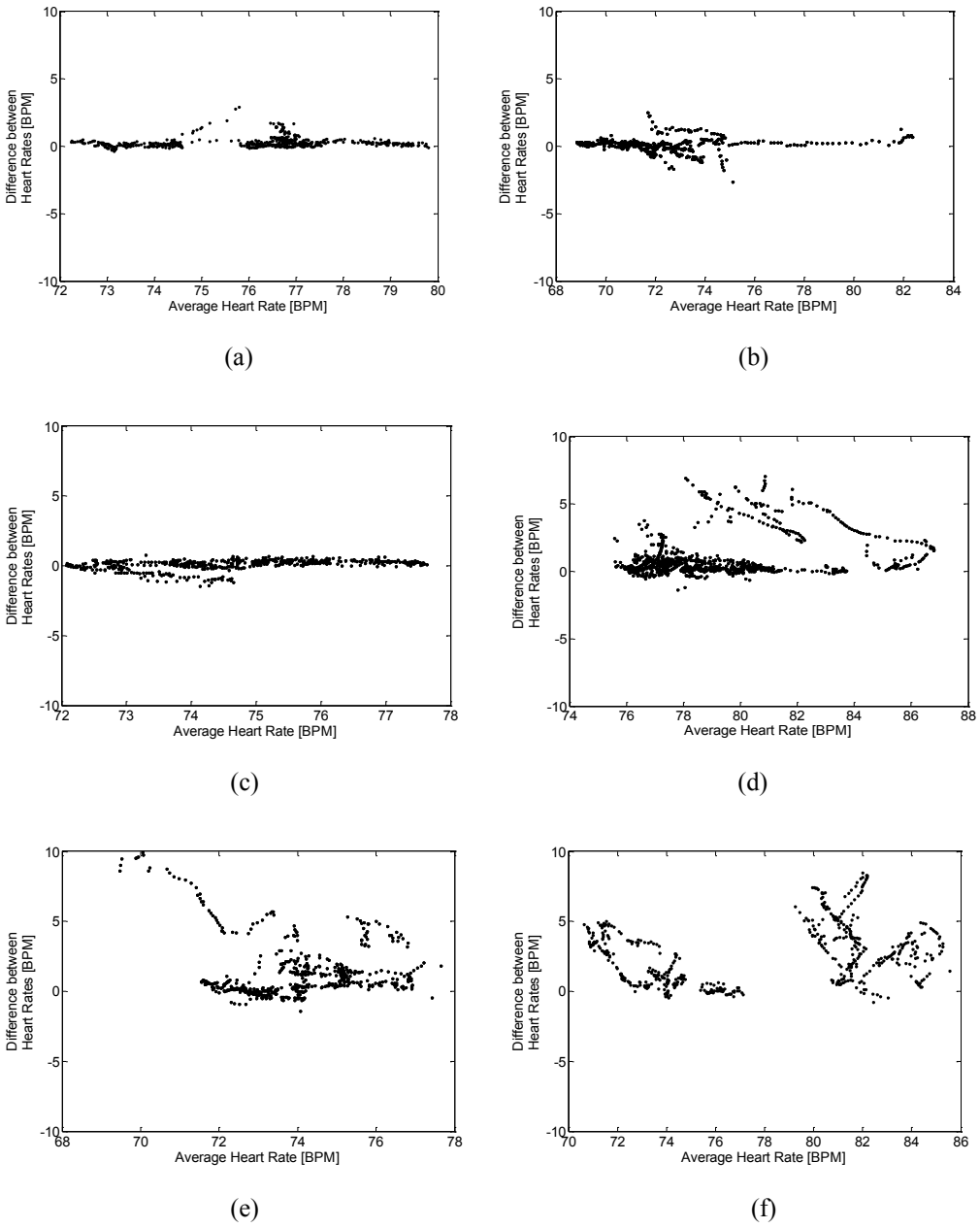

Figure 4.21: Bland-Altman plots for (a) 1 GHz, (b) 2.45 GHz, (c) 3.5 GHz, (d) 5.8 GHz, (e) 7 GHz, and (f) 9 GHz

Figure 4.22 shows the ECG graph and the filtered VNA heart graph for a 30 second duration of one 5 min input for the different frequencies. The reason for choosing a 30 seconds window was to make the graphs easier for the reader to view. The window was chosen after visual inspection to reflect the state of the signal throughout the measurement. Figure 4.23

shows the BPM versus time graph of one five minute measurement for the different frequencies.

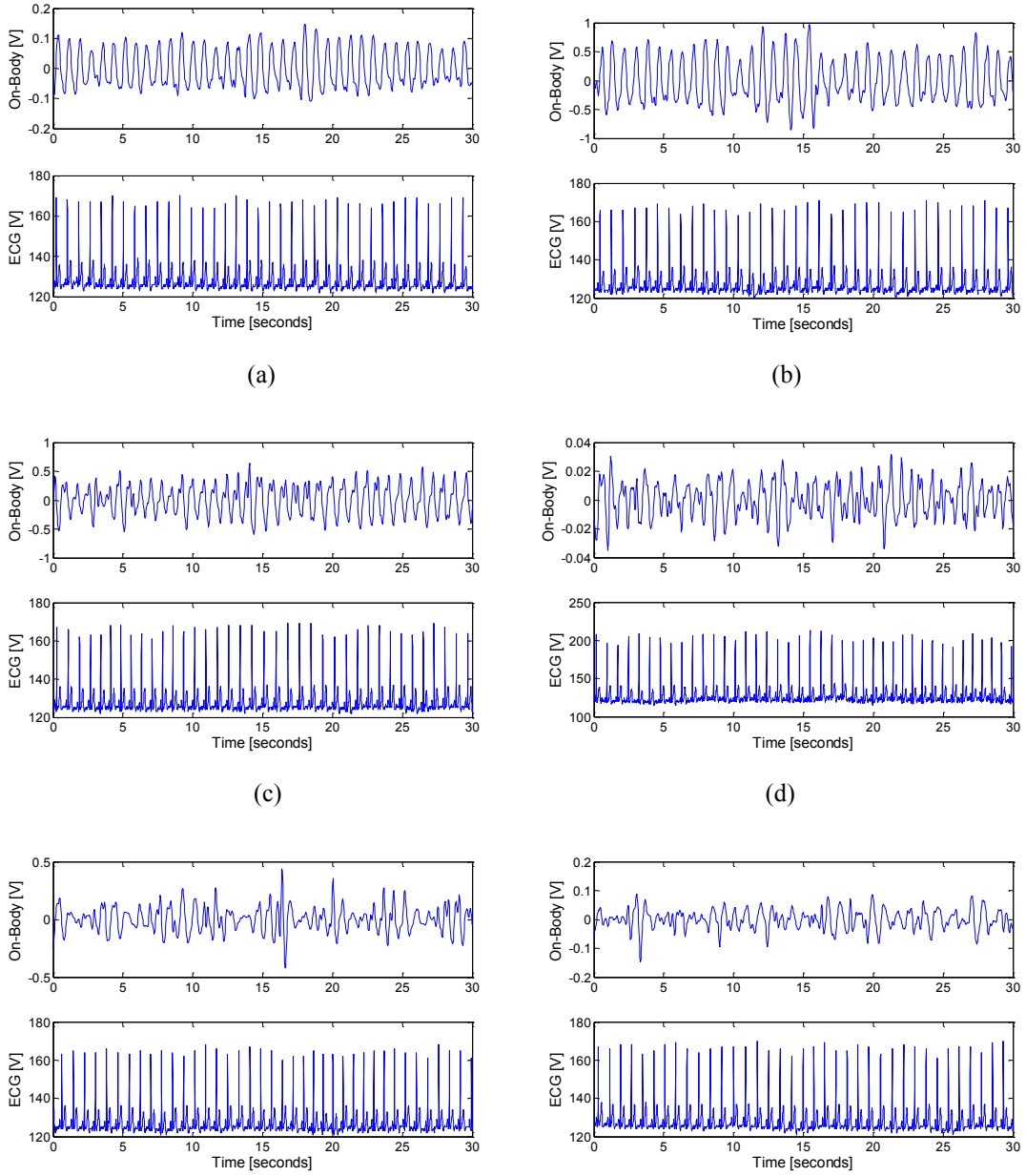

Figure 4.22: ECG signal and filtered On-Body heart rate plots for (a) 1 GHz, (b) 2.45 GHz, (c) 3.5 GHz, (d) 5.8 GHz, (e) 7 GHz, and (f) 9 GHz

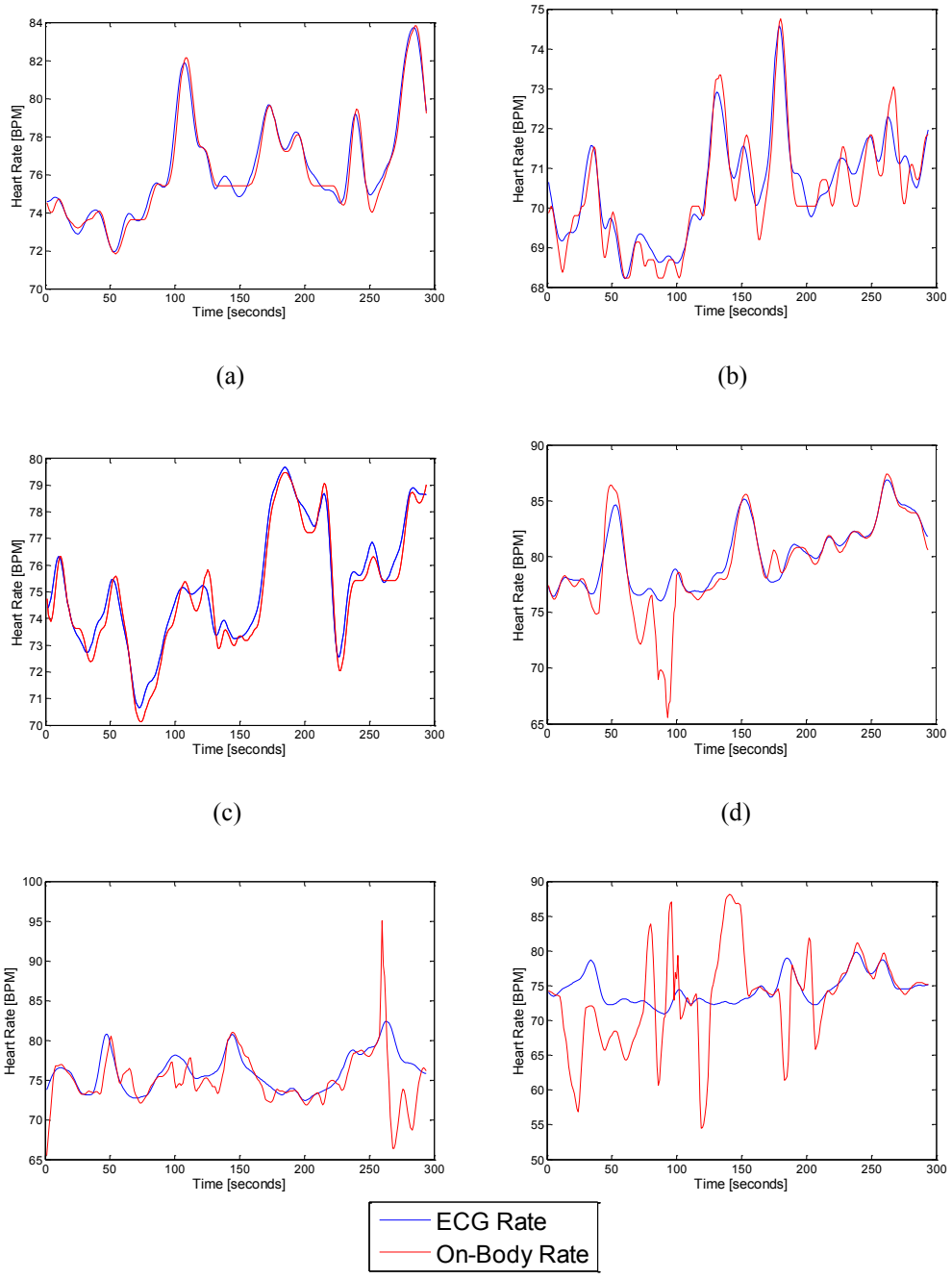

Figure 4.23: Heart rate [BPM] vs. Time for the ECG signal and On-Body monitor for (a) 1 GHz, (b) 2.45 GHz, (c) 3.5 GHz, (d) 5.8 GHz, (e) 7 GHz, and (f) 9 GHz

The reason for decreased performance at higher frequencies can be clearly seen in Figure 4.22 where it is observed that as the frequency increases the signal becomes noisier and the

individual heart beat cycles become difficult to distinguish. Also as the frequency increases the harmonic and intermodulation interference between the breathing and heart beating frequencies increases [20]. The interference has a negative effect on the detection accuracy. This harmonic and intermodulation interference was found to be worse in subjects with close heart and breathing rates in section 4.9. Besides this it was also observed that at higher frequencies the antenna reflection coefficient phase was very sensitive to any movements. So not only was it more sensitive to the breathing and heart beating movement of the chest, but also any other non-uniform or unwanted movements of the chest (sometimes due to extra fat or skin being loose). This extra sensitivity either caused sudden unwanted movement spikes or increased overall noise in the heart beat signal. The BPM vs. time graphs of fig. 4.23 also clearly point to the fact of low similarity at higher frequencies between the heart rates calculated from the ECG and On-Body Technique.

4.4.2.2 Respiration

Table 4.16 shows the accuracy, average On-Body and chest belt breathing rates, Bland-Altman mean difference, standard deviation and the 95 % confidence intervals for the breathing rates extracted using the On-Body monitoring method and MLT1132 chest belt for the tested frequencies. It is observed that the respiration accuracy is barely affected by the frequency of operation. It had excellent accuracy at all frequencies, even at 9 GHz the accuracy within 1 BPM was above 90% and all extracted results were within 5 breaths per minute for all frequencies. The Bland-Altman results provide more evidence of the excellent operation at all frequencies. This further enhances the argument that at higher frequencies the decreased heart rate accuracy is because of harmonic and intermodulation interference.

Table 4.16: Statistical analysis of breathing rate from MLT1132 chest belt and On-Body antenna at various frequencies. All BA results are in breaths per minute.

Frequency (GHz)	**1**	**2.45**	**3.5**	**5.8**	**7**	**9**
Accuracy (%) (within 1)	93.8	100	100	100	99.6	92.3
Accuracy (%) (within 2)	96.9	100	100	100	100	94.6
Accuracy (%) (within 3)	97.7	100	100	100	100	97.7
Accuracy (%) (within 4)	100	100	100	100	100	99.2
Accuracy (%) (within 5)	100	100	100	100	100	100
MLT1132 Belt Breathing Rate	15.3	14.7	12.9	15.7	14.8	16.7
On-Body Breathing Rate	15.5	14.7	12.9	15.6	14.9	16.4
Mean Diff (BA)	-0.2085	0.0131	0.0497	0.0628	-0.0459	0.2984
Standard Deviation (BA)	0.6405	0.3536	0.3953	0.2696	0.3144	0.7576
d +1.96 s_d (BA)	1.0469	0.7062	0.8245	0.5911	0.5703	1.7834
d -1.96 s_d (BA)	-1.4639	-0.6800	-0.7252	-0.4656	-0.6621	-1.1865

Figure 4.24 (a) and (b) show the breathing rate in breaths per minute from the On-Body monitor and the chest belt at 2.45 GHz and 9 GHz. Figure 4.24 (c) and (d) show a 50 sec breathing signal from the On-Body monitor and the chest belt at 2.45 GHz and 9 GHz . All these figures show quite good agreement, although a delay is noticed between the respiration results from the belt and the On-Body monitor. The delay is because the antenna starts moving slightly before the chest is able to expand enough to cause a change in the piezoresistive transducer of the belt.

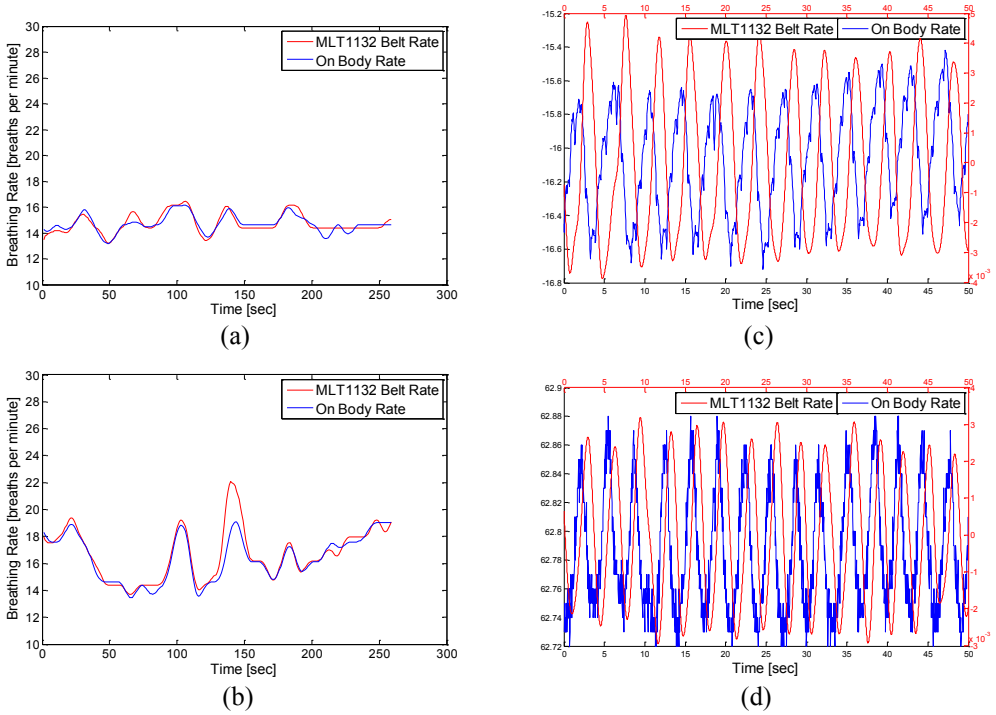

Figure 4.24: Breathing rate [Breaths per minute] vs. Time for the ECG signal and On-Body monitor for (a) 1 GHz, and (b) 9 GHz, Breathing signal from On-Body Monitor and filtered MLT1132 Chest Belt for (c) 1 GHz, and (d) 9 GHz

4.5 Effect of antenna structure and polarization

4.5.1 Experimental Setup

The basic setup as described in section 4.3.1 will be used here. For the purpose of determining the effect of antenna structure and polarization, many antennas available were tested while the other parameters were kept constant. These experiments were conducted on subject 1 (from 4.3.3) and the antenna was attached parallel to his chest. The subject was asked to sit on a chair and refrain from any sort of movements and the antenna was attached to his clothes using tape. The parameters which were kept constant were:

Power	-10 dBm	**Body Position**	Sitting
Duration	5 minutes	**Frequency**	2.45 GHz
Sampling Rate	30 samples/sec		

Most of the antennas chosen were specifically designed to be used for On-body Communication purposes at 2.45 GHz. They were utilized here to determine whether it was possible to use the antennas designed for communication purposes as a vital signs monitor as well. The antennas used include:

(1) Inverted F antenna (IFA) [8]

(2) Coplanar waveguide 3d monopole antenna (CPW3dM) [7]

(3) Dipole antenna [7]

(4) Loop antenna 1 (loop1) [8]

(5) Patch Antenna [8]

(6) Loop Antenna 2 (loop2) [7]

(7) 3d Monopole Antenna (3dM) [7]

(8) CPW planar Monopole (CPWM)

The antenna topologies are shown in figure 4.25 for the first 7 antennas while the topology of antenna 8 can be seen in figure 4.4. Antennas 1-7 are narrow bandwidth antennas specifically designed to operate at 2.45 GHz for on-Body communication purposes. Antenna 8 is an UWB antenna and was designed for general communication (on-body and off-body) purposes between 3.1-10.6 GHz.

For the IFA the inverted F was kept towards the chest. Normal on-body communications configuration is for the ground plane to be towards the chest. For the CPW3dM the ground plane was towards the chest. For the dipole antenna the ground plane was on opposite side of the chest. Normal on-body communications configuration is for the ground plane to be towards the chest. For loop antenna 1 the loop was away from the chest. For patch antenna two cases were considered, one in which the patch was towards the chest (PatchR), and the other in which the ground was towards the chest (PatchG). It should be noted that PatchG is

the normal configuration for the patch antenna when it is used for on-body communication purposes. PatchR cannot be used for on-body communication purposes. For loop antenna 2 the loop was on opposite side of the chest. For the 3dM the ground was towards the chest. For the CPWM the monopole was away from the chest. Antenna 2, 4, 5 (PatchG), 6, 7 and 8 were in their normal communication configuration state while antenna 1, 3, and 5 (PatchR) were not in their normal communication configuration state. Three measurements were taken of 5 minutes each, of which the 2 best were chosen for analysis depending on visual inspection of signals showing least signs of movement. Besides this the EG05000 as described in section 4.3.1 was used to measure the heart rate.

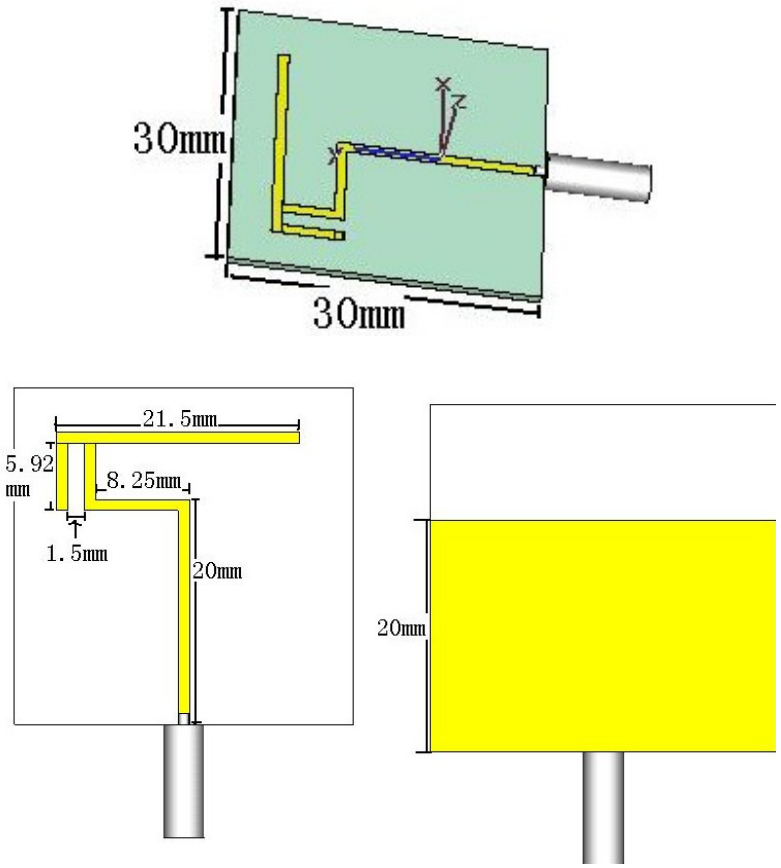

(a) Inverted F antenna (IFA) [8]

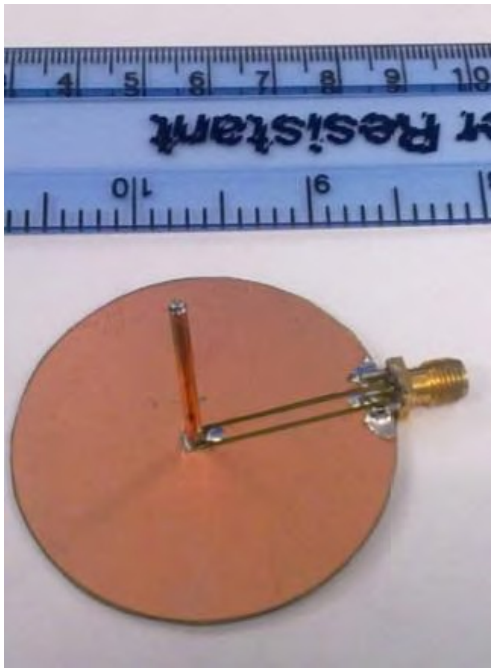

(b) Coplanar waveguide 3d monopole antenna [7]

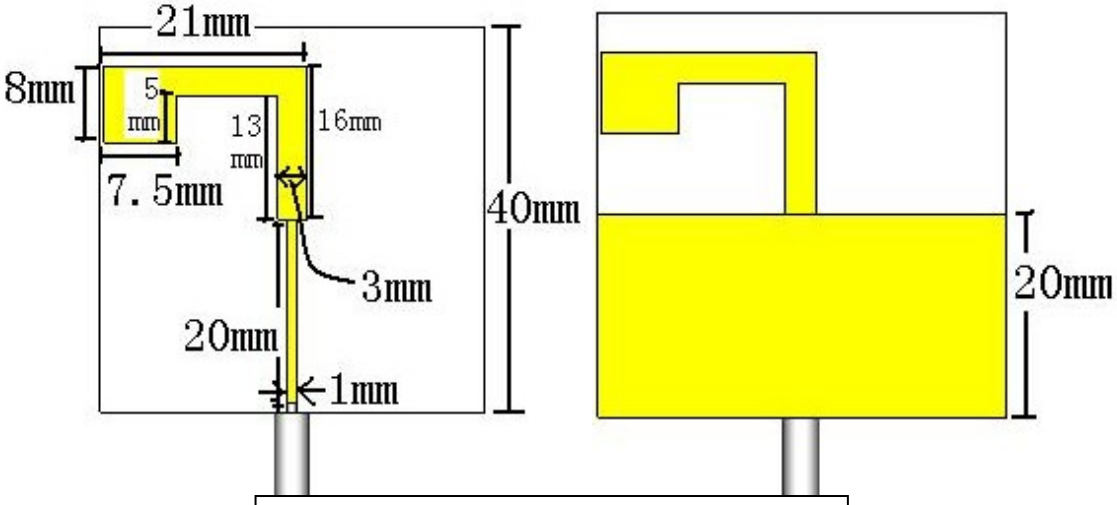

r_1 = 18 mm, w_1 = 2 mm, r_m = 10 mm, W_{f2} = 6 mm, W_{f1} = 2 mm, L_f = , S_f = 5 mm, l_m = 25 mm, w_m = 2 mm, T_m = 12 mm, h_d = 1.6 mm

(c) Dipole antenna [7]

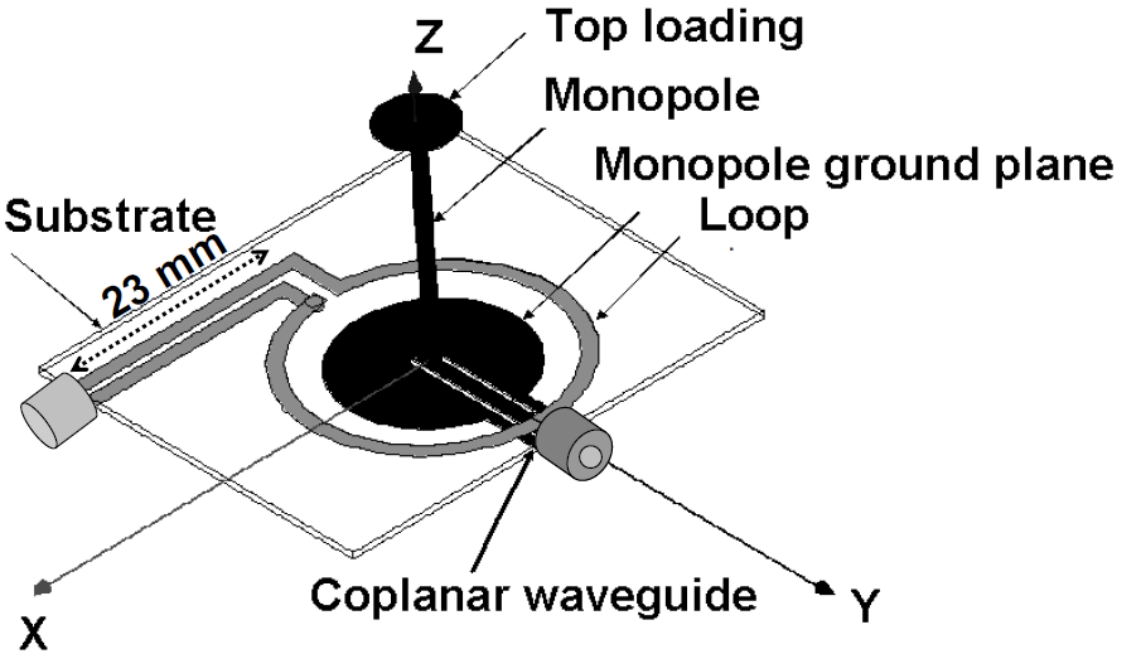

(d) Loop antenna 1 [8]

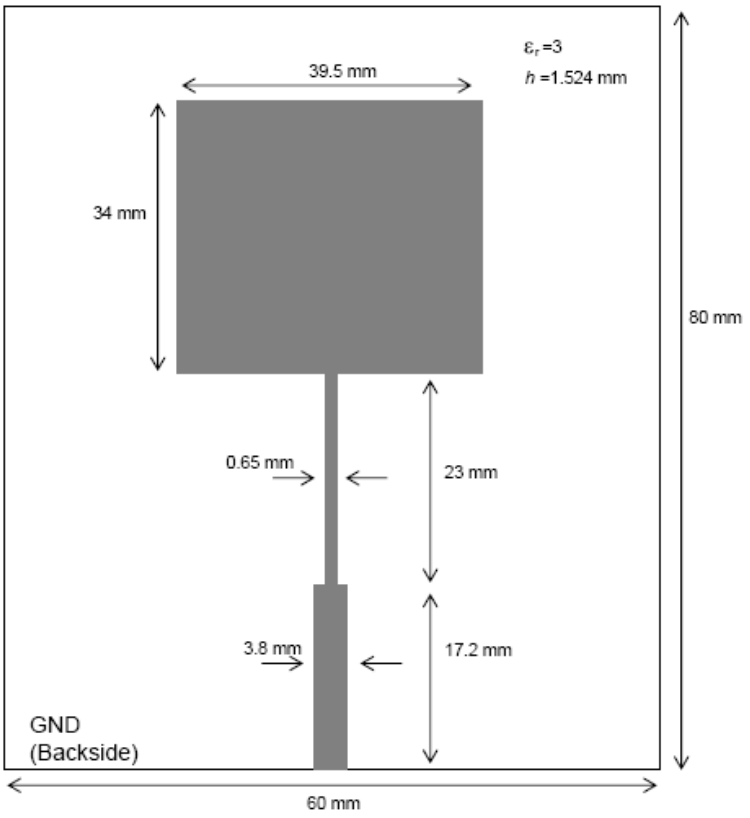

(e) Patch Antenna [8]

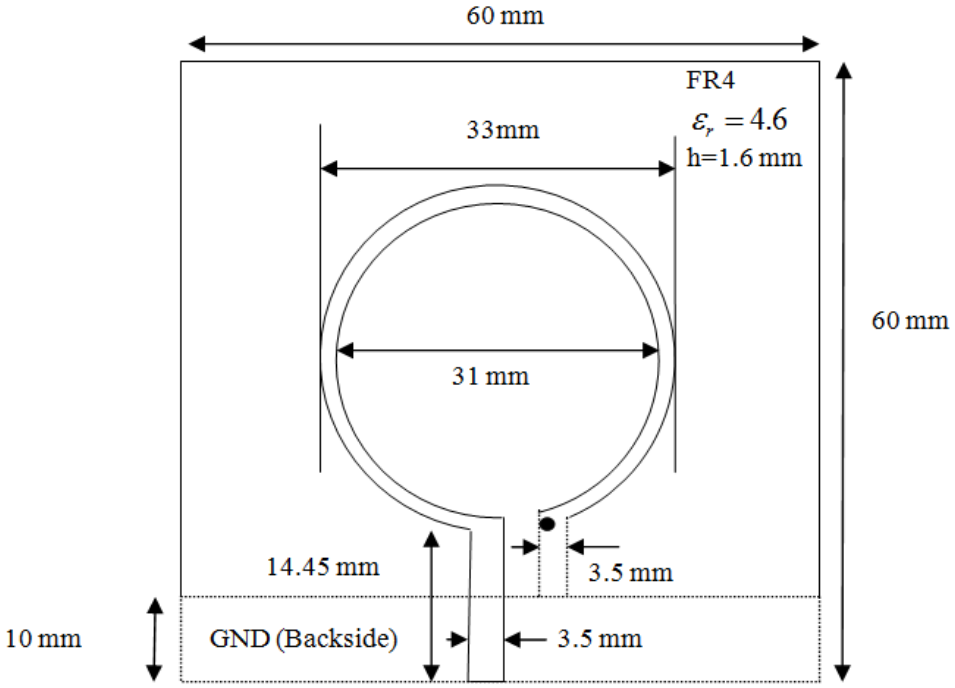

(f) Loop Antenna 2 [7]

Ground plane dia = 40 mm, top loading dia = 26 mm,

height = 18 mm, wire dia = 5 mm.

(g) 3d Monopole Antenna[7]

Figure 4.25: (a) Inverted F antenna (IFA) [8], (b) Coplanar waveguide 3d monopole antenna [7], (c) dipole antenna [7], (d) Loop antenna 1 [8], (e) Patch Antenna [8], (f) Loop Antenna 2 [7], (g) 3d Monopole Antenna[7],

4.5.2 Results and Discussion

Table 4.17 shows the SNR, Accuracy, ECG heart rate, On-Body heart rate, Bland-Altman mean difference, standard deviation and the 95 % confidence intervals for the tested antennas. Figure 4.26 shows the Bland-Altman plots for the tested antennas.

Table 4.17: Statistical analysis of heart rate from ECG and On-Body Monitor for tested antennas. All BA results are in BPM.

Antenna Type	IFA	CPW3dM	Dipole	Loop1	PatchR	PatchG	Loop 2	3dM	CPWM
SNR	1.113	0.8188	0.6174	1.3735	1.2937	0.6266	1.060	0.6879	1.3223
Accuracy (%) (within 1 BPM)	98	62.6	34.5	98.6	96.4	24.1	92.9	57.7	95.9
Accuracy (%) (within 2 BPM)	100	72.11	44.9	100	99.66	33	96.94	70.58	99.8
Accuracy (%) (within 3 BPM)	100	75.1	48.8	100	100	39.3	98.3	74	100
Accuracy (%) (within 4 BPM)	100	79.3	51.2	100	100	43.7	98.5	75.7	100
Accuracy (%) (within 5 BPM)	100	82.1	56	100	100	49.1	98.6	76.4	100
ECG Heart Rate(BPM)	70.52	77.9	75.92	75.23	76.37	79.4	88.12	80.18	87.38
On-Body Heart Rate (BPM)	70.37	75.84	76.7	75.1	76.21	73.34	87.64	76.32	87.16
Mean Diff (BA)	0.1452	2.0641	-0.7804	0.1372	0.1554	6.0548	0.6178	3.8607	0.2166
Standard Deviation (BA)	0.4347	4.3185	9.0052	0.3862	0.4701	8.0829	3.8279	6.9860	0.4301
d +1.96 s_d (BA)	0.99	10.53	16.87	0.89	1.08	21.9	8.12	17.55	1.06
d -1.96 s_d (BA)	-0.71	-6.4	-18.43	-0.62	-0.77	-9.79	-6.88	-9.89	-0.63

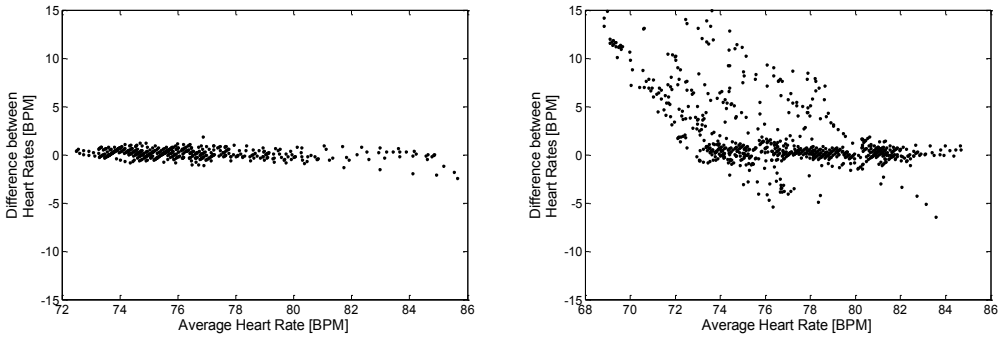

(a) (b)

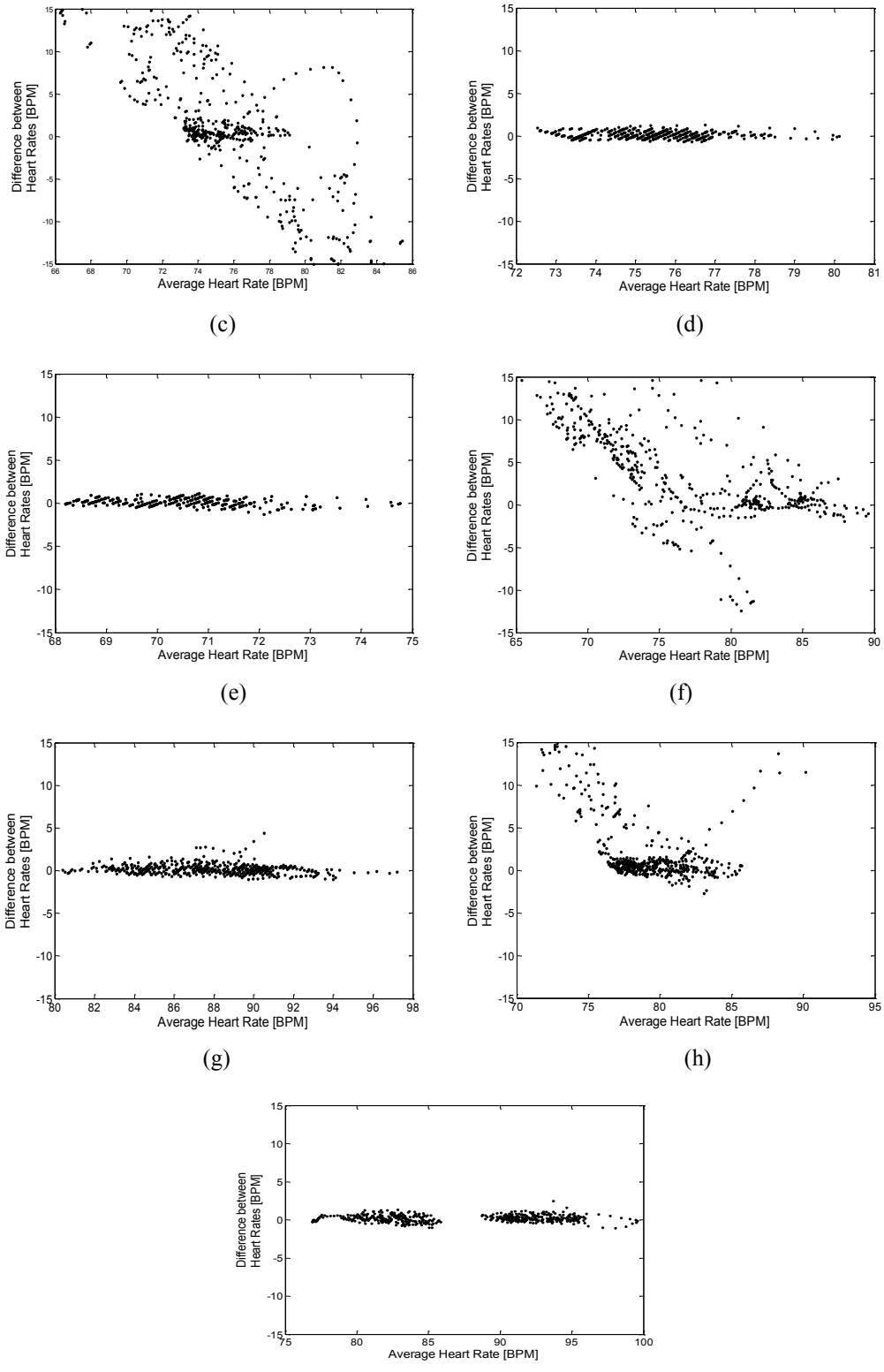

Figure 4.26: Bland-Altman plots for (a) IFA, (b) CPW3dM, (c) Dipole, (d) Loop1, (e) PatchR, (f) PatchG, (g) Loop2, (h) 3dM, and (i) CPWM

Figure 4.27 shows 30 second filtered On-Body antenna phase and ECG graphs for the various antennas. Figure 4.28 shows the BPM versus time graph of five minute duration for the different antennas. The 30 second windows for Figure 4.27 and the 5 min windows for Figure 4.28 were chosen so that they represent how the respective antenna signals looked throughout the duration of the measurement.

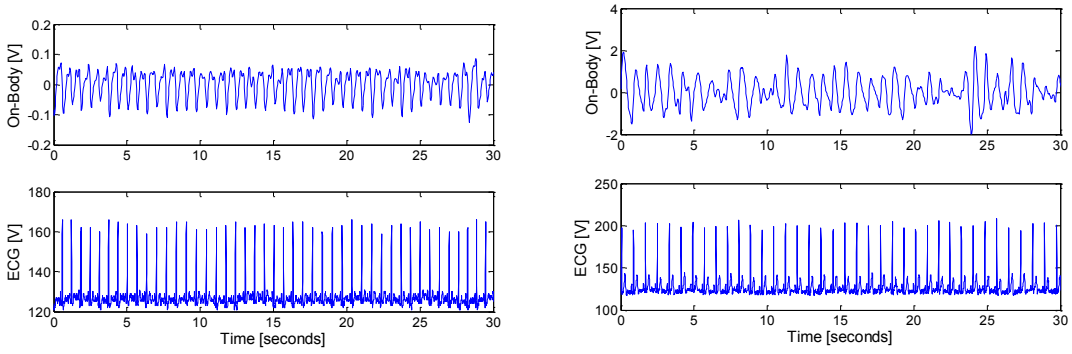

(a) (b)

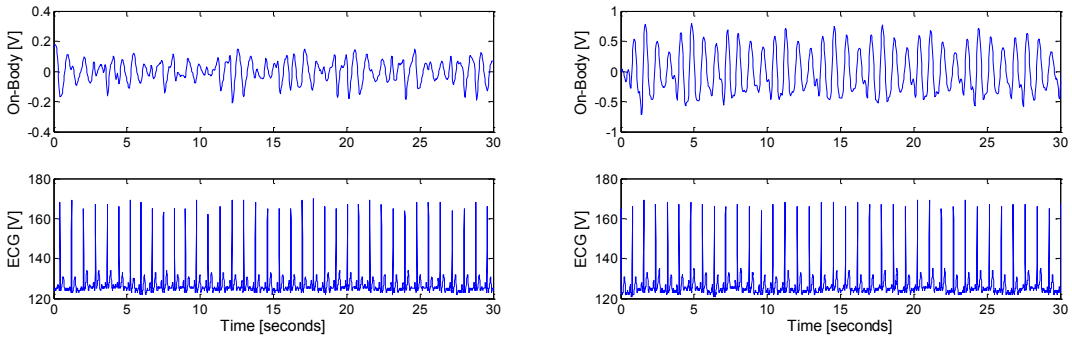

(c) (d)

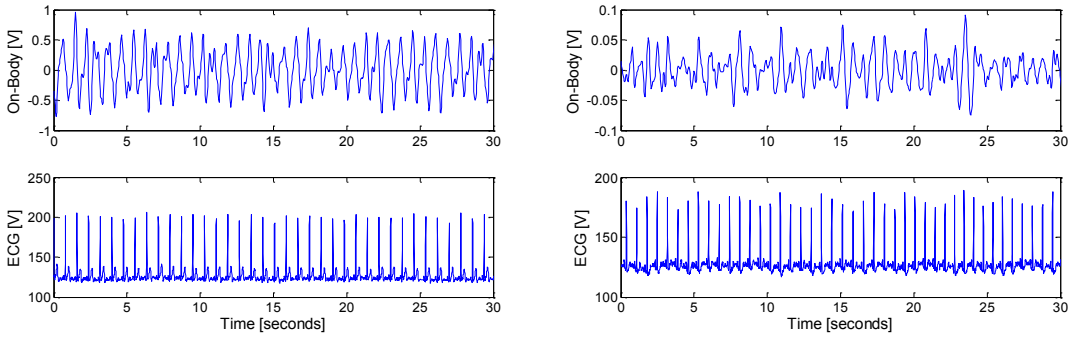

(e) (f)

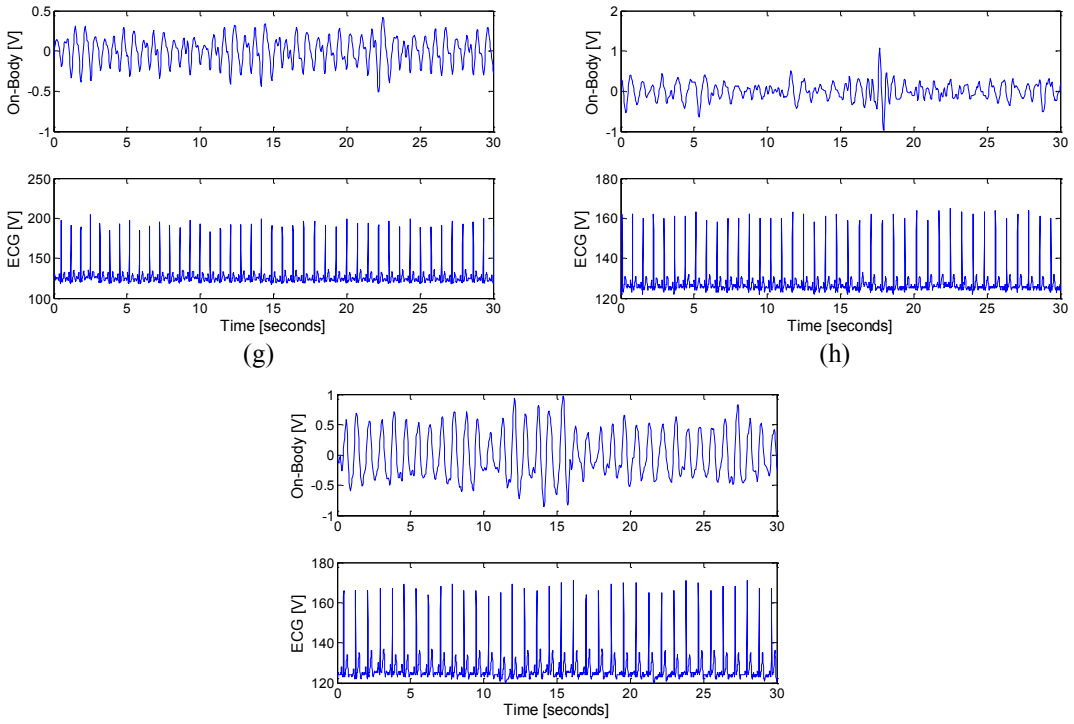

Figure 4.27: ECG signal and filtered On-Body heart rate plots for (a) IFA, (b) CPW3dM, (c) Dipole, (d) Loop1, (e) PatchR, (f) PatchG, (g) Loop2, (h) 3dM, and (i) CPWM

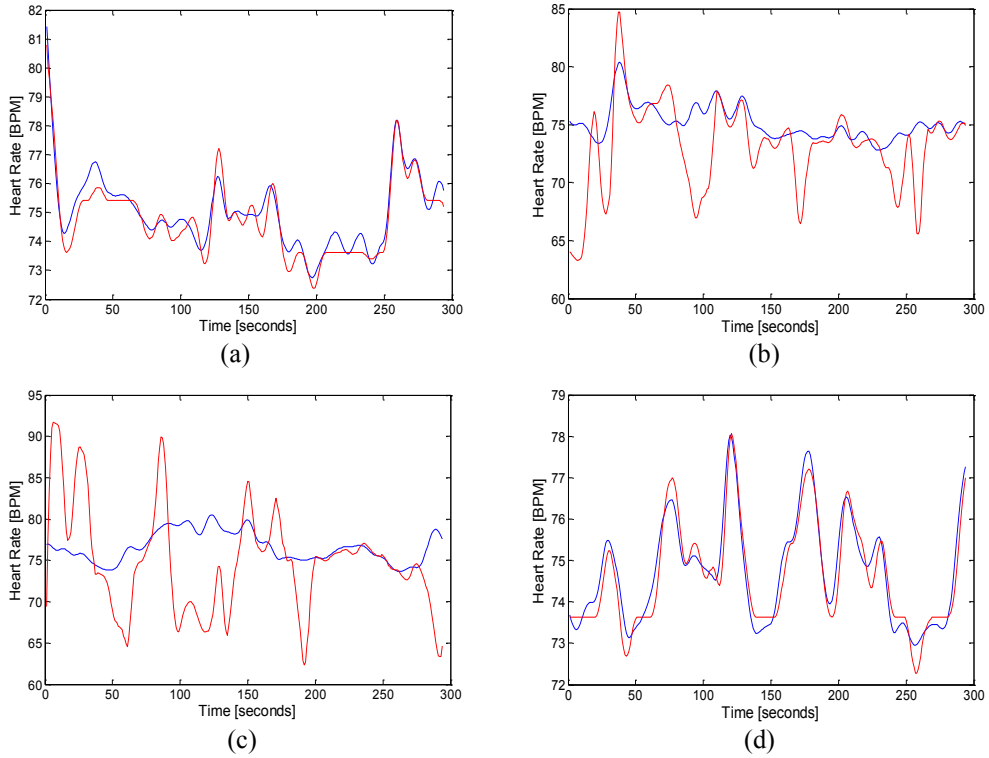

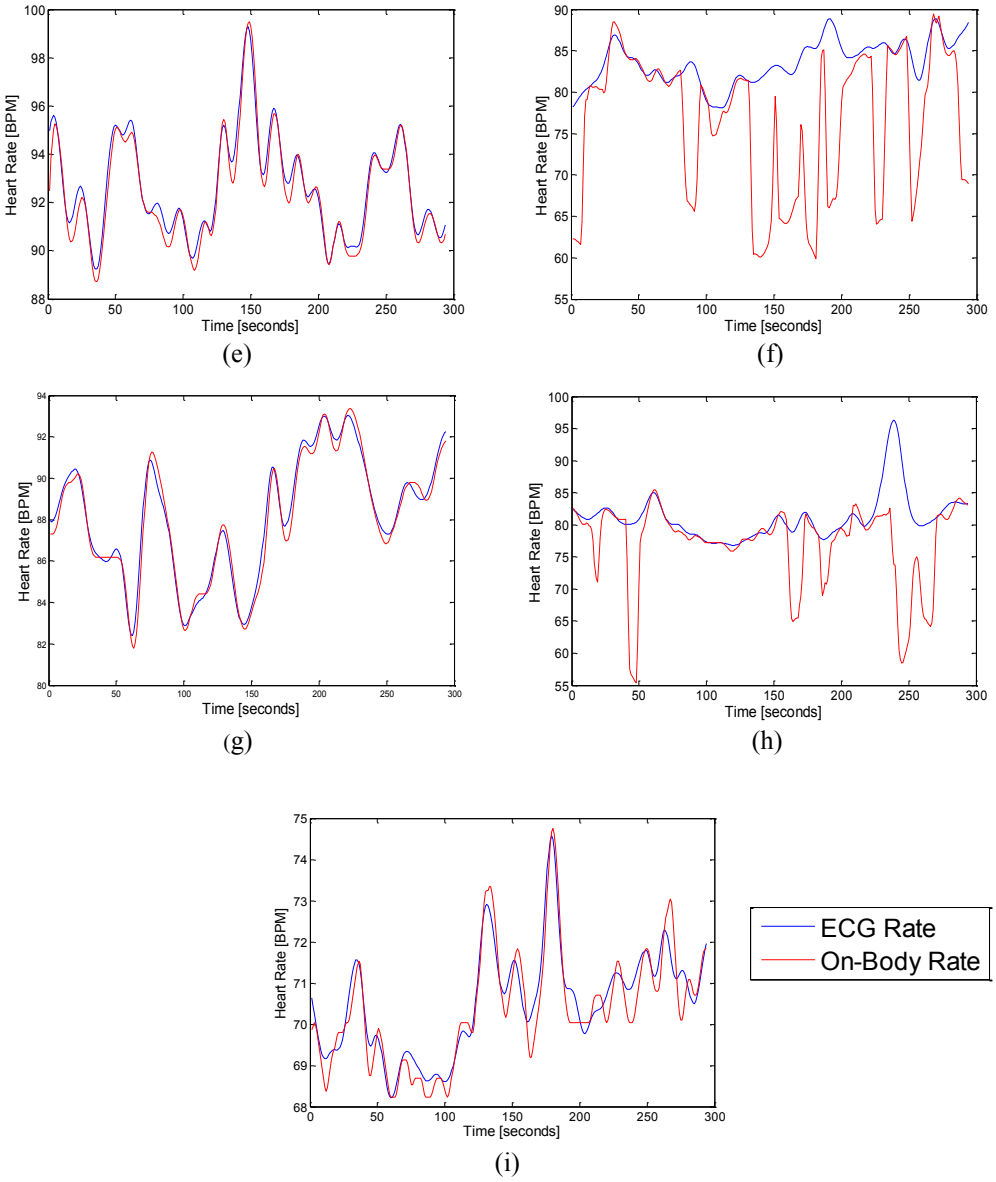

Figure 4.28: Heart rate [BPM] vs. Time for the ECG signal and On-Body monitor for (a) IFA, (b) CPW3dM, (c) Dipole, (d) Loop1, (e) PatchR, (f) PatchG, (g) Loop2, (h) 3dM, and (i) CPWM

The general trend obtained was that for more accurate monitoring of heart rate the characteristics which are required for On-Body Communication purposes should be reversed to ensure maximum coupling with the body. So if a device needs to be made to provide both communication and vital signs detection capabilities, there needs to be a compromise between communications robustness and vital signs detection accuracy. For all the antennas tested the

percentage accuracy within 2 BPM is written in the brackets after antenna names in this section.

In terms of structure requirements it was observed that smaller ground or no ground antennas fared much better in all measurement regards as can be seen in the statistical and analytical difference between IFA (100%), CPWM (99.8%), Loop antennas (100%, 96.94%) and the patch antenna with radiating element towards body (patchR (99.66%)) versus the 3d Monopole (3dM (72.11%)), and the patch antenna with ground element towards body (patchG (33%)). The reason for better performance of antennas with bigger grounds is that the antenna electric fields are concentrated in between the radiating element and the ground plane. If the ground plane is not present these fields easily couple with the chest and the antenna's reflection coefficient becomes more sensitive to chest movements.

Also of interest was polarization along or normal to the body. It was deduced that the antennas in which polarization was along the body (loop antennas (loop1, 100%; loop2, 96.94%), patch (PatchR (99.66%), IFA (100%), dipoles (44.9%), CPWM (99.8%)), performed considerably better (Higher accuracy, lower Bland-Altman confidence intervals) than the antennas with polarization normal to the body (CPW3dM (72.11%), 3dM (70.58%)).

The ground size determined the distance around the antenna, unwanted body movements had an effect. In the case of loop antennas (loop1, 100%; loop2, 96.94%) even 30 cm away from the antenna, body movements affected the phase of the reflection coefficient of the antenna. In the case of the patch with radiating element towards the body (PatchR (99.66%)) and the ground on the opposite side, a shielding effect from unwanted movements on the ground side was provided. Only up to 7cm there was an effect of these unwanted movements on the reflection coefficient phase of the antenna. It was also observed that wether the antenna was balanced or not; had no effect on the vital signs detection accuracy.

All non-planar antennas (CPW3dM (72.11%), 3dM (70.58%) were eliminated from further experiments as there detection accuracy was low. They were also difficult to attach to clothes and were not low profile. Dipoles (44.9%) and patchG (33%) were eliminated for the reason of having low detection accuracy.

In light of the performance, reasonable size, planar nature and better isolation from unwanted movements, patch antenna with radiating element towards body was chosen to be the On-body vital sign monitoring antenna of choice. Even though this antenna cannot be used for communication purposes, in this study of determining the effect of various parameters and validating principles it was considered an ideal choice. The capability of other antennas for On-body vital signs monitoring purposes that can perform communications operations as well has already been established and validated using the various analytical and statistical analysis techniques employed. It was also observed that there was very little difference if the antenna was specifically designed to work On-Body at 2.45 GHz or if it was designed for general purpose communication at 2.45 GHz. This can be confirmed by the fact that loop1 (100%) was designed specifically for working On-Body while CPWM (99.8%) was designed for general purpose communication. The difference of accuracy between loop1 and CPWM is very minimal.

Respiration was only measured for the loop, planar monopole and patch antennas, all of which gave excellent agreement with the MLT1132D belt measured results as expected.

4.6 Different power

4.6.1 Experimental Setup

The basic setup as described in section 4.3.1 will be used here. For the purpose of determining the effect of power, the power was varied from -10 dBm to -45 dBm using the

VNA while keeping the other parameters constant. The antenna chosen to be attached parallel to the front left chest of subject 3(from 4.3.3) was a patch antenna with radiating element directed towards the chest. The frequency of operation chosen was 2.45 GHz. The subject was asked to sit on a chair and refrain from any sort of movements and the antenna was attached to his clothes using tape. The parameters which were kept constant were:

Frequency	2.45 GHz	**Antenna**	Patch
Duration	5 minutes	**Position**	Sitting
Sampling Rate	30 samples/sec		

Three 5 minutes measurements were taken for the following powers: -10 dBm, -20 dBm, -30 dBm, -45 dBm. Two measurements which showed least signs of movement after visual inspection were chosen to be analysed. Besides this the EG05000 and the MLT1132D as described in section 4.3.1 were used to measure the heart and breathing rate respectively. MLT1132D was attached to the chest for only 1 out of the 3 measurements.

4.6.2 Results and Discussion

Table 4.7 shows the SNR, Accuracy, ECG Heart rate, On-Body heart rate, Bland-Altman mean difference, standard deviation and the 95 % confidence intervals for the tested powers. Figure 4.29 shows the Bland-Altman plots for the different powers. It is clearly observed that even up to -30 dBm the On-Body monitor is a very accurate and viable vital signs measuring device. Only at -45 dBm do the signs of degradation become clear and all the analysis results show this. Even up to -30 dBm the accuracy within 3 BPM is 100% after which it drops to 77.9% at -45 dBm. But the accuracy within 5 BPM is still above 95 % for all the tested powers. In the case of On-body vital signs monitoring the antenna is directly attached to the body and the phase of the reflection coefficient of the antenna is mainly affected by

movements in the proximity of the near field of the antenna. This causes it to be less dependent on power as compared to Doppler radar vital signs monitoring [12] in which the phase is affected by movements in the farfield. All this results in the effect of power being minimal up to -30 dBm. It can clearly be observed in the Bland-Altman plots of Figure 4.29 that the divergence from the zero difference centres is minimal up to -30 dBm while at -40 dBm the divergence is significantly more.

Table 4.18: Statistical analysis of heart rate from ECG and On-Body antenna for different powers. All BA results are in BPM.

Power	**-10 dBm**	**-20 dBm**	**-30 dBm**	**-45 dBm**
SNR	1.0077	0.7993	0.9530	0.6357
Accuracy (%) (within 1 BPM)	93.7	91.7	87.9	49.8
Accuracy (%) (within 2 BPM)	95.1	92.7	87.9	63.3
Accuracy (%) (within 3 BPM)	100	100	100	77.9
Accuracy (%) (within 4 BPM)	100	100	100	91.5
Accuracy (%) (within 5 BPM)	100	100	100	95.4
ECG Heart Rate(BPM)	71.7	72.4	73.2	73.1
On-Body Heart Rate (BPM)	72	72.7	74.6	74.7
Mean Difference	-0.2969	-0.3049	-1.4182	-3.3331
Standard Deviation	3.2386	3.0316	5.9533	7.1518
d +1.96 s_d (BA)	1.0587	1.2172	1.4726	2.1824
d -1.96 s_d (BA)	-0.8549	-0.6635	-0.6919	-5.2249

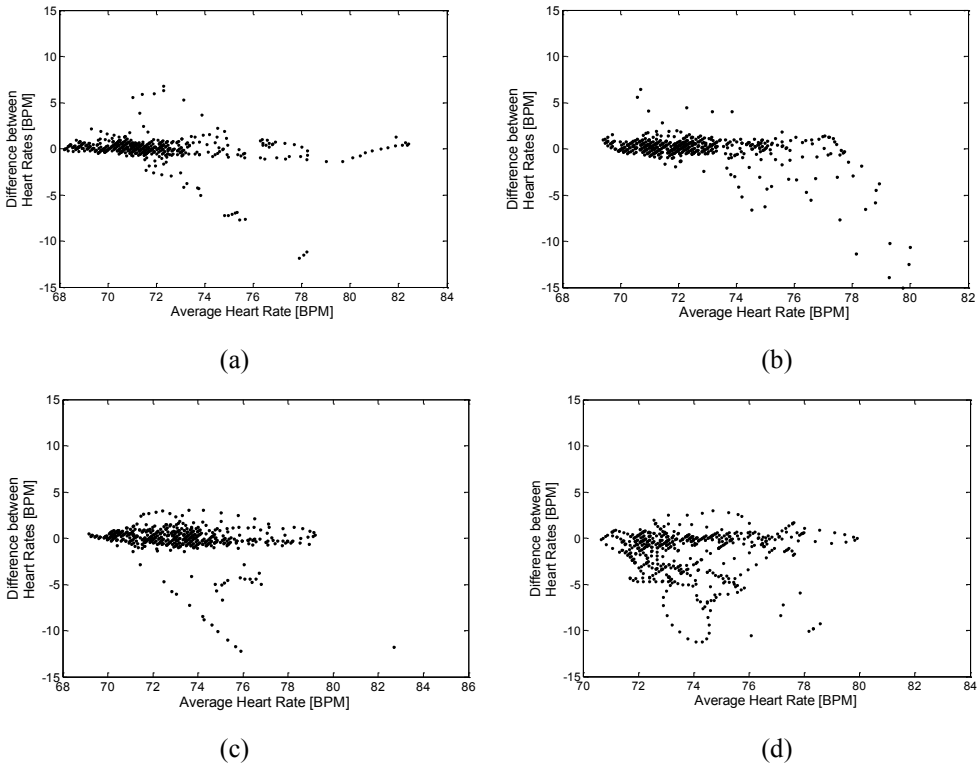

Figure 4.29: Bland-Altman plots for (a) -10 dBm, (b) -20 dBm, (c) -30 dBm, and (d) -45 dBm.

Figure 4.30 shows 30 second filtered On-Body antenna phase and ECG graphs for the various powers. Figure 4.31 shows the BPM versus time graph of five minute duration for the different powers.

Figure 4.31 shows a similar trend of excellent similarity between the BPM graph up to -30 dBm and then a drop in similarity at -45 dBm. But all the 30 second On-Body heart graphs of figure 4.30 look almost noise free. As can be seen in 4.30 (d) at -45 dBm power, the heart beat signal from the On-Body monitor still has fine peaks and very little distortions. With better signal processing algorithms, the detection accuracy (within 1 beat) of 49.8% at -45 dBm can be improved significantly. These results point to the possibility of creation of a device that requires very low power, which is a fundamental concern in all commercial devices especially the ones to be used over long periods of time.

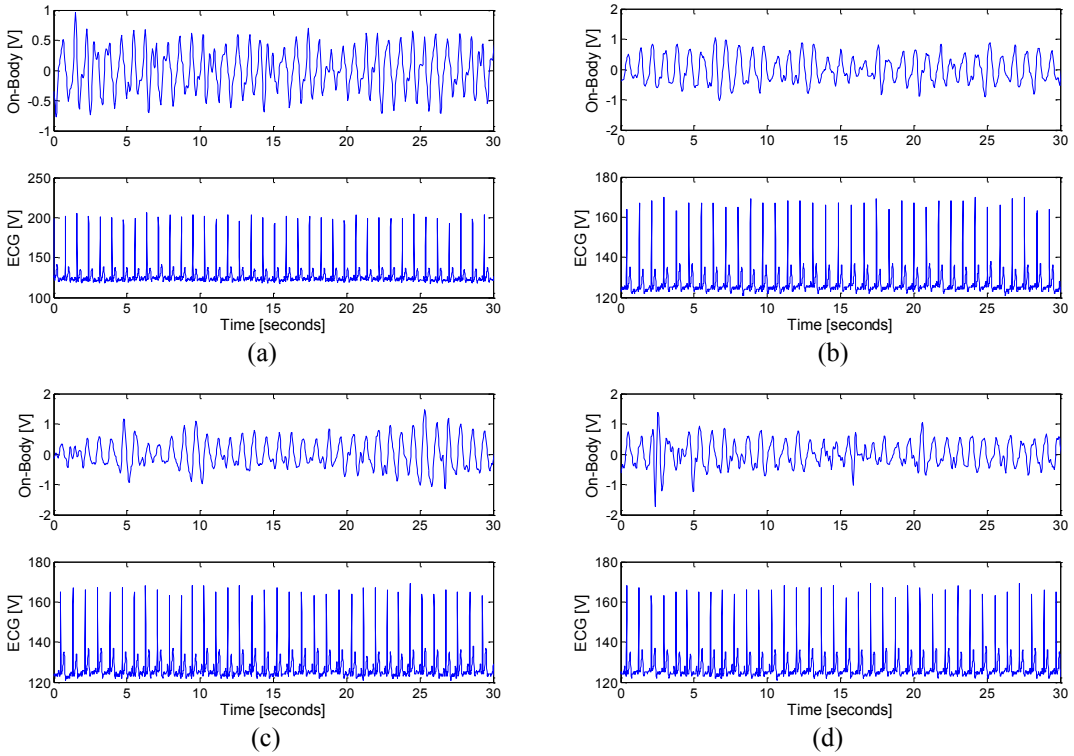

Figure 4.30: ECG signal and filtered On-Body heart rate plots for (a) -10 dBm, (b) -20 dBm, (c) -30 dBm, and (d) -45 dBm.

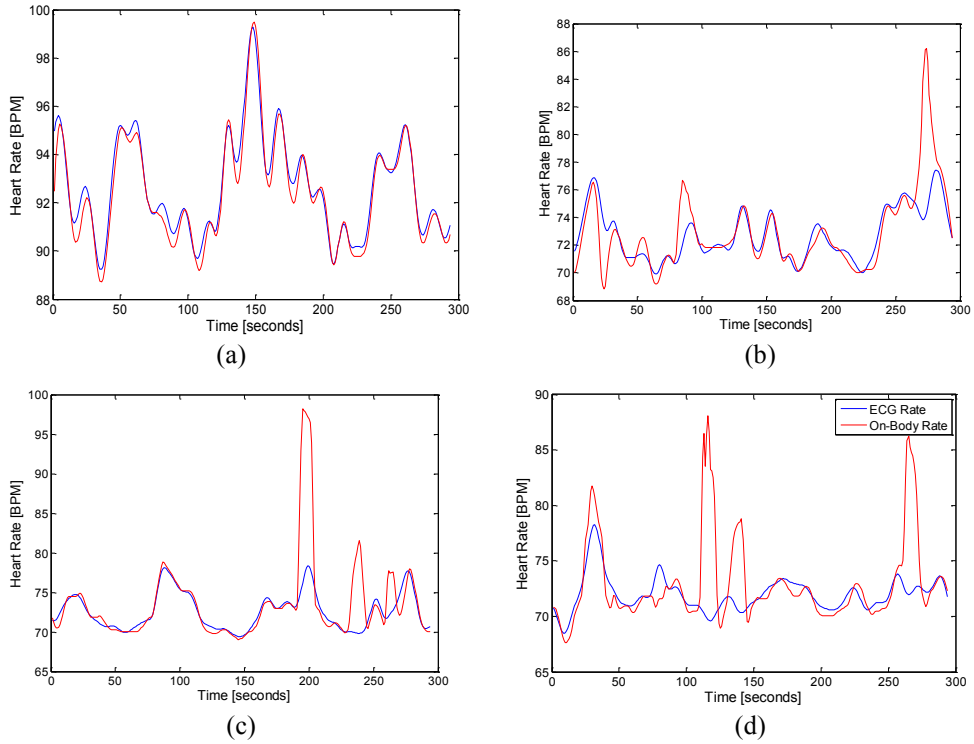

Figure 4.31: Heart rate [BPM] vs. Time for the ECG signal (blue) and On-Body monitor (red) for (a) -10 dBm, (b) -20 dBm, (c) -30 dBm, and (d) -45 dBm.

4.6.3 Respiration

Table 4.19 shows various analysis parameters as in previous sections at -10 dBm and -45 dBm for the respiration rate detection. Only these two powers are shown as the respiration rate is detectable with almost a 100% accuracy at all powers, this is in slight contrast to the heart rate detection. Figure 4.32 (a) shows the breathing rate in breaths per minute for the On-Body monitor at -45 dBm and MLT1132 chest belt. It can be clearly seen that they follow each other exactly. The reason for this 100% accuracy is that the respiration signal is a much stronger signal as compared to the heart signal and is not buried under a stronger signal (as the heart is with the breathing signal) and is much less affected by noise. All this is confirmed by figure 4.32 (b) where the breathing waveform from the On-Body antenna at -45 dBm is clearly visible and matching the one from the belt. Here the On-Body waveform is delayed as compared to the belt waveform, the reason being that the belt was in a position where the chest moved before as compared to the position where the antenna was.

Table 4.19: Statistical analysis of breathing rate from MLT1132D and On-Body antenna for -10 dBm and -45 dBm power.

Power	**Accuracy**					**MLT1132 Belt Breathing Rate**	**On-Body Breathing Rate**
	±1(%)	±2(%)	±3(%)	±4(%)	±5(%)		
-10 dBm	100	100	100	100	100	14.7	14.7
-45 dBm	96.9	100	100	100	100	17.3	17.2

Power	Bland Altman (breaths per minute)			
	Mean Difference	Standard Deviation	d +1.96 s_d (BA)	d -1.96 s_d (BA)
-10 dBm	0.0131	0.3536	0.7062	-0.6800
-45 dBm	0.1810	0.4479	1.0589	-0.6968

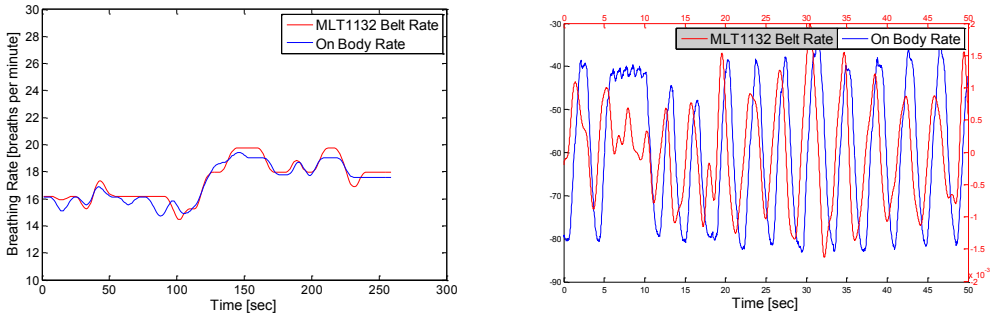

(a) (b)

Figure 4.32: a) Breathing rate [Breaths per minute] vs. Time for the MLT1132 signal and On-Body monitor at -45 dBm, (b) Breathing signal from On-Body Monitor and filtered MLT1132 Chest Belt Input at -45 dBm.

4.7 Antenna Location on body

The basic setup as described in section 4.3.1 will be used here. In order to determine the best possible position of the antenna on the body for maximum accuracy of vital signs detection 6 positions were tested as depicted in figure 4.33. The antenna chosen was a patch antenna with radiating element directed towards the chest and subject 3 (from section 4.3.3) was the tested subject for these measurements. The parameters which were kept constant were:

Frequency	2.45 GHz
Power	-10 dBm
Duration	5 minutes
Sampling Rate	30 samples/sec
Antenna	Patch
Body Position	Sitting

Three 5 minute measurements were taken for each antenna position. Two measurements which showed least signs of movement after visual inspection were chosen to be analyzed. Besides this the EG05000 and the MLT1132D as described in section 4.3.1 were used to measure the heart and breathing rate respectively. All these experiments were performed in normal lab environment.

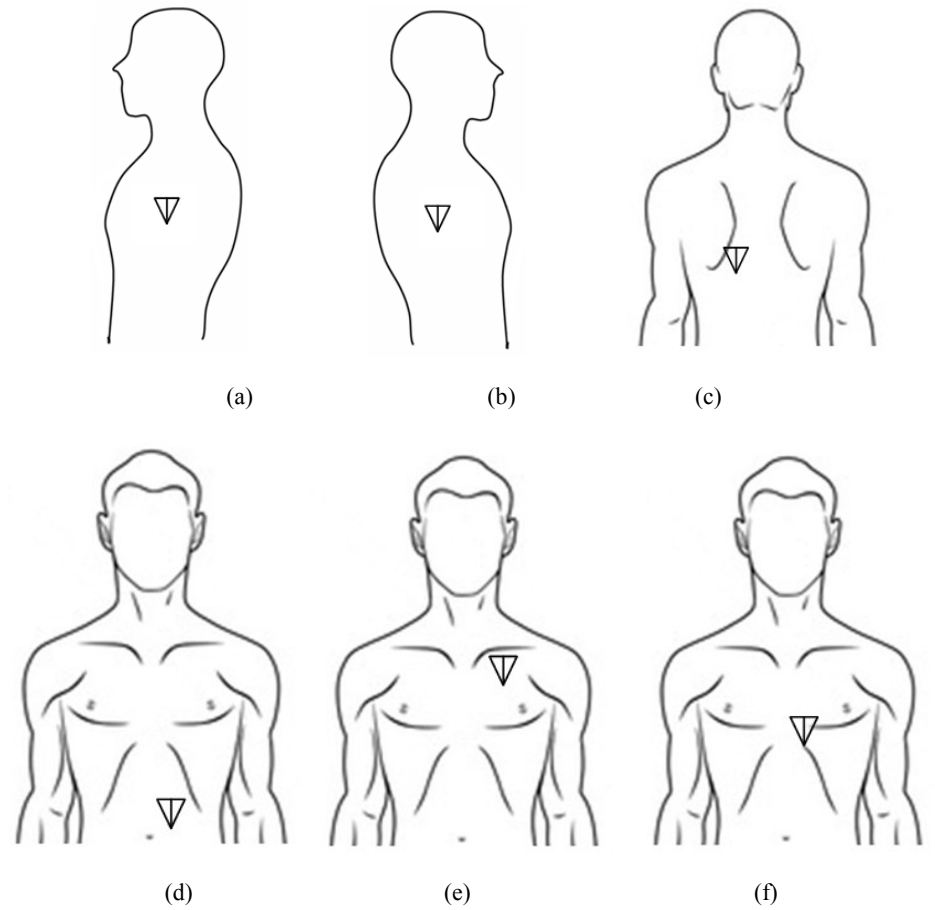

Figure 4.33: Antenna Locations on Body: (a) (Pos. 1) Left Side, (b) (Pos. 2) Right Side, (c) (Pos. 3) Left Backside, (d) (Pos. 4) Left Abdomen, (e) (Pos. 5) Top Left Chest (f) (Pos.6) Front Left Chest.

4.7.1 Results and Discussions

Heart Rate

As in previous sections, Table 4.20 shows the various statistical analysis results while Figure 4.34 shows the Bland-Altman plots for the different antenna positions on the human body.

As can be seen from the analysis results and figures, when the antenna was placed on the sides (pos. 1 and 2) or at the back (pos. 3) the heart rate detection was extremely inaccurate and the difference between reference and On-Body monitoring was massive. The accuracy within 1 beat was less than 30 %. On the other hand on the front side of the chest in positions 5 (top left chest) and 6 (front left chest on shirt) the accuracy within 1 beat was equal to

54.8% and 75%. The results obtained when the antenna was placed close to actual heart position (position 6 in figure 4.33(f)) were the best (75% when on shirt). When placed on the abdomen (pos. 4) as compared to the top chest (pos. 5) and front left chest (pos. 6) the heart rate detection again suffered as an accuracy (within 1 beat) of only 21.9% was achieved. The reason for this is that the chest is the major region affected by the heart movements and also gives much more uniform movements as compared to the abdomen for most individuals tested. In case of the abdomen the non-uniform movement is present because of loose skin and people breathing heavily through that region during unstressed rest state.

The reason for generally better accuracy on the chest compared to other areas is that the heart rate detection is heavily dependent on the movement of the chest due to heart beating rather than the actual heart movement by itself. The other locations are not as sensitive to heart beatings to cause a significant enough motion of the surface on that location. This observation of dependence on chest movement due to heart beating rather than the actual heart beating itself was also observed in the simulations in section 4.2.7 and 4.2.8. The variation in phase was minimal due to just heart movement when chest and antenna were supposed to be at rest. So the movement of the chest relative to the antenna is the reason for maximum sensitivity to heart beats. Even if the antenna is tightly attached using a belt directly on the body the heart rate is still measured with good accuracy suggesting the chest moves relatively to the antenna even then, which can also be observed visually. The change in dielectric in the proximity of the antenna due to chest movement affects the phase and this gives rise to heart rate detection ability. The heart rate is the most accurate in the case of position 6 (front left chest on clothes) because the chest movement is maximum due to heart beating in that position as the heart is located in that position. The heart rate is less accurate in position 6 (front left chest) with the antenna directly contacting the body rather than clothes. The reason for this is believed to be

the extra distortion in the antenna phase due to direct physical contact of the radiating part of the antenna with the human body. This direct contact might cause unwanted current paths. This can be mitigated by using a protective layer such as a tape on top of the radiating patch. Back side (position 3) gave the worst results as it moves the least due to heart beating compared to all other positions.

Table 4.20: Statistical analysis of heart rate from ECG and On-Body antenna for different antenna locations on the body. (antenna locations can be found in Figure 4.33). All BA results are in BPM.

Antenna Position	Leftside (position 1)	Rightside (position 2)	Left BackSide (position 3)	Left Abdomen (Position 4)	Top Left Chest (Position 5)	Front Left Chest (Position 6)	Directly on Skin (Position 6)
SNR	0.5201	0.6341	0.5581	0.6904	0.6624	1.3954	0.9662
Accuracy (%) (within 1 BPM)	22.8	28.6	7	21.9	54.8	75	57.1
Accuracy (%) (within 2 BPM)	34.4	37.2	15	37.1	68	95.1	77.6
Accuracy (%) (within 3 BPM)	38.78	43.37	23.3	48.81	75.17	96.77	84.7
Accuracy (%) (within 4 BPM)	41.8	46.8	31.6	61.2	83.7	98.3	87.1
Accuracy (%) (within 5 BPM)	42.9	49.3	37.4	69.6	85.7	99.5	89.8
ECG Heart Rate(BPM)	78.98	80.27	77.82	66.49	65.22	65.86	65.12
On-Body Heart Rate (BPM)	70.71	72.17	74.39	68.1	67.16	65.82	65.59
Mean	8.2684	8.0987	3.4343	-1.6061	-1.9403	0.0398	-0.0499
Standard Deviation	9.5057	8.4704	11.8107	6.2201	4.6824	1.1076	2.6200
d +1.96 s_d (BA)	26.8996	24.7007	26.5833	10.5853	7.2372	2.2106	5.0854
d -1.96 s_d (BA)	-10.3628	-8.5033	-19.7147	-13.7975	-11.1178	-2.1310	-5.1851

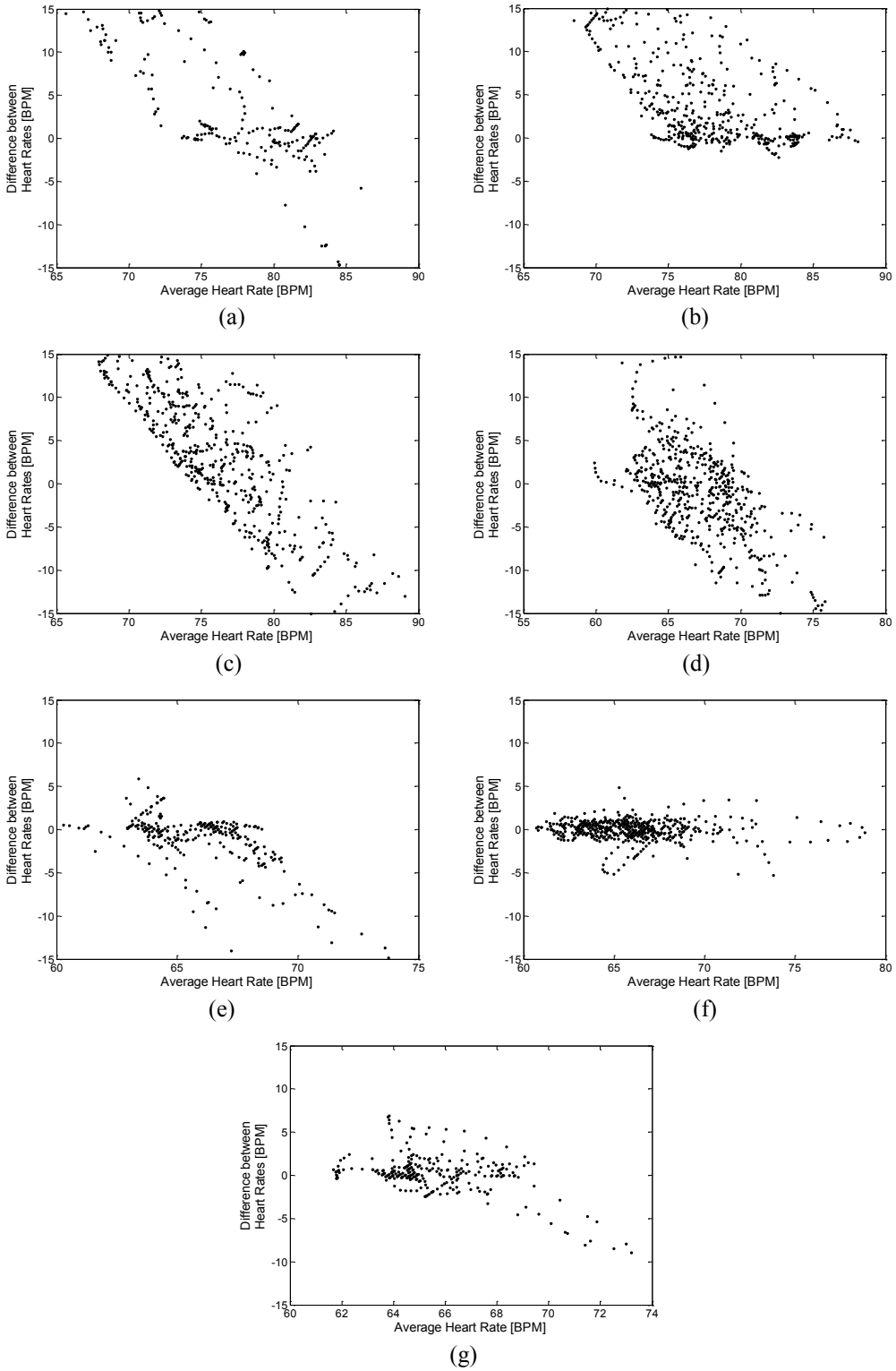

Figure 4.34: Bland-Altman plots for (a) Position 1, (b) Position 2, (c) Position 3, (d) Position 4, (e) Position 5, (f) Position 6, and (g) Position 6 (direct on skin). The Positions can be found in figure 4.33.

Figures 4.35 shows the 30 second ECG graphs and the filtered VNA heart graphs for the different antenna positions. Figure 4.36 shows the ECG and VNA BPM versus time graph for the different antenna positions.

The superiority of position 6 (on clothes and directly on skin) can be even more clearly seen in figure 4.35 (f) and (g) where the filtered heart graph obtained has clear peaks and a less noisy signal compared to all other positions. Similarly the BPM graphs from the ECG and VNA follow each other best in figure 4.36 (f) and (g) for position 6(on clothes and directly on skin) compared to all other positions.

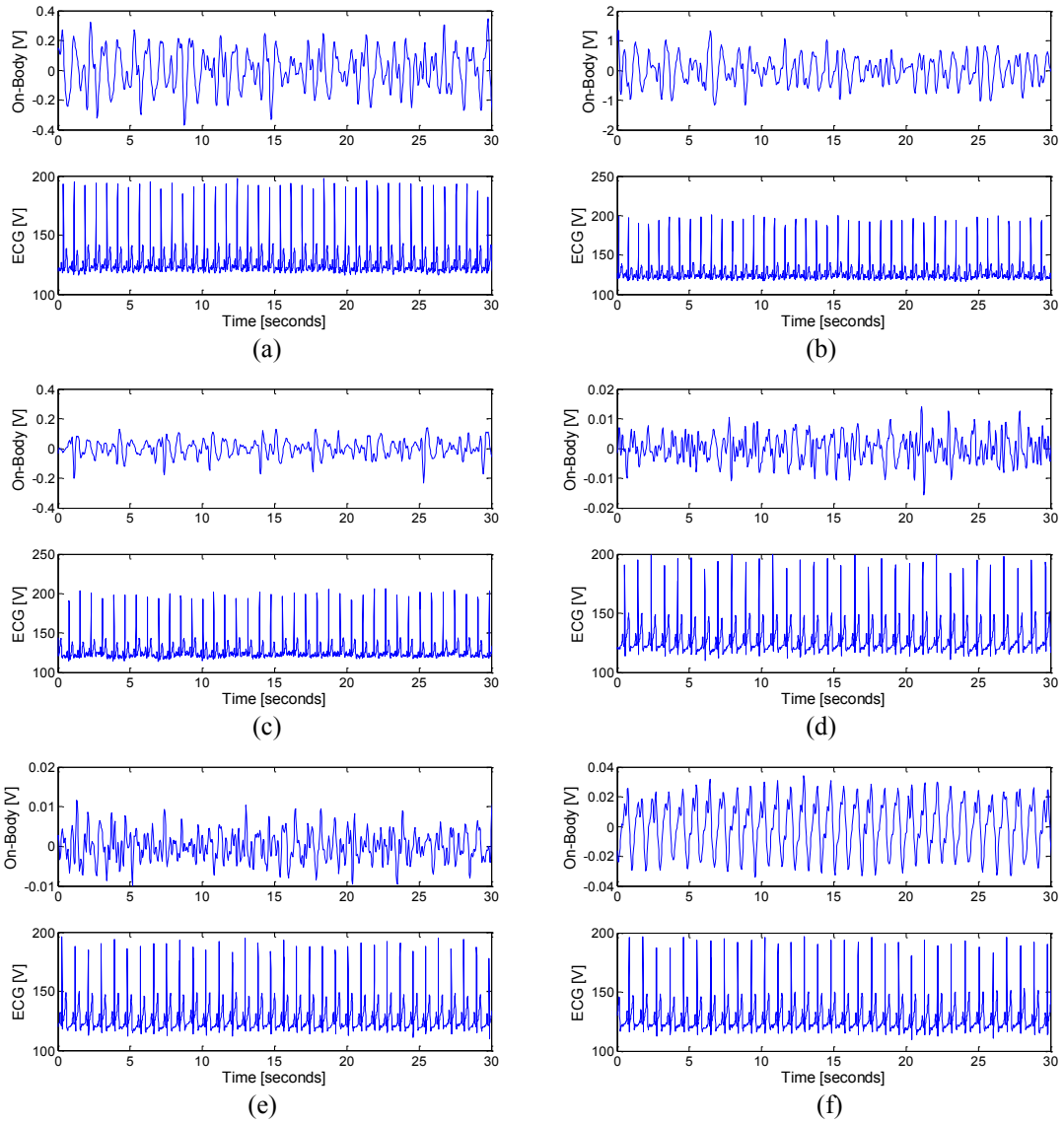

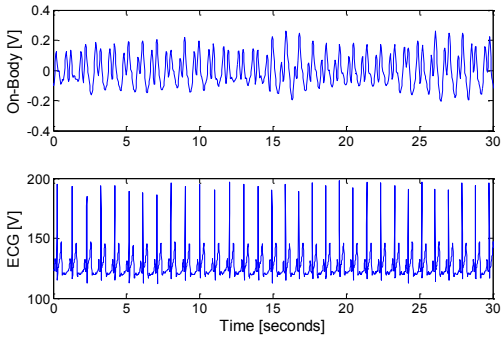

(g)

Figure 4.35: ECG signal and filtered On-Body heart rate plots for (a) Position 1, (b) Position 2, (c) Position 3, (d) Position 4, (e) Position 5, (f) Position 6, and (g) Position 6 (direct on skin). The Positions can be found in figure 4.33.

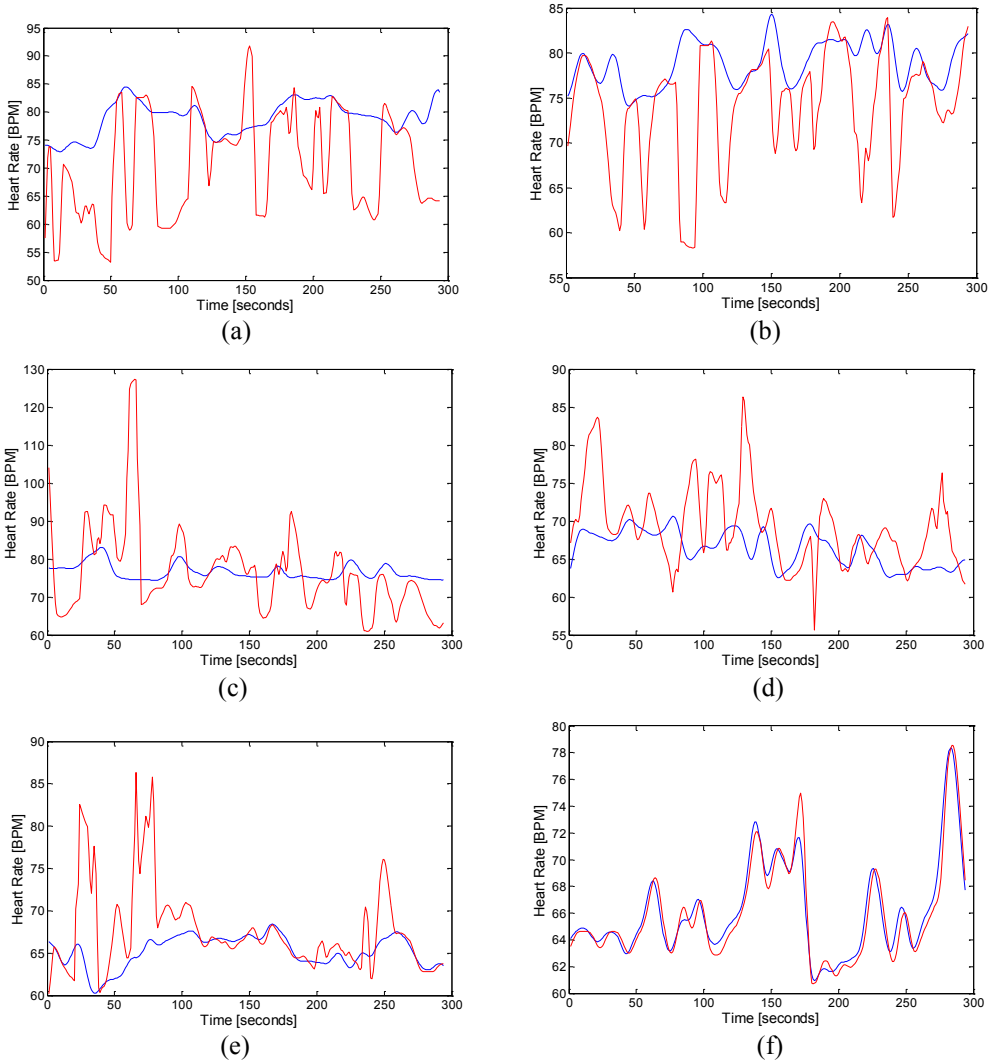

(a) (b) (c) (d) (e) (f)

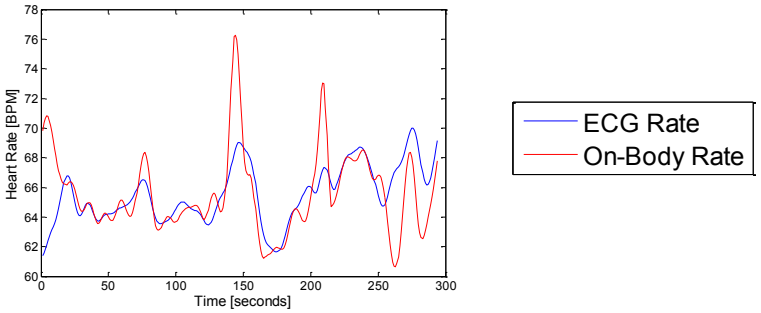

(g)

Figure 4.36: Heart rate [BPM] vs. Time for the ECG signal and On-Body monitor for (a) Position 1, (b) Position 2, (c) Position 3, (d) Position 4, (e) Position 5, (f) Position 6, and (g) Position 6 (direct on skin). The Positions can be found in figure 4.33.

Respiration

Table 4.21 shows various analysis parameters for assessing the respiration rate detection accuracy at different positions of the antenna on the body. It was discovered that the breathing rate could be detected fairly accurately at all positions except the abdomen location (position 4 in figure 4.33) whose accuracy (within 1 beat) is the only one less than 90%. The reason for the lower accuracy on the abdomen was the non-uniform motion of the antenna on the abdomen. The abdomen usually is not as uniform and does not have as stable movements as the other positions and has loosened skin which can introduce unwanted motions in the abdomen. This may cause multiple peaks in one respiration cycle as can be seen in figure 4.37. Multiple measurements were done on a 4 people and it was realized that a similar phenomenon happened for 3 of them. Every other position the movement due to breathing was quite linear as confirmed in the analysis results of table 4.21.

Table 4.21: Respiration rate statistical considering breathing signal from MLT1132D chest belt and On-Body monitor for different antenna positions on body (Positions can be seen in fig. 4.33). All BA results are in breaths per minute.

Frequency (GHz)	**Leftside** (position 1)	**Rightside** (position 2)	**Left BackSide** (position 3)	**Left Abdomen** (Position 4)	**Top Left Chest** (Position 5)	**Front Left Chest** (Position 6)	**Directly on Skin** (Position 6)
Accuracy (%) (within 1)	98.8	98.1	90.3	81.1	93.4	96.9	90.7
Accuracy (%) (within 2)	100	100	96.9	89.6	97.3	100	100
Accuracy (%) (within 3)	100	100	100	93	99.6	100	100
Accuracy (%) (within 4)	100	100	100	95	100	100	100
Accuracy (%) (within 5)	100	100	100	99	100	100	100
MLT1132 Belt Breathing Rate	19.3	17.6	16.8	16.4	13.0	17.2	19.7
On-Body Breathing Rate	19.3	17.6	17	16.9	12.96	17.3	19.7
Mean Diff (BA)	-0.0224	0.0488	-0.1829	-0.4313	0.0528	0.1810	0.0745
Standard Deviation (BA)	0.3708	0.4268	0.6407	1.2626	0.6362	0.4479	0.5130
d +1.96 s_d (BA)	0.7043	0.8954	1.0730	2.0434	1.2998	1.0589	1.0800
d -1.96 s_d (BA)	-0.7490	-0.7778	-1.4387	-2.9060	-1.1942	-0.6968	-0.9310

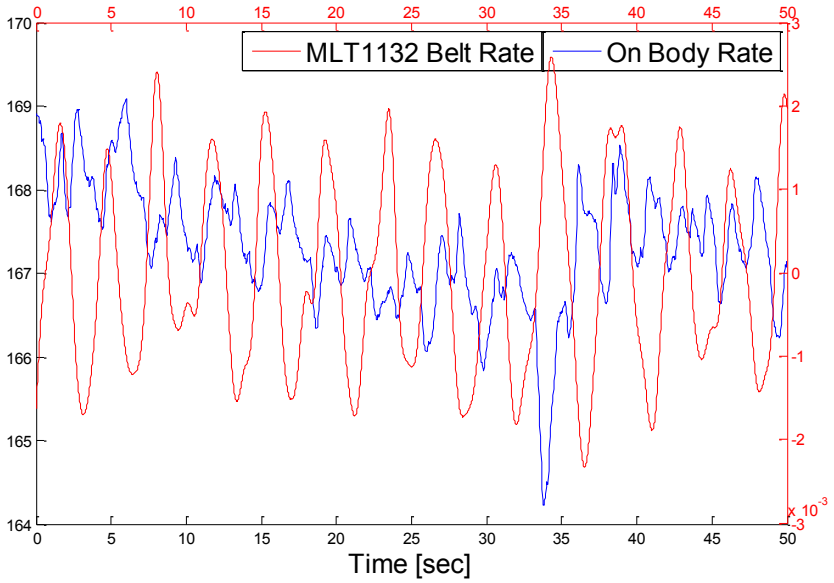

Figure 4.37: Respiration graph obtained from MLT1132 belt (red) and On-Body Monitor when antenna was attached to left abdomen (pos. 4)

4.8 Different distances

4.8.1 Experimental Setup

In this section, the effect of the distance between the chest and the antenna on the accuracy of the On-Body vital signs monitoring technique is studied. The distance was varied from 5cm to 1 m while the other parameters were kept constant. Also included were the results for the antenna attached directly to the (i) clothes and (ii) skin. The basic setup of section 4.3.1 was used here. The antenna chosen to be attached parallel to the front left chest of subject 3(see 4.3.3) was a patch antenna with radiating element directed towards the chest. The frequency of operation chosen was 2.45 GHz. The subject was asked to sit on a chair and refrain from any sort of movements. The antenna was mounted on a fixed platform with the front left chest of the subject parallel to it. The distance between the chest and the antenna was changed according to requirements. The parameters which were kept constant were:

Frequency	2.45 GHz	**Antenna**	Patch
Duration	5 minutes	**Position**	Sitting
Sampling Rate	30 samples/sec		

Three 5 minutes measurements were taken for the following distances: 5cm, 10cm, 25cm, 50cm and 1m. Two measurements which showed least signs of movement after visual inspection were chosen to be analysed. Besides this the EG05000 and the MLT1132D as described in section 4.3.1 were used to measure the heart and breathing rate, respectively. MLT1132D was attached to the chest for only 1 out of the 3 measurements.

4.8.2 Results and Discussion

Table 4.22 shows the statistical analysis of the results obtained from the ECG module and VNA for the antenna at various distances (5cm, 10cm, 25 cm, 50 cm and 1m) including the

antenna directly attached to skin and clothes case. The analysis includes SNR, Bland-Altman analysis and the accuracy of On-Body vital signs measurements within 1,2,3,4 and 5 BPM of the ECG reference module. It can be seen that when the antenna is directly connected to the skin the accuracy within 3 BPM is 84.7 % while when the antenna is directly connected to the clothes the accuracy is 96.77 %. The accuracy within 3 BPM when the antenna is 5cm, 10 cm, 20 cm ,50 cm and 1m away clearly shows that increasing distance between the antenna and the chest decreases the accuracy of the vital signs measurement.

Table 4.22: Statistical Analysis of heart rate from ECG and On-Body antenna for different distances between antenna and chest. All BA results are in BPM.

Distance (cm)	**Directly on Skin 0 cm**	**Over Clothes 0 cm**	**5cm**	**10 cm**	**25cm**	**50 cm**	**1 m**
SNR	0.9662	1.3954	0.6632	0.6225	0.6849	0.5122	0.5508
Accuracy (%) (within 1 BPM)	57.1	75	71.8	57.7	46.4	41.2	30.95
Accuracy (%) (within 2 BPM)	77.6	95.1	80.4	72.1	62.2	56	43.7
Accuracy (%) (within 3 BPM)	84.7	96.77	84.7	75.5	71.8	60.2	50
Accuracy (%) (within 4 BPM)	87.1	98.3	86.1	77.6	77.6	63.6	52.7
Accuracy (%) (within 5 BPM)	89.8	99.5	87.2	78.9	81.1	66	57.1
ECG Heart Rate(BPM)	65.12	65.86	89.6	89.7	89.1	91.5	84
On-Body Heart Rate (BPM)	65.59	65.82	87.1	85.3	87.4	86.9	79.9
Mean	-0.0499	0.0398	2.4808	4.4297	1.6869	4.5635	4.1399
Standard Deviation	2.6200	1.1076	6.2532	9.0585	6.1515	8.9285	7.9183
d +1.96 s_d (BA)	5.0854	2.2106	14.7370	22.1843	13.7439	22.0635	19.6598
d -1.96 s_d (BA)	-5.1851	-2.1310	-9.7755	-13.3249	-10.3701	-12.9364	-11.3799

Figure 4.38 shows the Bland-Altman plots for the various distances and it can be clearly seen that the difference between the On-Body results and the reference ECG module is near the zero line up to 10 cm and deteriorates thereafter.

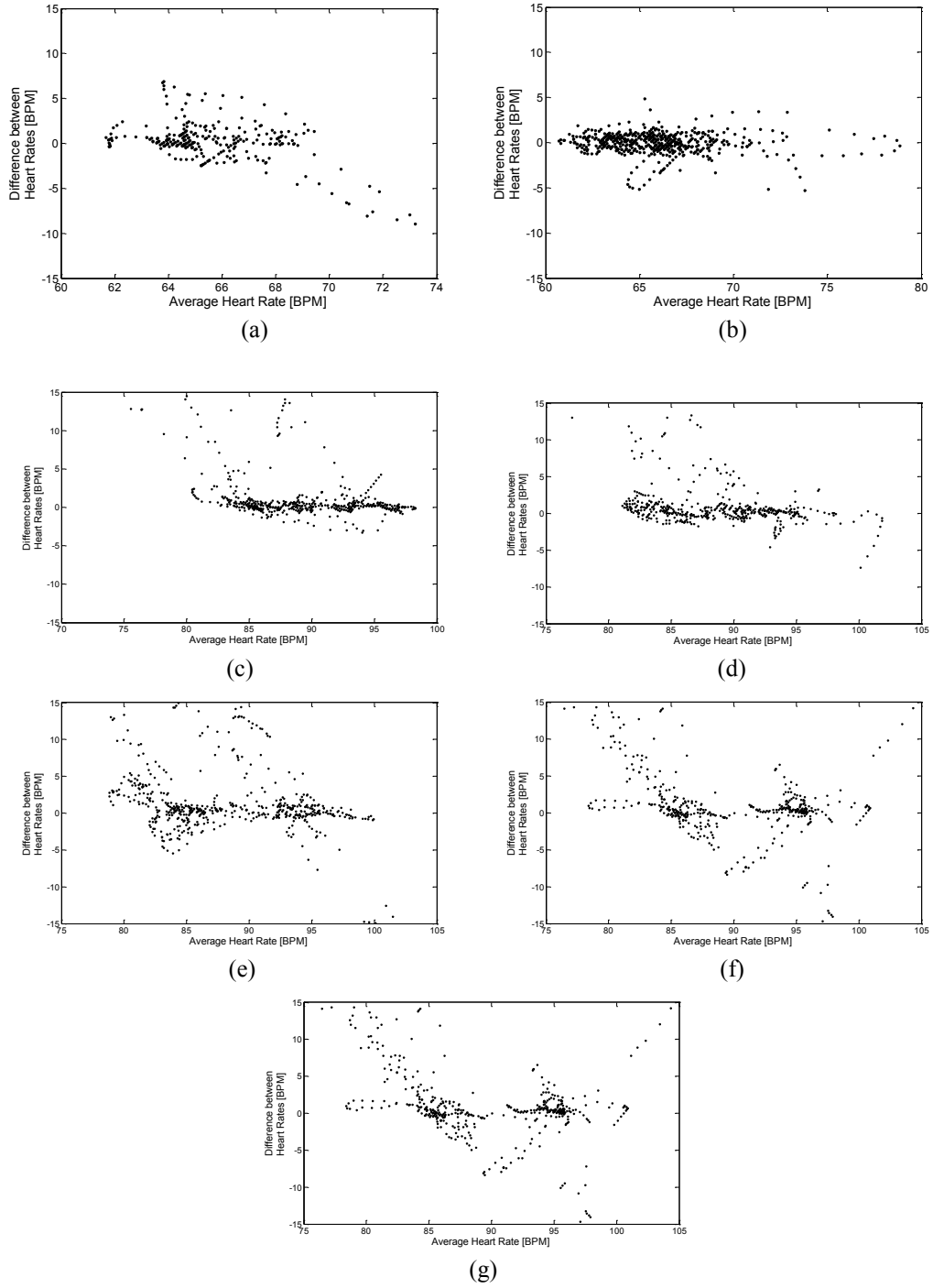

Figure 4.38: Bland-Altman plots for heart rate calculated using ECG device and Doppler radar for different distances, (a) Directly on skin , (b) Directly on clothes, (c) 5 cm, (d) 10 cm and (e) 20 cm, (f) 50 cm and (g) 1 m.

Figure 4.39 shows the ECG graphs versus the corresponding filtered On-Body graphs. Clear heart beat peaks for the On-Body graphs with good matches to corresponding ECG graphs are observed for the directly on body and skin cases. At 5cm, 10 cm and 25 cm again visible peaks and good matches are observed although less accurate compared with the first two cases. At 50 cm and 1 m very weak, erroneous and noisy peaks are observed.

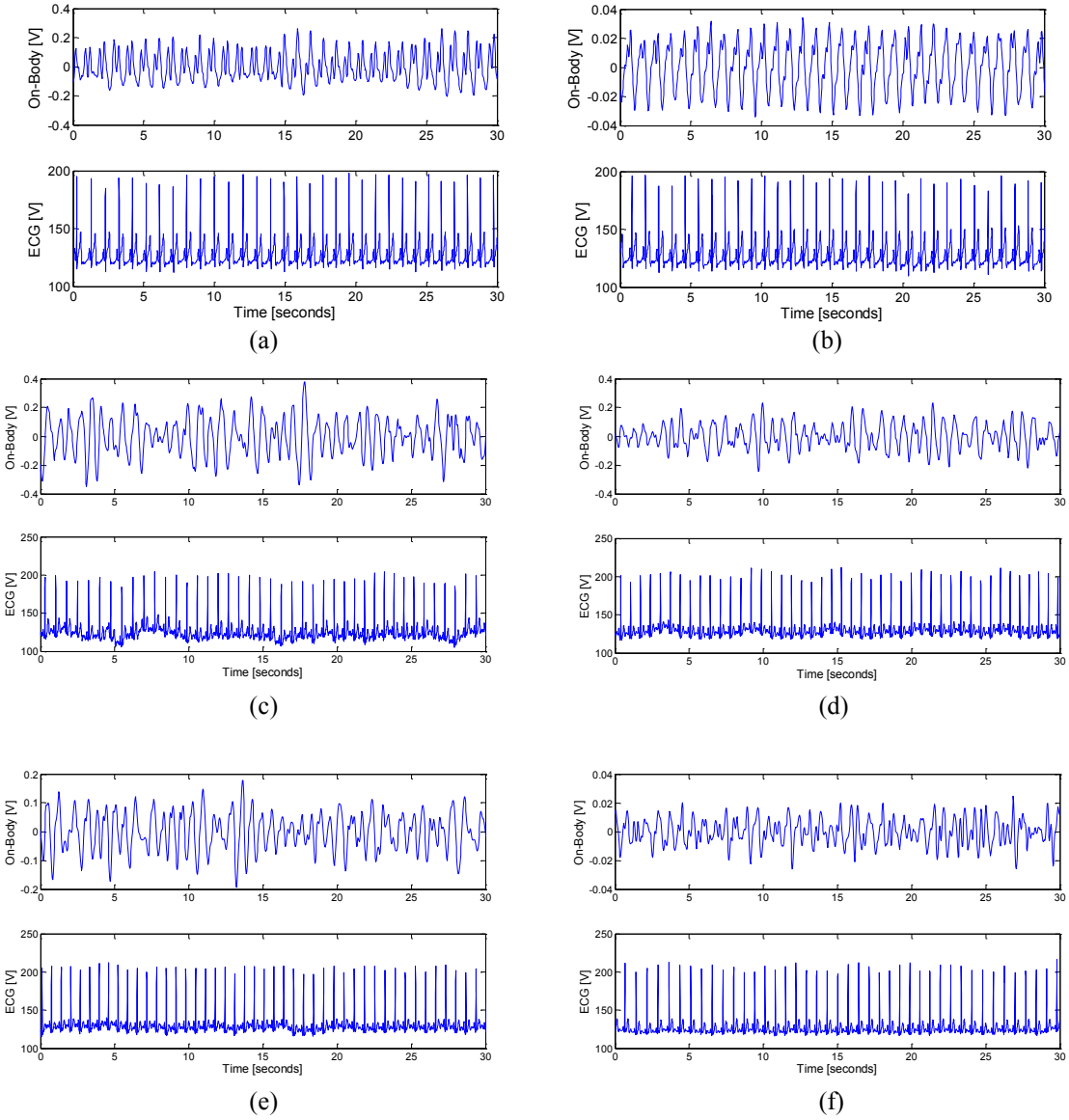

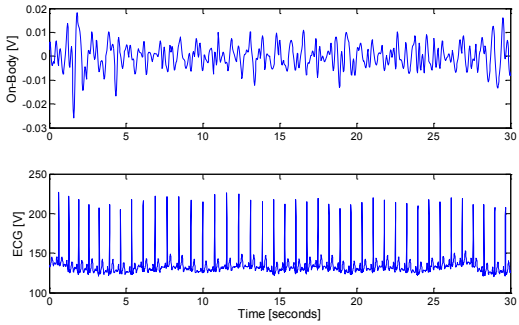

(g)

Figure 4.39: ECG signal and filtered On-Body antenna heart rate plots for different distances, (a) Directly on skin , (b) Directly on clothes, (c) 5 cm, (d) 10 cm and (e) 20 cm, (f) 50 cm and (g) 1 m.

Figure 4.40 shows the beats per minute (BPM) versus time graph for both the ECG module and On-Body antenna. Up to 25 cm excellent match between the two graphs is observed. Even at 50 cm , the On-Body BPM graph follows the ECG BPM graph well but at 1m the graphs don't follow each other.

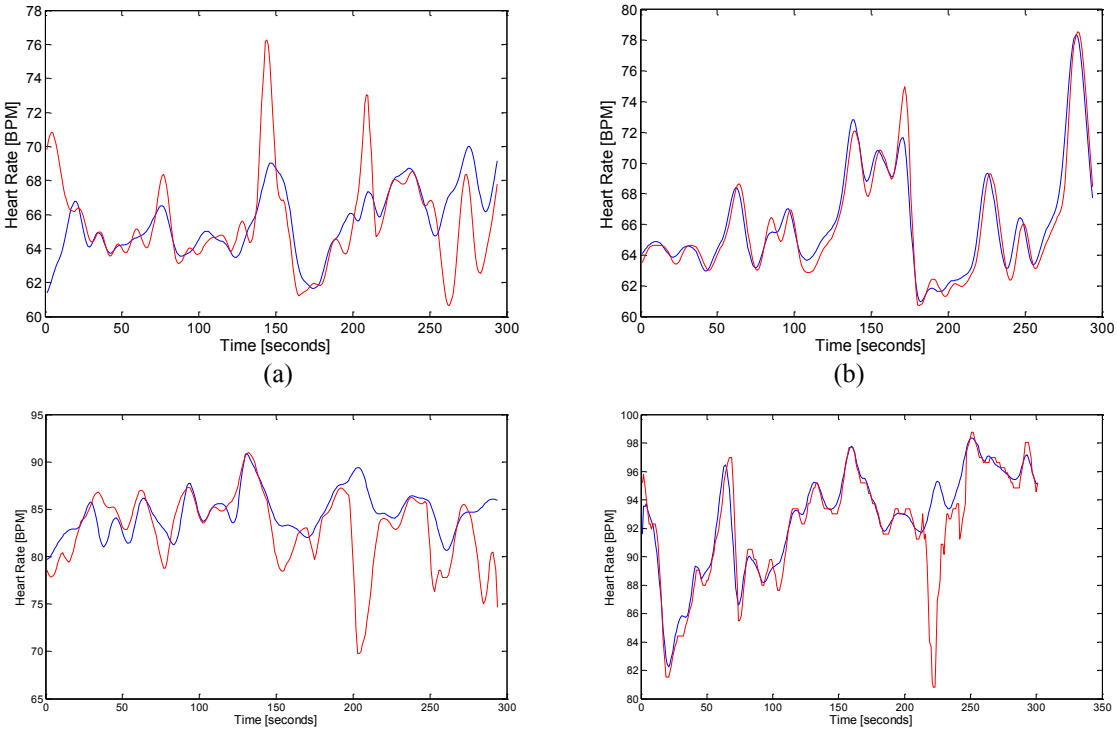

(a) (b)

(c) (d)

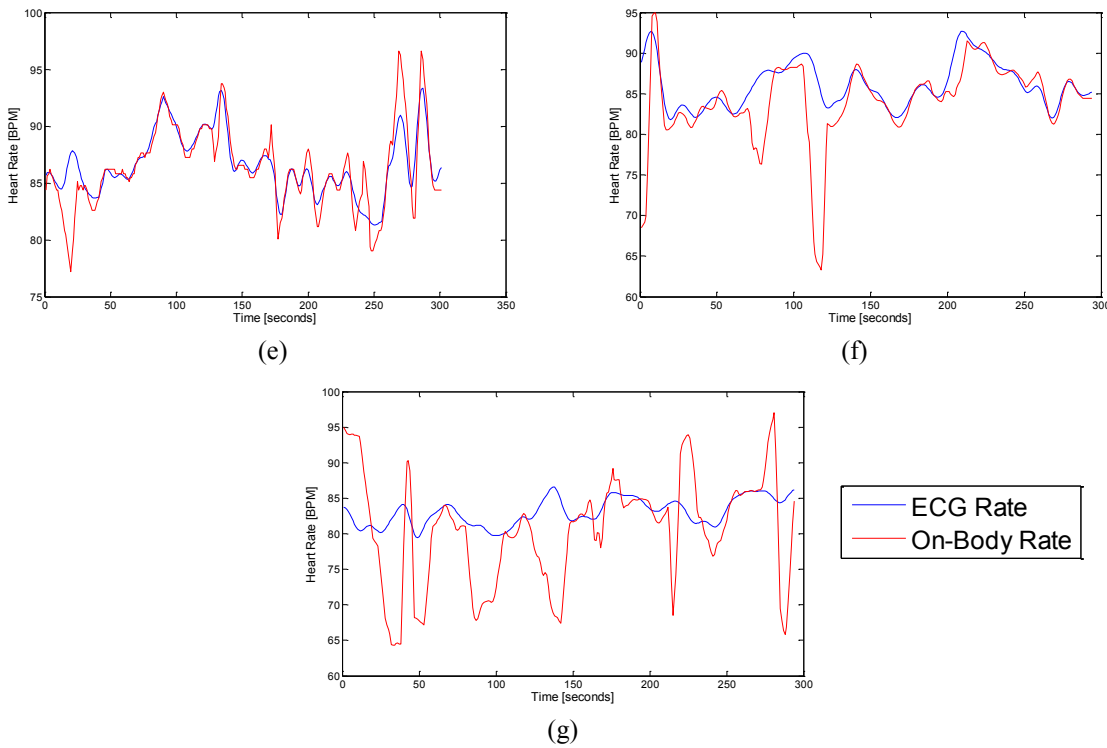

Figure 4.40: Heart rate [BPM] vs. Time for the ECG signal(blue) and On-Body antenna(red) for different distances, (a) Directly on skin , (b) Directly on clothes, (c) 5 cm, (d) 10 cm and (e) 20 cm, (f) 50 cm and (g) 1 m.

The case of the antenna being directly on the chest and skin has already been discussed in section 4.7 and its results were put in this section for thoroughness. When the distance between the chest and the antenna is increased the sensitivity of the antenna to chest movements is decreased. This is due to the fact that the chest movement in the near field of the antenna is the cause of the modulation of the chest movement on the reflection coefficient phase of the antenna. The greater the distance between chest and antenna, the lower the effect chest movements have on the reflection coefficient phase of the antenna. The near field of the antenna is about 24.4 cm and we see that up to 25 cm the accuracy within 3 BPM is above 70 %. As the person under test was sitting it was difficult to keep the distance between chest and mounted antenna stable due to which unwanted movements were observed. However, this does not change the trend of the results observed. It is suggested that future experiments

considering distance be performed with the person under test in supine position. The results in this section showed that the On-Body technique can detect the vital signs best when the antenna is directly attached to the clothes as that allows the antenna to move with the chest on most occasions. Also a fixed device which can be kept very close (up to 10 cm) of the chest can also be used but has the problem of unwanted motion artefacts of a non-stationary subject. In the case of the antenna being directly attached on clothes or skin the antenna moves with the chest and this removes some unwanted motion artefacts.

4.8.3 Respiration

Table 4.23 shows statistical analysis results for the breathing rates extracted using the On-Body monitoring method and MLT1132 chest belt at different distances between chest and antenna. The statistical analyses include the accuracy, average On-Body and chest belt breathing rates, and the Bland-Altman measures (mean difference, standard deviation and the 95 % confidence intervals). It is observed that the respiration accuracy is barely affected by the distance between the antenna and chest. Excellent accuracy is obtained at all distances. At even 1m, the accuracy (within 1 BPM) is above 90% and all extracted results are within 5 breaths per minute for all distances. Only at 10 cm the accuracy (within 1 BPM) is less than 90% and this is more due to unwanted motion by the person under test and incorrect operation of the chest belt.

Figure 4.41 (a), (b) and (c) show the Breathing rate in breaths per minute from the On-Body monitor and the chest Belt when the antenna is directly on the clothes, 5cm away from chest and 1m away from chest, respectively. Figure 4.41 (d),(e) and (f) show a 50 sec breathing signal from the On-Body monitor and the chest Belt when the antenna is directly on the clothes, 5cm away from chest and 1m away from chest, respectively.. All these graphs show

quite good agreement with each other. In Figure 4.41 (e) we see that the chest belt signal and the On-Body signal are opposite (crest replaced by trough) of each other, but the breathing rate is still the same. This shows that even at 1m away from the antenna the reflection coefficient phase is affected by the respiration induced movement of the chest.

Table 4.23: Statistical analysis of breathing rate from MLT1132 chest belt and On-Body antenna at various distances. All BA results are in breaths per minute.

Distance	**Directly on clothes**	**Directly on skin**	**5cm**	**10cm**	**25cm**	**50cm**	**1m**
Accuracy (%) (within 1)	96.9	90.7	98.1	88.4	96.5	95	96.5
Accuracy (%) (within 2)	100	100	100	95	100	97	100
Accuracy (%) (within 3)	100	100	100	99.6	100	99	100
Accuracy (%) (within 4)	100	100	100	100	100	100	100
Accuracy (%) (within 5)	100	100	100	100	100	100	100
MLT1132 Belt Breathing Rate	17.2	19.7	15.3	12.8	13.8	13.9	12
On-Body Breathing Rate	17.3	19.7	15.2	12.8	13.8	14.1	12.1
Mean Diff (BA)	0.1810	0.0745	0.1228	0.0602	0.0087	-0.1760	-0.1017
Standard Deviation (BA)	0.4479	0.5130	0.3900	0.8026	0.4326	0.6449	0.5124
d +1.96 s_d (BA)	1.0589	1.0800	0.8872	1.6334	0.8566	1.0879	0.9026
d -1.96 s_d (BA)	-0.6968	-0.9310	-0.6417	-1.5129	-0.8393	-1.4400	-1.1060

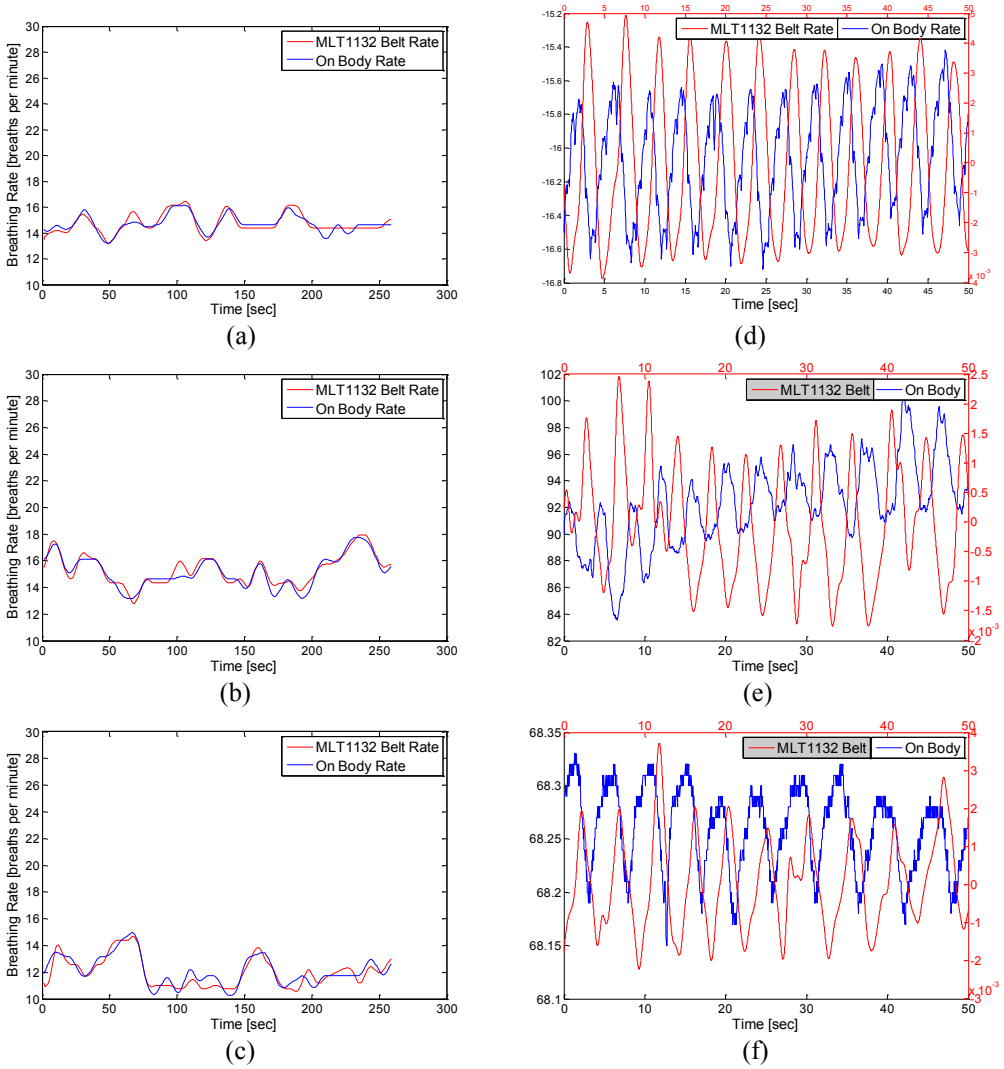

Figure 4.41: Breathing rate [Breaths per minute] vs. Time for the ECG signal and On-Body monitor when the antenna is (a) directly on the clothes, (b) 5cm away from chest and (c) 1m away from chest. Breathing signal from On-Body Monitor and filtered MLT1132 Chest Belt when the antenna is (d) directly on the clothes, (e) 5cm away from chest and (f) 1m away from chest.

4.9 Human body measurement results

4.9.1 Experimental setup

The basic experimental setup described in section 4.3.1 will be used here. In this section the results of the experiments carried on 13 people in the sitting position and 10 people in the supine position will be analysed and discussed. These experiments were conducted using the

patch antenna with radiating element towards the chest and the location of the antenna was the front left chest region (position 6 in figure 4.18). The person under test was asked to sit on a chair for the sitting position measurements. The person was asked to lay flat on the floor on top of a sheet for the supine experiments. He/She was asked to refrain from any sort of movements and the antenna was attached to his/her clothes using tape. The following parameters were kept constant during these experiments:

Frequency	2.45 GHz
Power	-10 dBm
Duration	5 minutes
Sampling Rate	30 samples/sec
Antenna	Patch

Three readings of five minutes each were taken, but only two were chosen for analysis after visual inspection, considering the most movement artefact free measurements. Besides this the EG05000 and the MLT1132D as described in section 4.3.1 were used to measure the heart and breathing rate respectively. The MLT1132D was attached for only one or two of the measurements. All these experiments were performed in normal lab environment with the subjects wearing their own clothes. If the subject was wearing a jacket or sweater he/she was asked to remove it, so all the experiments were conducted on thin layer clothes. These experiments were also performed considering loop antenna and monopole antenna for some people but here the most complete study using patch antenna is presented.

4.9.2 Results and Discussion

4.9.2.1 Heart Rate calculation

The Bland-Altman measures (Mean Difference, Standard Deviation of Difference and 95 % confidence intervals) along with the Average Heart rates, accuracy within 1,2,3,4,5 BPM, and SNR for 13 people in sitting position and supine position were calculated and are shown in Tables 4.24 and 4.25 respectively.

Table 4.24: Statistical analysis of heart rate calculated from ECG and On-Body monitor for different subjects in sitting position.

No	Bland Altman (BPM)		Limits of Agreement (BPM)		Avg. HR [BPM]		Accuracy within					SNR
	Mean	Standard Deviation	Mean+1.96 STD	Mean-1.96 STD	Onbody	ECG	1	2	3	4	5	
1	-0.1628	2.3997	4.5406	-4.8663	71.88	71.7	88.26	93.7	95.2	95.7	96.1	1.0878
2	0.1757	1.2870	2.6982	-2.3469	73.70	73.9	89.46	97.3	98	98.1	98.6	1.1689
3	-0.1079	1.0168	1.8851	-2.1009	64.84	64.7	84.18	95.2	96.8	98.3	99.3	1.2957
4	0.1785	0.5906	1.3362	-0.9791	64.49	64.7	89.62	99.5	100	100	100	1.9162
5	0.4791	1.8441	4.0934	-3.1353	67.16	67.6	75.5	89.6	93	94.6	95.8	1.4152
6	-2.2762	2.8669	3.3428	-7.8953	51.5	49.2	17.35	35.9	54.4	70.2	80.3	0.7718
7	3.3188	2.2949	7.8169	-1.1793	76	79.3	17	33.8	49	57.5	70.6	0.6716
8	1.4766	1.9328	5.2649	-2.3118	80	81.5	30.44	63.8	77.6	87.9	95.1	0.6242
9	1.0240	2.2046	5.3450	-3.2970	86.7	87.7	26.87	61.4	84.4	91	96.4	0.6104
10	0.0677	4.1573	8.2160	-8.0807	68.55	68.6	45.07	61.2	69.6	77.2	80.9	0.7660
11	0.4658	0.5600	1.5635	-0.6318	69.77	70.2	82.82	99.3	100	100	100	0.9190
12	0.5647	1.9570	4.4004	-3.2710	81.75	82.3	69.05	85.4	90.6	93.5	96.6	0.9538
13	0.0597	0.4197	0.8823	-0.7630	60.03	60.1	98.47	100	100	100	100	0.9662
Avg	0.1785	1.9328	4.0934	-2.3469	69.77	70.2	70.9	86	91.4	94.2	96.3	0.9538
Std	1.2304	1.0523	2.3369	2.4646	9.4	10.3	25.2	16	10.1	6.9	5.4	0.3709

Table 4.25: Statistical analysis of heart rate calculated from ECG and On-Body monitor for different subjects in supine position.

No	Bland Altman (BPM)		Limits of Agreement (BPM)		Avg. HR [BPM]		Accuracy within					SNR
	Mean	Standard Deviation	Mean+1.96 STD	Mean-1.96 STD	Onbody	ECG	1	2	3	4	5	
1	-0.1296	2.1132	4	-4.3	67.29	67.16	88.9	97.6	98	98.1	98.1	1.5077
3	-0.2971	1.8412	3.3	-3.9	57.85	57.55	82	94.2	95.6	96.3	96.6	0.6897
4	-1.0932	8.2016	14.9	-17.2	55.8	54.71	76.9	94.9	97.1	97.6	98.8	0.4690
5	0.4791	1.8441	4.1	-3.1	67.17	67.64	75.5	89.6	93	94.6	95.8	1.4152
6	1.8140	3.1655	8	-4.4	45.81	47.62	30.8	52.6	65	73.5	80.3	1.0422
7	1.5793	3.7762	8.9	-5.8	66.87	68.45	25.3	44.2	59.7	69.6	78.6	1.1032
10	0.0646	4.3299	8.6	-8.4	69.12	69.18	34.0	51.0	64.3	73.1	80.4	0.8233
11	1.0397	3.2216	7.4	-5.3	64.96	66	65.5	78.2	83.3	88.1	91.2	1.2494
12	0.3459	1.4130	3.1	-2.4	69.42	69.76	83	93.2	95.6	97.1	97.6	1.6333
13	0.3019	0.5742	1.4	-0.8	62.85	63.15	90.5	100	100	100	100	1.0792
Avg	0.3239	2.6393	5.75	-4.35	65.91	66.58	74.5	87.4	90.9	93.1	94.8	1.0912
StD	0.8772	2.1434	3.99	4.57	7.5	7.4	18.2	16.1	11.9	8.8	6.4	0.3680

Many of results that will be discussed here represent the average of the results obtained for all the population tested. The mean difference and the standard deviation of differences for the sitting position were 0.1785 and 1.9328 respectively, while the 95% confidence intervals were 4.0932 and -2.3469. The mean accuracy within 2 and 5 BPM for sitting position is 86 % and 96.3 % respectively. The average SNR is 0.9538. These values indicate that the On-Body monitor was able to successfully detect the heart rate of people in the sitting position. The mean difference and the standard deviation of differences for the supine position were 0.3239 and 2.6393 respectively, while the 95% confidence intervals were 5.75 and -4.35. The mean accuracy within 2 and 5 BPM for sitting position is 87.4 % and 94.8 % respectively. The average SNR is 1.0912. The results for the supine position also indicate its suitability as a sleep monitor and its reliable use in the supine position. It was expected that the heart rate would be better detectable in the supine position as there were fewer unwanted movements in

this position and the chest movement due to respiration was less in this position. But overall not much difference between the supine and sitting position was observed and the heart rate was equally detectable in both positions.

The usability of On-Body monitor as a commercial product or in a practical environment depends upon the accuracy required by the particular application. For example if it is to be deduced whether an individual's heart rate is normal or abnormal than a difference of 5 BPM from the ECG device can be tolerated. For the sitting and the supine positions mean accuracy within 5 BPM was 96.43 % and 96.18 % respectively. So it is feasible to use the On-Body monitor for applications that require accuracy within 5 BPM. But if an application requires more exact monitoring (accuracy within 1 beat) like in an ambulance, operation room or the measurement of metabolic rate than the average accuracy for sitting and supine position is 75.5 % and 76.19 %. This accuracy renders it unsuitable with the current system and signal processing used. The accuracy within 3 BPM is suitable for determining heart rate for normal, non-urgent use and the mean accuracy for that is 89.63% and 86.65% for sitting and supine positions which is reasonable.

The difference between the Heart Rate calculated using the ECG and On-Body device was plotted versus the SNR for all measurements in the sitting and supine position and is shown in figure 4.42.

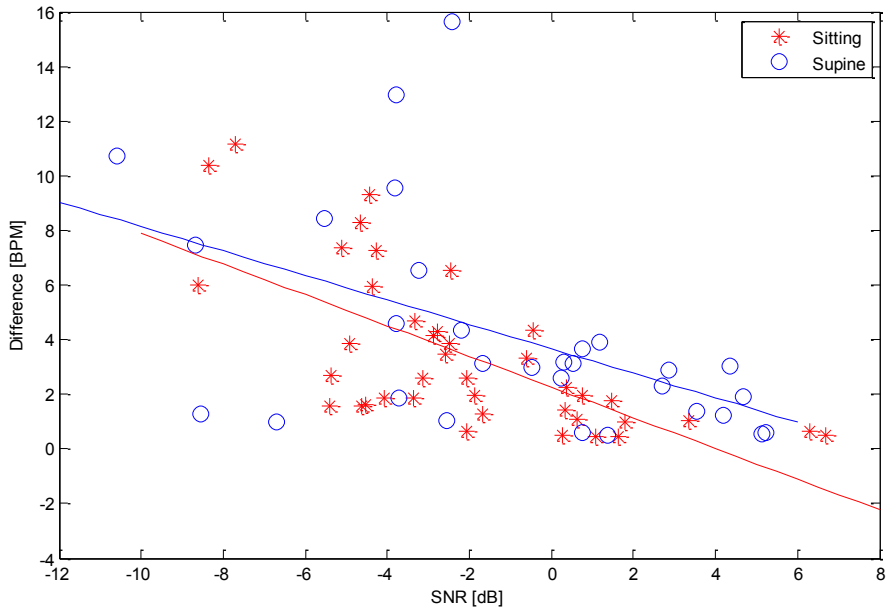

Figure 4.42: Difference in the Heart rate[BPM] between the ECG and On-Body monitor versus the SNR for all measurements in sitting(red) and supine(blue) position. The Linear regression lines are also shown.

It was observed that at higher SNR the difference was low and a maximum difference of 3.89 above 0 dB SNR was seen. At low SNR's as expected the error in BPM is generally higher but even at a SNR of -8.5 dB, difference of 1.26 was achieved for one measurement. The general trend however suggests better accuracy with increased SNR. The SNR can be improved by using equipment with lower residual phase noise, base band noise and RF additive white Gaussian noise [19]. It can also be improved by increasing the signal power and providing better shielding to the On-Body antenna from outside movements other than chest movements. Better signal processing can also improve SNR and thus accuracy. Even at low SNR with advanced signal processing techniques (especially spectral estimation methods), accurate detection is still possible.

Some of the subjects were moving quite frequently and this contributed considerably to decrease the accuracy especially in the case of subjects 8 and 11. No movement removing signal processing was employed. Sudden movements can be filtered out but not continuous

movements. So diversity (antenna and frequency) techniques and better signal processing can improve the accuracy in cases in which the subject moves excessively and consistently. The diversity techniques are proposed as future work.

The correlations between accuracy(within 3 BPM)/SNR and all the body parameters described in section 4.3.3 for both sitting and supine positions were calculated and are shown in Table 4.26. No meaningful correlations were discovered in the sitting position results. Some correlations ($p<0.05$) were discovered in the supine position. These included:

(i) negative correlation (-0.72) between accuracy and chest circumference at exhale,

(ii) negative correlation (-0.8) between accuracy and waist circumference at inhale,

(iii) negative correlation (-0.77) between accuracy and BMI,

(iv) positive correlation (0.78) between accuracy and height,

(v) negative correlation (-0.76) between SNR and chest depth at inhale, and

(vi) negative correlation (-0.7) between SNR and chest depth at exhale.

It was expected that people with higher BMI might have lower accuracy for On-Body heart rate detection results as the extra fat might cause attenuation and the movement of chest due to heart beating might be lower. This was observed for the accuracy correlations in supine position. Larger chest and waist circumferences were also pointing to less accurate results. Again this could be attributed to extra fat causing less movement due to heart beat, generation of unwanted movements (due to loose skin) , and attenuation. As the population size was only 10 and 13 for supine and sitting positions respectively, the authors feel that the obtained correlations might be misleading especially considering that no correlations were discovered in the sitting position. For correlations to be significant a study considering 20-80 people should be conducted [21]. Although one reason for no correlations in the sitting position could be the fact that many more unwanted movements are possible in the sitting position

compared to the supine position. This movement introduces more errors compared to the supine position and this hides any correlations from appearing.

Table 4.26: SNR/accuracy (within 3 BPM) correlation (Pearson correlation coefficient r and the p-value) with body measurements (from 4.3.3) for sitting and supine positions. A p-value less than 0.05 means a significant correlation is present.

Parameter	**Supine SNR**		**Supine Accuracy (within 3 BPM)**		**Sitting SNR**		**Sitting Accuracy (within 3 BPM)**	
	r	P	R	p	r	p	r	P
Height	0.20	0.67	**0.78**	**0.02**	0.16	0.59	0.15	0.63
Chest Circumference at Inhale	-0.35	0.39	-0.63	0.095	0.18	0.54	0.06	0.84
Chest Circumference at Exhale	-0.19	0.65	**-0.72**	**0.04**	0.16	0.59	0.03	0.92
Waist Circumference at Inhale	-0.18	0.67	**-0.8**	**0.02**	0.06	0.84	0.01	0.98
Waist Circumference at Inhale	-0.01	0.99	-0.67	0.07	0.1	0.97	0.04	0.89
Weight	-0.42	0.3	-0.25	0.55	0.18	0.54	0.01	0.96
Chest Depth at Inhale	**-0.76**	**0.03**	-0.51	0.2	0.12	0.70	0.11	0.73
Chest Depth at Exhale	**-0.7**	**0.05**	-0.64	0.087	0.22	0.48	0.12	0.69
Chest Width at Inhale	-0.18	0.67	-0.19	0.65	0.11	0.72	0.17	0.58
Chest Width at Exhale	-0.33	0.42	-0.23	0.58	0.08	0.79	0.02	0.96
Height x Chest Circumference at Inhale	-0.17	0.68	0.13	0.75	0.22	0.47	0.11	0.73
Height x Chest Circumference at Exhale	-0.04	0.93	-0.04	0.93	0.21	0.49	0.08	0.79
Height x Waist Circumference at Inhale	-0.12	0.77	-0.51	0.2	0.10	0.73	0.05	0.87
Height x Waist Circumference at Inhale	0.10	0.81	-0.27	0.52	0.06	0.85	0.09	0.78
Height x Chest Width at Inhale	-0.03	0.94	0.3	0.48	0.14	0.66	0.18	0.55
Height x Chest Width at Exhale	-0.24	0.56	0.08	0.84	0.11	0.72	0.05	0.87
BMI	-0.41	0.32	**-0.77**	**0.03**	0.1	0.75	-0.06	0.84

4.9.2.2 Respiration Rate Calculation

For the case of measuring respiration of all the subjects the major stumbling block was the MLT1132 Belt Transducer. It required expansion of the belt to create a voltage change, but

many people's chest movement was not able to provide the sufficient expansion especially in the supine position, so results are only available for 9 people in the sitting state and 5 people in the supine state. The statistical analysis (as in previous sections) of the respiration measurements for the sitting and supine positions is shown in table 4.27 and 4.28 respectively. The average accuracy (within 5 breaths) was 96.5% and 100% for the sitting and supine position. The average accuracy (within 1 breath) was 77.9% and 92.5% for the sitting and supine position. In the case of sitting position for 8 out of the 9 people more than 80% of the results were within 3 breaths per minute. In the case of the supine position for 4 out of five people more than 98.8% of the results were within 3 breaths per minute. The errors that occurred were more due to the MLT1132 chest belt than the On-Body monitor. As stated before, this was due to the inability of the MLT1132 chest belt to detect weak respiration chest movements. These weak respiration chest movements were detectable with the On-Body monitor. Other errors included non-uniform and non-linear movement of the chest, excess fat causing unwanted movements in some cases, and unwanted body movements. There was also the problem of general unwanted movement due to the non-uniform and vibratory movement of the shirt when the shirt is not directly parallel to the body and is hanging freely. This also caused errors in the Heart Rate detection. In these cases a belt to hold the antenna directly parallel to the body solved the problem. It can also be solved by connecting the antenna directly to the skin parallel to the chest. In the supine position the movement due to breathing was much less detectable for the MLT1132 belt because the expansion of the piezoresitive transducer was less in the supine position as compared to the sitting position. This was due to the belt being placed around the stomach in this position as it was observed visually that most people breathe through the stomach in the supine position. The expansion of the abdomen for most people was not strong enough to get a voltage

change. The expansion and contraction of the chest in the supine position was even less than the expansion and contraction of the abdomen in that position.

Table 4.27: Respiration rate statistical analysis for different subjects in sitting position. (Numbers correspond to 4.4.3 subject numbers). Average does not include subject 8.

No	Bland Altman (breaths per minute)		Limits of Agreement (breaths per minute)		Avg. Breathing Rate [Breaths Per Minute]		Accuracy within				
	Mean	Standard Deviation	Mean+1.96 STD	Mean-1.96 STD	Onbody	Belt	±1	±2	±3	±4	±5
1	0.0131	0.3536	0.7062	-0.6800	14.7	14.7	100	100	100	100	100
3	0.1810	0.4479	1.0589	-0.6968	17.2	17.3	96.9	100	100	100	100
4	-0.0833	0.4112	0.7227	-0.8892	21.3	21.3	99.6	100	100	100	100
5	-0.4949	2.1199	3.6601	-4.6499	18.3	17.8	65.3	77.6	85.3	90.7	93.4
6	-1.2445	2.4345	3.5271	-6.0161	17.2	16	64.1	78	83.4	86.1	89.6
7	0.1151	3.2216	6.4294	-6.1992	14.1	14.2	66.0	84.6	88.8	93.4	95
8	-3.1630	4.4111	5.4828	-11.8087	22.8	19.7	42.9	53.7	65.3	69.9	76.1
9	0.4319	2.0571	4.4639	-3.6001	13.2	13.6	51.7	73.7	85.7	92.7	95.4
10	0.0356	1.3488	2.6794	-2.6081	12.7	12.8	79.2	87.6	94.2	97.3	98.8
Avg	-0.13075	1.54933	2.9069	-3.1674	16.09	15.96	77.9	87.7	92.2	95	96.5

Table 4.28: Respiration rate statistical analysis for different subjects in supine position. (Numbers correspond to 4.4.3 subject numbers). Average does not include subject 6.

No	Bland Altman (breaths per minute)		Limits of Agreement (breaths per minute)		Avg. Breathing Rate [Breaths Per Minute]		Accuracy within				
	Mean	Standard Deviation	Mean+1.96 STD	Mean-1.96 STD	Onbody	Belt	±1	±2	±3	±4	±5
1	-0.1091	0.4925	0.8563	-1.0745	15.7	15.6	96.5	98.5	100	100	100
3	0.0538	0.2831	0.6086	-0.5010	17.5	17.6	100	100	100	100	100
4	-0.1079	1.0168	1.8851	-2.1009	15.7	15.9	88.4	95.8	98.8	98.8	100
6	-1.6961	9.4263	16.7795	-20.1717	19.5	17.8	17.6	30.3	38.0	43	48.4
10	-0.0088	0.8038	1.5666	-1.5842	12.5	12.5	84.9	93.8	100	100	100
Avg	-0.043	0.64905	1.22915	-1.31515	15.35	15.4	92.5	97.03	99.7	99.7	100

Figures 4.43,4.44,4.45, and 4.46 show the breathing rates in breaths per minute and the respiration signals from the MLT1132 belt and the On-Body monitor for subject 5 sitting, subject 1 supine, subject 4 sitting, subject 4 supine. It is seen in Fig. 4.43 that even though the respiration signals from the two devices don't follow each other exactly the respiration rate is still accurately detectable. From Fig. 4.44 (b) and 4.45 (b) it is observed that the respiration

signals have opposite response to expansion and contraction. This makes it difficult to know whether during the crest the chest is expanding or contracting when using the On-Body monitor. Furthermore it was also observed that in the supine position the heart beats are more pronounced and the breathing signal is slightly less evident as can be seen in Figure 4.44(b). In Figure 4.46 (b) the heart beats are even more clearly visible. The reason is that the chest moves less due to breathing in this position so the chest movement due to heart beating is more detectable. This improved the SNR slightly in the supine position for the heart signal but did not have any significant effect on the heart rate detection accuracy. It was also observed that in general, the On-Body monitor is more sensitive to both minute and significant respiration chest movements than the MLT1132 chest belt. The On-Body monitor can thus be used in place of commercial chest belts as a more sensitive and accurate respiration rate monitor.

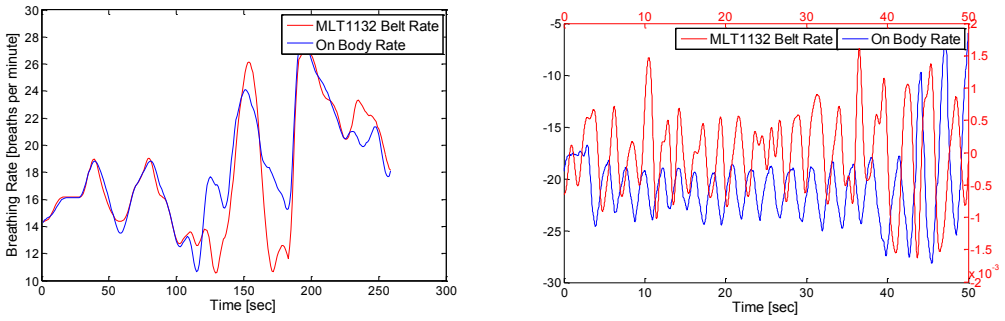

(a) (b)

Figure 4.43: (a) Breathing rate [Breaths per minute] vs time [sec] calculated for MLT1132 Chest Belt (red) and On-Body Monitor (Blue) ,(b) On-Body respiration signal (blue) vs. MLT1132 chest belt respiration signal for subject 5(from 4.4.3) sitting.

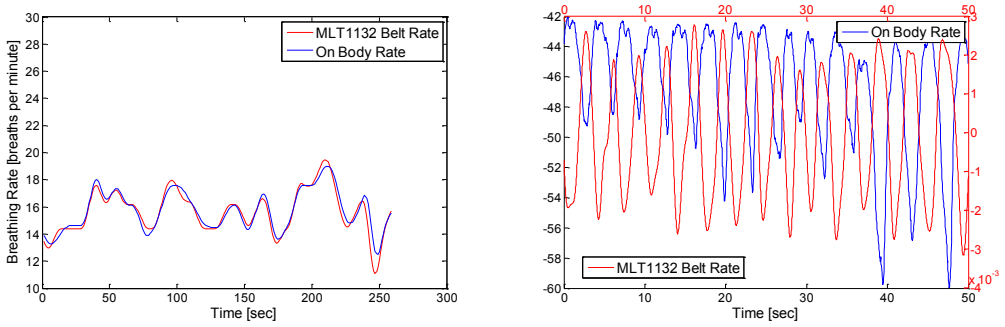

(a) (b)

Figure 4.44: (a) Breathing rate [Breaths per minute] vs time [sec] calculated for MLT1132 Chest Belt (red) and On-Body Monitor (Blue) ,(b) On-Body respiration signal (blue) vs. MLT1132 chest belt respiration signal for subject 1(from 4.4.3) supine.

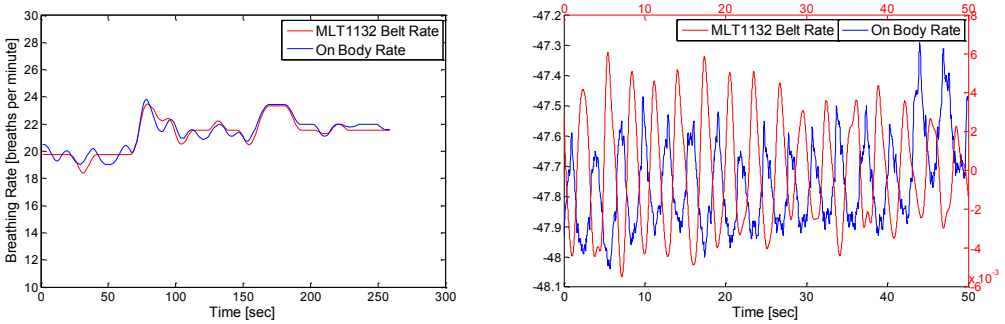

(a) (b)

Figure 4.45: (a) Breathing rate [Breaths per minute] vs time [sec] calculated for MLT1132 Chest Belt (red) and On-Body Monitor (Blue) ,(b) On-Body respiration signal (blue) vs. MLT1132 chest belt respiration signal for subject 4(from 4.4.3) sitting.

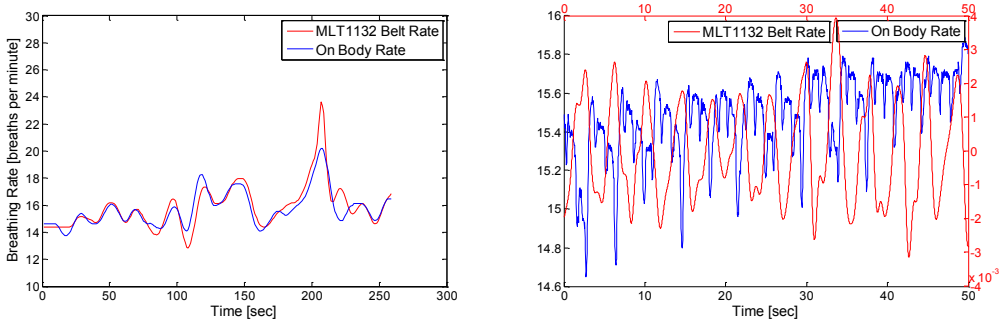

(a) (b)

Figure 4.46: (a) Breathing rate [Breaths per minute] vs. time [sec] calculated for MLT1132 Chest Belt (red) and On-Body Monitor (Blue) ,(b) On-Body respiration signal (blue) vs. MLT1132 chest belt respiration signal for subject 4(from 4.4.3) supine.

4.10 Heart rate Variability

The heart rate (HR) of a person during normal sinus rhythm has a variation between beats. Heart Rate Variability (HRV) is the measure of the variation in the beat-to-beat interval of the heart. It provides an indication of the capability of the heart to detect and quickly adapt to unexpected stimuli [22]. This variation results from the dynamic interplay between the many psychological mechanisms that govern the instantaneous HR [23]. A study of this HR variation gives insight into the state and integrity of the autonomic nervous system (ANS). [23]. HRV thus provides an indication of the ANS response to demands, stress and illnesses as they are reflected in the variation [24]. HRV has been linked to cardiovascular mortality including sudden death due to cardiac arrest[25], obstructive sleep apnoea syndrome diagnosis[26] diabetic neuropathy sensing [27], renal failure detection [28] and increased risk of sudden cardiac death after acute myocardial infarction [29], etc. It changes with age and thus can give an indication about the person's age [30]. It is also affected by smoking [31], drug use [32], and alcohol intake [33]. Different sleep states [34] also have an effect on the HRV and it can be used to determine the quality and type of sleep a person is having. From all the above discussion it can be reasonably established that HRV is a very promising method for the future of health assessment. A brief overview of HRV can be found in [22-24].

There are many factors which contribute to the variability of the heart rate including [24]:

1) Cardiac rhythm (which effects variation over 5-hour cycles)

2) Temperature regulation (25-second cycles)

3) Cardiac sympathetic nerve activity (6-second cycles)

4) Respiratory Rhythm (2.5 to 6 second cycles)

The most popular and accurate method to detect HRV is with an electrocardiogram. Photoplethysmogaraph obtained using a pulse oximeter is also a commonly applied technique.

Here the reflection coefficient phase of an antenna connected parallel to the body will be used to measure HRV. It will be determined whether it is possible to detect HRV accurately up to 5 min durations (which is the normally chosen short term duration) [35]. Experiments will be conducted in both the supine and sitting position. The heart signal from the On-Body Vital signs monitor as seen in the previous sections has less well defined peaks than the ECG since it measures mechanical motion of the chest rather than the electrical activity of the heart. There is also the effect of unwanted movements and environmental noise, both of which cause distortion in the On-Body heart signal. If these challenges are overcome and the On-body monitor is found feasible for HRV monitoring, then it could prove to be a very useful and low profile alternative for HRV assessment.

4.10.1 Time domain measures of HRV

HRV assessment first requires the detection of each heart beat. In the case of ECG signal the R peak is used and in the case of On-Body Heart signal the peak point of the crest of the wave will be used. Then the duration between these peaks is measured. Common time domain measures used to assess HRV include standard deviation of normal beat-to-beat intervals (SDNNs), Root mean square of differences of successive beat-to-beat intervals (RMSSDs), the triangular index (HRV TI) and HRV TI max bin (calculated using histograms). SDNN reflects the overall HRV. The SDNN can be calculated by applying the standard deviation formula to the durations of individual intervals [35]. In mathematical form this is written as:

$$SDNN = \sqrt{\frac{1}{n-1}\sum_{i=1}^{n}(NN_i - m)^2}$$

where NN_i is the duration of the i-th beat to beat interval, n is the total number of beat-to-beat intervals and m is the mean of all the beat-to-beat intervals

RMSSD reflects the high frequency components of HRV. The RMSSD can be calculated by applying the formula of standard deviation to the difference of adjacent beat-to-beat intervals with the assumption that the mean of the difference between adjacent intervals is zero [35]. In mathematical form this is written as:

$$RMSSD = \sqrt{\frac{1}{n-1}\sum_{i=1}^{n-1}(NN_{i+1} - NN_i)^2}$$

where NN_i is the duration of the i-th beat to beat interval, n is the total number of beat-to-beat intervals.

HRV TI gives an indication of the shape of the beat-to-beat interval distribution and is calculated using histograms. Histograms which have a single high peak have low values and histograms with uniform distribution have high values of HRV TI. The standard bin size (of beat-to-beat interval) for the histogram most commonly used is 8 msec and will be used here [27]. The formula for calculating HRV TI is as follows:

$$HRVTI = \frac{1}{\max_i b(t_i)}\sum_{i=1}^{N_b} b(t_i)$$

Where $b(t_i)$ is the number of intervals in the *i*-th bin which is centred at t_i. N_b is the total number of valid bins. Details explanations and methods of calculating all these HRV parameters can be found in [35-36].

4.10.2 Experimental data

The data gathered from the human body measurement results (in section 4.9) will be used here to investigate HRV detection feasibility using On-Body vital signs monitor. The only difference is that the signal processing for this section involved changing the parameters for the peak detector for many subjects individually to detect all the peaks as the same parameters were unable to detect all the peaks for all the users. Thus unlike in previous sections where the same parameters for Fourier transform and filters were sufficient for accurate vital signs monitoring, the HRV requires the On-body Monitor's signal processing part to be trained for the specific user in order to operate correctly. Also only one 5 min measurement out of the three obtained from the experiments in section 4.9 will be used for HRV assessment. A population size of same 10 people for both the sitting and supine position was used for this time domain measurement of HRV.

4.10.3 Results and Discussion

In order to calculate HRV parameters, the first step requires the accurate detection of the peaks of heart beat from both the ECG and the ON-Body Monitor. The results of such detection for subject 4 (from 4.3.3) in sitting position and subject 3 (from 4.3.3) in supine position are shown in figures 4.47 and 4.48 respectively. As can be clearly seen all the peaks are accurately detected but there is a slight delay between the heart signals from both sources. The delay is quite small and we are measuring the duration of the interval between the peaks so it does not have an effect on the results.

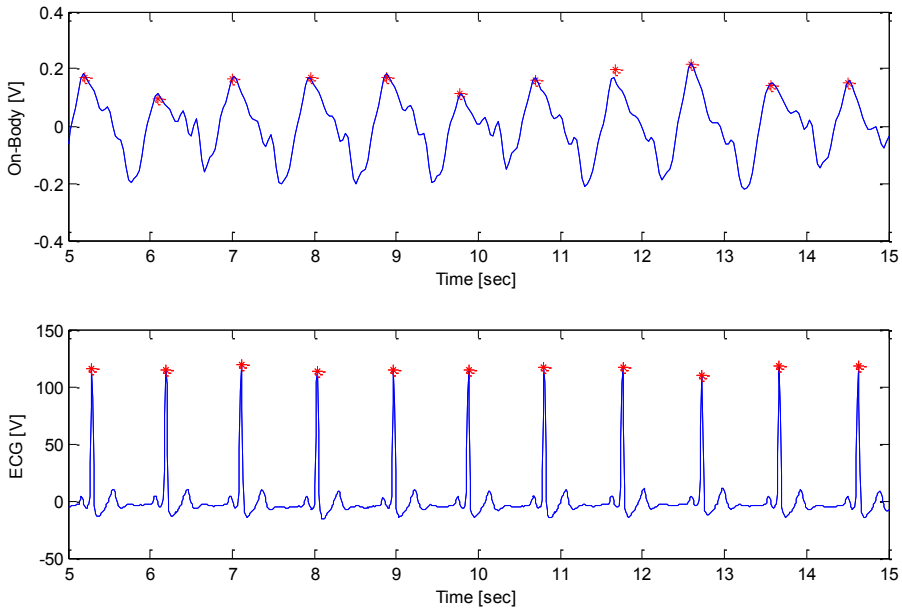

Figure 4.47: Peak detection results in a 15 second duration for subject 4 (from section 4.3.3) in sitting position.

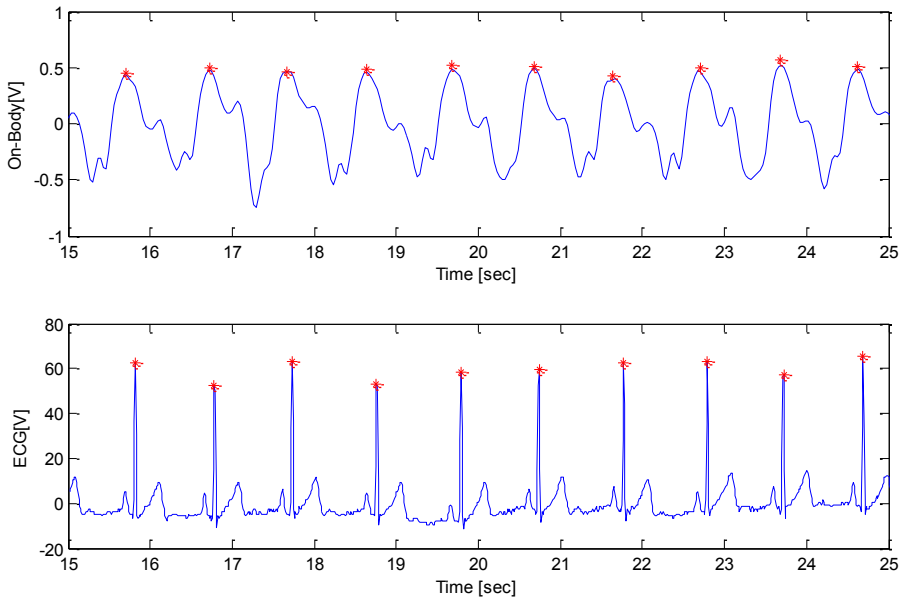

Figure 4.48: Peak detection results in a 15 second duration for subject 3 (from section 4.3.3) in supine position.

Figure 4.49 (a) and (b) shows the histograms of the beat-to-beat intervals for the ECG and On-body monitor in sitting position for subject 3 while Figure 4.49 (c) and (d) show the histograms of the beat-to-beat intervals for the ECG and On-body monitor in the supine position for subject 3. Figure 4.50 shows the same histograms as Figure 4.49 for subject 4.

The max bin count among all the bins along with its bin centre is shown for ECG and the On-body monitor. If the bin with the maximum count differ between the ECG and On-Body Monitor than the bin count for the equivalent maximum bin of ECG is also shown in the On-Body histogram. The beat-to-beat intervals that fell outside the range of 500-1500 ms for the On-Body heart signal or the ECG signal were not considered for Histogram analysis. It can be seen that the bin count of the On-Body monitor is more spread out as compared to the ECG and the total bin count for the On-Body monitor is generally a little less than the ECG monitor. The reason for this is the (i) incapability of detecting all the correct peaks in the On-Body signal, (ii) the non-sharp peaks and (iii) the elimination of wrong beat-to-beat intervals. These histograms were used for HRV TI calculations.

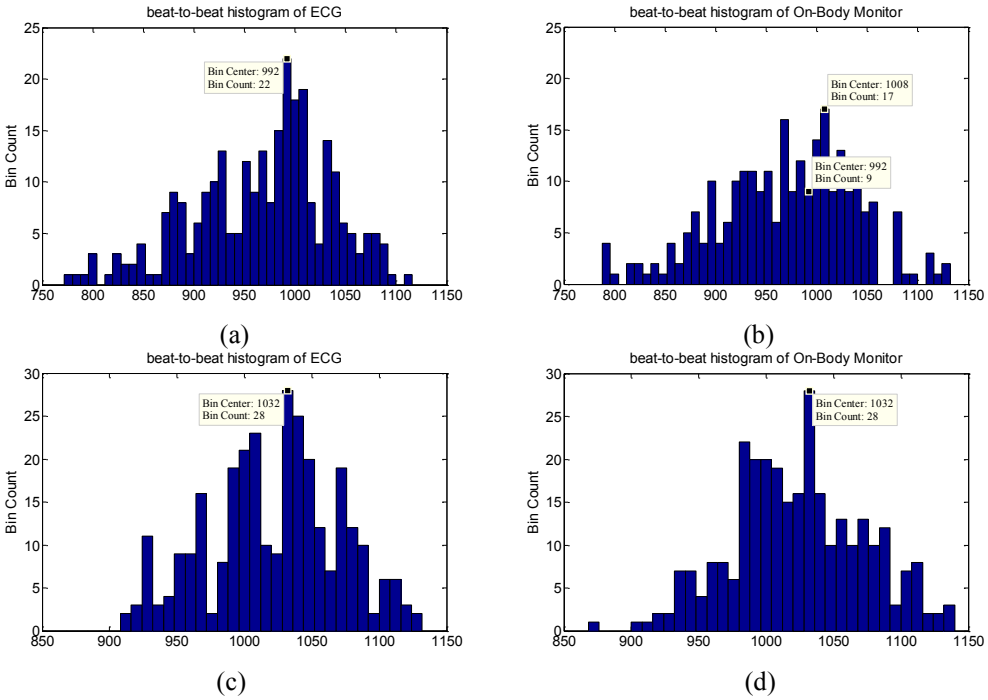

Figure 4.49: Histograms with 8 msec bins for subject 3 (a) sitting (from ECG) (b) sitting (from On-Body), (c) supine (from ECG), (d) sitting (from On-Body). Also shown are the max bins count and the maximum bin centres. (x-axis is in ms)

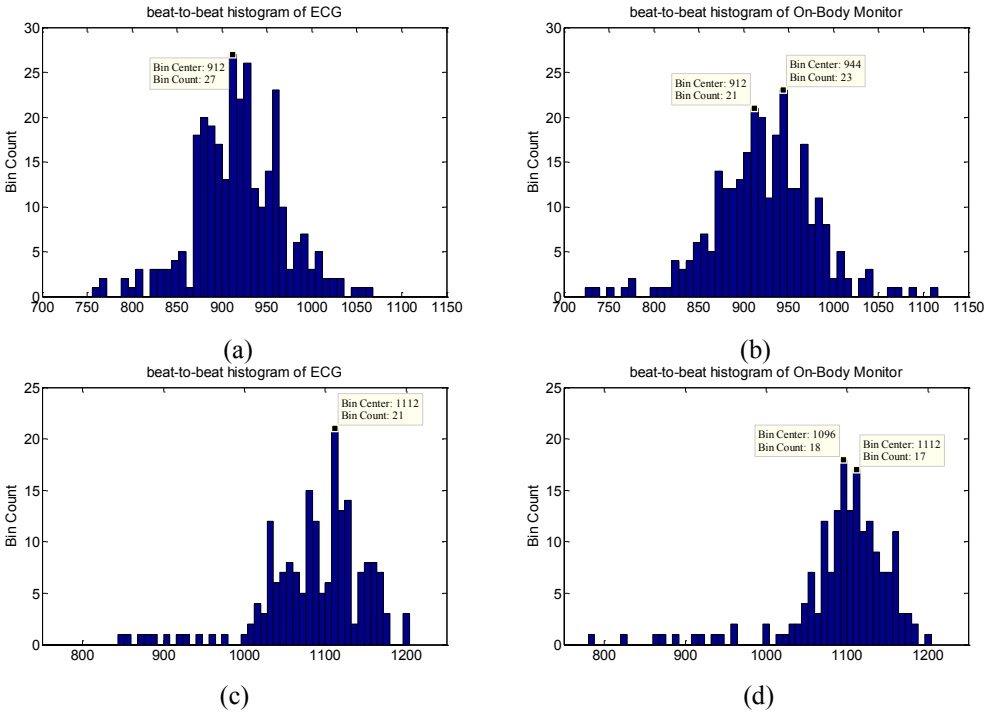

Figure 4.50: Histograms with 8 msec bins for subject 4 (a) sitting (from ECG) (b) sitting (from On-Body), (c) supine (from ECG), (d) sitting (from On-Body). Also shown are the max bins count and the maximum bin centres. (x-axis is in ms)

The analysis of the data obtained (using the experiments in section 4.9) will be achieved by using Bland-Altman parameters, average heart rates form both On-Body vital signs monitor and ECG device, the HRV parameters (as described in Section 4.10.1) along with HRV TI max bin. The above mentioned analysis measures are shown in Table 4.29 and 4.30 for the sitting and supine positions respectively.

The supine position leads to more accurate results for HRV assessment. In the supine position as compared to the sitting position, the HRV measures vary more (have higher values) as there is a greater percentage change in the mean beat-to-beat intervals. This fact of higher HRV in supine position is also confirmed in other studies on HRV in supine position using ECG [37, 38]. As stated before, the heart rate variability parameters obtained from the ECG and On-Body monitor agree more in the supine position than in the sitting position, the reason for this is less movement in the supine position and more prominent heart signal as discussed

in section 4.9.2.2 (which also caused an increase in SNR). In the supine position, the SDNN differs (between On-Body and ECG) less than 5.52 ms for 8 of the measurements and the RMSSD differs less than 35.48 for 7 of the measurements. The HRV TI is within 4.04 for 9 measurements and the HRV TI max bin is within 48 ms for all measurements. In the case of sitting position the SDNN was within 26.67ms for 8 measurements, the RMSSD was within 60.1 ms for 7 of the measurements. The HRV TI is within 5.5 for 9 measurements and the HRV TI max bin is within 200 ms for all measurements. Overall from the above mentioned observations and the two tables the general trend of better agreement between On-Body and ECG HRV measures in the supine position is observed. This gives rise to the possibility of creating a device to assess HRV during sleep which is very low profile and does not disturb sleep or cause unease.

Table 4.29: HRV assessment in the sitting position (Numbers correspond to 4.4.3 subject numbers)

Subject	Avg. HR [BPM]		Bland-Altman		SDNN		RMSSD		HRV TI Index		HRV TI max bin (ms)	
	Onbody	Ecg	Mean	Standard deviation	On-body	Ecg	Onbody	Ecg	On-body	Ecg	Onbody	Ecg
1	74.69	74.87	0.1723	0.8158	43.84	38.92	50.92	21.41	8.57	9.37	808	832
3	61.49	61.68	0.1913	0.3925	68.4	67.58	74.68	62.69	15.47	12.64	1008	992
4	65.35	65.58	0.2303	0.5068	55.85	49.41	51.16	26.7	12.35	10.81	944	912
5	68.15	68.68	0.5308	2.3075	65.55	57.6	73.79	27.59	15.4	10.87	880	888
6	53.91	46.41	-7.4992	7.6586	157.95	91.12	215.35	67.13	19.17	5.23	1200	1400
7	86.46	76.01	-10.45	10.89	94.53	64.34	136.64	31.11	12.69	11.23	712	792
10	68.1	68.44	0.3468	5.1409	72.58	51.45	98.56	38.46	16.71	13.26	904	888
11	71.16	73.22	0.3992	1.3267	71.85	45.18	97.02	35.99	15.47	9.97	840	792
12	81.86	81.52	0.3324	1.9469	43.9	50.84	52.36	29.34	12.67	11.58	768	728
13	65.78	66.17	0.3895	1.4576	60.06	62.31	67.61	37.95	11.75	9.16	920	928

Table 4.30: HRV assessment in the supine position (Numbers correspond to 4.4.3 subject numbers)

Subject	Avg. HR [BPM]		Bland-Altman		SDNN		RMSSD		HRV TI Index		HRV TI max bin (ms)	
	Onbody	Ecg	Mean	Standard deviation	On-body	Ecg	On-body	Ecg	Onbody	Ecg	On-body	Ecg
1	66.63	66.82	0.1871	0.6104	54.67	54.03	68.77	62.25	13	11.09	908	896
3	58.49	58.44	0.0555	0.3078	48.49	48.36	61.36	62.86	10.32	10.52	1032	1032
4	54.44	54.84	0.3920	0.9202	63.98	63.59	73.4	73	9.94	9.05	1096	1112
5	66.19	66.60	0.4122	1.1351	59.58	57.93	60.98	25.5	12.56	10.7	912	912
6	46	48	2.0082	3.1297	137.2	81.74	194.5	69.76	14.75	11.5	1264	1288
7	81.13	81.06	-1.0761	2.9343	68.71	63.19	98.40	35.16	13.46	15.2	744	792
10	71.7	69.8	-1.9115	4.9036	86.12	58.72	128.0	33.42	18.5	11.1	856	856
11	65	65.4	0.3992	1.3267	54.67	50.9	45.89	38.33	13.92	9.88	948	920
12	67.4	67.7	0.2912	0.5331	47.87	50.11	60.55	51.67	9.43	8.28	916	904
13	63.36	63.21	-0.1562	0.9712	46.92	45.27	55.21	25.95	9.08	8.24	944	952

The On-Body HRV monitor with the parameters and system shown here requires training of the signal processing parameters for each person but was successful in monitoring the HRV in the supine position. Work still needs to be done to improve HRV assessment in the sitting state. Better detection of peaks using more advanced signal processing (especially filtering to remove noise) can help achieve better accuracy in the sitting state.

4.11 Conclusion

In this chapter the capability of monitoring heart and breathing rate using an On-Body antenna attached parallel to the chest of a person is studied and validated. First a simulation study is conducted which showed that the reflection coefficient phase variation obtained for an on-body antenna was mainly due to the chest movement relative to the antenna. It was also shown that antenna with minimal grounds were the most sensitive to chest movements. A detailed description of the experimental setup, statistical analysis techniques and signal

processing algorithms used is provided. A parametric study is performed to determine the parameters which lead to best accuracy.

It is observed that lower frequencies in the UWB range lead to better heart rate detection as at higher frequencies the harmonic and intermodulation interference between the breathing and heart beating frequencies increases and this reduces accuracy. Also at higher frequencies the antenna is more sensitive to noise from the environment and non-uniform or unwanted motion of the chest and other parts of the body. The respiration was detectable accurately at all frequencies.

Antennas with smaller ground planes, polarization along the body and radiation pattern towards the chest were found to be the best heart beat detectors. Power as low as -30 dBm was found to be feasible to detect heart rate accurately, while power even as low as -45 dBm was found to be enough to detect respiration rate accurately. The best position on the body for measuring heart rate was the chest area right in front of the heart as this area moved the most due to heart beats (this is explained in section 2.2.2). The respiration rate was accurately detectable at all locations on the body accurately except for the abdomen which was less accurate. The reason for this was the non-uniform and unpredictable motion of the abdomen due to respiration effort. The On-Body monitor worked best as a heart rate detector when the antenna was attached to clothes in front of the chest (where heart is located). As the distance from the chest increased the heart rate detection accuracy suffered. The reason for this was that motion in the near field of the antenna brought about a reflection coefficient phase (RCP) change of the antenna, as the distance increased the effect of motion on antenna RCP also decreased. When the antenna was directly attached to the skin accuracy was slightly lower as the direct contact of the skin with the antenna radiating element introduced new current paths. This can be overcome by using a material to separate the skin and radiating element. Also it

was observed that the relative motion of the chest with respect to the antenna or the antenna movement along with the chest was the major cause of modulation of the RCP with heart and breathing rate information. The breathing rate was accurately detectable at all distances between chest and antenna, even when antenna was in direct contact with the skin.

A study was conducted on 13 people in the sitting position and 10 people in the supine position. The average heart rate detection accuracy (within 5 BM) was 96.4% and 94.8% for the sitting and supine position. Within 3 BPM, the accuracy dropped to 91.4% and 90.9% in the sitting and supine position. The average breathing rate accuracy (within 5 breaths per minute) was 96.5% and 100% for the sitting and supine position. Within 1 breath, the accuracy dropped to 77.9% and 92.5% for the sitting and supine position. Overall the heart rate and breathing rate were detectable with good accuracy in both positions. SNR was found to be better for the supine position as in this position there was less unwanted movement and the heart beats were more pronounced than in the sitting position. No significant correlation between the heart rate detection accuracy and body type were observed in the sitting position while as expected in the supine position there was a negative correlation between accuracy and chest circumference, waist circumference, BMI, etc.

HRV is becoming a very popular diagnostic technique and a lot of research is being conducted on it. Here the HRV was calculated using On-Body monitor in both the sitting and supine position. It was discovered that HRV is only reasonably detectable in the supine position. The reason for this is again less movement in the supine position and more pronounced heart beat peaks compared to the sitting position. Thus the On-Body monitor can be used as a low profile sleep monitor. At the end different signal processing algorithms were studied which led to the use of Fast Fourier transform for spectral analysis and fundamental frequency calculation as it detected the heart rate with most consistent accuracy.

All these experiments point to the feasibility of the On-Body monitor as a low profile, comfortable, cost effective and accurate vital signs monitor which can be used instead of already present commercial devices. The frequency, power and antenna type studies showed that a compact device can be designed which can be either clipped on, taped on, stitched on, etc. and will utilize very little power. The design of a similar device is discussed in [12], [19] and [36]. That device operates as a Doppler radar. A reflection coefficient measurement device will be simpler. The design of such a device and experimentation with it is proposed as future work.

4.12 References

[1] Khan, I.; Hall, P.S.; Serra, A.A.; Guraliuc, A.R.; Nepa, P.; , "Diversity Performance Analysis for On-Body Communication Channels at 2.45 GHz," *Antennas and Propagation, IEEE Transactions on* , vol.57, no.4, pp.956-963, April 2009

[2] Hedman, E.; Wilder-Smith, O.; Goodwin, M.S.; Poh, M.-Z.; Fletcher, R.; Picard, R.; , "iCalm: Measuring electrodermal activity in almost any setting," *Affective Computing and Intelligent Interaction and Workshops, 2009. ACII 2009. 3rd International Conference on* , vol., no., pp.1-2, 10-12 Sept. 2009

[3] Shahhaidar, E.; Boric-Lubecke, O.; Ghorbani, R.; Wolfe, M.; , "Electromagnetic generator: As respiratory effort energy harvester," *Power and Energy Conference at Illinois (PECI), 2011 IEEE* , vol., no., pp.1-4, 25-26 Feb. 2011

[4] Serra, A.A.; Nepa, P.; Manara, G.; Corsini, G.; Volakis, J.L.; , "A Single On-Body Antenna as a Sensor for Cardiopulmonary Monitoring," *Antennas and Wireless Propagation Letters, IEEE* , vol.9, no., pp.930-933, 2010

[5] Fletcher, R.R.; Kulkarni, S.; , "Wearable Doppler radar with integrated antenna for patient vital sign monitoring," *Radio and Wireless Symposium (RWS), 2010 IEEE* , vol., no., pp.276-279, 10-14 Jan. 2010

[6] P.S. Hall and Y.Hao,” Antennas and Propagation for Body Centric Communication Systems,” Norwood, MA, Artech House, 2006, ISBN-10: 1-58053-493-7.

[7] Lida Akhoondzadehasl, " Polarization Behaviour of On-Body Communication Channels at 2.45 GHz," *Ph.D. Dissertation, University of Birmingham, UK*, May 2011.

[8] Mohammad Monirujjaman Khan, "Antenna and Radio Chanel Characterization for Low-Power Personal and Body Area Networks," *Ph.D. Dissertation, Queen Mary, University of London*, Feb. 2012.

[9] Tariq, A.; Ghafouri-Shiraz, H.; , "On-body antenna for vital signs and heart rate variability monitoring," *Antennas and Propagation Conference (LAPC), 2011 Loughborough* , vol., no., pp.1-4, 14-15 Nov. 2011

[10] Gentili, G.B.; Tesi, V.; Linari, M.; Marsili, M.; , "A versatile microwave plethysmograph for the monitoring of physiological parameters," *Biomedical Engineering, IEEE Transactions on* , vol.49, no.10, pp.1204-1210, Oct. 2002

[11] ''Calculation of the dielectric properties of body tissues," *Institute for Applied Physics*, *Italian National Research Council, URL: http://niremf.ifac.cnr.it/tissprop/*.

[12] A.D. Droitcour, "Non-contact measurement of heart and respiration rates with single chip microwave Doppler radar," *Ph.D. Dissertation, Stanford University, USA*, July 2006.

[13] NHLBI Obesity Education Initiative, The Practical Guide: Identification, Evaluation, and Treatment of Overweight and Obesity in Adults, Bethesda, MD: National Institutes of Health, 2000. (NIH publication no. 00-4084)

[14] N. G. Norgan, "Anthromorphic assessment of body fat and fatness," in Anthromorphic Assessment of Nutritional Status, (J. H. Himes, Ed.), New York: Wiley-Liss, 1991.

[15] World Health Organization, 2011, Global Database on Body Mass Index, [online] Available at:< http://apps.who.int/bmi/index.jsp?introPage=intro_3.html> [Accessed 31 October 2011]

[16] J. M. Bland and D. G. Altman, "Measuring agreement in method comparison studies," *Statistical Methods in Medical Research*, vol. 8, pp. 135-160, 1999.

[17] J. M. Bland and D. G. Altman, “Statistical methods for assessing agreement between two methods of clinical measurement,” *Lancet*, vol. 1, no. 8476, pp. 307-310, 1986.

[18] Edwards, A. L. "The Correlation Coefficient." Ch. 4 in *An Introduction to Linear Regression and Correlation.* San Francisco, CA: W. H. Freeman, pp. 33-46, 1976.

[19] Droitcour, A.D.; Boric-Lubecke, O.; Kovacs, G.T.A.; , "Signal-to-Noise Ratio in Doppler Radar System for Heart and Respiratory Rate Measurements," *Microwave Theory and Techniques, IEEE Transactions on* , vol.57, no.10, pp.2498-2507, Oct. 2009

[20] C. Li, Y. Xiao, J. Lin, “Optimal carrier frequency of Non-contact Vital Sign Detectors,” *IEEE Radio and Wireless Symposium*, 2007, pp.281-284, 9-11 Jan 2007.

[21] <http://www.canadatrials.com/AboutClinicalResearch.php, April 26,2008>

[22] U.R. Acharya, P.K. Joseph, N. Kannathal, C.M. Lim and J.S. Suri,” Heart rate variability: a review”. *IFMBE Journal of Medical & Biological Engineering & Computing Journal*, Vol 44 (12) pp. 1031–1051, (2006).

[23] Bilchick KC, Berger RD, “ Heart rate variability,”. *J Cardiovasc Electrophysiol* vol. 17, pp. 691–694, 2006.

[24] H. Stauss, “Heart rate variability,” *Amer. J. Physiol.*, vol. 285, no. 5,pp. R927–R931, 2003. 354–381

[25] M Malik et al. ,” Heart rate variability: Standards of measurement, physiological interpretation, and clinical use,” *in Eur Heart J* Vol. 17(3) pp. 354-381, 1996.

[26] Roche F, Pichot V, Sforza E, Court-Fortune I, Duverney D, Costes F, Garet M, Barthe´ le´my J-C ,”Predicting sleep apnoea syndrome from heart period: a time-frequency wavelet analysis.” *Eur Respir J* 22:937–942, 2003.

[27] Wheeler T, Watkins PJ ,”Cardiac denervation in diabetes”. *Br Med J* 4:584–586, 1973.

[28] Tsai AC, Chiu HW, “Relationship between heart rate variability and electrolyte concentration in chronic renal failure patients under hemodialysis”. *Int J Bioelectromagn* 4(2):307–308, 2002.

[29] Carney RM, Blumenthal JA, Stein PK, Watkins L, Catellier D, Berkman LF, Czajkowski SM, O’Connor C, Stone PH, Freedland KE ,”Depression, heart rate variability, and acute myocardial infarction”. *Circulation* 104:2024, 2001.

[30] Davy KP, Desouza CA, Jones PP, Seals DR ,”Elevated heart rate variability in physically active young and older adult women”. *Clin Sci* 94:579-584, 1998.

[31] Hayano J, Yamada M, Sakakibara Y et al,”short, longterm effects of cigarette smoking on heart rate variability”. *Am J Cardiol* 65:84-88, 1990.

[32] Bekheit S, Tangella M, el-Sakr A, Rasheed Q, Craelius W, el-Sherif N,”Use of heart rate spectral analysis to study the effects of calcium channel blockers on sympathetic activity after myocardial infarction”. *Am Heart J* 119:79-85,1990.

[33] Malpas SC, Whiteside EA, Maling TJ ,” Heart rate variability and cardiac autonomic function in men with chronic alcohol dependence”. *Br Heart J* 65:84-88, 1991.

[34] Togo F, Yamamoto Y ,”Decreased fractal component of human heart rate variability during non-REM sleep”. *Am J Physiol Heart Circ Physiol* 280:H17-H21, 2000.

[35] Malik M. Time-Domain measurement of heart rate variability. *Card Electrophysiol Rev.*1997;1:329-34.

[36] Massagram, W.; Lubecke, V.M.; Host-Madsen, A.; Boric-Lubecke, O.; , "Assessment of Heart Rate Variability and Respiratory Sinus Arrhythmia via Doppler Radar," *Microwave Theory and Techniques, IEEE Transactions on* , vol.57, no.10, pp.2542-2549, Oct. 2009

[37] G. Y. Chen, C. D. Kuo, M. J. Yang, H. M. Lo, and Y. S. Tsai, “Comparison of supine and upright positions on autonomic nervous activity in late pregnancy: The role of aortocaval compression,” *Anaesthesia*, vol. 54, no. 3, pp. 215–219, Mar. 1999.

[38] Malliani *et al.*, “Individual recognition by heart rate variability of two different autonomic profiles related to posture,” *Circulation*, vol. 96, no. 12, pp. 4143–4145, Dec. 1997.

5 Chapter 5

Frequency Reconfigurable Monopole Antennas

Abstract— A novel Coplanar Waveguide (CPW) bandpass filter using short circuit slotlines and varactor diodes is introduced. This bandpass filter when integrated with a CPW wideband antenna produces frequency agility with a wideband mode and a continuous narrowband mode. The design of another CPW filter based on a square ring resonator with switches is also shown and applied to a wideband antenna making it reconfigurable. Both filters are based on controlling two stop bands far enough apart so that there is a pass band between them. When the stop band frequencies are altered using switches or varactors, the pass band is altered. Complete working and design principles along with simulated S-parameter results of the filters are presented. The simulated and measured reflection coefficients of the antennas incorporating the filters are also shown. Good monopole like radiation characteristics are observed for both antennas. The filters are small in size and can be incorporated in any CPW antenna design to make it reconfigurable. The benefits of the novel varactor filter antenna over the switch filter antenna are also described. A novel antenna having stop-band, narrow-band and wide-band modes is also proposed. This antenna is then designed and its various characteristics (reflection coefficient, radiation pattern etc.) are measured and compared with simulated results.

5.1 Introduction

THERE has been rapid progress in wireless communication technologies during recent years. Communication devices nowadays can operate with different standards and their associated frequencies (GSM, UMTS, WiFi, PCS, Bluetooth e.g.). This has led to an increased interest in the efficient use of electromagnetic spectrum and the development of frequency agile antennas. Conventionally the problem of frequency reconfigurability was solved by switching between elements [1]. This method has the disadvantages of increased size, complexity and undesirable coupling between elements. Thus frequency agile antennas need to be designed which incorporate filters or slots within the antenna structure to obtain agility so that the aforementioned disadvantages can be overcome.

Frequency agile antennas which can scan the spectrum in a wideband mode and choose an available narrowband mode also provide the best solution for software defined and cognitive radios [2]-[3].

Frequency reconfigurable antennas can be also be utilized for vital signs monitoring. If the vital signs can't be monitored at a particular frequency, the antenna can be tuned to a frequency that is more sensitive to chest movements. Also in a frequency agile antenna some frequencies can be used for communication purposes while others for vital signs monitoring purposes eliminating the need for separate antennas.

Considering the advantages and uses of frequency reconfigurable antennas, significant research has been reported on it [1]-[9]. Reference [4] gave a comprehensive review of various methods used to achieve frequency agility using patch, wire, planar inverted F antennas etc. They also provided a study of the pros and cons associated with existing solutions for wireless mobile platforms. Compact slot antenna reconfigurability was achieved using switches in [5] and varactors in [6] providing good tuning ranges along with maintaining similar radiation characteristics at all frequencies. A very wide tuning ratio of 3.52:1 was achieved in a slot antenna using only a PIN diode and a varactor diode while maintaining consistent radiation pattern throughout the tuning range [1]. Vivaldi antenna reconfigurability was achieved in [7-8] providing three narrowband (low, mid, high) and a wideband operation. Dynamic control of band rejection along with a wideband state was achieved in [9] using pin diodes. A conceptual model for the design was also introduced.

The components usually used to achieve reconfigurability are switches and varicap diodes and will be utilized by the authors. Switches can either be PIN diodes or Micro-electromechanical systems (MEMS). MEMS have the advantage of low power consumption, because the application of voltage can turn the switch on or off without any current flow but

the actuation voltage required is quiet high. Switches obtain agility (pattern, polarization, frequency) by physically changing the connectivity or length of certain elements (resonators, filters, stubs) within an antenna. Varicap diodes provide reconfigurability by capacitively loading antennas or by changing electrically the length of antennas or filters.

In this chapter two methods of introducing frequency agility to wideband monopole antennas are presented, one employing pin diodes and the other using varactors. Both methods use the same principle of combining a wideband antenna with a frequency reconfigurable band-pass filter. This filter is incorporated into the structure of the antenna. The pass band of the first filter is controlled by actually changing the length of two $\lambda_g/4$ slots by placing switches along the length of the slots. The two $\lambda_g/4$ slots produce two stop-bands with a pass-band resulting in between them. Thus changing the length, changes the stop-band frequencies causing a change in the pass-band frequency. For the 2nd design, a novel filter with a short circuit slot and varactor is introduced. Two stop-bands are produced in the short circuit slot by a fundamental $\lambda_g/4$ resonator and its first harmonic at $3\lambda_g/4$. Variation of the stop-bands is achieved by introducing the varactor at a suitable point along the resonator that affects both the fundamental and harmonic resonance. Due to variation of stop-bands the pass-band between them is varied as well. This design using varactors instead of switches provides the added advantages of low power consumption, smaller area, simpler feed network, fewer lumped elements, low cost and a continuous pass band range rather than a discrete one. This chapter will also include the design of a novel CPW monopole antenna with notch, narrow and wide-band modes. Its design is based on the integration of a square ring filter with a wideband CPW monopole antenna.

Section 5.2 describes the filter design procedure and validates the working principle. Section 5.3 presents the simulated and measured results of the fabricated antennas using the filters

described in section 5.2. Then section 5.4 contains the design and analysis of a novel antenna with stop-band, narrow-band and wide-band modes. At the end there are conclusions in Section 5.5.

5.2 Antenna Filter Design

This section will contain the design of two narrowband filters which will be integrated with a wideband antenna to form the frequency agile antenna.

5.2.1 Switched Filter Design

The design in this section is modified from the unequal resonator filter design of [10]. The filter in [10] was used to switch between single, double and 2 triple passbands. The proposed filter using switches in this paper is designed to achieve reconfigurability of a single passband by placing switches along the rings. This filter when integrated with a wideband antenna results in a frequency agile system with a wideband operation when the filter is disconnected by placing switches in the on state at the entrance of the square rings and narrowband operations when different diode switch combinations along the square ring are biased On/Off. The basic structure for the filter was a CPW with a square ring resonator as shown in Fig. 5.1. One permanent copper strip is present to avoid the use of an RF choke inductor in the square ring resonator because of its effect on the S-parameter response at the frequencies used. This permanent copper strip divides the square ring into two unequal $\lambda_g/4$ stop-band resonators. Along the larger $\lambda_g/4$ resonator three RF diode switches are placed which change the length of this $\lambda_g/4$ resonator resulting in shifting of the stop band frequency at which it resonates. Although the shorter $\lambda_g/4$ resonator's length remains constant, its resonant frequency varies very slightly. When the signal at point X in Fig. 5.1 enters the square ring resonator it sees

two unequal $\lambda_g/4$ resonators. These resonators produce two transmission zeroes resulting in two stop bands. By controlling the length of these resonators the stop-band positions can be controlled and hence the pass-band can be controlled resulting in a frequency agile pass band filter. This will first be demonstrated in simulation using CST. In the initial study switches were modeled as 0.3 mm wide copper wires to demonstrate the design principle so that the effect of non ideal nature of diode is not taken into account. In the antenna design stage actual diode parameters provided by the relevant manufacturers will be used in simulations.

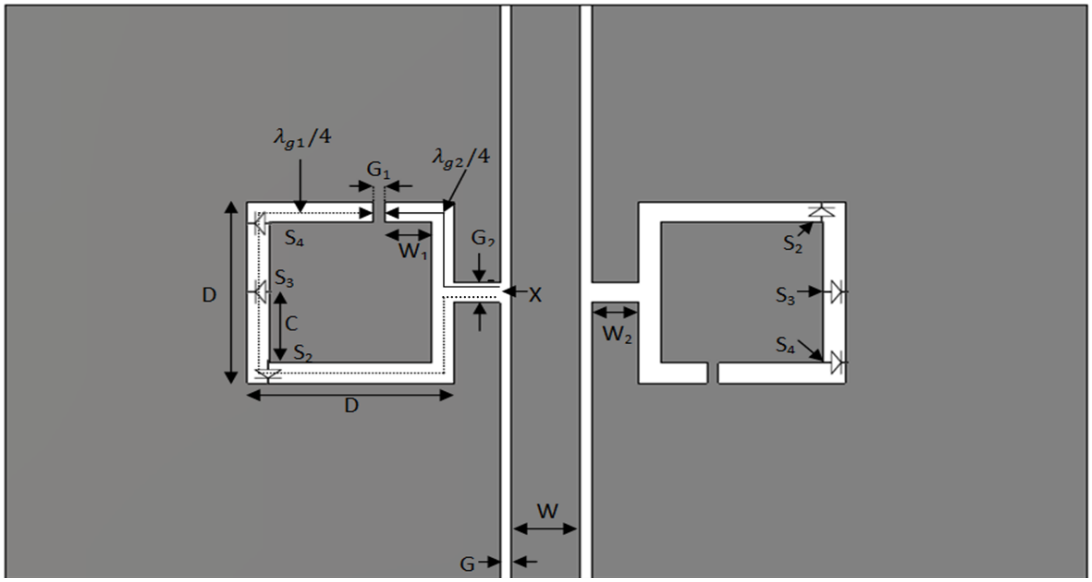

Figure 5.1: Topology of CPW switched Filter. G_1= 0.5 mm, G_2=1 mm, D=8 mm, W_1=2 mm, W_2=2 mm, C=3.35 mm, G=0.5 mm, W=3 mm.

In Fig. 5.1 when switch combination S_3 is on the effective length of the larger and smaller $\lambda_g/4$ resonators are 18.35 mm and 9 mm which correspond to frequencies of 3.32 GHz and 6.58 GHz respectively, calculated using TXLINE from AWR. The simulated S-parameter results of this combination of $\lambda_g/4$ resonators filter is shown in Fig. 5.2. Two stop bands at 3.56 GHz and 6.698 GHz can clearly be observed with a pass band at 5.432 GHz in between them. This agrees well with the calculated values obtained from TXLINE. Fig. 5.3(a) and 5.3(b) show the electric field distribution at 3.56 GHz and 6.698 GHz respectively. It can be

clearly seen that slot lengths of 18.35mm and 9mm are resonating at 3.56 GHz and 6.698 GHz respectively.

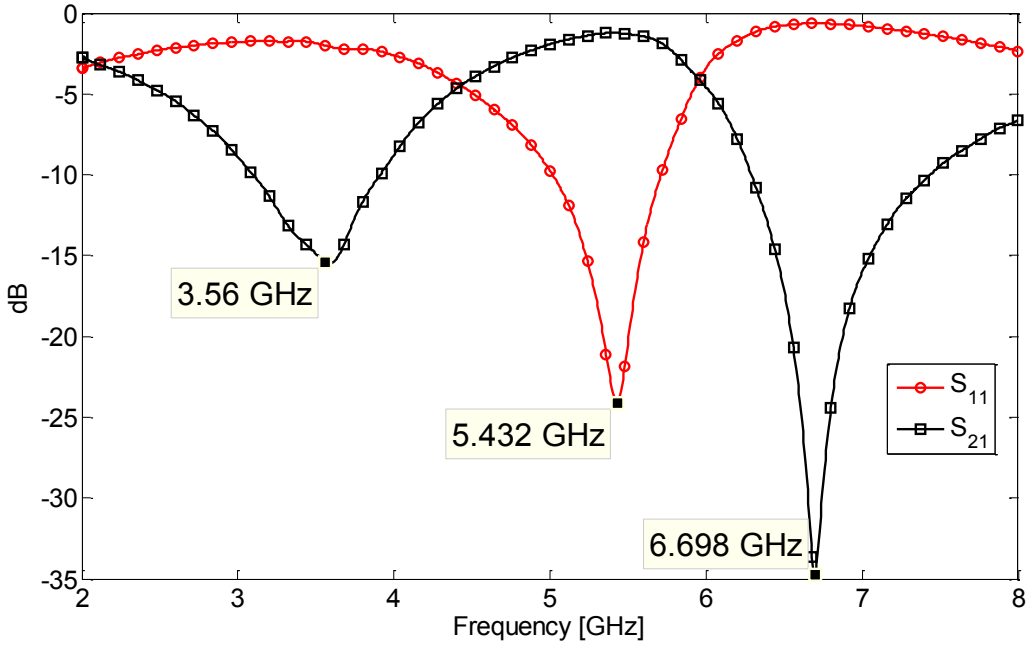

Figure 5.2: S-Parameter simulation results of CPW switched filter shown in Fig. 5.1 with S_3 on resulting in $\lambda_g/4$ resonators of length 18.35 mm and 9 mm.

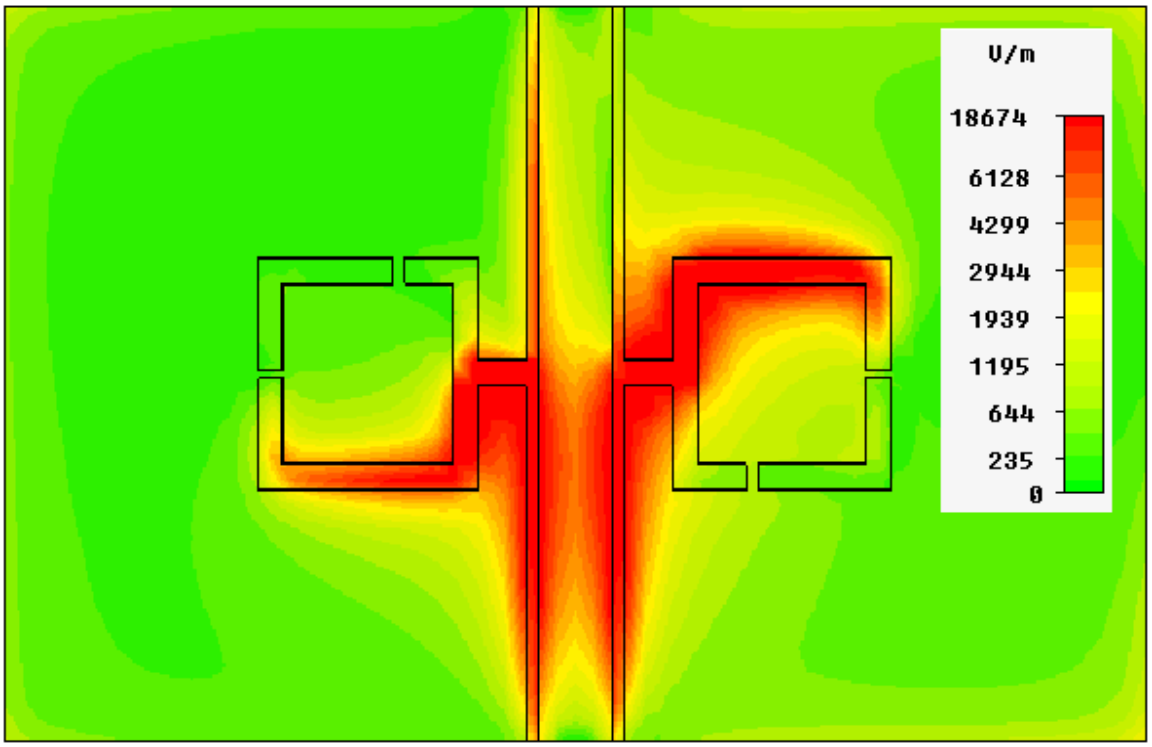

(a)

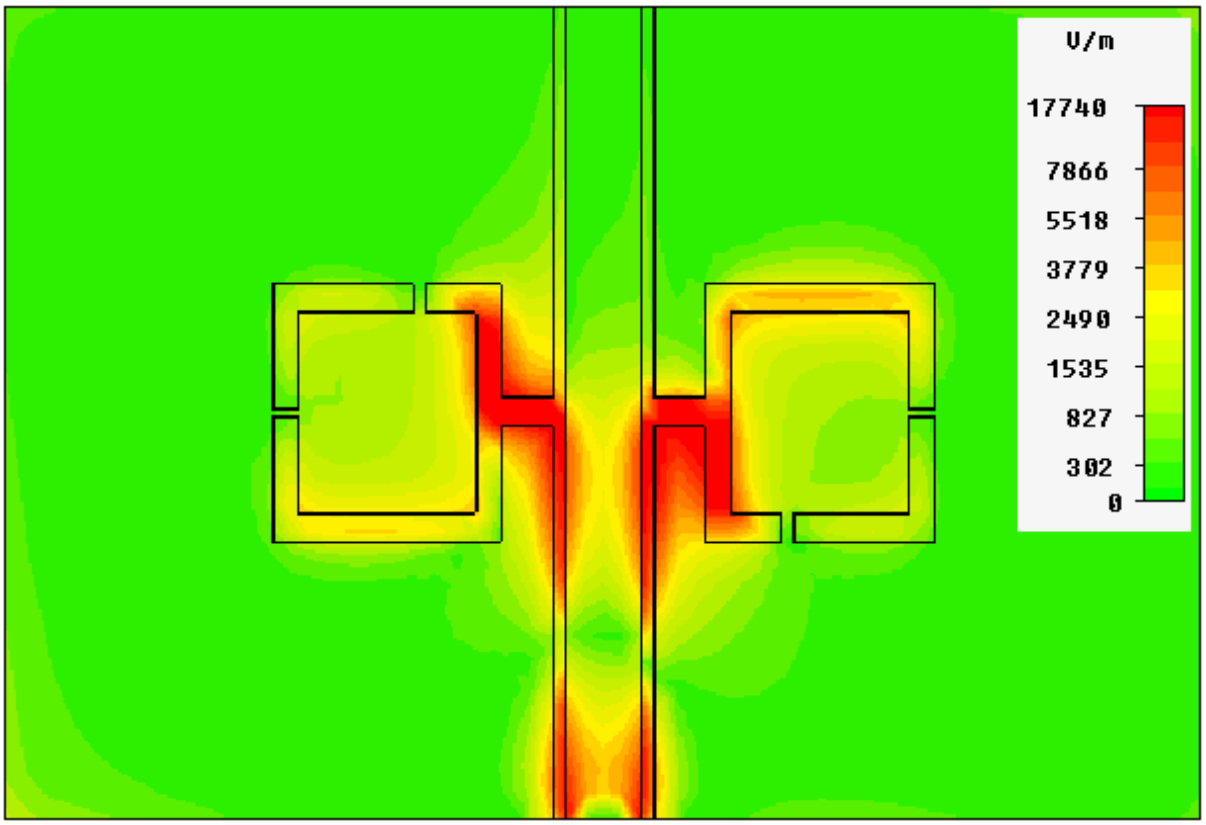

(b)

Figure 5.3: Electric Field Distribution at (a) 3.56 GHz and (b) 6.698 GHz clearly showing larger and smaller $\lambda_g/4$ resonators.

For the other switch combinations in Fig. 5.1, the simulation of the stop band and pass band frequencies are shown in Fig. 5.4(a) and 5.4(b) respectively. The lower stop band frequency moves considerably as different switch combinations are used and the higher stop band frequency remains almost constant. This higher stop band frequency can be moved as well if more switches are placed in the path of the smaller 9 mm $\lambda_g/4$ resonator. However, in this design, obtaining the most number of pass bands with the least number of switches was desired. A tuning ratio of 1.7 (3.63 GHz to 6.18 GHz) is achieved with this filter.

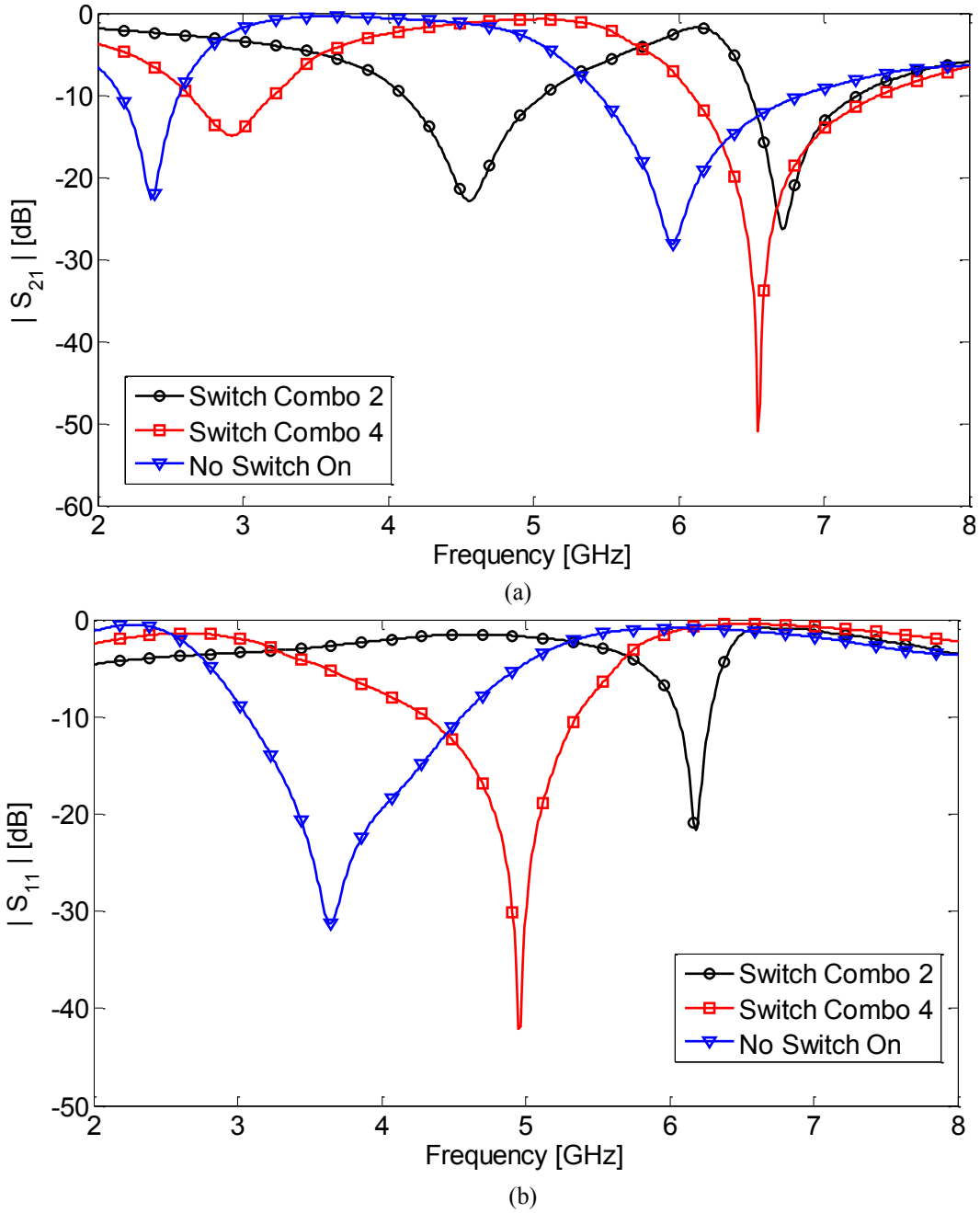

Figure 5.4: Simulation results of (a) S_{21} and (b) S_{11} of the filter shown in Fig. 5.1 for different switch combinations. Resonant frequencies of 3.63 GHz, 4.95 GHz and 6.18 GHz are achieved in (b).

5.2.2 Varactor Filter

This section will introduce a novel filter with a continuous frequency tuning range. It employs varactor diodes as the tuning element. The basic idea is a slot which resonates at $\lambda_g/4$ and $3\lambda_g/4$ (1st Harmonic) producing two transmission zeroes resulting in two stop bands. Fig.

5.5 shows the varactor filter along with its dimensions. This slot of length 13 mm without any varactors resonates at $\lambda_g/4$ and $3\lambda_g/4$ which corresponds to frequencies of 4.62 GHz and 13.3 GHz respectively, calculated using TXLINE form AWR. The S-parameter simulation of the filter shown in Fig. 5.5 without any varactors is shown in Fig. 5.6. The values calculated using TXLINE and simulated using CST agree quite well.

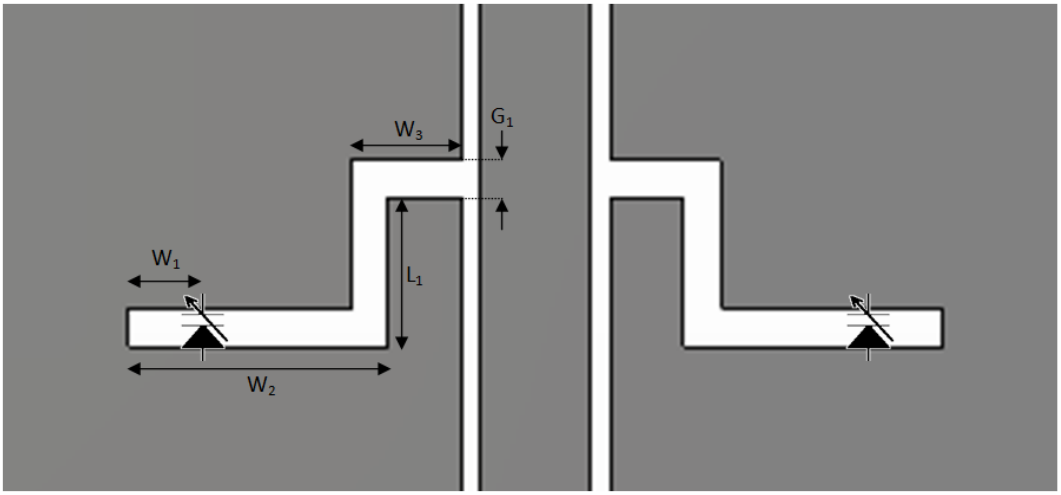

Figure 5.5: Topology of CPW varactor Filter, the dimensions are W_1=2.1 mm, W_2=7 mm, W_3=3 mm, L_1=4 mm, G_1=1 mm. CPW dimensions same as Fig. 5.1.

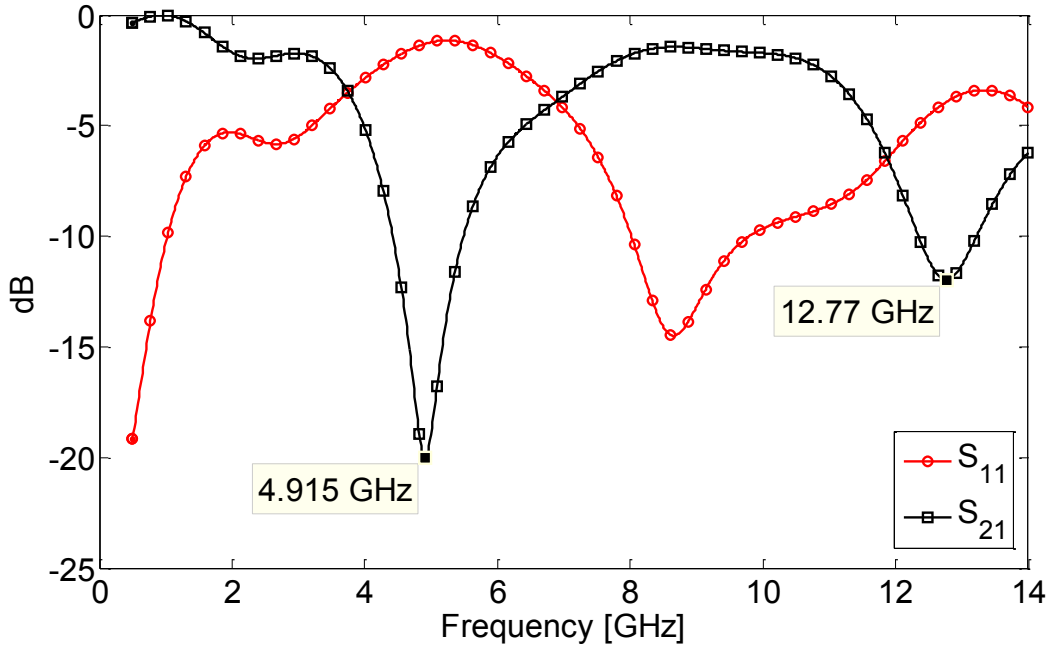

Figure 5.6: Simulation results of S-parameters of CPW filter shown in Fig. 5.5 without using varactor diode.

Fig. 5.7 shows the normalized voltage wave of the $\lambda_g/4$ resonator shorted at one end and open ended at the other. The first harmonic at $3\lambda_g/4$ is also shown. Point S and O represent the short and open circuit points respectively. Point B represents the null point of the first harmonic and point A represents the position at which the varactor will be placed in our filter design. The varactor was modeled in CST MWS as a capacitor with a forward resistance of 2.5 Ω which was the forward resistance of the varactor diode obtained from manufacturer's data sheet.

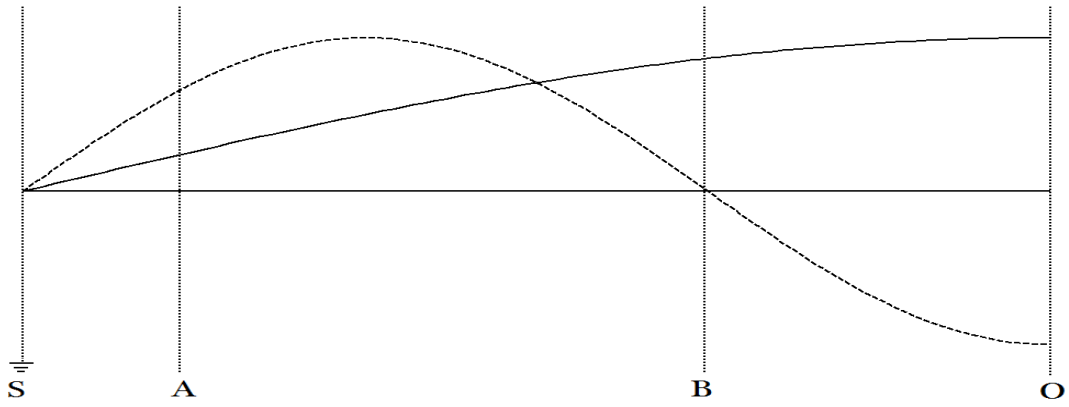

Figure 5.7: Normalized voltage wave in the short circuit slotline at the fundamental frequency and 1st Harmonic.

In order to verify the working of the filter a varactor was placed at point B. The resulting simulation is shown in Fig. 5.8. It can be clearly observed as expected that the $3\lambda_g/4$ resonators resonance does not change from a value of 12.7 GHz as the varactor is placed at its null point but the resonance of the $\lambda_g/4$ resonator changes.

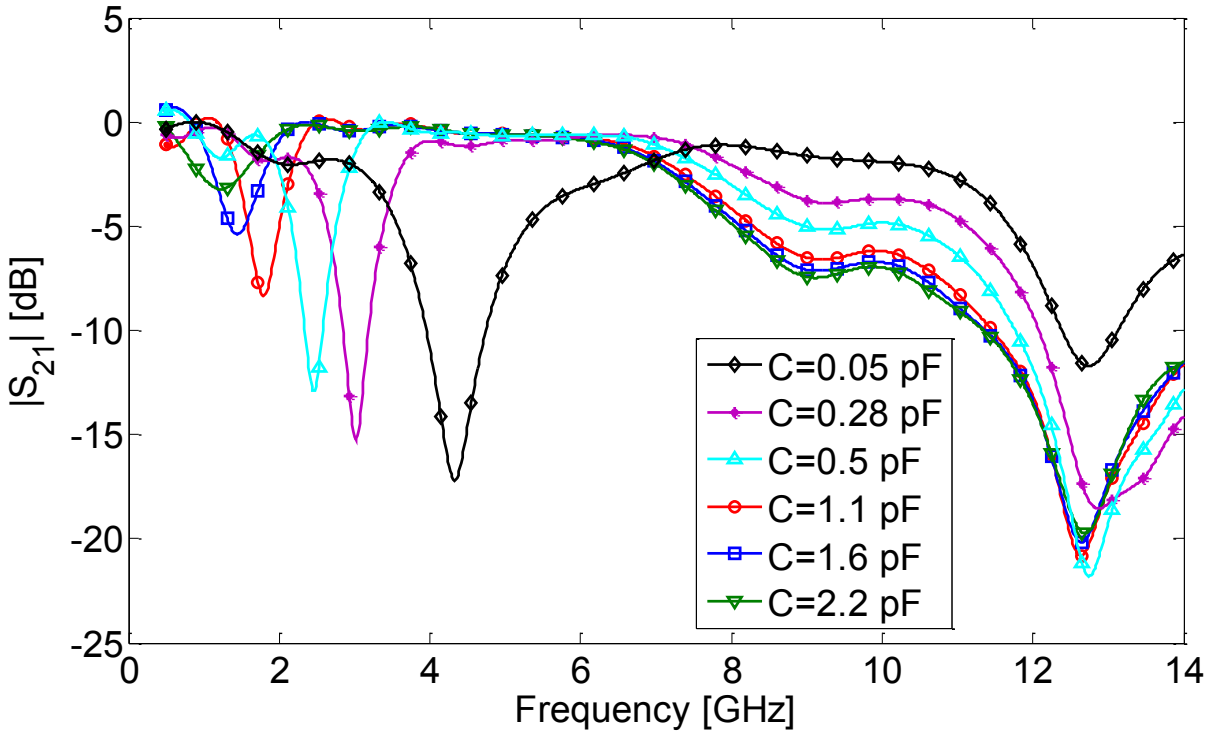

Figure 5.8: Simulation results of reflection coefficient of short circuit slotline with varactor at position B (Null point of 1st Harmonic, see Fig.5.7) for different values of capacitors.

When the varactor position is optimized and it is placed at point A it can affect both the fundamental and 1st harmonic resonators resulting in S-parameters shown in Fig.5.9 and 5.10. Thus a continuous pass band from 2.57 GHz to 5.54 GHz is obtained giving a tuning range of 2.16. This design has several advantages over the switched filter design and the filter in [10] including simpler structure, fewer lumped elements, low cost, low power consumption, continuous pass band and smaller size.

Varactors are non-linear devices. DC voltages are used to control their capacitance but they are also affected by induced RF voltages across them. These induced voltages can generate high-order harmonic currents leading to harmonic radiation [11]. Varactors are more non-linear at lower bias voltages and higher input power levels at a given voltage [12]. An analysis

of harmonic radiated power and solutions to improve varactor non-linearity problems can be found in [11-12]

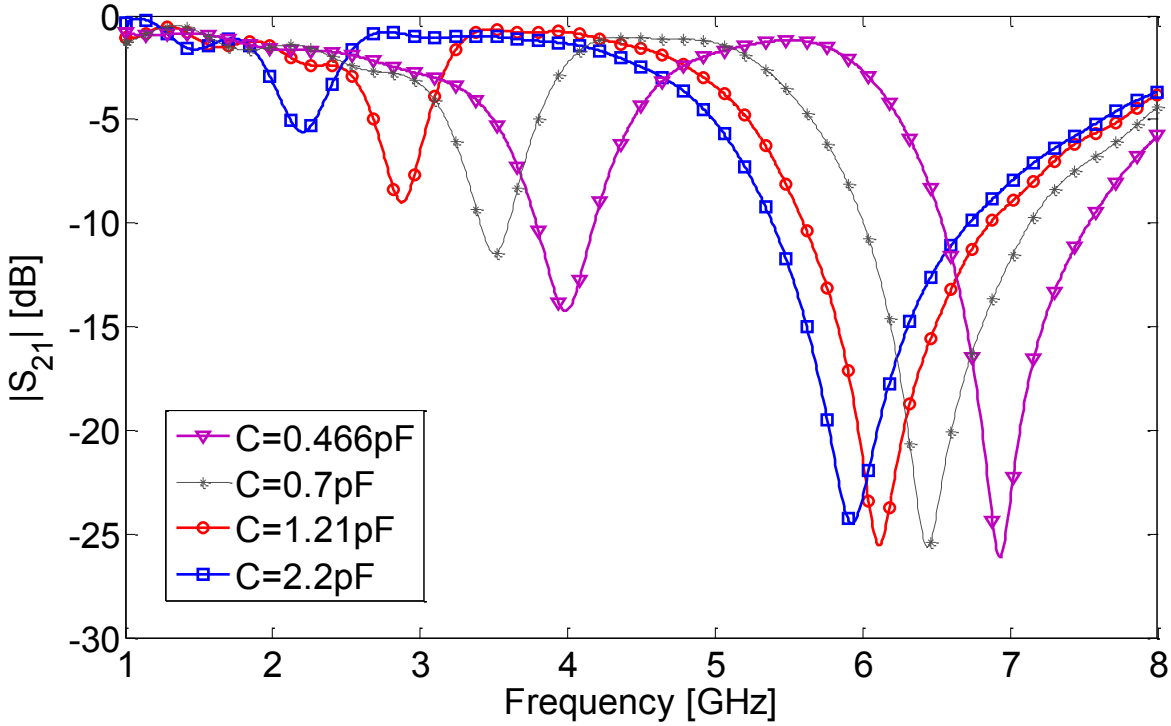

Figure 5.9: Simulation results of S_{21} for the short circuit slotline with varactor at position A(see Fig.5.7) for different values of capacitors.

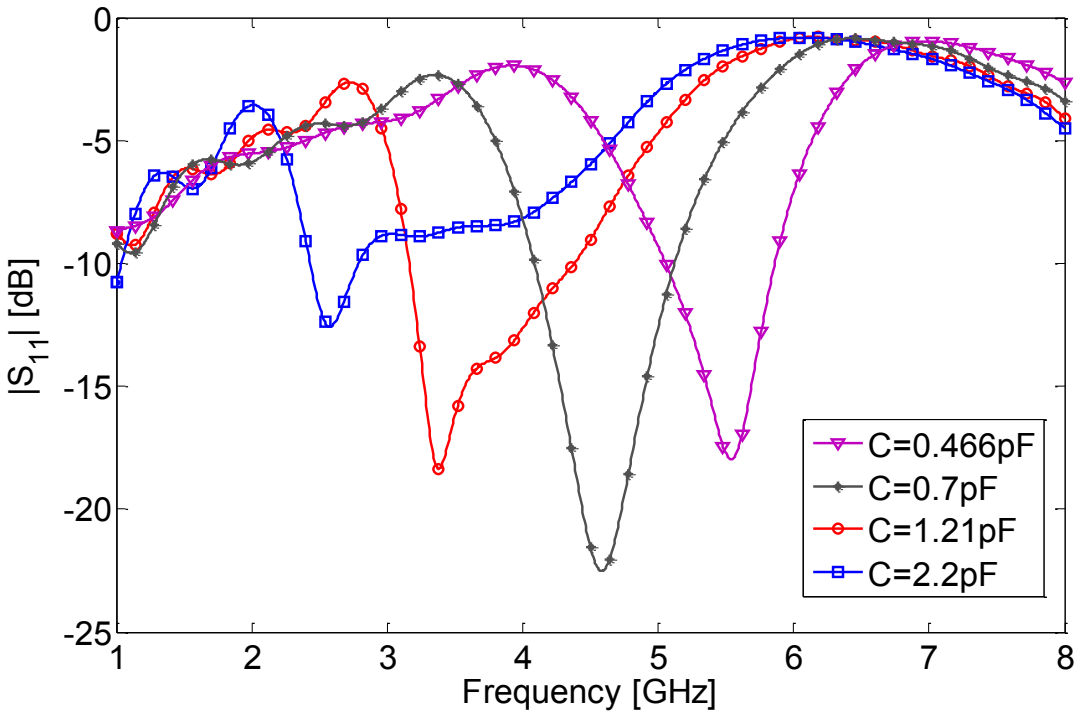

Figure 5.10: Simulation results of reflection coefficient of short circuit slotline with varactor at position A(see Fig.5.7) for different values of capacitors. Resonant frequencies vary from 2.57 GHz to 5.54 GHz.

5.3 Antenna Design

The two filters described in the previous section when combined with any wideband CPW antenna provide frequency reconfigurable operation along with a wideband operation when the entrance to the square resonator or short circuit slot is blocked.

5.3.1 Wideband Antenna

The CPW antenna chosen here to demonstrate the working of the two filters is an elliptical monopole antenna which is shown in Fig. 4.4 along with its dimensions. The antenna was fabricated on a TLC-30 substrate with ε_r=3 and a thickness of 1.56718mm. The S-parameter measured and simulated results are shown in Fig.11 and both show general agreement with each other. The reflection coefficient becomes below -10 dB at 2 GHz for simulation results and at 2.7 GHz for measurement results. This difference can be attributed to fabrication errors.

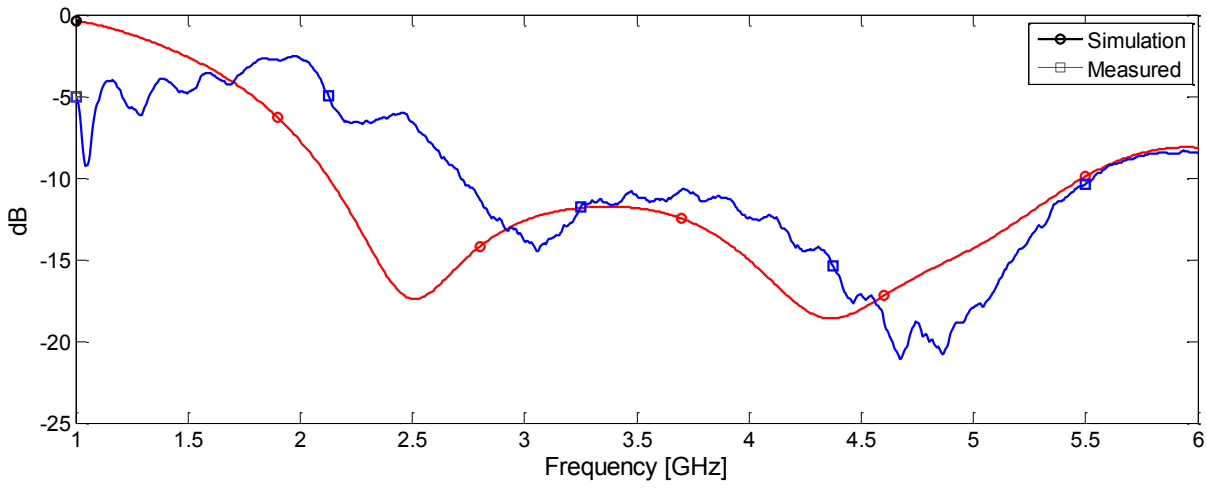

Figure 5.11: Measured and simulated results of the reflection coefficient for antenna shown in Fig. 4.4.

5.3.2 Switched Monopole Antenna

The switched monopole antenna will combine the switched filter from section 5.2.1 and the wideband monopole antenna introduced in the previous section 5.3.1. The diodes used as switches are BAR50-02V from Infineon. They were chosen because of their wide frequency range (10 MHz to 6 GHz), low capacitance 0.15 pF at zero bias voltage above frequencies of 1 GHz and low forward resistance. Accu-P-0603-22pf-25V capacitors from AVX were used as DC blockers and 0604HQ-2N6XJLB inductors from coilcraft served as RF chokes. Fig. 5.12 shows the antenna along with the biasing circuit. The total size of the antenna is 51 mm x 71 mm including the biasing circuit.

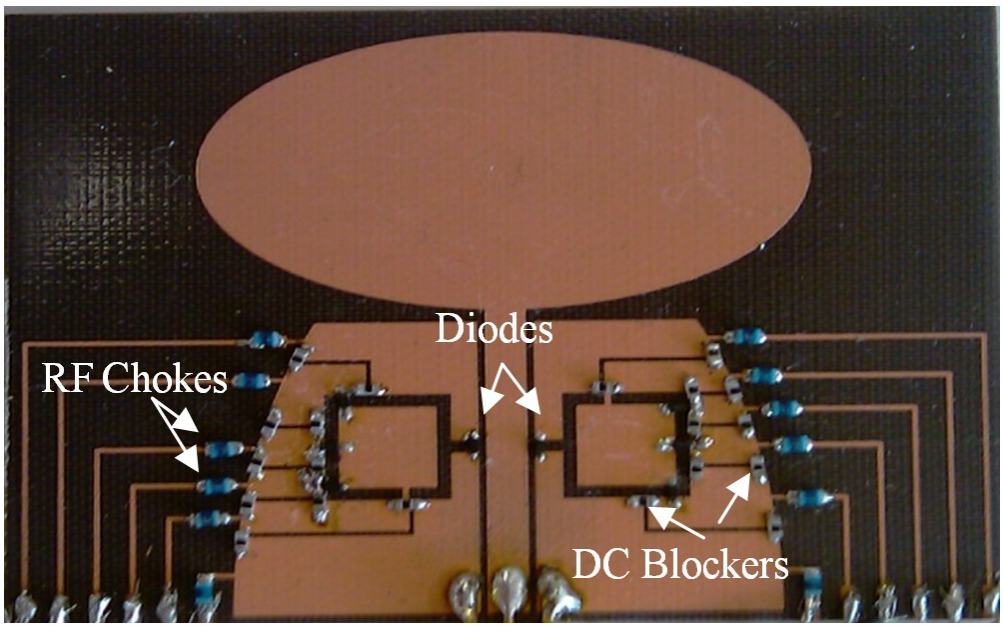

Figure 5.12: Switched monopole antenna along with biasing circuit, the lumped element connecting with the bias lines are the RF chokes (inductors), the lumped elements connecting cut portions of copper are DC blockers (capacitors), the rest are diode switches.

This switched monopole antenna has 5 modes of operation. When the diode switches (switch combination 1) placed at the entrance of the square ring are ON, a wideband is obtained because no current flows into the square slot effectively disconnecting the square ring

resonator resulting in wideband operation. The measured and simulated results for wideband operation are shown in Fig. 5.13.

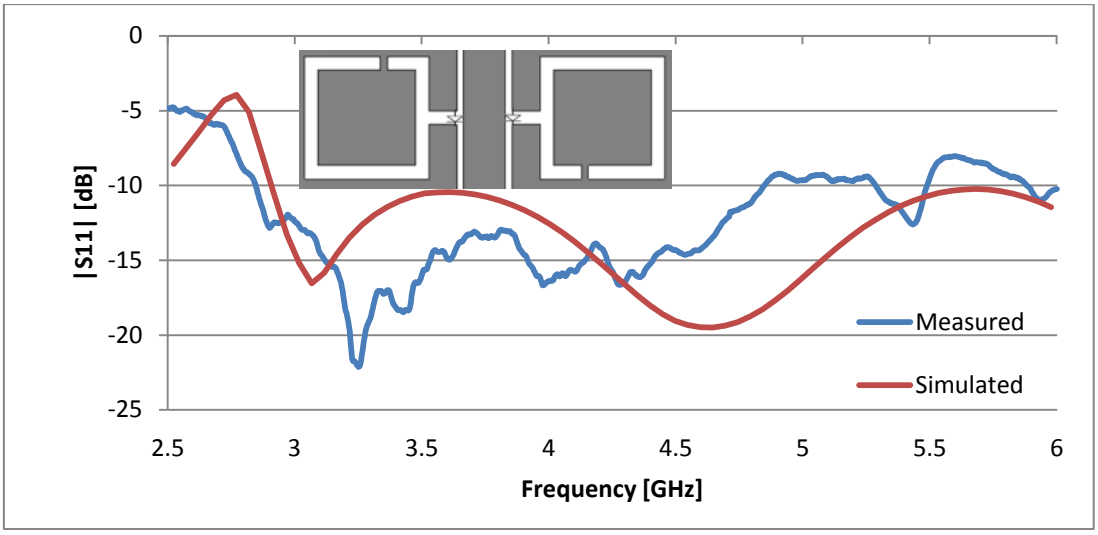

Figure 5.13: Wideband measured and simulated results of reflection coefficient when switch combination 1 is ON.

The other 4 narrowband modes of operation are obtained by switching ON the three switch combinations along the longer $\lambda_g/4$ resonator as described in II-A one at a time or keeping them all OFF. The different switch combinations producing the two $\lambda_g/4$ short circuit slots along with the measured and simulated reflection coefficients are shown in Fig. 5.14.(a)-(d).

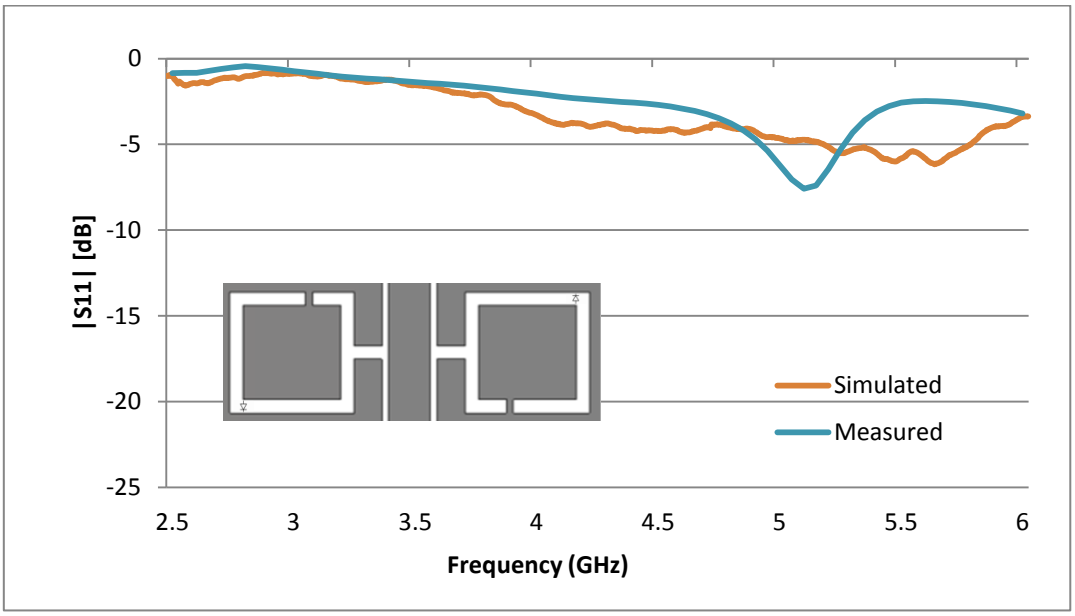

Figure 5.14: (a) Narrowband measured and simulated results of reflection coefficient when switch combination 2 is ON. Measured resonance at 4.45 GHz.

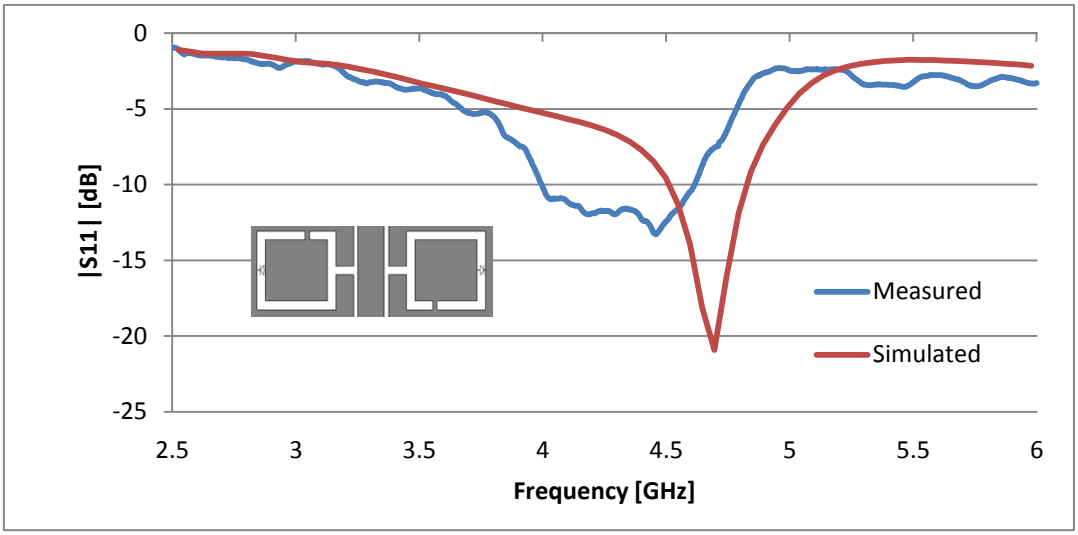

Figure 5.14: (b) Narrowband measured and simulated results of reflection coefficient when switch combination 3 is ON. Measured resonance at 4.45 GHz.

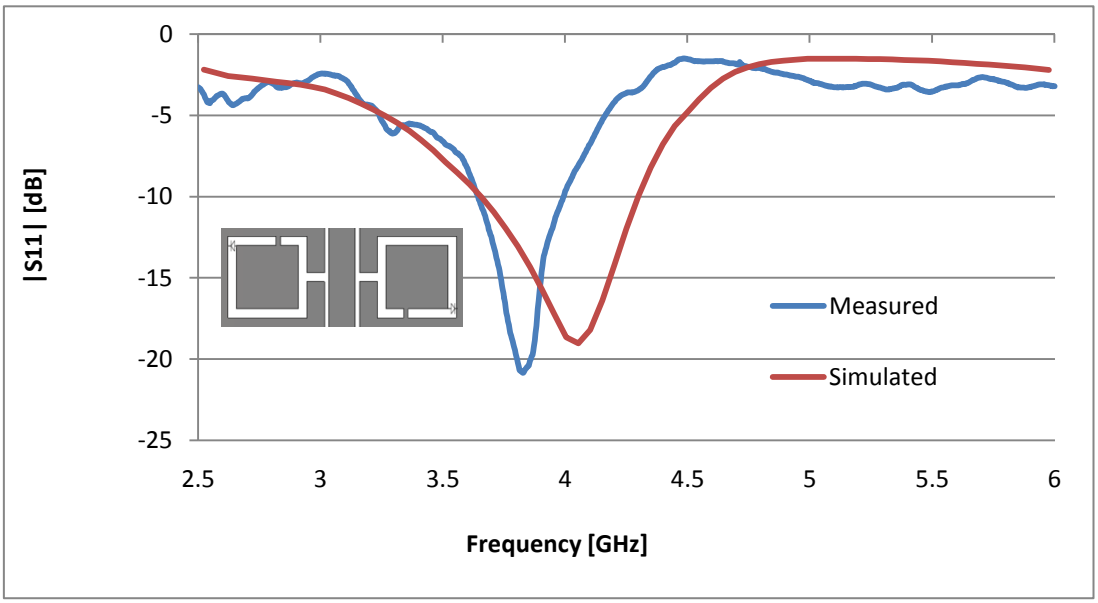

Figure 5.14: (c) Narrowband measured and simulated results of reflection coefficient when switch combination 4 is ON. Measured resonance at 3.8 GHz.

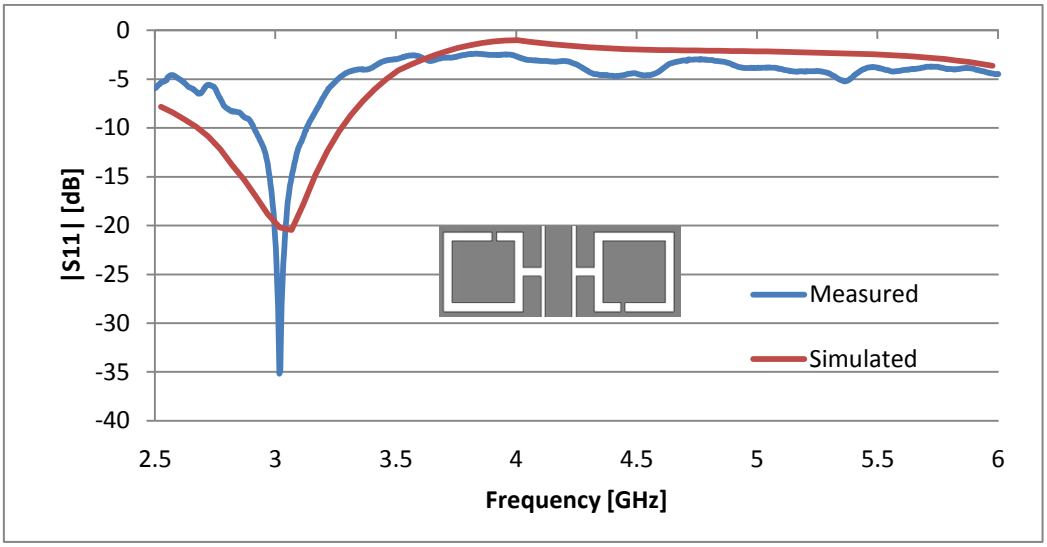

Figure 5.14: (d) Narrowband measured and simulated results of reflection coefficient when no switch is ON. Measured resonance at 3 GHz.

As shown in Fig. 5.4 in section 5.2.1, switch combination 2 produced excellent results when perfect copper strip was used but in the actual design result in Fig. 5.14(a) when the off state capacitance of the diode was taken into account the results were unsatisfactory but some agreement was still observed between the simulated and measured results.

Fig. 5.15 shows the combined measured results for all switch combinations. As can be seen a tuning range from 3 GHz to 4.45 GHz is observed. For simulations actual diode parameters were used for both ON and OFF state of the diode obtained from Infineon. Both simulation and measurements show good agreement with each other. All the errors can be attributed to fabrication problems and the fact that the feed network along with the feeding wires was not included in the simulation. Also the capacitor and inductors used are imperfect and introduce errors of their own.

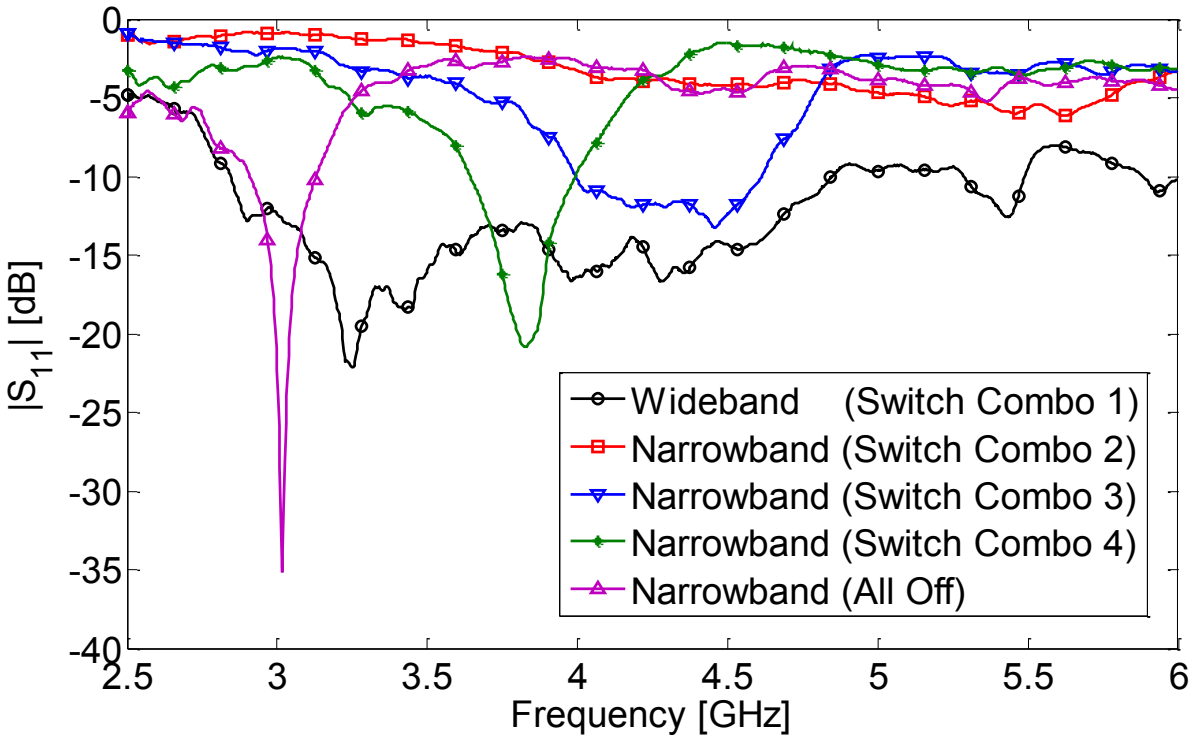

Figure 5.15: The reflection coefficient measured results for all switch combinations.

Fig 5.16 shows the simulated reflection coefficient for switch combination 3 for the following cases:

1) Ideal 0.3mm width copper line is used for ON state and open circuit for OFF state.

2) When actual diode parameters obtained from Infineon are used for ON state and open circuit for OFF state.

3) When actual diode parameters obtained from Infineon are used for both ON state and OFF state.

As can be clearly observed the resonance for case 1 is occurring at 5.35 GHz, for case 2 at 5.05 GHz and for case 3 at 4.75 GHz. The reasons for this change in resonance is that for case 1 both the diode ON and OFF state capacitances are neglected, while for case 2 the diode OFF state capacitance is neglected. In case 3 all capacitances are accounted. An increase in

capacitance in the slot increases the electrical length of the slot which in turn results in lowering of the resonant frequency.

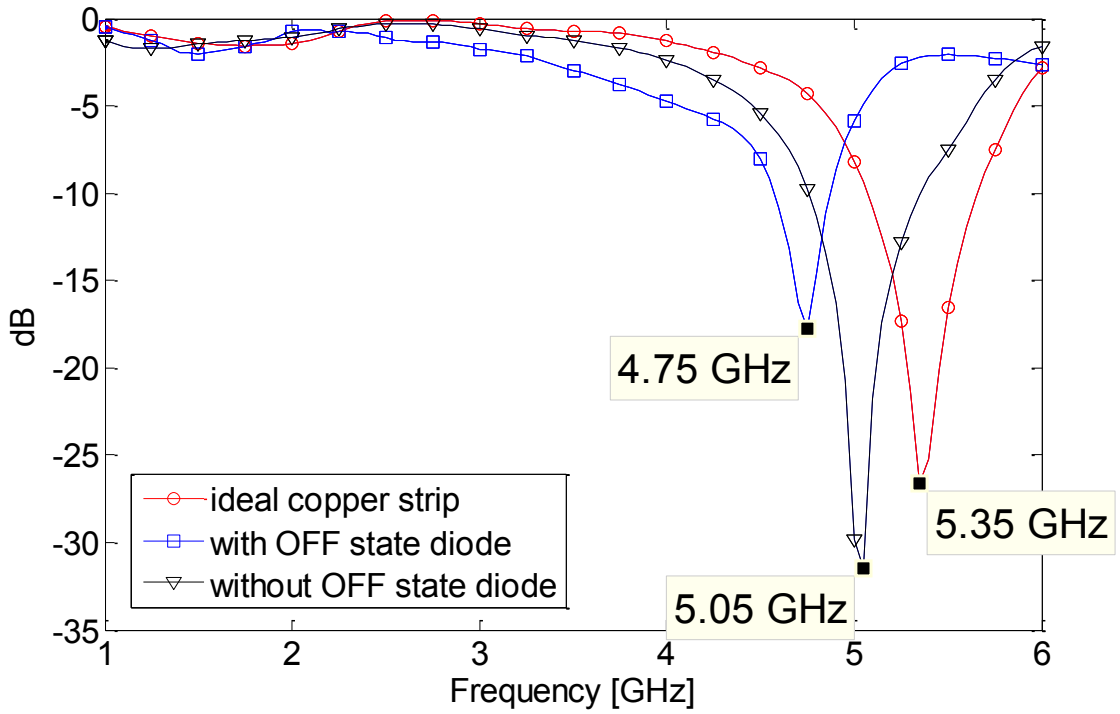

Figure 5.16: Simulation results of reflection coefficients for switch combination 3 when ideal copper strip is used as ON state diode and open circuit for OFF state diode, when actual diode parameters obtained from Infenion are used for ON state diode and open circuit for OFF state diode, when actual diode parameters obtained from Infenion are used for both ON and OFF state diode.

5.3.3 Varactor Antenna

For the varactor tuned antenna the varactor filter design from section 5.2.2 is combined with the wideband monopole antenna from section 5.3.1. The varactor diodes used were SMV1231 from Skyworks which have a tuning range from 2.2 pF to 0.466 pF when the voltage is changed from 0 to 8 volts. It has a forward resistance of 2.5 ohms. Accu-P-0603-22pf-25V capacitors from AVX were used as DC blockers and 0604HQ-2N6XJLB inductors from Coilcraft served as RF chokes. The antenna along with its biasing circuit is shown in Fig. 5.17. The total size of the antenna including the feed structure is 51 mm x 51 mm.

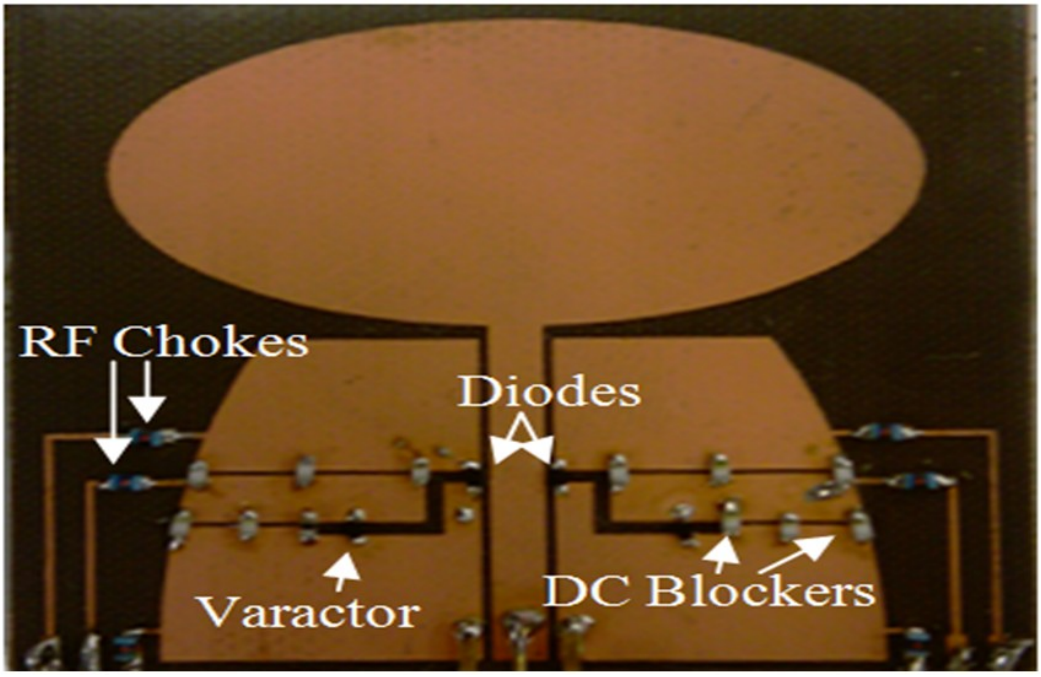

Figure 5.17: Varactor monopole antenna along with biasing circuit, the lumped element connecting with the bias lines are the RF chokes (inductors), the lumped elements connecting cut portions of copper are DC blockers (capacitors), the lumped element at the entrance of the slot are switches and along the slot are varactors.

The varactor monopole antenna has a wide band operation when diodes placed at the entrance of the short circuit slot are turned on. This is because no current flows into the short circuit slot, thus effectively removing it which results in wideband operation. Besides this it has a continuous narrowband mode of operation ranging from 2.88 GHz to 4.62 GHz when the voltage is changed from 0 to 8 volts. Simulations took into account the 2.5 ohm forward resistance of the varactor along with the off state capacitance of the diode. Fig. 5.18 shows the measured and simulated reflection coefficients for the narrowband and wideband operation. Both simulation and measured results show good agreement with one another but the range of the narrowband operation in simulation is higher compared to measured results. The range difference could be accounted to the actual capacitive range of the varactor being smaller compared to the datasheet. All the other differences can be attributed to fabrication errors,

feed network and wires, imperfections of the components (varactor diode, PIN diode RF choke and DC blockers).

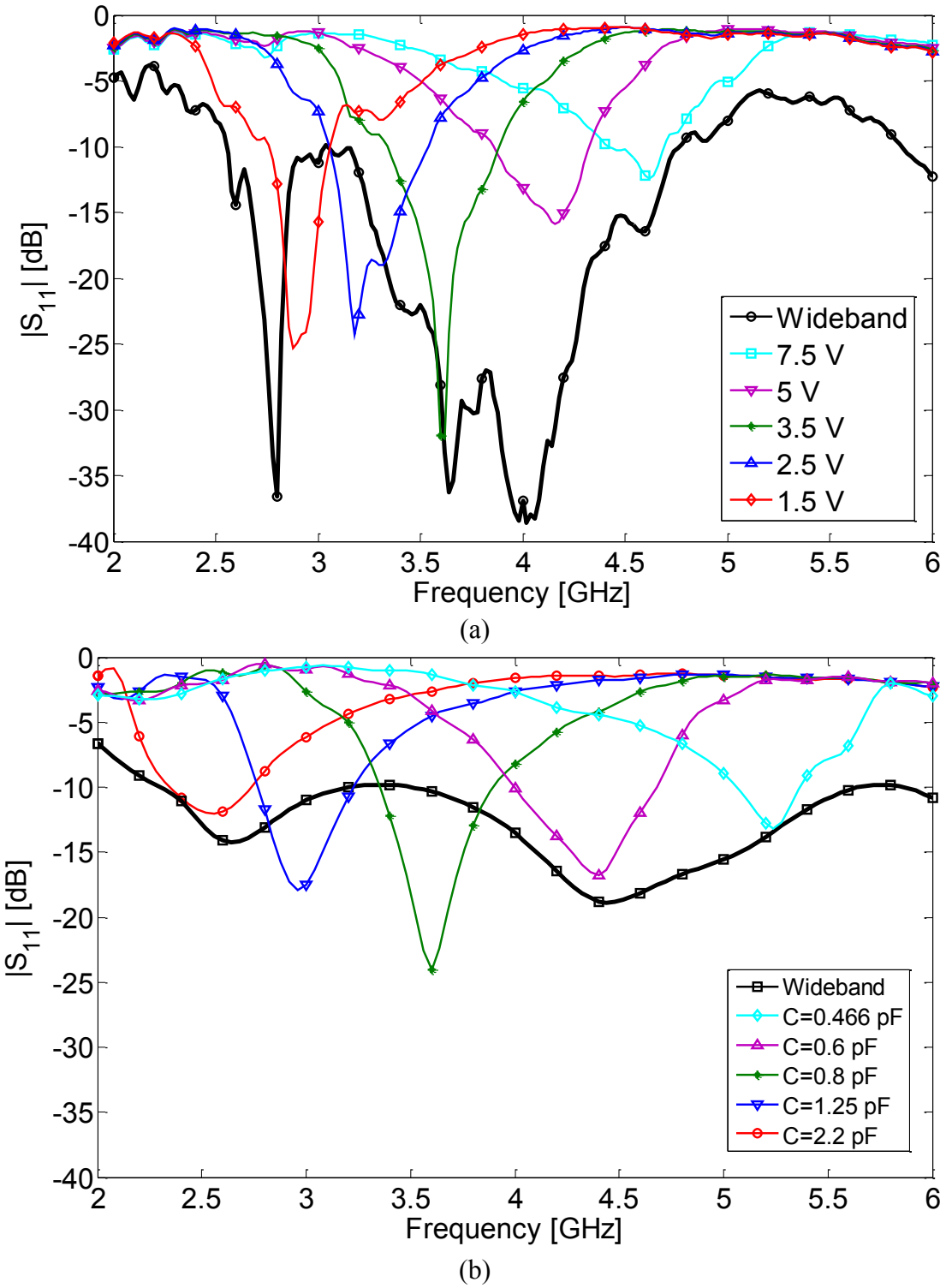

Figure 5.18: (a) Measured, (b) Simulation results of reflection coefficients of varactor monopole showing both wideband and narrowband modes for different capacitor values.

The slots which make the filters are demonstrated on CPW fed antennas, but when these slots are applied to tapered slot antennas such as Vivaldi antennas shown in fig. 5.19, similar results are obtained as shown in figure 5.20 and same principles apply. So this design is applicable to tapered slot antennas as well.

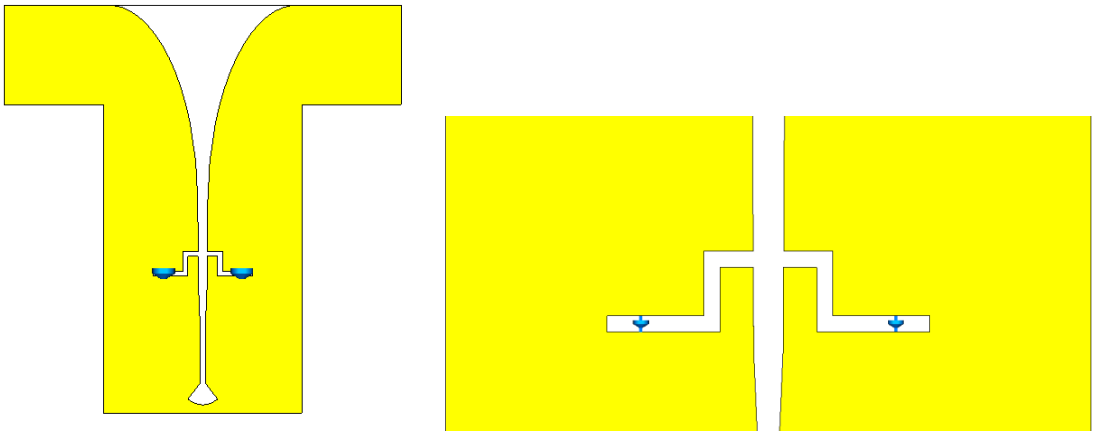

Figure 5.19: Vivaldi tapered slot antenna using varactor filter described in section 5.2.2.

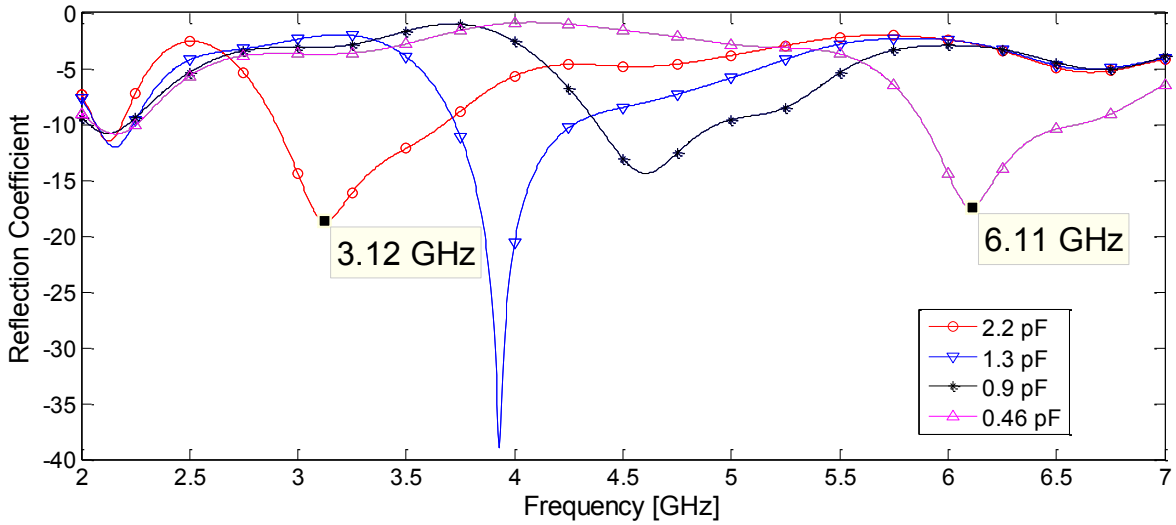

Figure 5.20: Simulated reflection coefficient of tapered slot Vivaldi antenna using varactor filter described in section 5.2.2.

5.4 Radiation Pattern

The radiation pattern of both the switched monopole antenna and the varactor tuned antenna were measured and simulated. In simulations it was found that there was very little difference

between the radiation pattern of the antenna without any square ring resonator or slotline and the antennas with these elements. In order to verify that the slots had negligible effect on the radiation pattern of the antenna, antennas without DC bias structure and actual diodes were fabricated. This involved three cases:

1) Wideband antenna (from section 5.3.1) without any square ring resonator.
2) Wideband antenna with square ring resonator blocked by ideal switches (copper strip)
3) Narrow band mode antenna with square ring not blocked (obtained when no switch or bias network is present in antenna of fig. 5.12)

The radiation pattern of these three cases at 3.6 GHz is shown in Fig. 5.21. The reason 3.6 GHz is chosen is because that is the resonant frequency of the narrow band mode antenna when no bias networks or OFF state diodes are present. The radiation pattern of fig 5.21 shows that there is very little difference between the antennas in the co-polarization mode. This is because the slots are very weakly excited in the narrow band mode (case 3) and the wideband with ring slots blocked mode (case 2). However there is a major increase in cross-polarization because of the ring slots present in case 2 and case 3 as compared to case 1.

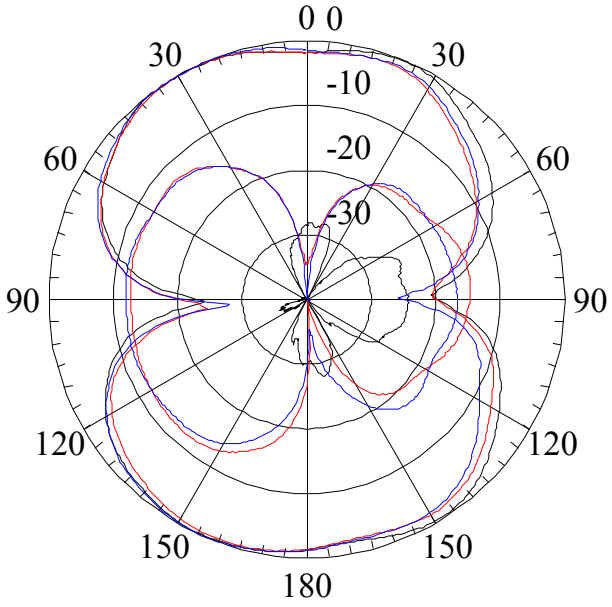

(a)

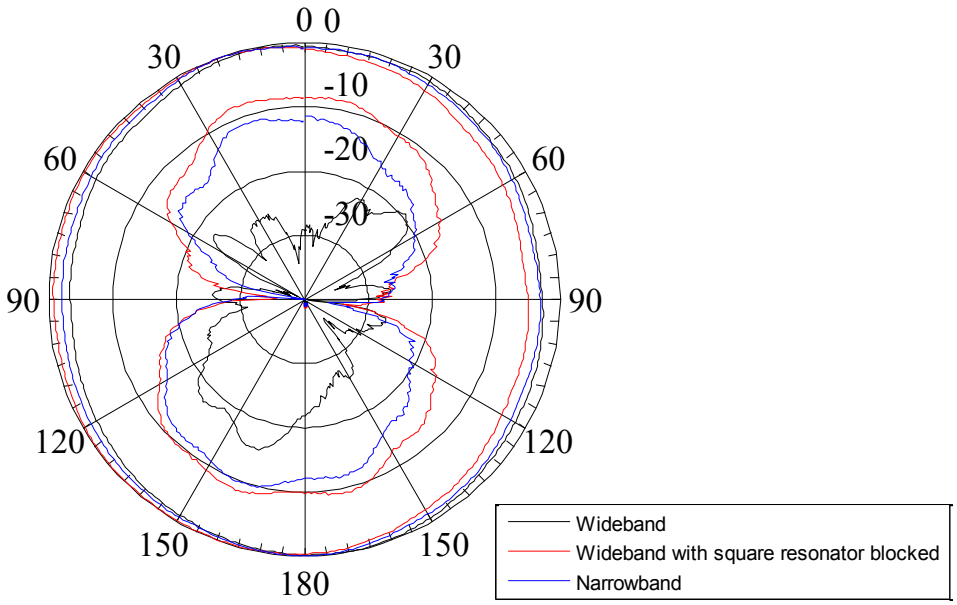

(b)

Figure 5.21: Measured radiation patterns in (a) e-plane and (b) h-plane at 3.6 GHz for wideband antenna with no ring slots, wideband antenna with ring slots blocked and narrow band antenna with ring slots not blocked.

Fig. 5.22 shows the measured and simulated radiation patterns in the E and H plane of the switched monopole antenna with all the biasing networks, wires, diodes (as shown in fig. 5.12) at 3 GHz and 4.45 GHz. Fig. 5.23 shows the measured and simulated radiation patterns in the E and H plane of the varactor tuned monopole antenna with all the biasing networks, wires, diodes, varactors (as shown in fig. 5.17) at 2.88 GHz and 4.62 GHz. There are differences between the simulated and measured results in both the co and cross-polarization patterns which can be accounted to the fact that the DC feed wires and feed network were not used in simulations. The differences in the switched monopole antenna are more pronounced as it has got more DC feeding wires. When an antenna with square ring slot using copper strip instead of PIN diodes, without feeding wires was tested the results obtained were much closer to simulated results, showing the wires are causing the major degradation. This observation is

also made in [9]. The radiation pattern degradation can be improved by using a system containing chips which can all be controlled by a single DC feed line[13] or by using a DS bias network with a coin battery which makes the length of the DC bias lines minimal [14].

The switches and varactors used have an effect on the overall efficiency and gain of the antenna as they introduce losses. When actual switch parameters instead of ideal switch parameters are used the efficiency reduces from 89.13% to 88.72 % at 3.2 GHz and from 96.83 % to 93.97 % at 4.4 GHz for the switch monopole antenna according to simulation results. When gain measurements are done in an anechoic chamber for the antenna with all the RF elements, wires and feed network compared to an antenna with 0.3 mm copper strips as switches, the gain reduces from 0.19 dB to 0.06 dB at 3GHz and from 2.87 dB to 0.04dB at 4.4 GHz respectively. For the varactor antenna the results are better as fewer RF elements, wires and a smaller feed network is used. When actual switch and varactor parameters instead of ideal switch and varactors are used, the efficiency reduces from 92.47 % to 90.57 % at 2.8 GHz and from 96.83 % to 93.76 % at 4.62 GHz for the switch monopole antenna according to simulation results. When gain measurements are done in an anechoic chamber for the varactor tuned antenna with all the RF elements, wires and feed network compared to an antenna with 0.3 mm copper strips as switches and a fixed capacitor the gain reduces from 0.34 dB to 0.21 dB at 2.8 GHz and from 2.58 dB to 1.2 dB at 4.62 GHz. It is observed that there is a greater reduction in gain at higher frequencies compared to lower frequencies for both types of antennas. This can be attributed to the fact that at higher frequencies the insertion loss of the RF components used is higher. This is also confirmed from the component datasheets provided by the manufacturers.

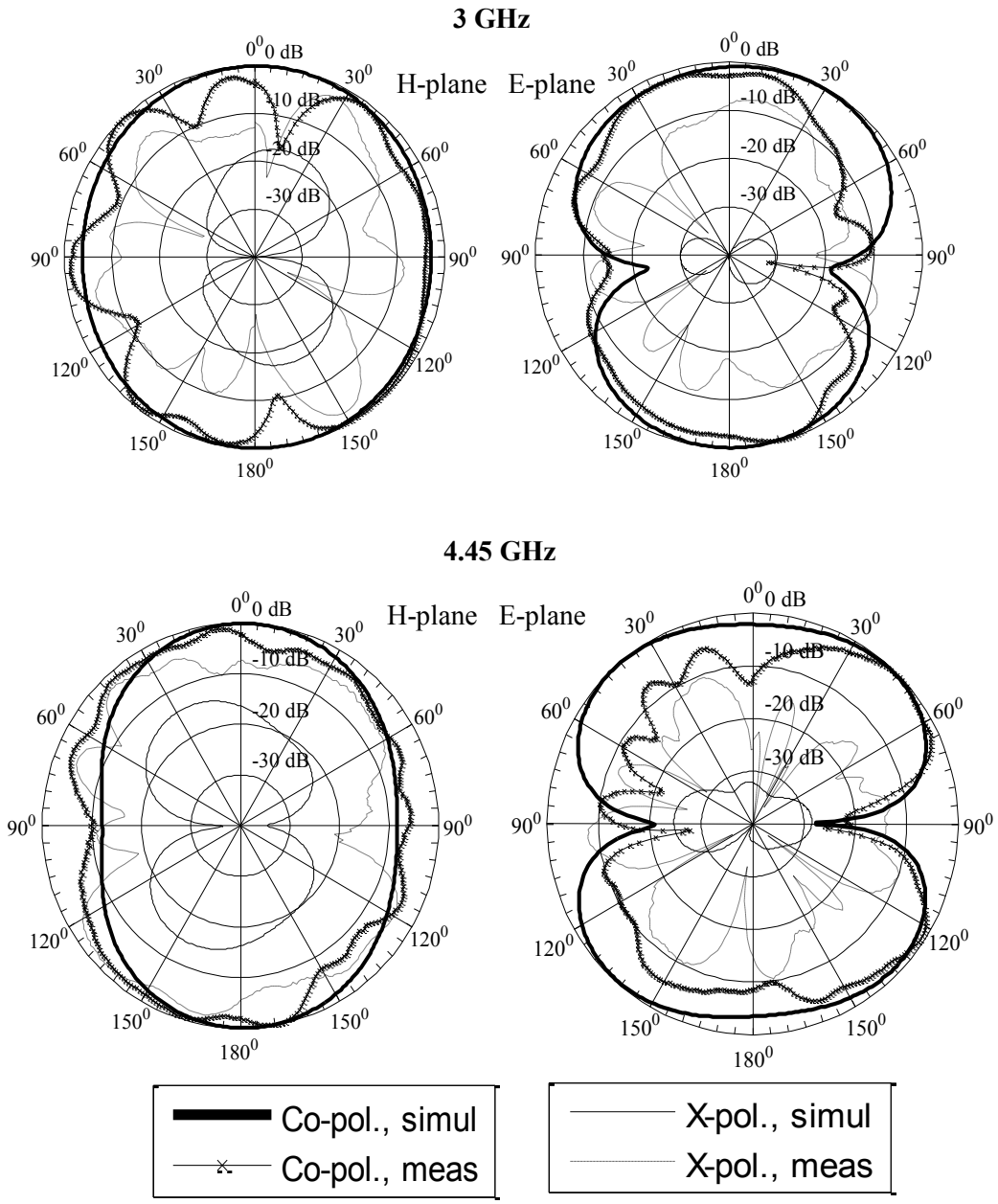

Figure 5.22: Measured and Simulated radiation patterns at 3 GHz and 4.45 GHz for the switched monopole antenna.

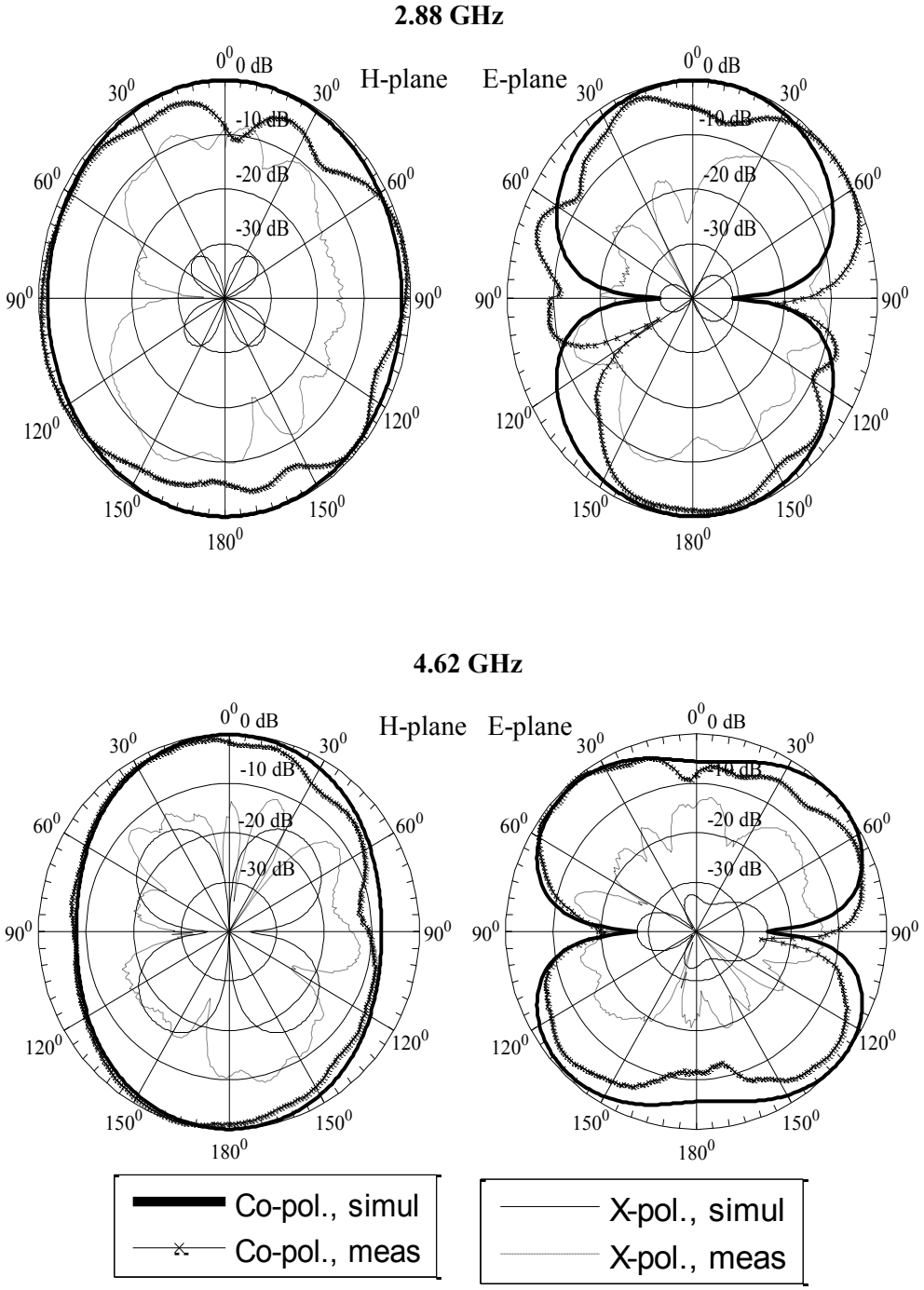

Figure 5.23: Measured and Simulated radiation patterns at 2.88 GHz and 4.62 GHz for the varactor monopole antenna.

5.5 Three modes antenna

The switched monopole antenna of section 5.3.2 was modified to add a stop-band mode to the already present wide-band and narrow-band modes. This stop-band mode was added without the need of extra slots or switches. The wideband antenna from section 5.3.1 was used with modified ring slots on the CPW structure. The topology of the new ring slot structure is shown in fig. 5.24. The principle of the narrowband operation is again to create two stop-bands using two $\lambda/4$ resonators far apart so that a pass-band is possible between them. When the signal at X in fig 5.25 enters the square resonator it sees two $\lambda/4$ unequal resonators. Turning on different switches will result in different lengths of the $\lambda/4$ unequal resonators, which in turn will result in different stop bands and the resulting pass-bands will shift as well.

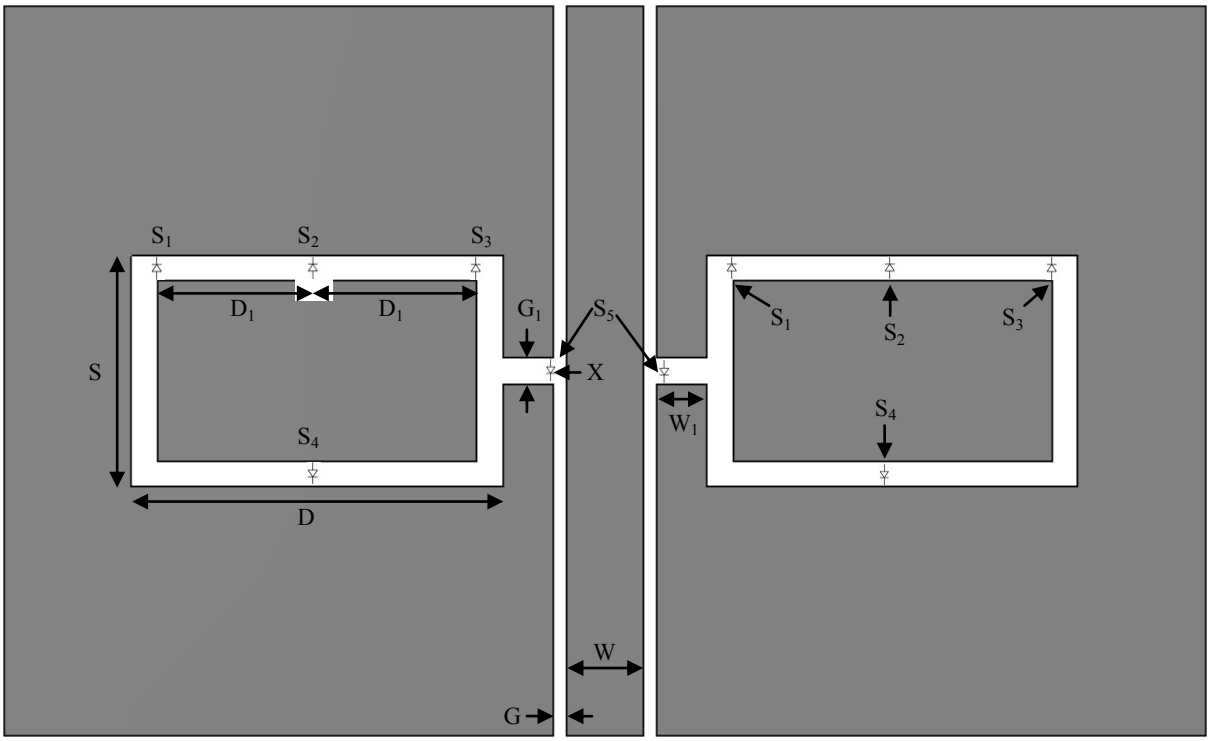

Figure 5.24: Topology of CPW Filter. G_1= 1mm, G=0.5mm, W_1=2mm, W=3mm, D_1= 6.25mm, D=14.5mm, S=9mm.

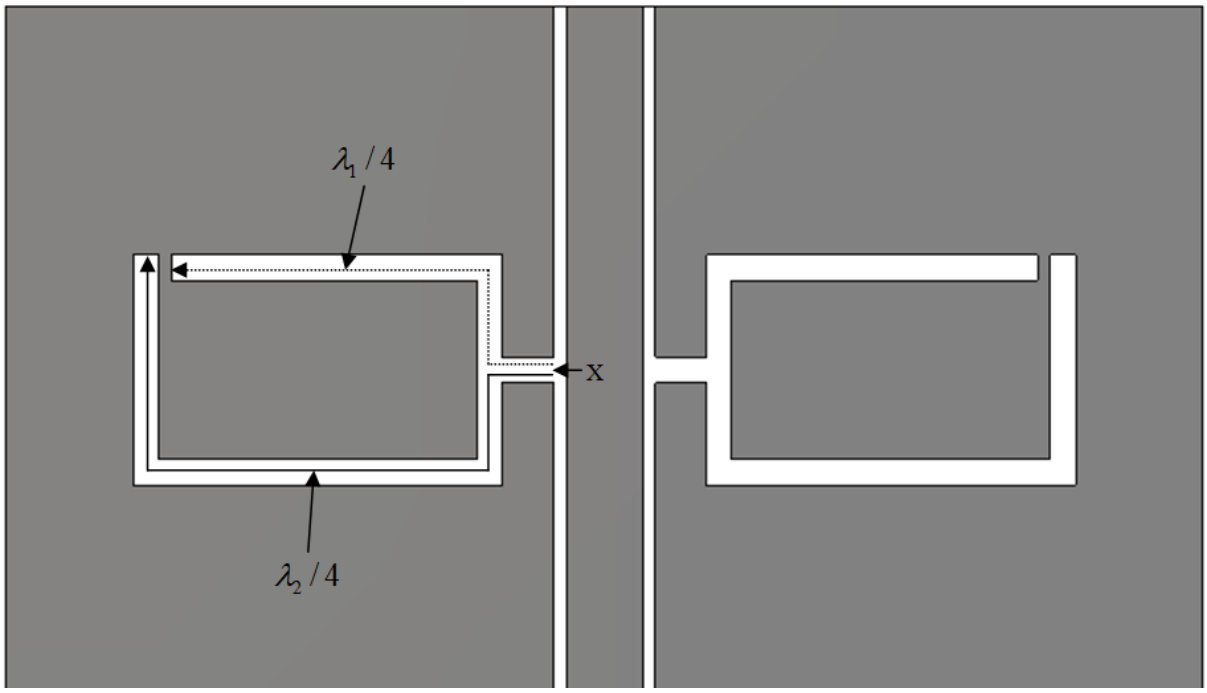

Figure 5.25: CPW filter with two $\lambda/4$ unequal resonators from entry point X.

Fig. 5.26 shows the S_{11} and S_{21} parameters for the filter with switch combination 1 ON. In it the stop-band frequencies are at 2.159 GHz and 3.251 GHz respectively. The frequencies calculated using TX line software from AWR for the $\lambda/4$ lengths of 28.5 mm and 19mm are 2.33 GHz and 3.46 GHz respectively. The calculated values show good agreement with the simulated values. The other narrowband modes can be achieved by using switch combinations S1 & S2, and S1 & S3.

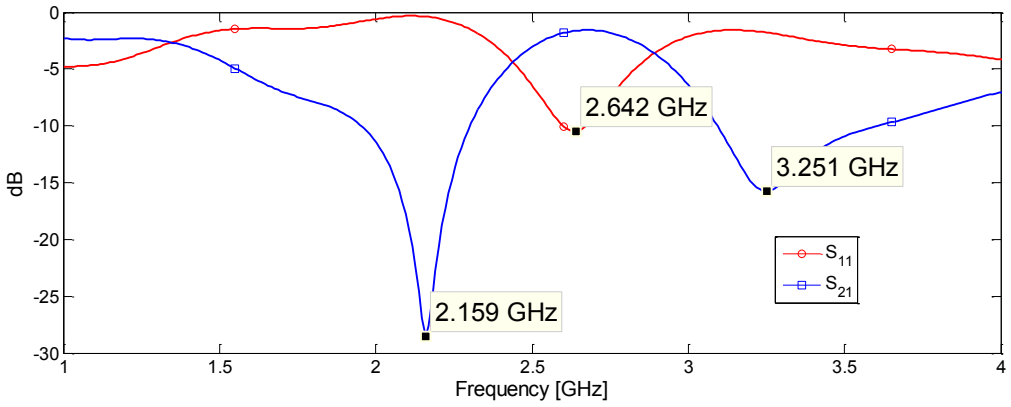

Figure 5.26: S-parameters for filter in fig. 5.25.

Fig. 5.27 shows the electric field and surface current at 2.159 GHz and 3.251 GHz when switch combination 1 is on. As can be clearly seen the larger $\lambda/4$ resonator is resonating at 2.159 GHz and the smaller $\lambda/4$ resonator is resonating at 3.251 GHz.

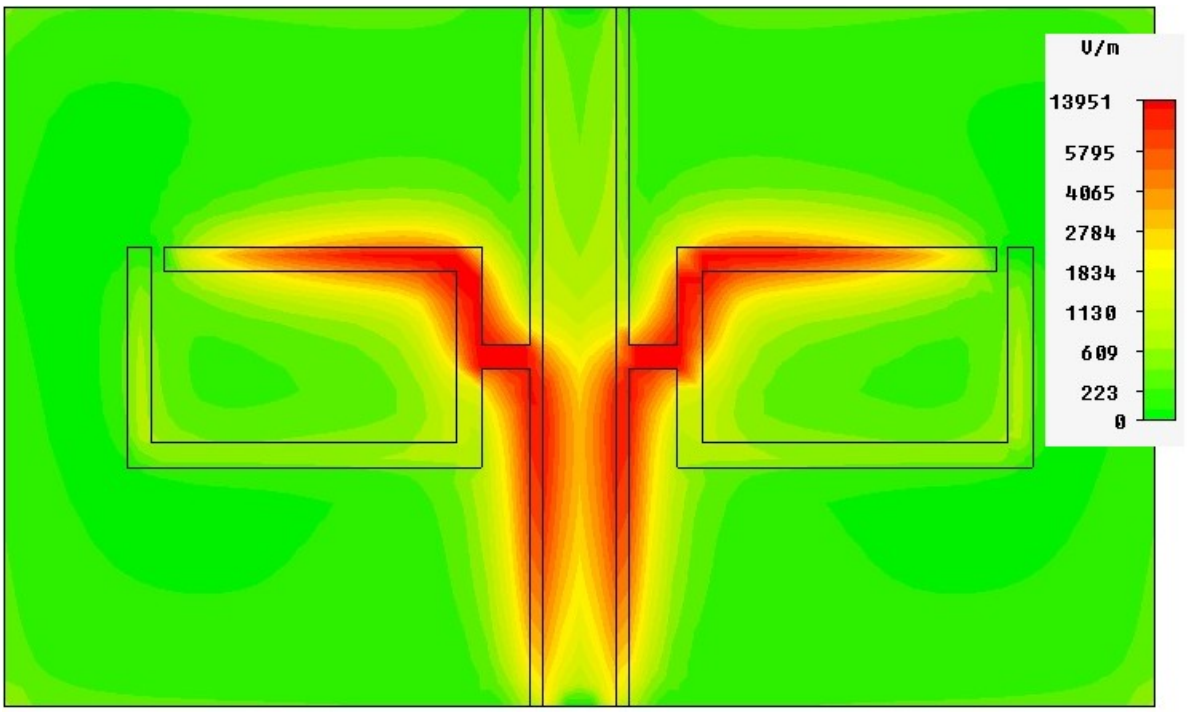

(a)

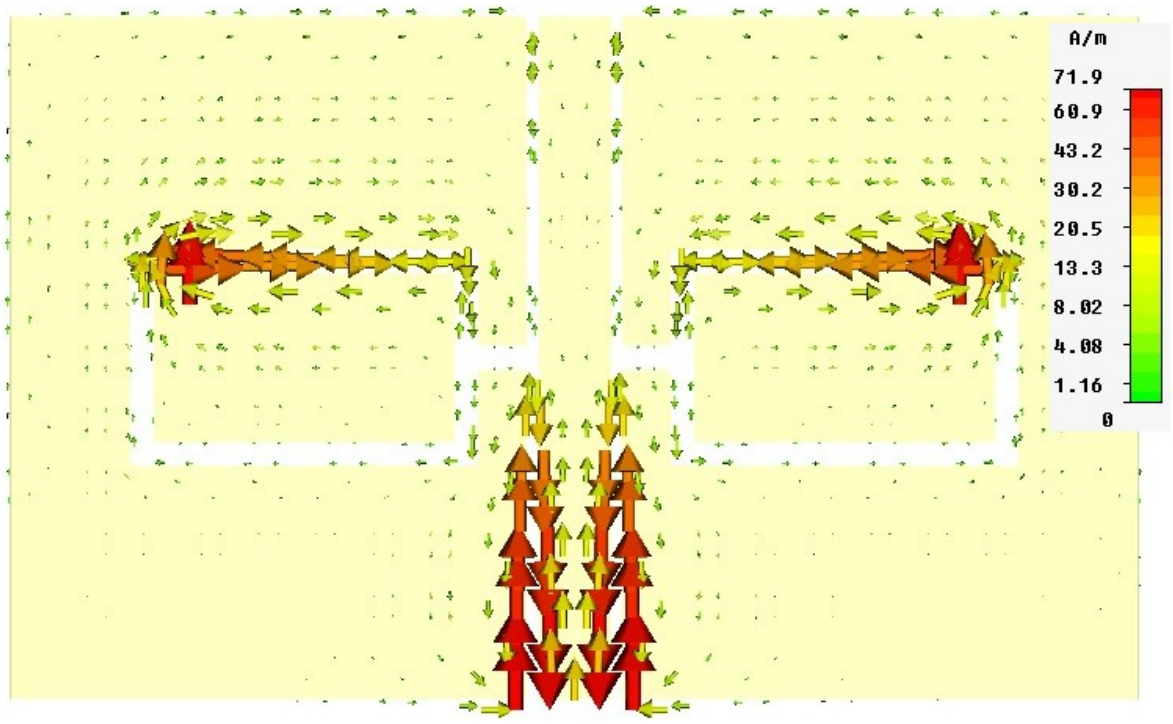

(b)

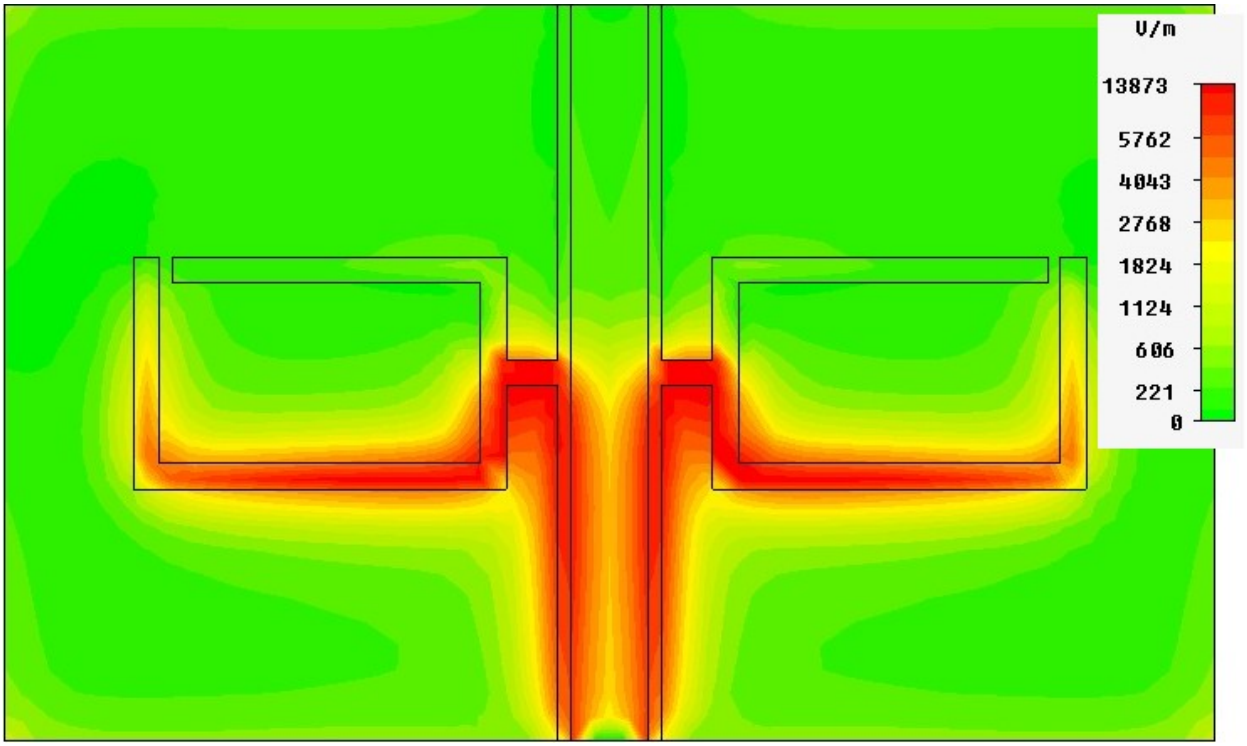

(c)

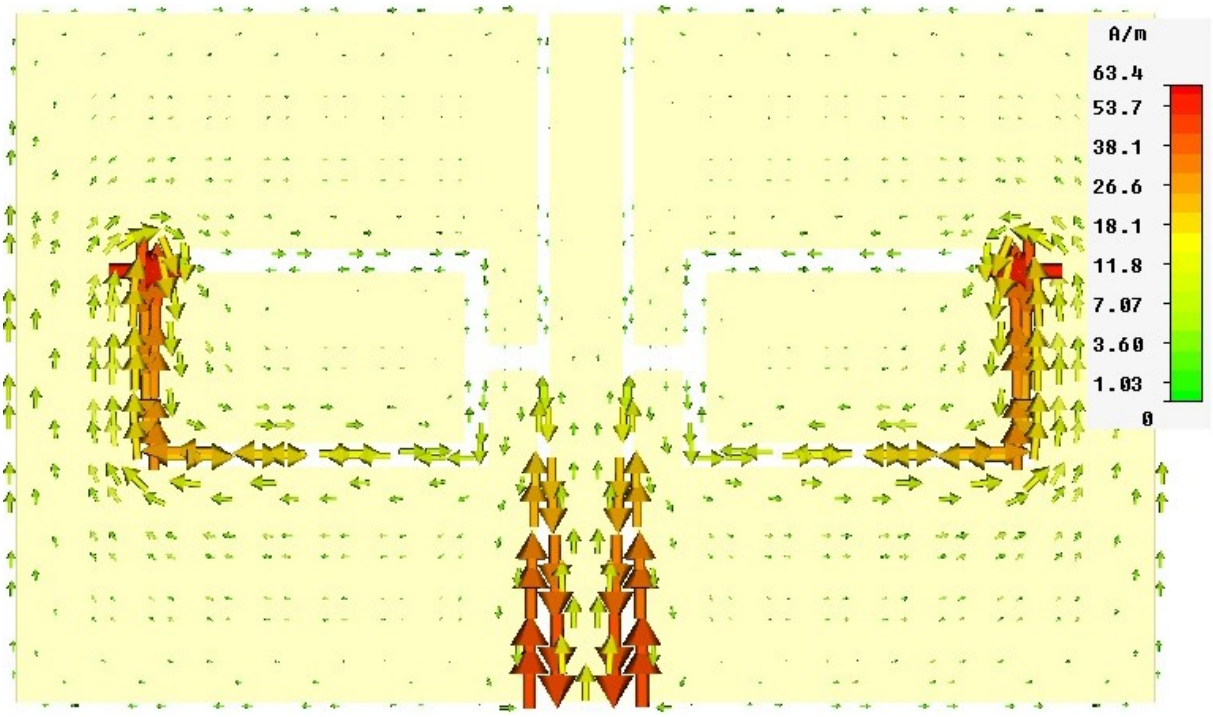

(d)

Figure 5.27: (a) Electric field strength at 2.159 GHz, (b) Surface current density at 2.159 GHz, (c) Electric field strength at 3.251 GHz, and (d) Surface current density at 3.251 GHz for filter in fig. 5.24 with switch combination S_1 on.

The filter shown in fig. 5.24 is employed on a wideband CPW antenna, as in section 5.3. The principle of adding a notch band mode involves resonating $\lambda/2$ slots. When the entrance to the square resonator is blocked and switch combination 1 is on, the resulting slot in the CPW structure as shown in fig.5.28 resonates at $\lambda/2$.

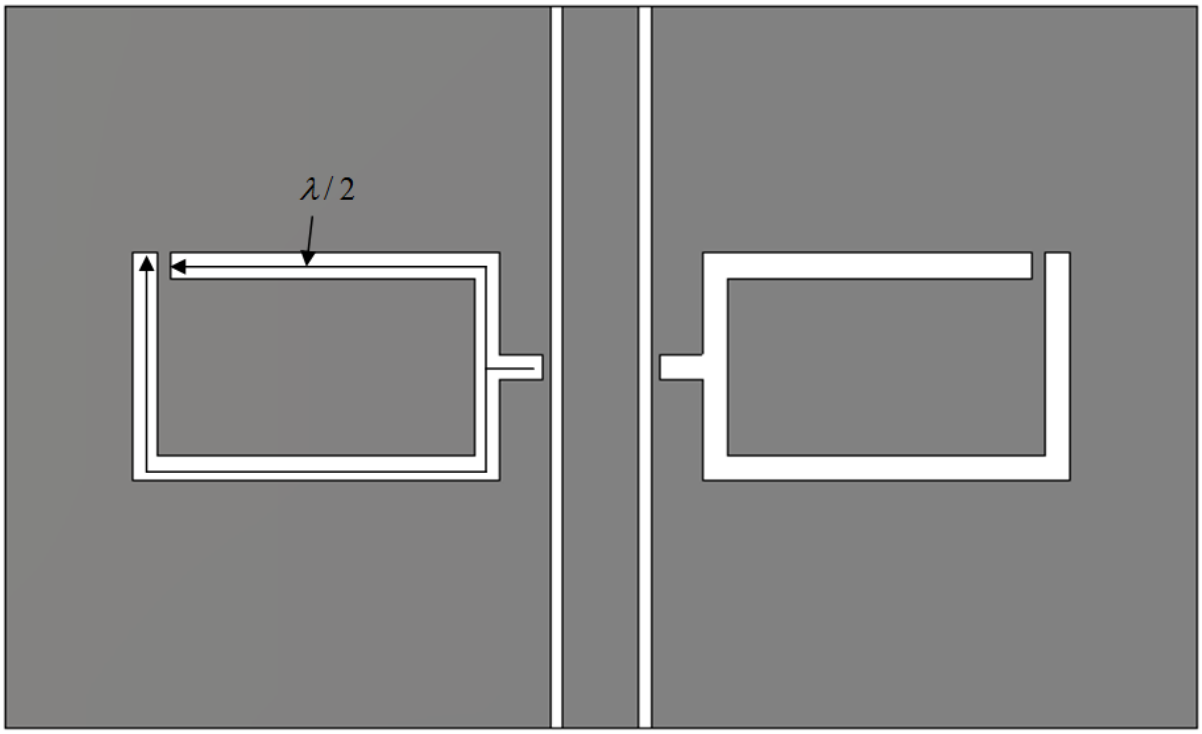

Figure 5.28: $\lambda/2$ resonator formed when filter of fig. 5.24 has switch combination S_1 and S_5 ON.

This causes a simulated stop band at 2.828 GHz in the CPW antenna (from section 5.3.1) as shown in fig. 5.29. The resonant frequency of this 44.7 mm $\lambda/2$ line calculated using TX line from AWR is 2.96 GHz which agrees well with the simulated value.

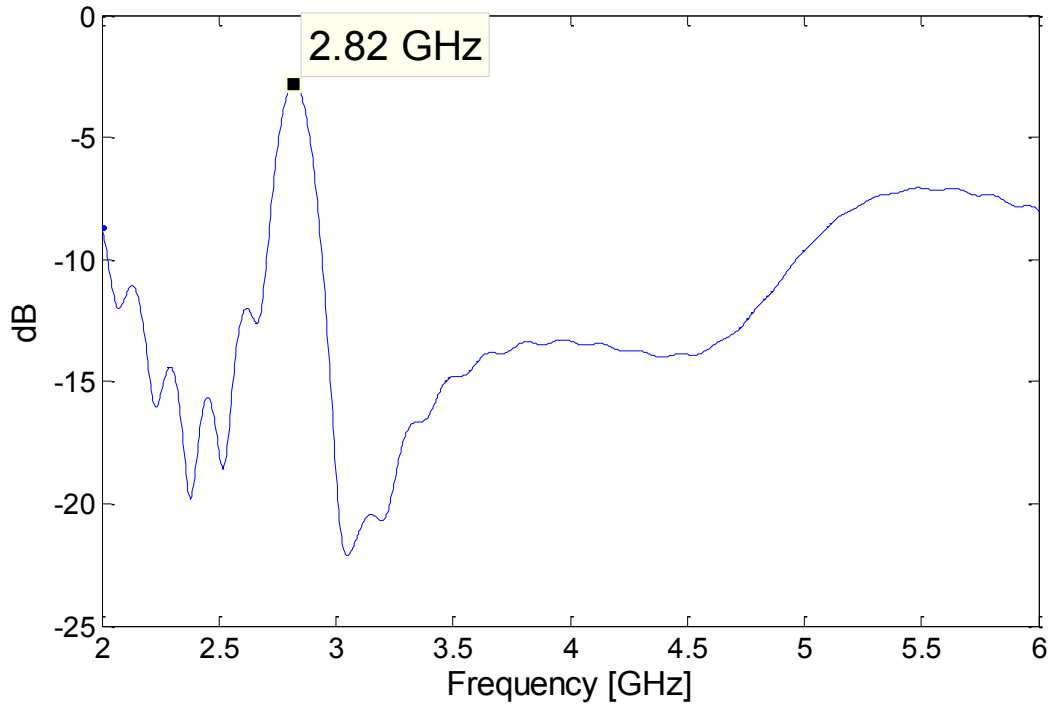

Figure 5.29: S_{11} parameter results for wideband CPW antenna (from section 5.3.1) integrated with the filter shown in Fig. 5.28.

Fig 5.30 shows the electric field and surface current distribution at 2.828 GHz. The resonating $\lambda/2$ slot can be clearly seen. Similarly for the other switch combinations S1 & S2, and S1 & S3 two more stop bands are obtained.

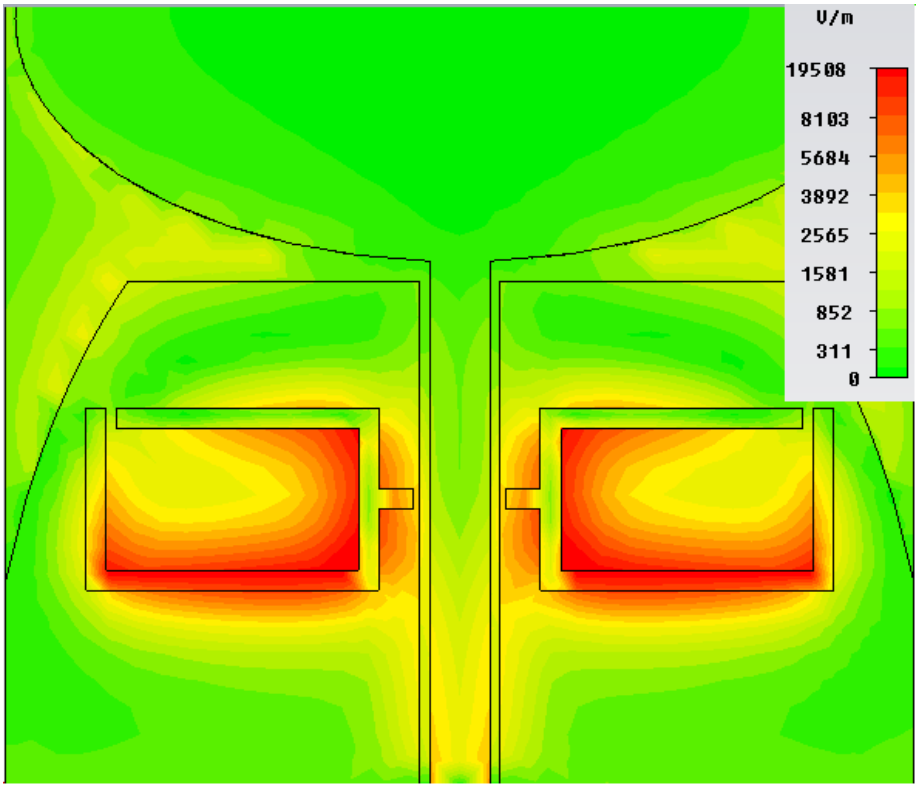

(a)

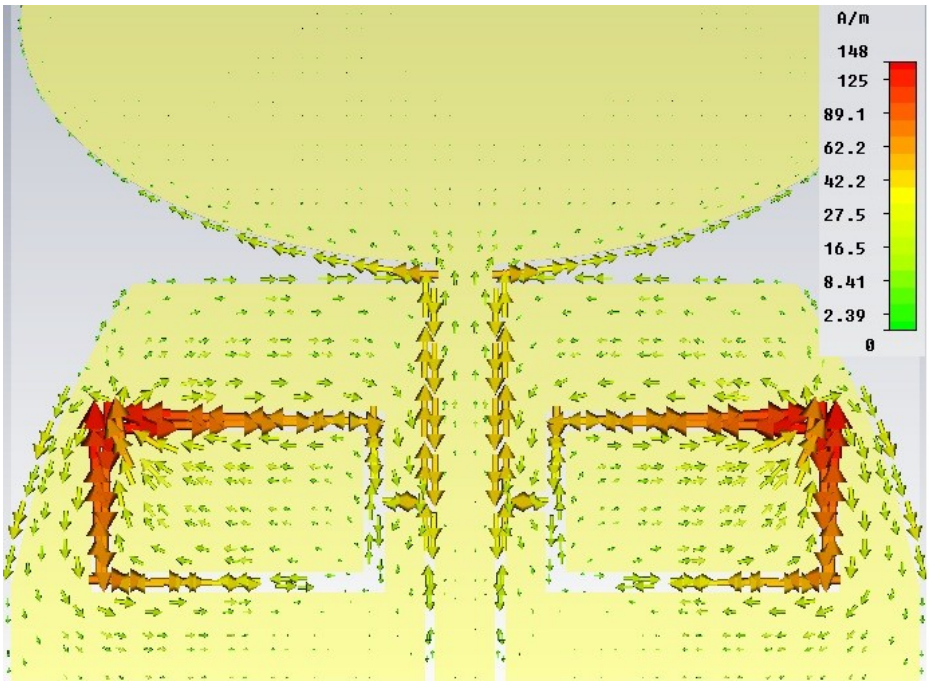

(b)

Figure 5.30: (a) Electric field (b) Surface current density at 2.828 GHz when switch combination S_1 is on for filter in fig. 5.24 on a CPW antenna

The wideband mode is achieved by turning ON the entrance switches and producing a switch combination which yields a notch band outside the frequency of operation. The combination S_1 and S_4 yields such a notch band. In order to prove the concept 3mm copper strips were used as ideal switches instead of actual diode switches. Antenna design using actual diode switches has already been demonstrated in section 5.3. Fig 5.31 shows the simulated and measured notch band modes. The measured notches occur at 2.7 GHz, 3.2 GHz and 3.6 GHz. Fig. 5.32 shows the simulated and measured pass band modes. The measured resonant pass band frequencies are at 2.9 GHz, 3.7 GHz and 4.7 GHz. Figure 5.33 shows the simulated and measured wide band mode. The antenna has measured reflection coefficient below -10 dB from 2.8 – 6 GHz, and a measured reflection coefficient below – 6 dB from 2.6 – 6 GHz. All of these show good agreement with each other. Fig. 5.34 shows the measured results of all the three modes.

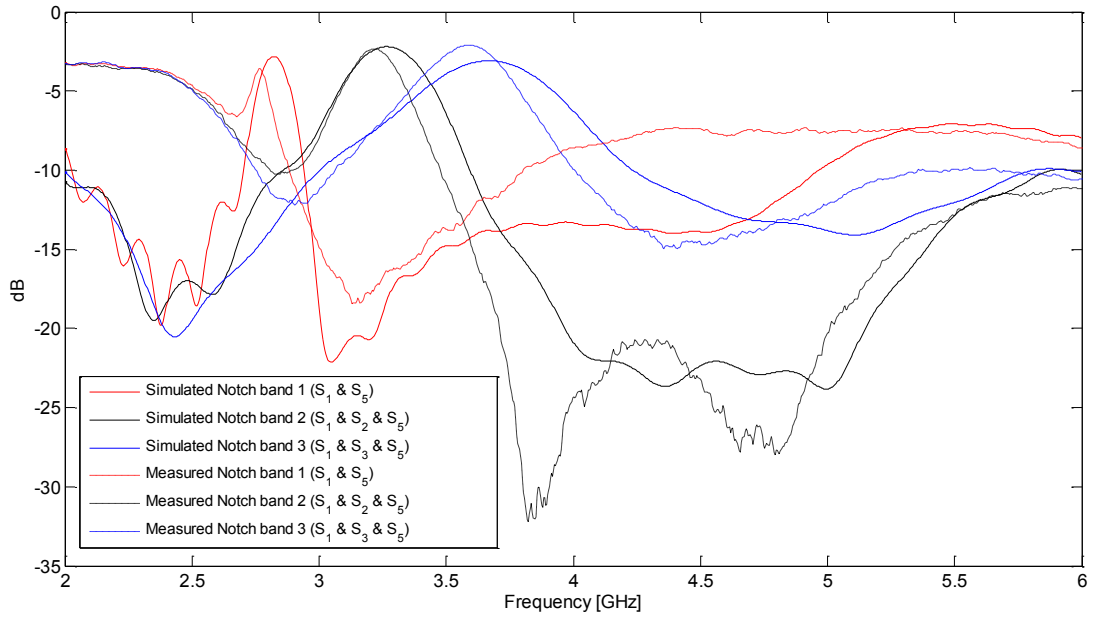

Figure 5.31: Simulated and Measured notch band modes for 3 mode antenna. The measured notches occur at 2.7 GHz, 3.2 GHz and 3.6 GHz

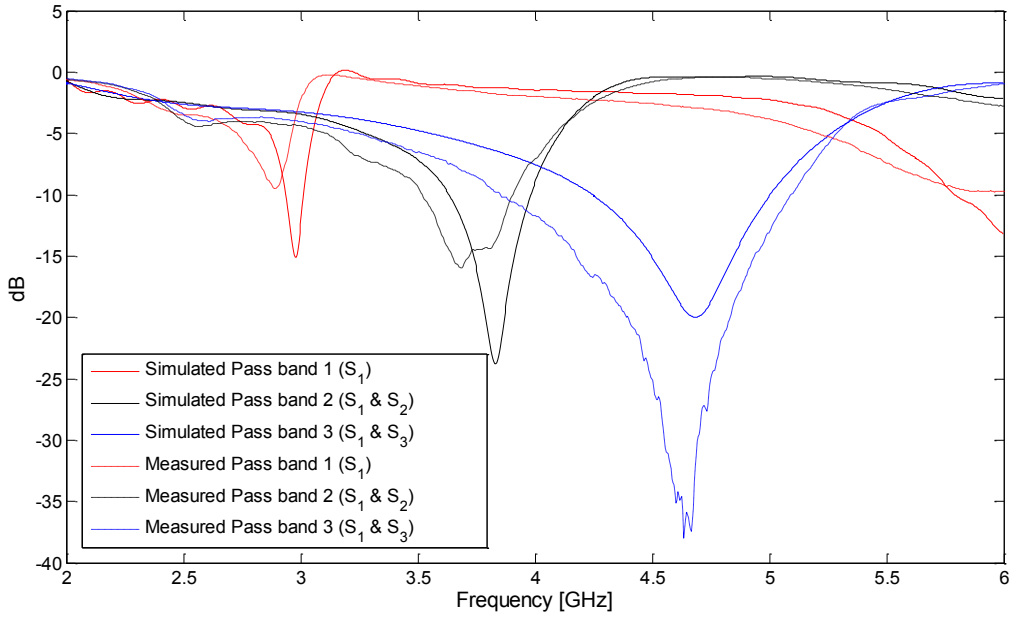

Figure 5.32: Simulated and Measured pass band modes for 3 mode antenna. The measured resonant pass band frequencies are at 2.9 GHz, 3.7 GHz and 4.7 GHz.

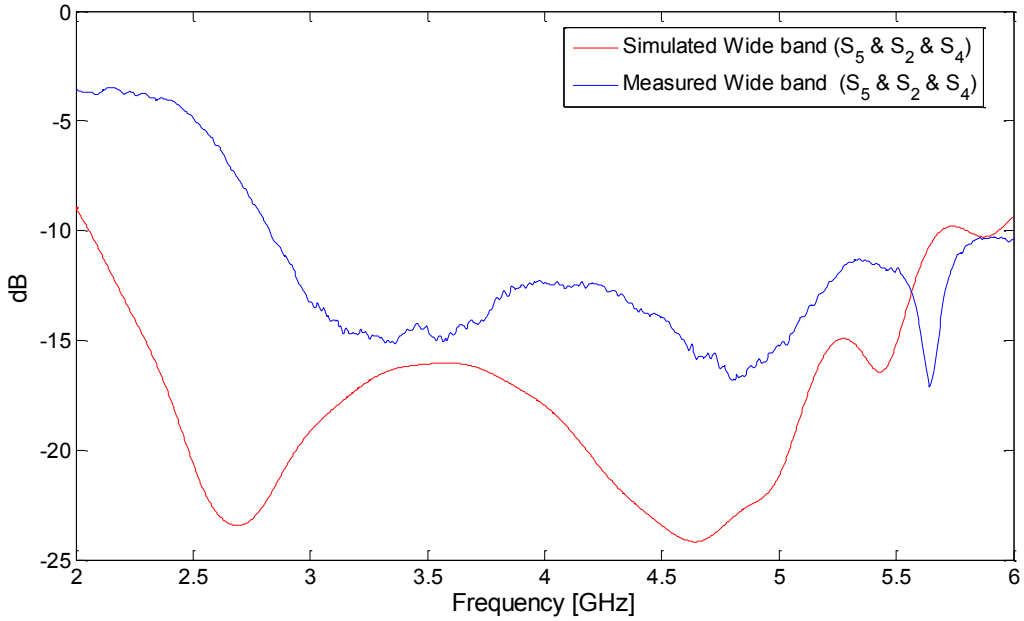

Figure 5.33: Simulated and Measured wide band mode for 3 mode antenna. The antenna has measured reflection coefficient below -10 dB from 2.8 – 6 GHz, and a measured reflection coefficient below – 6 dB from 2.6 – 6 GHz.

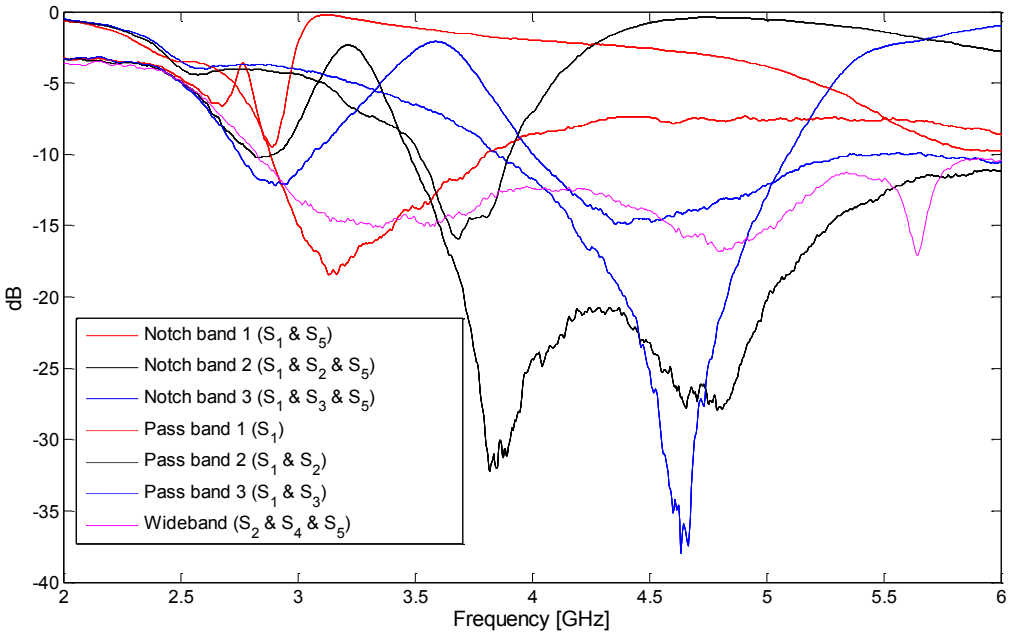

Figure 5.34: Measured Reflection coefficient results for 3 mode antenna considering notch-band, pass-band and wideband modes.

Fig 5.35 shows the E-plane and H- plane measured and simulated radiation pattern of the antenna at 2.89 GHz and 4.635 GHz. Both of them show good agreement with each other.

Fig. 5.36 shows the measured gain of the antenna for the wideband mode and three notch band modes. The measured gain results clearly show a drop in gain at the notch points.

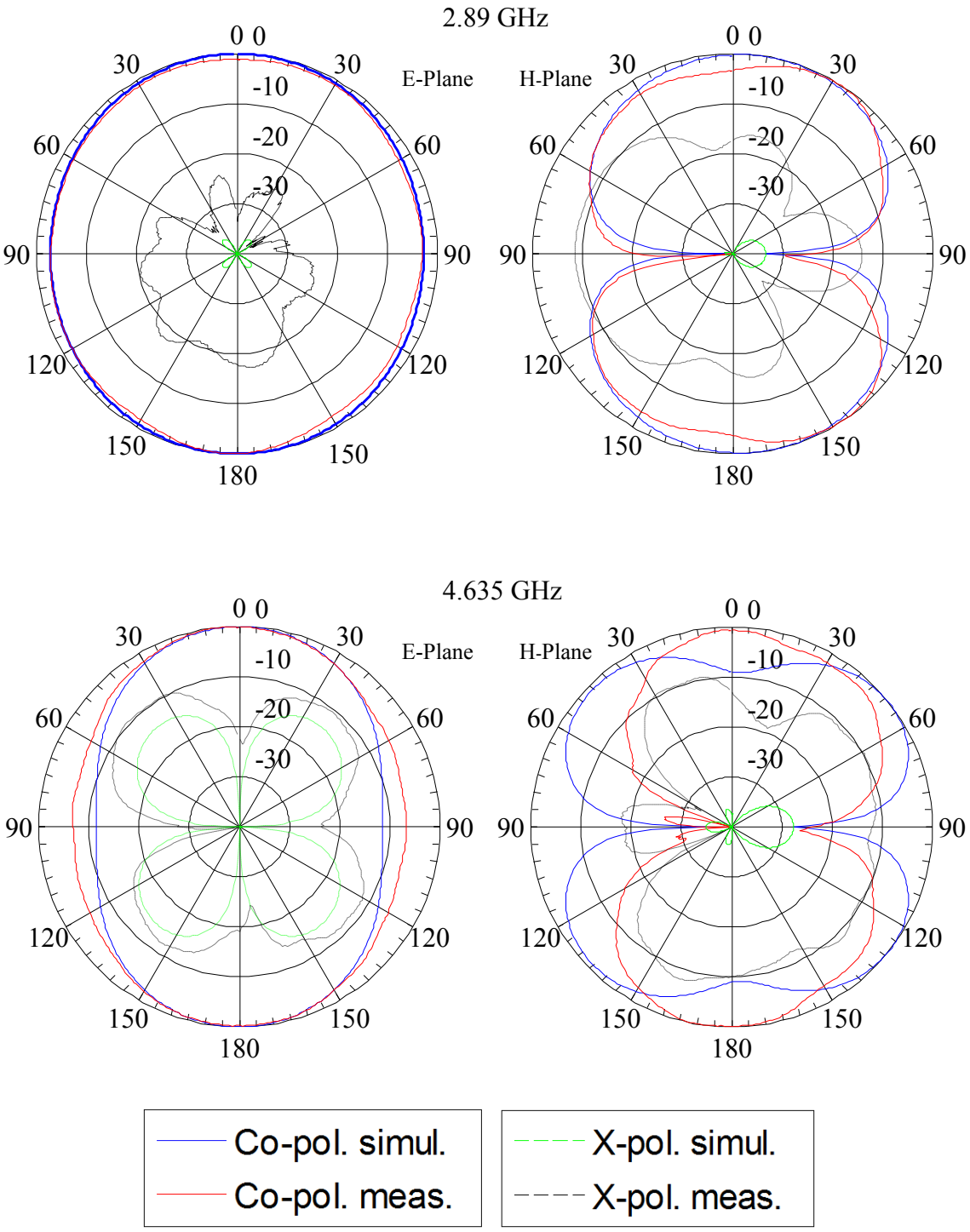

Figure 5.35: Measured and Simulated radiation patterns at 2.89 GHz and 4.635 GHz respectively.

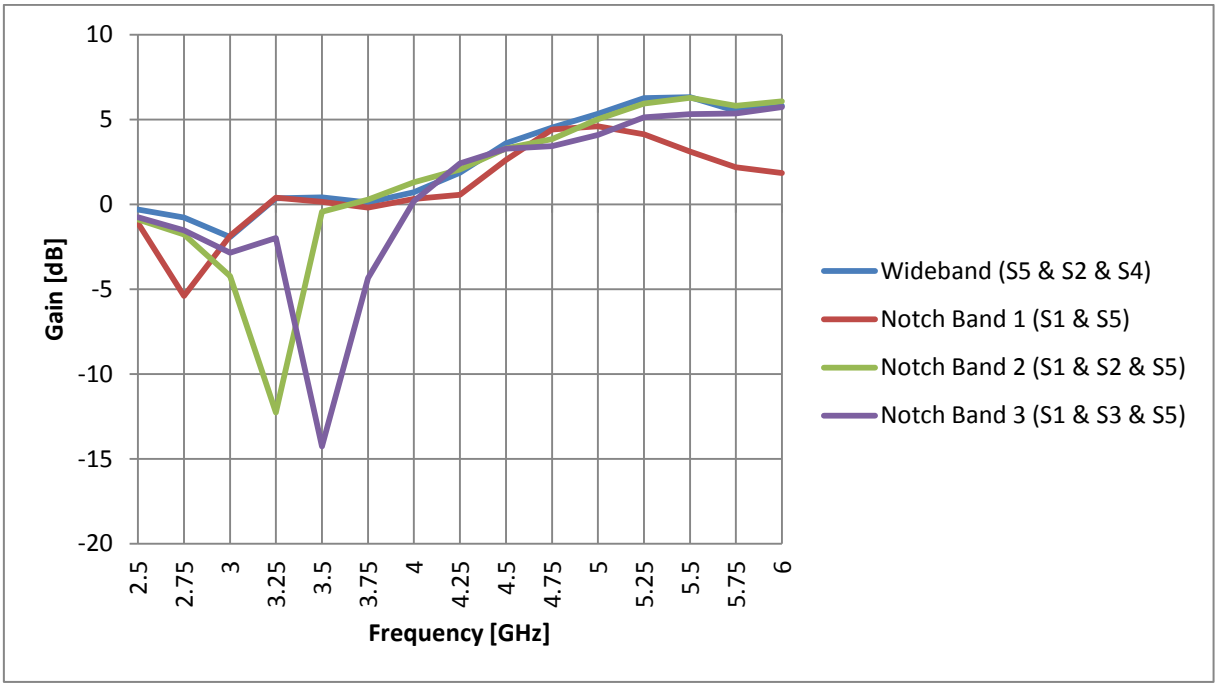

Figure 5.36: Measured gain results for boresight for notch and wideband modes.

5.6 Conclusions

A novel CPW varactor filter is introduced which can achieve a wide tuning range by changing the resonant frequency of $\lambda_g/4$ and $3\lambda_g/4$ resonators using varactors. Another CPW filter using switches to control two $\lambda_g/4$ resonators is also designed. These CPW filters are very compact and can be integrated within the structure of an antenna without taking any extra space. The integration of these filters with CPW wideband antennas results in frequency agility. Good agreements between simulated and measured results are obtained for the S-parameters of both the filters and their respective antennas. The working principles of both filters are validated by using slotline equations and simulations.

A novel three modes (Wide-band, Narrow-band, and Notch-Band) antenna is proposed and validated using measurements. This antenna adds a notch band mode to the switched antenna.

The notch band is added by utilizing $\lambda/2$ resonators which are created when the entrance to the square ring resonator is blocked.

Because wide-band, narrow-band and notch-band operation is obtained, these CPW wideband antennas with integrated filters are excellent for Cognitive radio applications.

The radiation pattern of all the antennas are simulated and measured and ways to improve the pattern degradation have been suggested.

5.7 References

[1] H.Li, J. Xiong, Y. Yu, S. He, , "A Simple Compact Reconfigurable Slot Antenna With a Very Wide Tuning Range," *Antennas and Propagation, IEEE Transactions on* , vol.58, no.11, pp.3725-3728, Nov. 2010

[2]P. S. Hall, P. Gardner, J. Kelly, E. Ebrahimi, M. R. Hamid, F. Ghanem, F. J. Herraiz-Martinez, and D. Segovia-Vargas, "Reconfigurable antenna challenges or future radio systems," in *Proc. 3rd Eur. Conf. on Antennas and Propagation*, Berlin, Germany, 2009, pp. 949–955.

[3]S.-H. Oh, J. T. Aberle, S. Anantharaman, K. Arai, H. L. Chong, and S. C. Koay, "Electronically tunable antenna pair and novel RF front-end architecture for software-defined radios," *EURASIP J. Appl. Signal Processing*, vol. 2005, pp. 2701–2707, 2005.

[4] S. Yang, C. Zhang, H. K. Pan, A. E. Fathy, and V. K. Nair, "Frequency reconfigurable antennas for multiradio wireless platforms," *IEEE Microwave Mag.*, vol. 10, no. 1, pp. 66–83, Feb. 2009.

[5] D. Peroulis, K. Sarabandi, L.P.B. Katehi, "Design of reconfigurable slot antennas," *Antennas and Propagation, IEEE Transactions on* , vol.53, no.2, pp.645-654, Feb. 2005.

[6] N. Behdad, K. Sarabandi, "A varactor-tuned dual-band slot antenna," *Antennas and Propagation, IEEE Transactions on* , vol.54, no.2, pp. 401- 408, Feb. 2006

[7] M.R. Hamid, P. Gardner, P.S. Hall, F.Ghanem, "Switched-Band Vivaldi Antenna," *Antennas and Propagation, IEEE Transactions on,* vol. 59, no. 5, pp. 1472-1480, May 2011.

[8] M.R. Hamid, P. Gardner, P.S. Hall, F.Ghanem, "Vivaldi Antenna with Integrated Switchable Band Pass Resonator," *Antennas and Propagation, IEEE Transactions on*, vol. 59, no. 11, pp. 4008-4015, Nov. 2011.

[9] J. Perruisseau-Carrier, P. Pardo-Carrera, P. Miskovsky, "Modeling, Design and Characterization of a Very Wideband Slot Antenna With Reconfigurable Band Rejection," *Antennas and Propagation, IEEE Transactions on* , vol.58, no.7, pp.2218-2226, July 2010

[10] H.B. El-Shaarawy, F. Coccetti, R. Plana, M. El-Said, E.A. Hashish, "Novel Reconfigurable Defected Ground Structure Resonator on Coplanar Waveguide," *Antennas and Propagation, IEEE Transactions on* , vol.58, no.11, pp.3622-3628, Nov. 2010

[11] Y. Zheng; A. Hristov; A. Giere ; R. Jakpby, "Suppression of harmonic radiation of tunable Planar Inverted-F Antenna by ferroelectric varactor loading," *Microwave Symposium Digest, 2008 IEEE MIT-S International*, vol., no., pp.959-962, 15-20 June 2008

[12] C. Kalialakis; P. Gardner; P.S. Hall, "Harmonic Radiation from Varactor-Loaded Microstrip Antenna," *Microwave Conference, 2001, 31st European*, vol., no., pp.1-4, 24-26 Sept. 2001

[13] T.H. Hand, S.A. Cummer, "Controllable Magnetic Metamaterial Using Digitally Addressable Split-Ring Resonators," *Antennas and Wireless Propagation Letters, IEEE* , vol.8, no., pp.262-265, 2009

[14] S.J. Wu, T.G. Ma, "A Wideband Slotted Bow-Tie Antenna With Reconfigurable CPW-to-Slotline Transition for Pattern Diversity," *Antennas and Propagation, IEEE Transactions on* , vol.56, no.2, pp.327-334, Feb. 2008

6 Chapter 6

Pattern Reconfigurable Antennas

Abstract— In this chapter novel pattern reconfigurable antennas based on the Vivaldi structure are investigated, designed and tested. A novel single port antenna in which switches are used to switch between 4 radiation patterns is introduced. The antenna operates over a wideband and uses 4 diode switches to divert the current to the appropriate paths to achieve 4 quadrant directionality. The radiation pattern, reflection coefficient and gain of this antenna are measured. The experimental and simulation results are presented and compared.

6.1 Introduction

A lot of research is being conducted on frequency, pattern and polarization reconfigurable antennas. Communication signals are usually transmitted and received in extreme multipath environments with a lot of interferences. Adjacent frequency channels overlapping is one of the major causes of interference. These interferences can be overcome using spatial, temporal, angle and polarization diversity. Diversity techniques improve signal to noise (SNR). In this chapter pattern reconfigurability will be used to achieve diversity. Pattern diversity improves energy efficiency, avoids noisy environments, mitigates electronic jamming and improves wireless security. In this chapter a single port antenna with switches will be used to obtain 4-way radiation pattern reconfigurability over a wideband.

Pattern reconfigurable antennas have been heavily studied in literature. In [1] a pattern and frequency reconfigurable annular slot antenna was proposed. The antenna used PIN diodes along the annular slot to move the position of a null along the circular slot. This antenna was also frequency reconfigurable as a designed matching circuit allows it to operate between 5.2-

6.4 GHz. In [2] diversity was achieved using an antenna (shown in Fig. 6.1) consisting of a pair of reconfigurable CPW-to-slotline transitions, a pair of Vivaldi shaped radiating tapered slots and PIN diodes. It operated in the 3.5 to 6.5 GHz range and could switch between a broadside radiation with fairly omnidirectional pattern and two end-fire radiations with main beams in opposite directions using the Vivaldi slots.

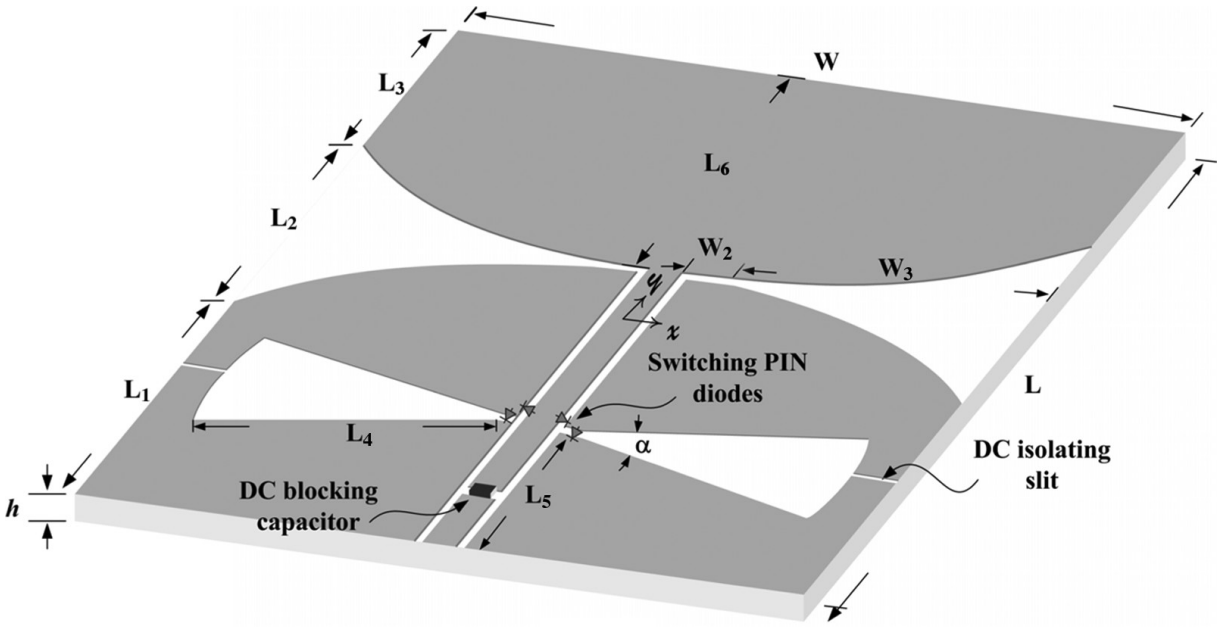

Figure 6.1: Schematic of reconfigurable antenna with CPW-to-slotline transition and a pair of Vivaldi shaped radiating slots [2].

In [3] a wideband circular antenna array (shown in Fig. 6.2) consisting of 8 TEM Horn antennas was used to obtain pattern agility. It had an omnidirectional mode when all the antennas were excited. A notch band filter was used to provide a single directional pattern null in any specific direction at any desired frequency. It operated from 0.8-3 GHz.

Figure 6.2: Wideband circular antenna array [3].

In [4] a metallic cubic cavity (shown in Fig. 6.3) achieved pattern reconfigurable operation by short circuiting radiating rectangular slots at the center of the cubic cavity. The antenna was capable of receiving any incident field polarization and had 3 switchable patterns in the steradian range depending on the shorted slot.

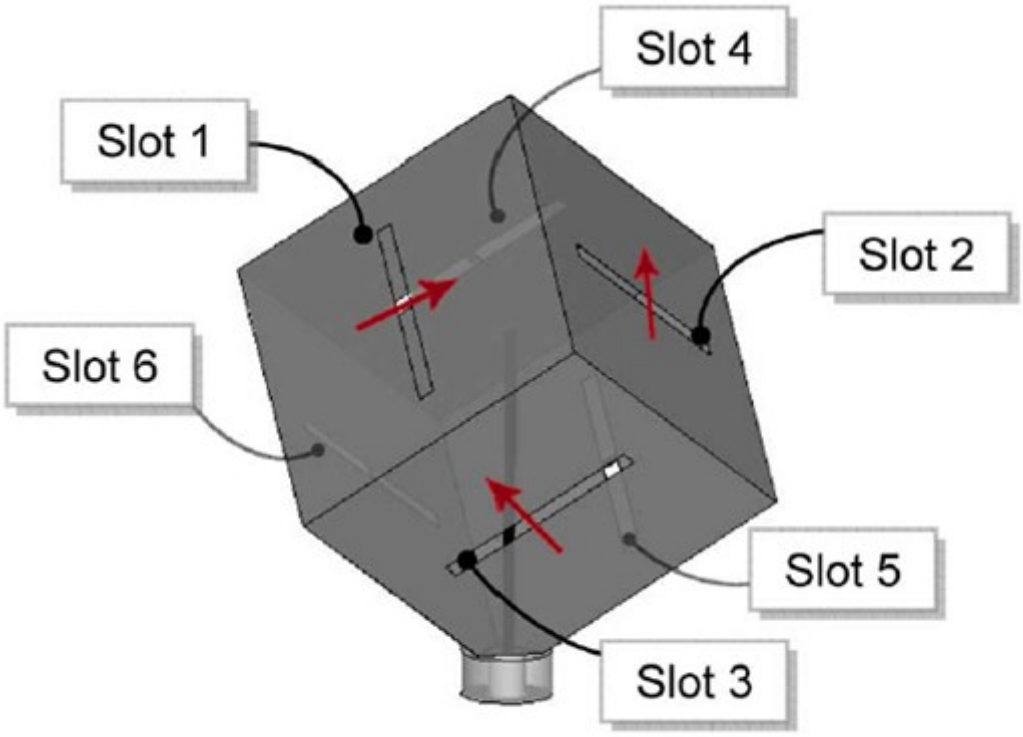

Figure 6.3: Schematic diagram of metallic cubic cavity [4].

A 5-port star shaped antenna shown in Fig. 6.4 could achieve a doughnut shaped pattern and 4 tilted beam radiation patterns [5]. When fed at the centre doughnut shaped radiation pattern was generated while feeding at the edges of the star resulted in 4 tilted beam radiation patterns in four different quadrants. The directivity of the antenna was controlled by the flare angle of the star.

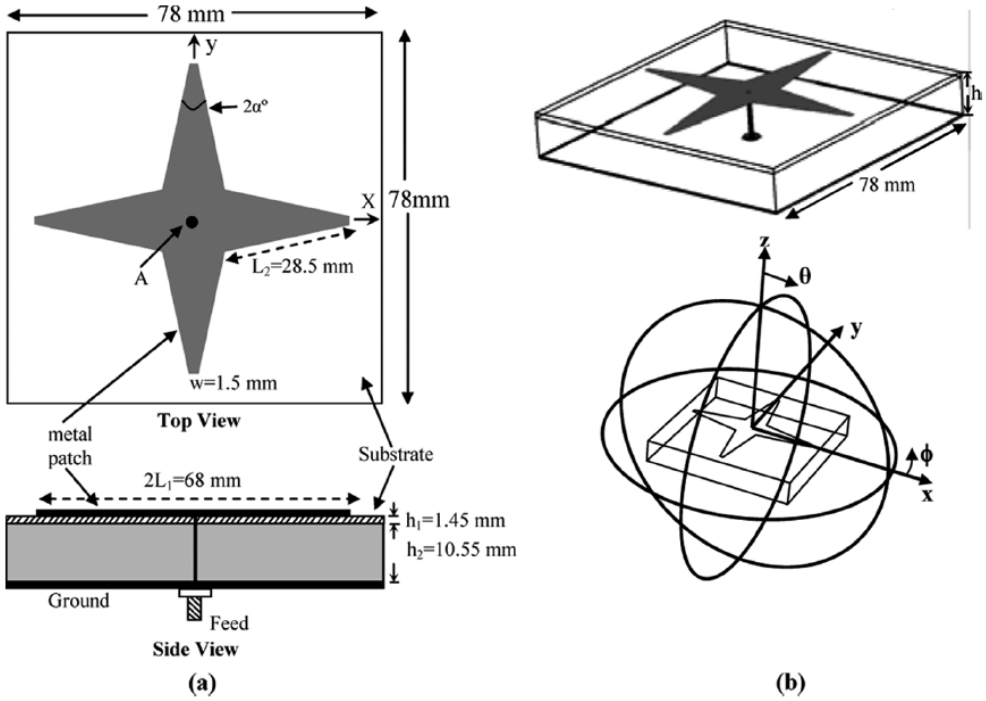

Figure 6.4: (a) Top and side views and (b) perspective view of the printed star antenna [5].

A spiral antenna shown in Fig. 6.5 produced pattern agility using 5 RF-MEMS monolithically integrated on the substrate [6]. These RF-MEMS were placed strategically along the spiral arm, activating them resulted in different spiral arm lengths which in turn resulted in beam steering operation. Improved performance was obtained as a result of the integration of the RF-MEMS within the substrate.

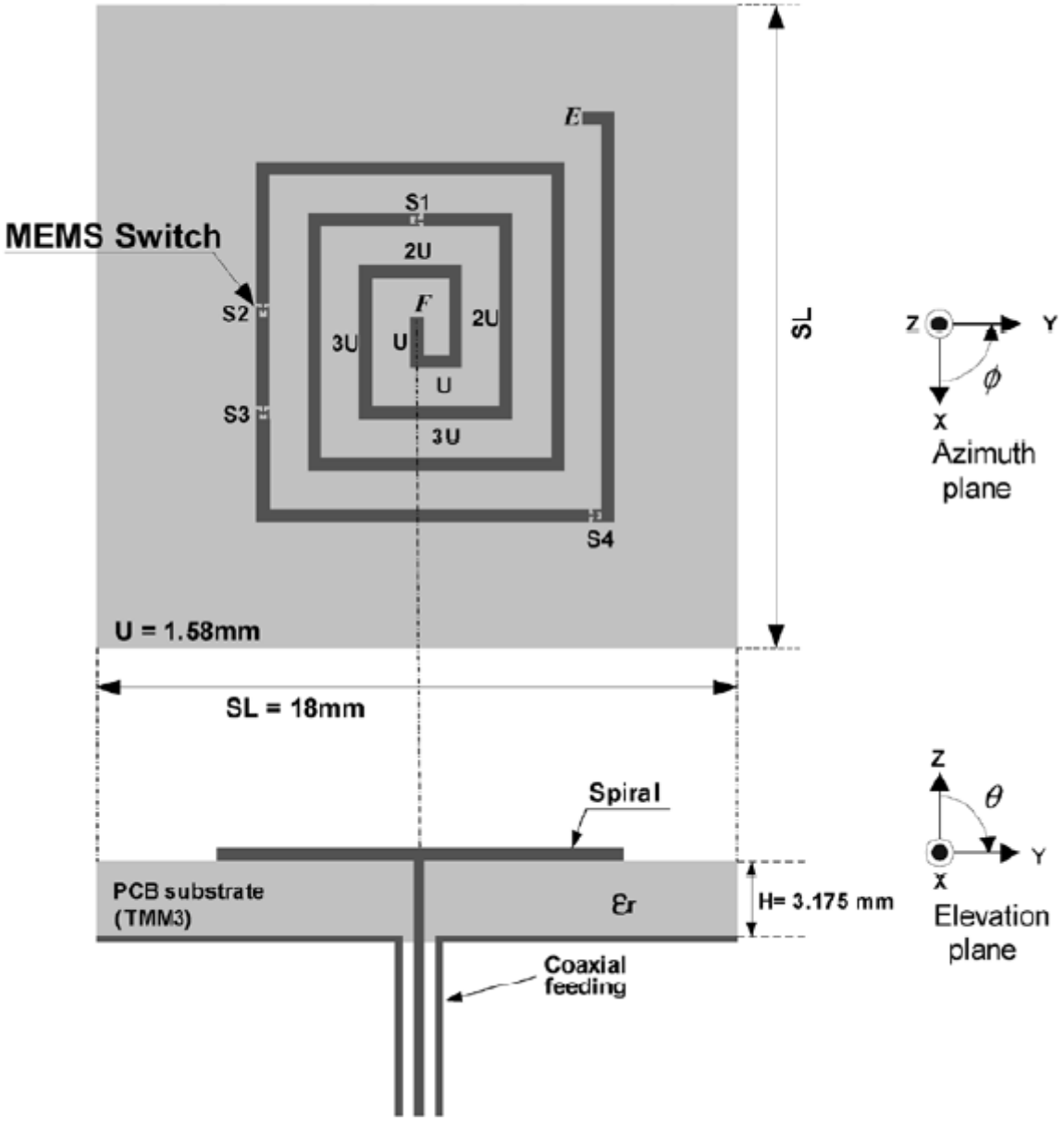

Figure 6.5: Spiral antenna with monolithically integrated RF- MEMS, U=1.58mm [6].

Fig. 6.6 shows the concept of a pattern reconfigurable antenna which has two operating states that can be changed by using switches [7]. It can operate as a monopole antenna with omni-directional radiation pattern or as a dipole antenna with a reflector that has got a directional radiation pattern.

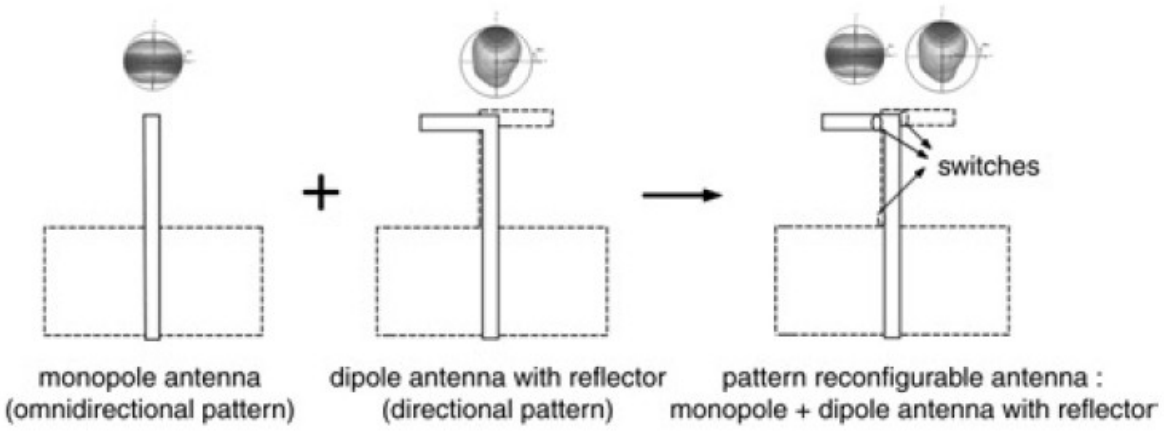

Figure 6.6: Concept of proposed pattern reconfiguration antenna [7].

Pattern reconfigurable antennas usually operate in three ways [8]:

1) Shifting the Main Beam while maintaining beam shape.

2) Shifting the Main Beam while changing beam shape.

3) Having multiple Reconfigurable operations (Frequency, pattern and polarization).

Reconfigurability can be achieved by [9]:

1) Re-routing the current to different paths by using switches.

2) Having multiple ports exciting different parts of the antenna structure.

3) Changing the behaviour of current in various parts of the antenna using agile loading, by adding or subtracting variable parasitic elements.

In this chapter the pattern reconfigurable antenna designed shifts the main beam while almost maintaining beam shape. It achieves this operation by re-routing the current to different paths by utilizing diode switches.

In Section 6.2 the single port flower Vivaldi principle and design is presented. In section 6.2.1 a single port flower Vivaldi with copper strips as diodes is fabricated and tested. After that section 6.2.2 discusses the results of the flower Vivaldi with actual diodes as switches. At the end there are conclusions and references.

6.2 Single Port Flower Vivaldi

In this section a single port antenna shown in Fig. 6.7and 6.8 is designed and tested. The antenna generates four different radiation patterns in four different quadrants. This antenna uses four diode switches to achieve the four different radiation patterns. The principle of operation involves the shifting of the current path to the appropriate tapered slot structure resulting in radiation emitting from that particular tapered slot. The Balun is designed to obtain as wide a bandwidth as possible.

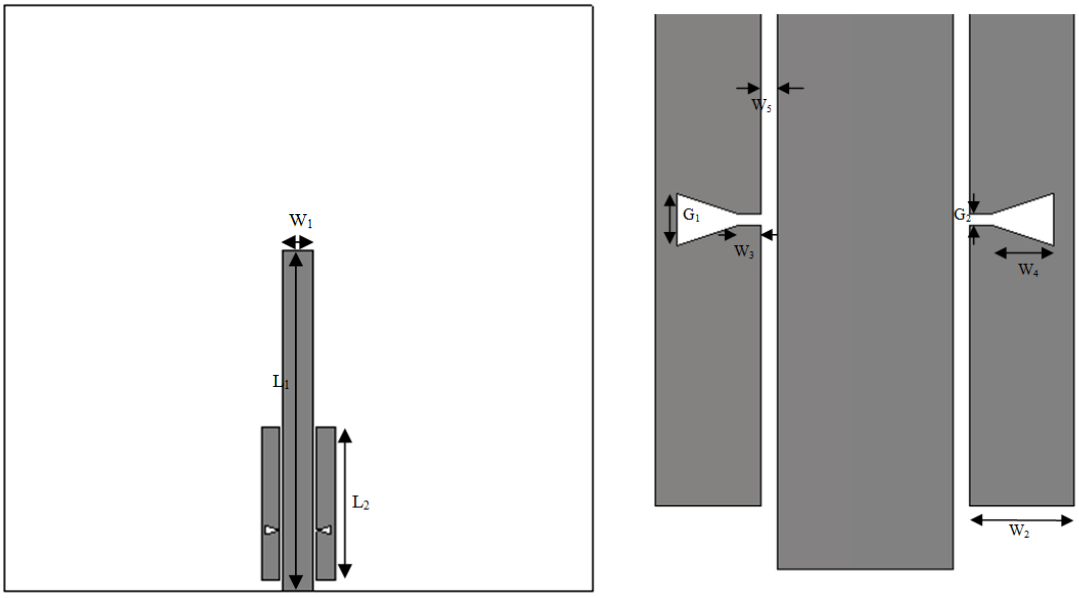

Figure 6.7: Topology of feed structure of antenna. (W_1=4.2 mm, L_1=46.67 mm, L_2=21 mm. W_2=2.5 mm, W_3=0.5 mm, W_4=1.5 mm, W_5=0.4 mm, G_1=1.25 mm, G_2=0.25 mm)

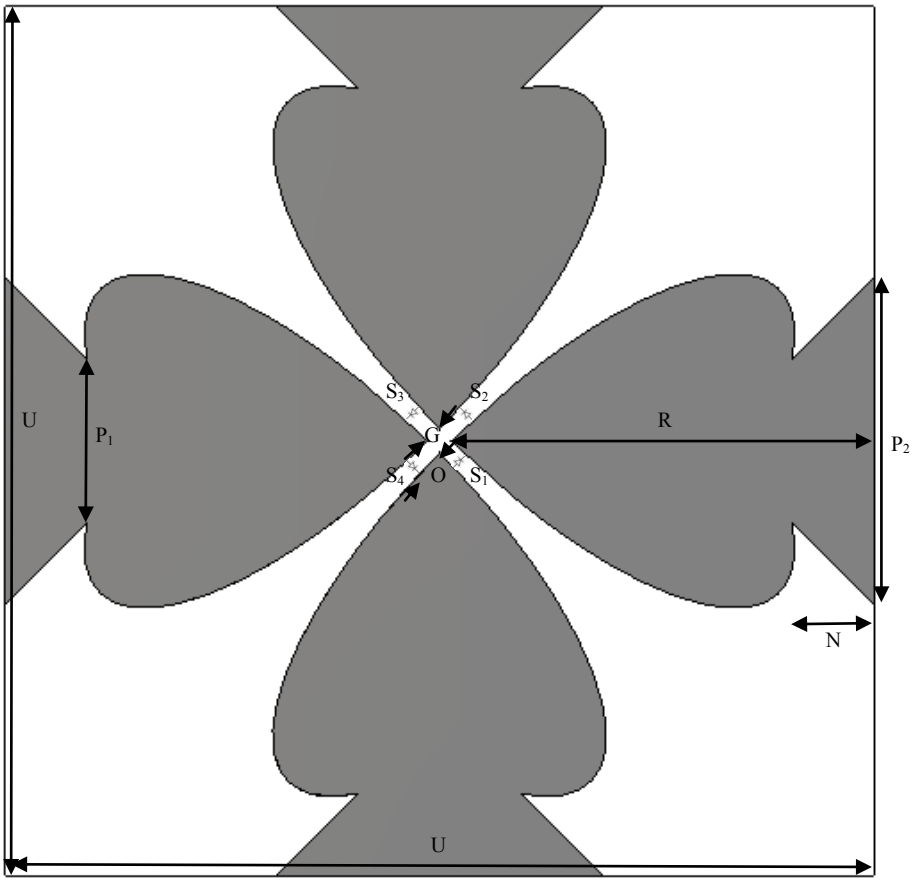

Figure 6.8: Topology of the ground structure of antenna. (G=1.5 mm, P_1=15.2 m, P_2=30.2 mm, R= 38.9 mm, U=80mm, N=7.5 mm, O=4mm)

As can be seen from Fig. 6.8, three switches need to be turned on at a time so that the antenna can direct the current to the required tapered slot. When switch combination S1-S2-S3 is on, the current is directed towards the lower left and the antenna radiates in that particular direction. For proof of concept ON switches were modelled in CST using 3mm copper strips and OFF switches as open circuit. Figure 6.9 shows the electric field intensity at 5.8 GHz when switch combination S1-S2-S3 is on. It is observed that the electric field is concentrated in the lower left and this is thus the area of maximum radiation. The simulated electric field intensity at 6 GHz for switch combination S4-S1-S2 is shown in Fig. 6.10. It is clear that the antenna is radiating in the upper left corner for this switch combination.

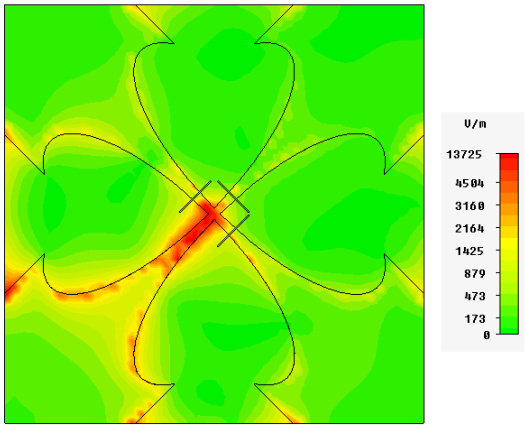

Figure 6.9: Electric Field Intensity at 6 GHz for Switch Combination S1-S2-S3.

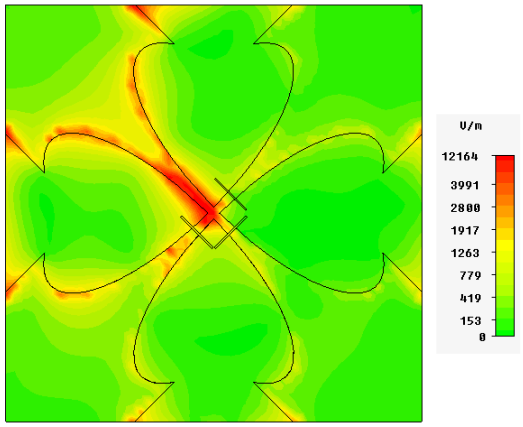

Figure 6.10: Electric Field Intensity at 6 GHz for Switch Combination S4-S1-S2.

6.2.1 Ideal Switch four way flower Vivaldi

To prove the principle, antennas with 3mm copper strips as switch S1-S2-S3 and S4-S1-S2 were fabricated and tested. The OFF switch was considered to be an open circuit. Figure 6.11 shows the measured and simulated reflection coefficient of the antenna with S1-S2-S3 on. There are slight differences between the measured and simulated results. These differences can be attributed to the fact that the antenna is very sensitive to errors in the alignment between the feed side and the centre of the ground side. Even slight fabrication and alignment errors have an effect on the reflection coefficient.

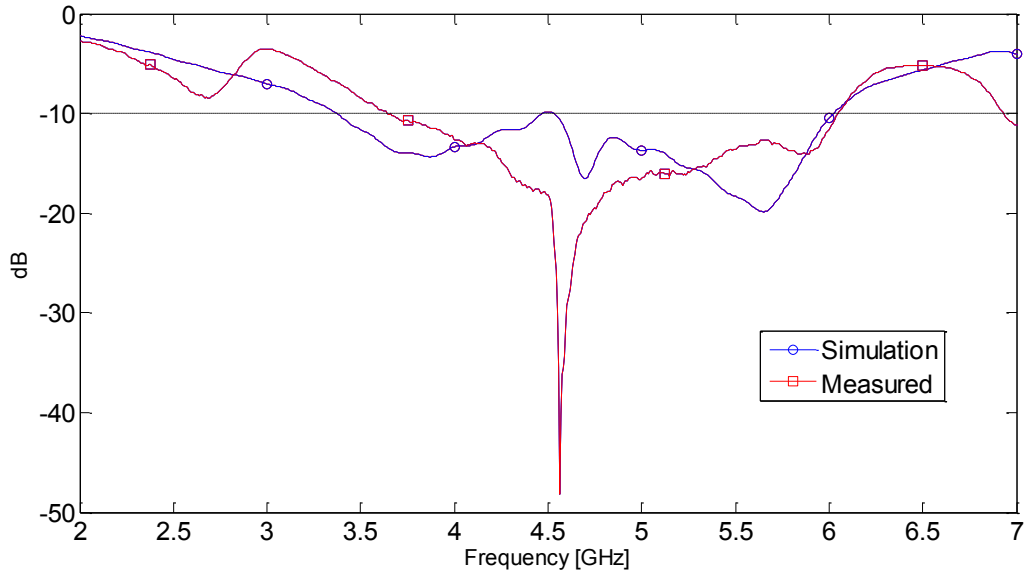

Figure 6.11: Reflection coefficient of ideal switch flower Vivaldi with S4-S1-S2 ON.

The measured and simulated radiation pattern of the antenna at 3.5 GHz, 4.75 GHz and 6 GHz in the H-plane is shown in Fig. 6.12 and 6.13. The antenna radiation pattern shape agrees well at 6 GHz and 4.75 GHz. The radiation pattern agrees slightly less well at 3.7 GHz but it is still in the same quadrant. The counterpart E-plane results are shown in Fig. 6.13 In this case the measured results are better than the simulation results for radiation pattern as the antenna radiation main beam is more concentrated and the side and back lobes are weaker.

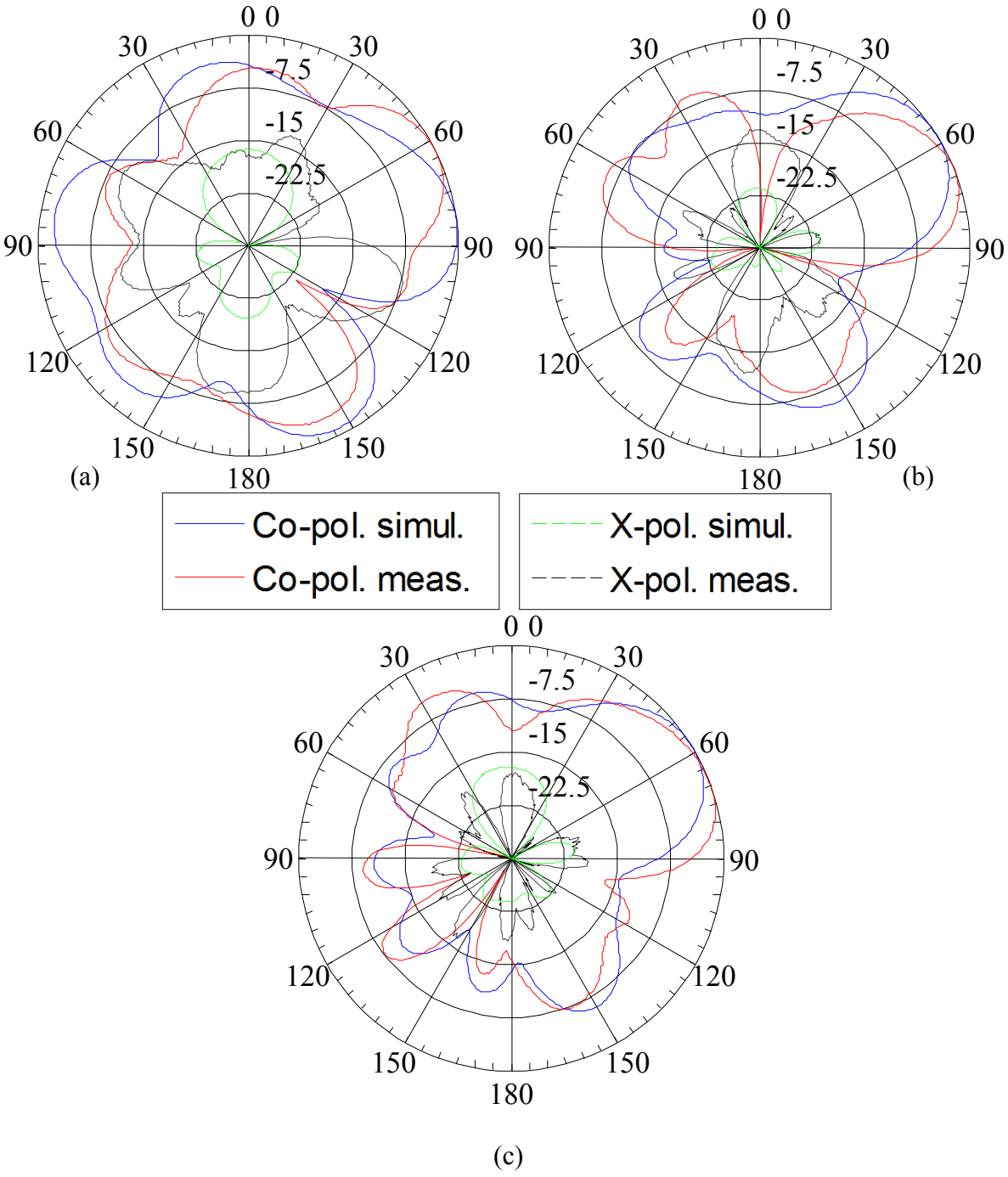

Figure 6.12: Radiation pattern (H-plane) of ideal switch flower vivaldi with S4-S1-S2 ON at (a) 3.5 GHz, (b) 4.75 GHz, and (c) 6 GHz

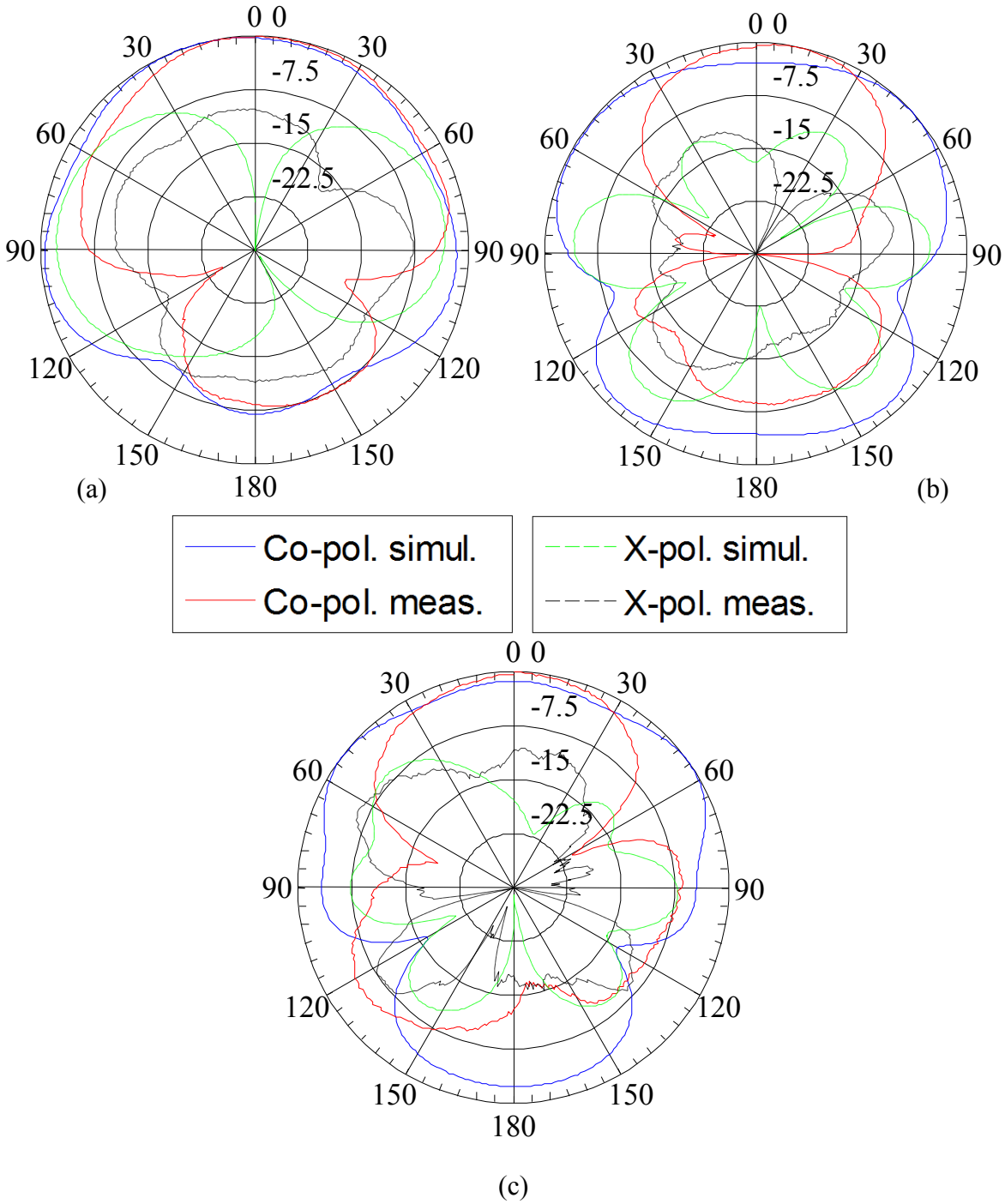

Figure 6.13: Radiation pattern (E-plane) of ideal switch flower vivaldi with S4-S1-S2 ON at (a) 3.5 GHz, (b) 4.75 GHz, and (c) 6 GHz

The reflection coefficient (measured and simulated) of the ideal switch flower Vivaldi antenna for switch combination S1-S2-S3 is shown in Fig. 6.14. Both of them show excellent agreement.

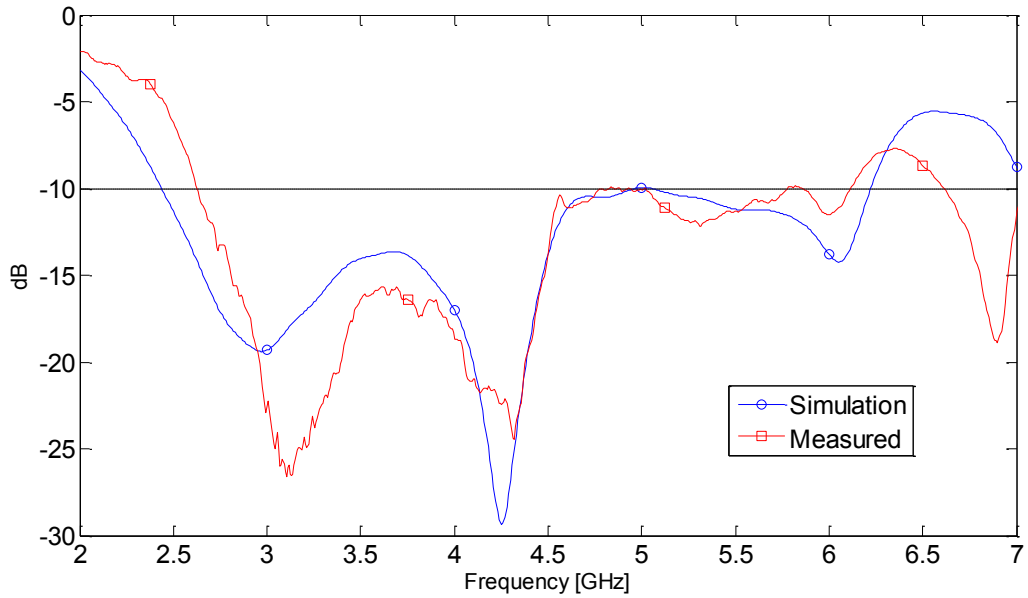

Figure 6.14: Reflection coefficient of ideal switch flower Vivaldi with S1-S2-S3 ON.

Figures 6.15 and 6.16 show the H-plane and E-plane radiation pattern (measured and simulated) results of the antenna at 3.5GHz, 4.75 GHz and 6 GHz. Again the same trend as for the previous case of H-plane results is observed. Excellent similarity at 4.75 GHz and 6 GHz is achieved. Slightly less similarity at 3.5 GHz is seen. E-plane measured results are again better as compared to the simulated results.

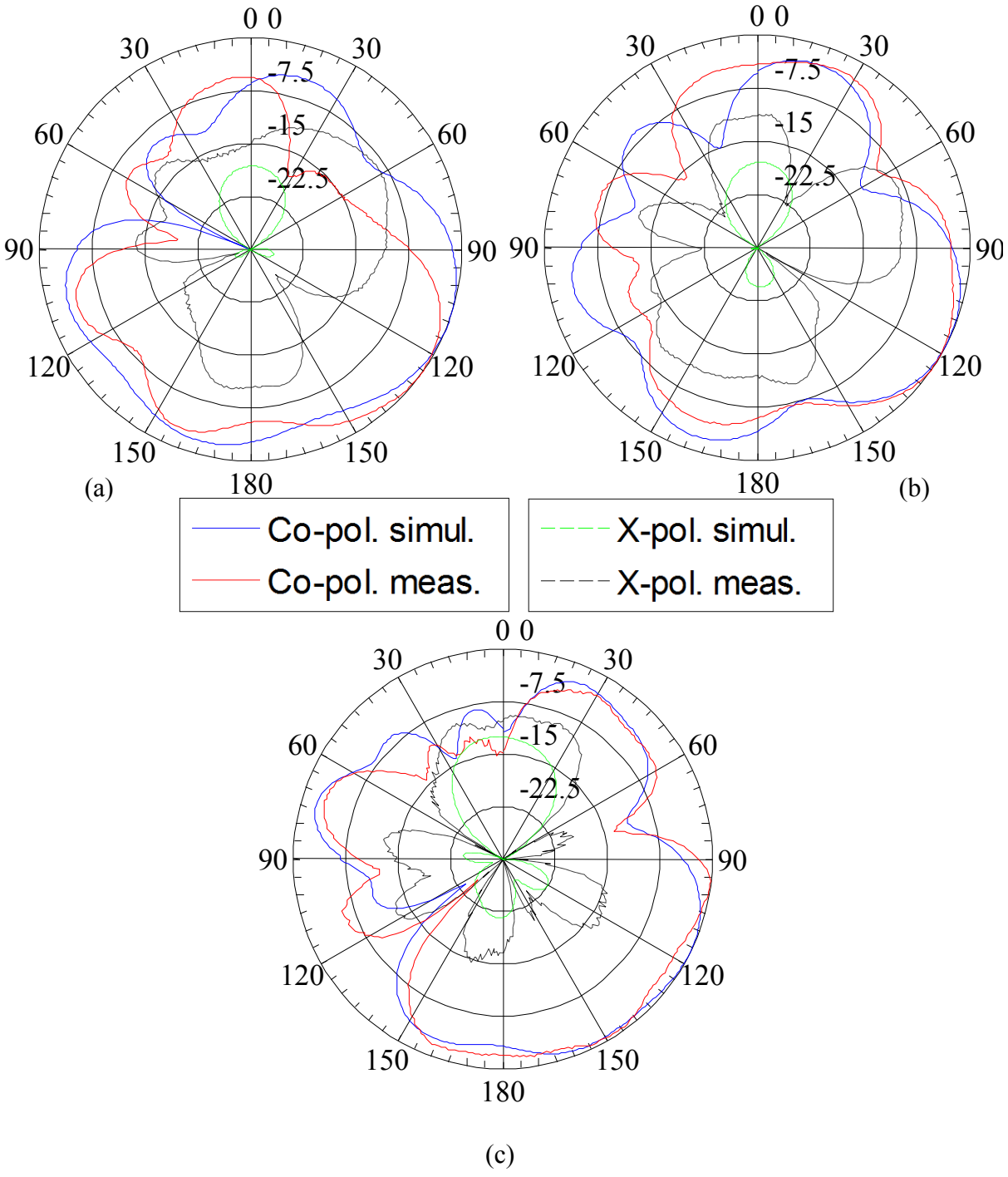

Figure 6.15: Radiation pattern (H-plane) of ideal switch flower vivaldi with S1-S2-S3 ON at (a) 3.5 GHz, (b) 4.75 GHz, and (c) 6 GHz

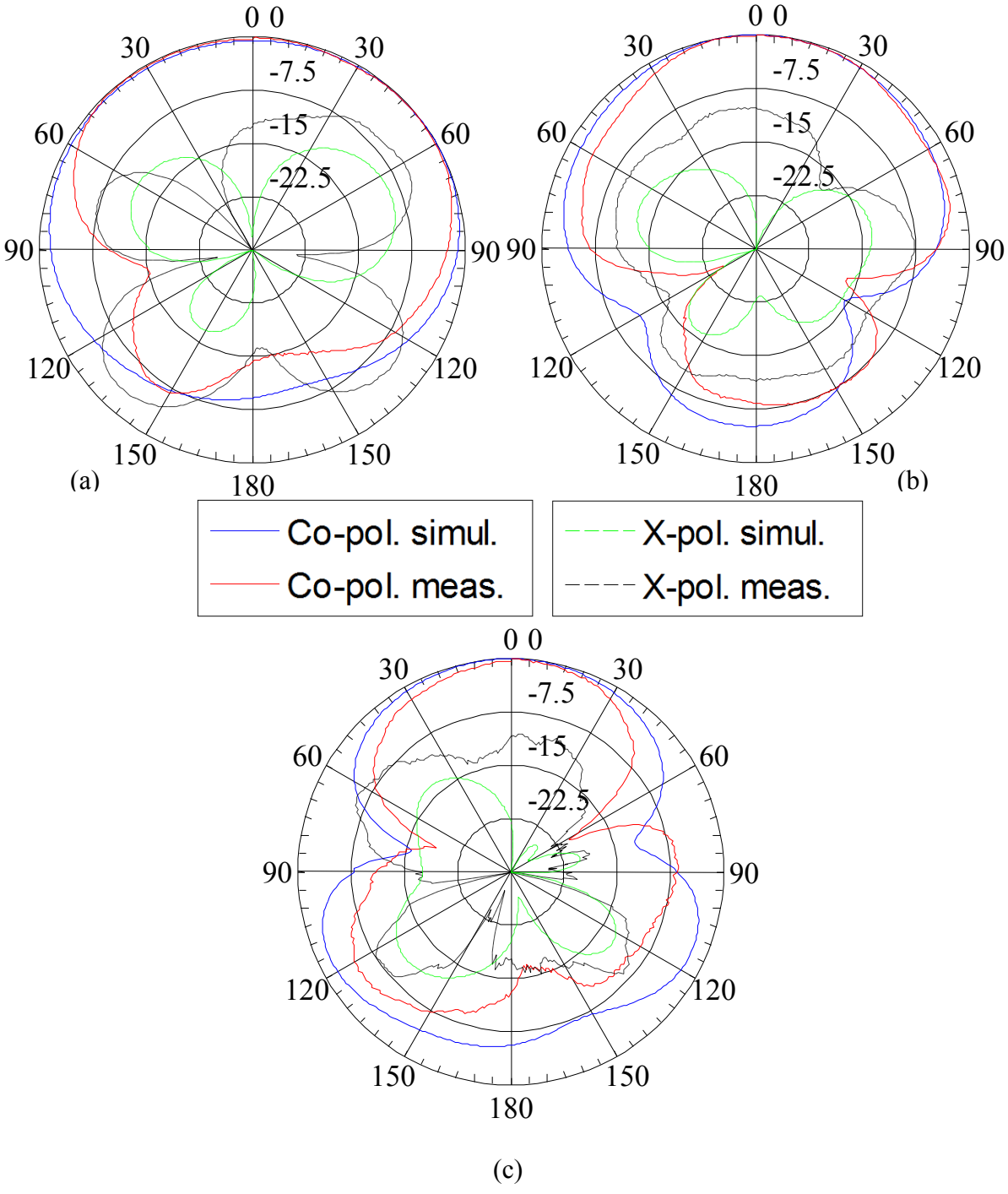

Figure 6.16: Radiation pattern (E-plane) of ideal switch flower vivaldi with S1-S2-S3 ON at (a) 3.5 GHz, (b) 4.75 GHz, and (c) 6 GHz

Figure 6.17 shows the measured gain results of the ideal switch flower Vivaldi antenna for switch combination S1, S2 & S3 and S4, S1 & S2. A maximum gain of 9.4 dB for switch combination S1, S2 & S3 and of 6.5 dB for switch combination S4, S1 & S2 is observed. There is sudden drop in gain for switch combination S4, S1 & S2; this is due to the notch occurring at 3 GHz which is also observed in Fig. 6.11.

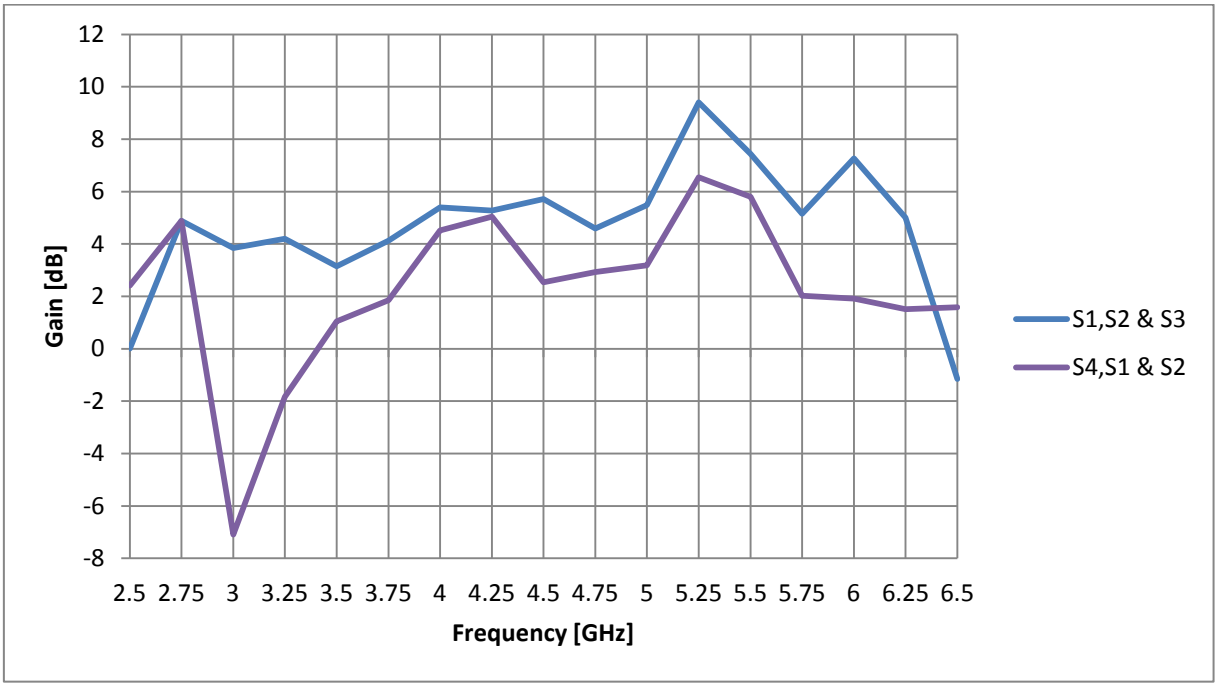

Figure 6. 17: Gain of ideal switch flower Vivaldi for two switch combinations (S1,S2 & S3 : S4,S1 & S2)

6.2.2 Single Port Flower Vivaldi Antenna

In this section, a single port flower Vivaldi antenna is fabricated with BAR 50-02V diode from Infineon used as a switch to direct the current to the required tapered slots. The antenna requires a biasing circuit to switch the diodes ON and OFF. Accu-P-0603-22pf-25V capacitors from AVX were used as DC blockers and 0604HQ-2N6XJLB inductors from coilcraft served as RF chokes. The fabricated antenna along with its biasing circuit is shown

in Fig. 6.18. The total length of this antenna is equal to 86 mm x 86 mm including the biasing circuit.

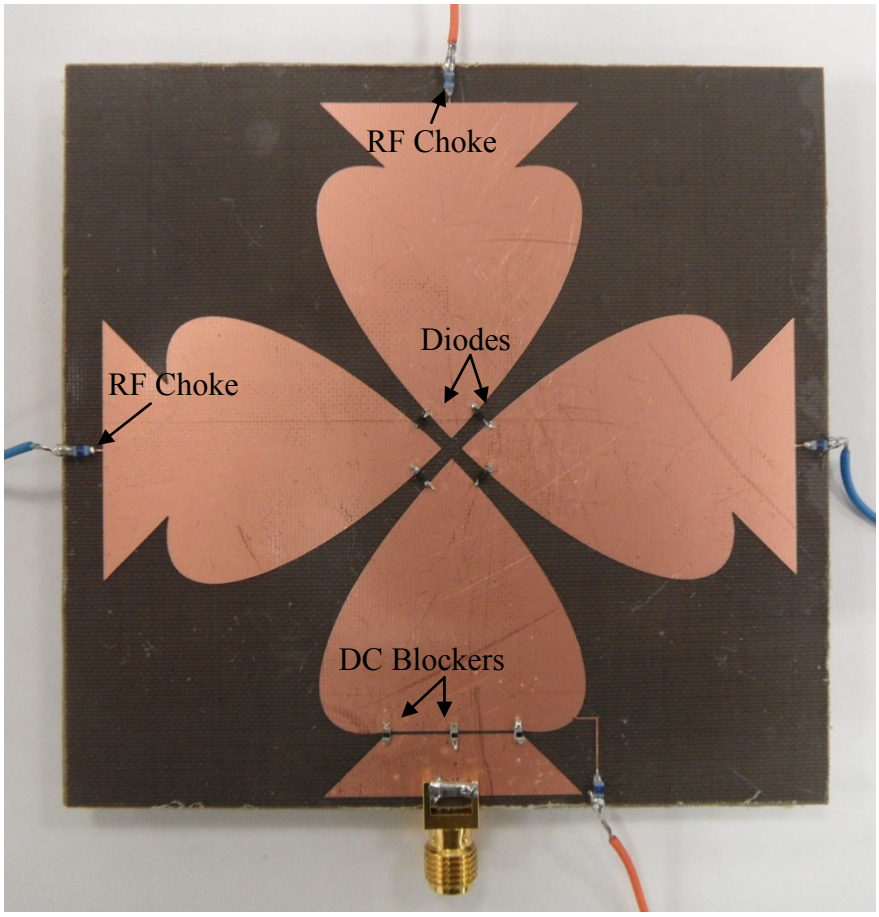

Figure 6.18: Single feed flower Vivaldi along with biasing circuit, the lumped element connecting with the bias lines are the RF chokes (inductors), the lumped elements connecting cut portions of copper are DC blockers (capacitors), the lumped element in the center are diodes.

This antenna had 4 modes of operation with radiating emitting in 4 different quadrants depending on the switch combinations. Table 6.1 shows the switch combinations along with the expected quadrant of radiation emission.

In the case of Switch Comb 1, the diodes are biased by connecting the positive of the battery with anode of 1st diode and connecting the ground of the battery with the cathode of the third diode. In this way the three diodes (S1, S2, and S3 as shown in Figure 6.8) are connected

across the battery in series. This process is repeated accordingly for the other three switch combinations.

Table 6.1: Switch Combinations vs. Antenna Radiation Emission

Switch Combination	Antenna Radiation Emission
Switch Combination 1 (S1-S2-S3 ON)	Lower Left
Switch Combination 2 (S2-S3-S4 ON)	Lower Right
Switch Combination 3 (S3-S4-S1 ON)	Upper Right
Switch Combination 4 (S4-S1-S2 ON)	Upper Left

The antenna reflection coefficient (measured and simulated) for switch combination 1, 2, 3 and 4 are shown in figures 6.19, 6.20, 6.21 and 6.22 respectively. For the simulations actual BAR 50-02V diode model is used. The -6 dB and -10 dB bandwidths for the four combinations are shown in table 6.2.

Table 6.2: Switch Combination vs. -6dB and -10dB Bandwidths

Switch Combination	-6dB	-10dB
Switch Comb 1 (S1-S2-S3)	2.6 GHz - 6 GHz	3.4 GHz-6GHz
Switch Comb 2 (S2-S3-S4)	2.95 GHz - 6GHz	3.4 GHz – 6GHz
Switch Comb 3 (S3-S4-S1)	2.5 GHz - 6GHz	4.88 GHz - 6GHz 2.64 GHz - 4.1 GHz(-9dB)
Switch Comb 4 (S4-S1-S2)	2.6 GHz - 6 GHz	2.84 GHz - 4.49 GHz (-8.5 dB) 4.7GHz - 6GHz

It is observed that the measured reflection coefficient for switch combinations 1 and 2 (where the antenna radiates in the lower left and lower right quadrants respectively) agrees well with the simulated values. For switch combinations 3 and 4 (upper right and upper left quadrant

radiation emission) the reflection coefficient had few weak notches between 4GHz – 5 GHz. Overall a wideband range is still achieved for all switch combinations. The extra errors and notches can be attributed to the non-ideal RF components (RF choke, DC blocker, diodes), biasing circuit, wires (which supplied DC bias), and fabrication errors.

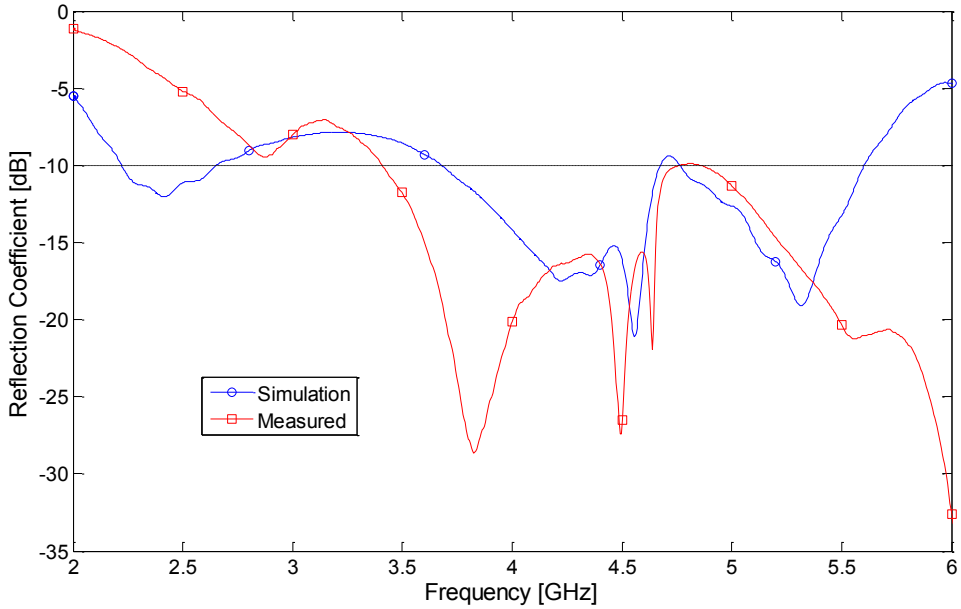

Figure 6.19: Reflection coefficient of single port flower Vivaldi antenna for switch combination 1.

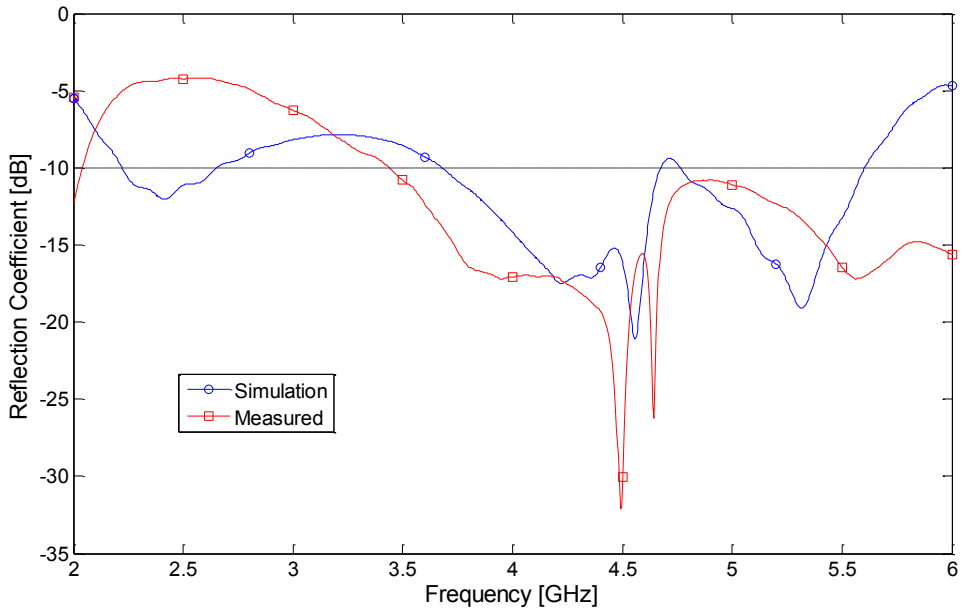

Figure 6.20: Reflection coefficient of single port flower Vivaldi antenna for switch combination 2.

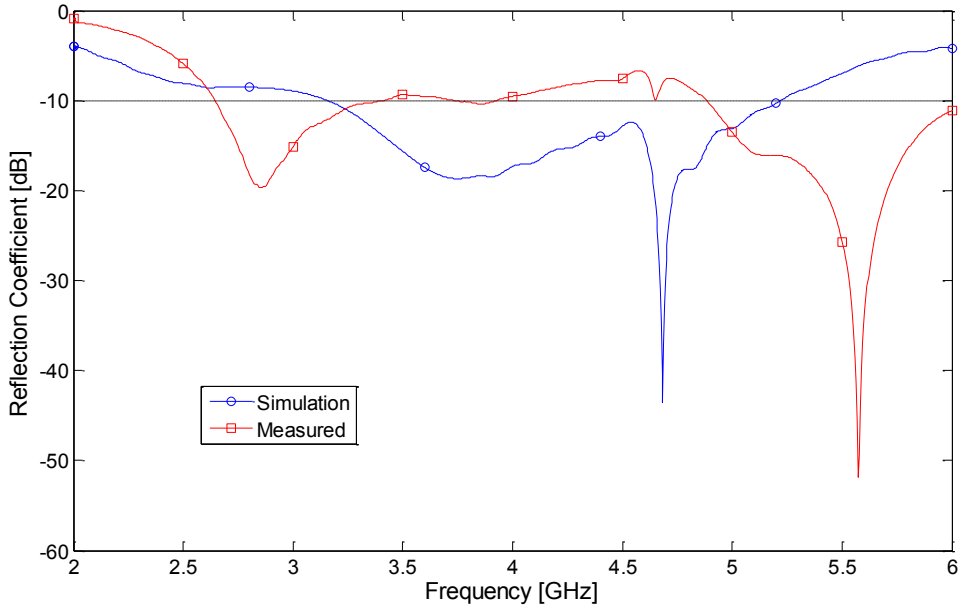

Figure 6.21: Reflection coefficient of single port flower Vivaldi antenna for switch combination 3.

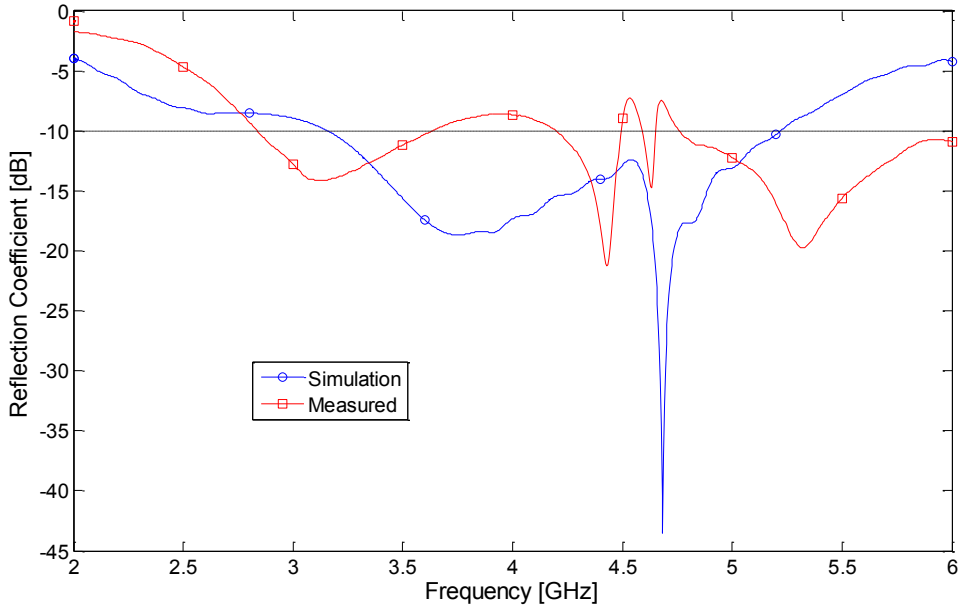

Figure 6.22: Reflection coefficient of single port flower Vivaldi antenna for switch combination 4.

6.2.2.1 Radiation pattern

The radiation pattern of the single port flower Vivaldi antenna was measured and simulated. The H-plane simulated and measured radiation pattern for switch combination 1 is shown in figure 6.23. The co-polar radiation patterns agree well with each other but the cross

polarization is significantly higher for the measured results as compared to the simulation results. The reason is that the biasing wires, biasing circuit and the biasing components (RF choke, DC blocker) along with the diode are not modelled in simulation.

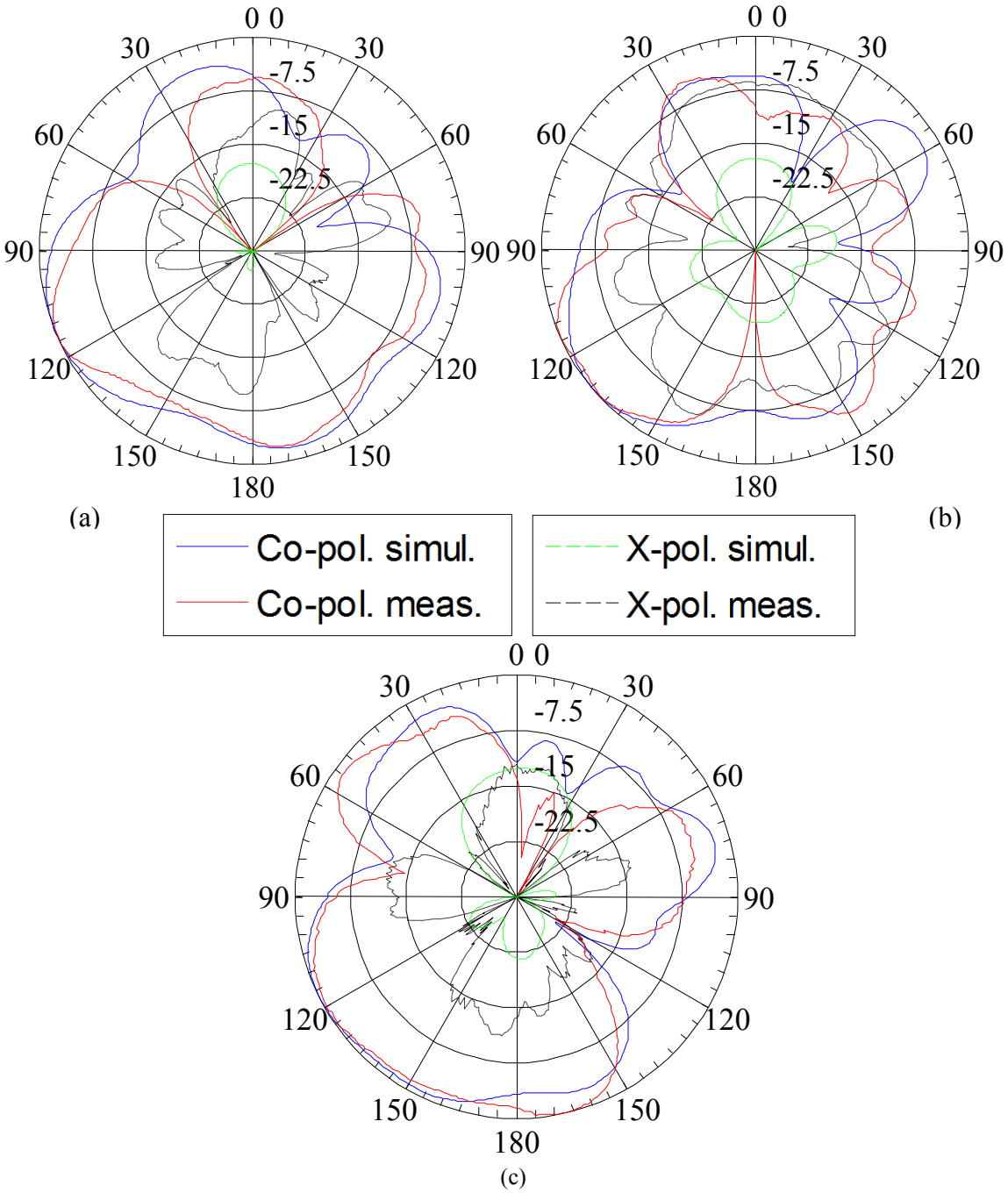

Figure 6.23: Radiation pattern (H-plane) of single port flower vivaldi with switch combination 1at (a) 3.5 GHz, (b) 4.75 GHz, and (c) 6 GHz

The E-plane simulated and measured radiation pattern for switch combination 1 is shown in figure 6.24. The measured results have lower side and back lobes as compared to the simulated results, which leads to better antenna interference rejection in these lobes.

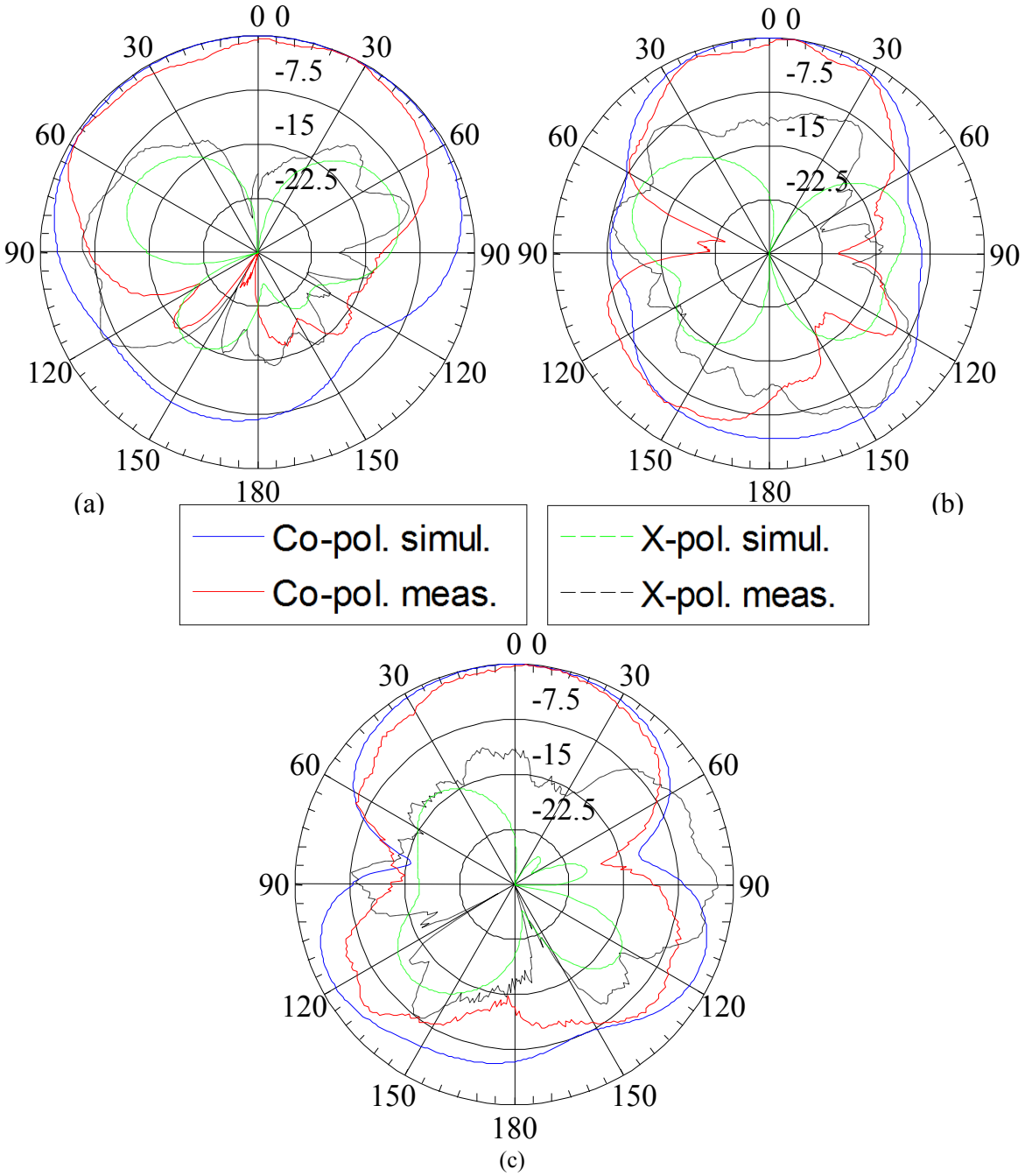

Figure 6.24: Radiation pattern (E-plane) of single port flower vivaldi with switch combination 1at (a) 3.5 GHz, (b) 4.75 GHz, and (c) 6 GHz

The H-plane simulated and measured radiation pattern for switch combination 3 is shown in figure 6.25. For this case excellent agreement is observed at 4.75 GHz and 6 GHz. At 3.5 GHz there is a slight radiation pattern mismatch but still the main direction is towards right.

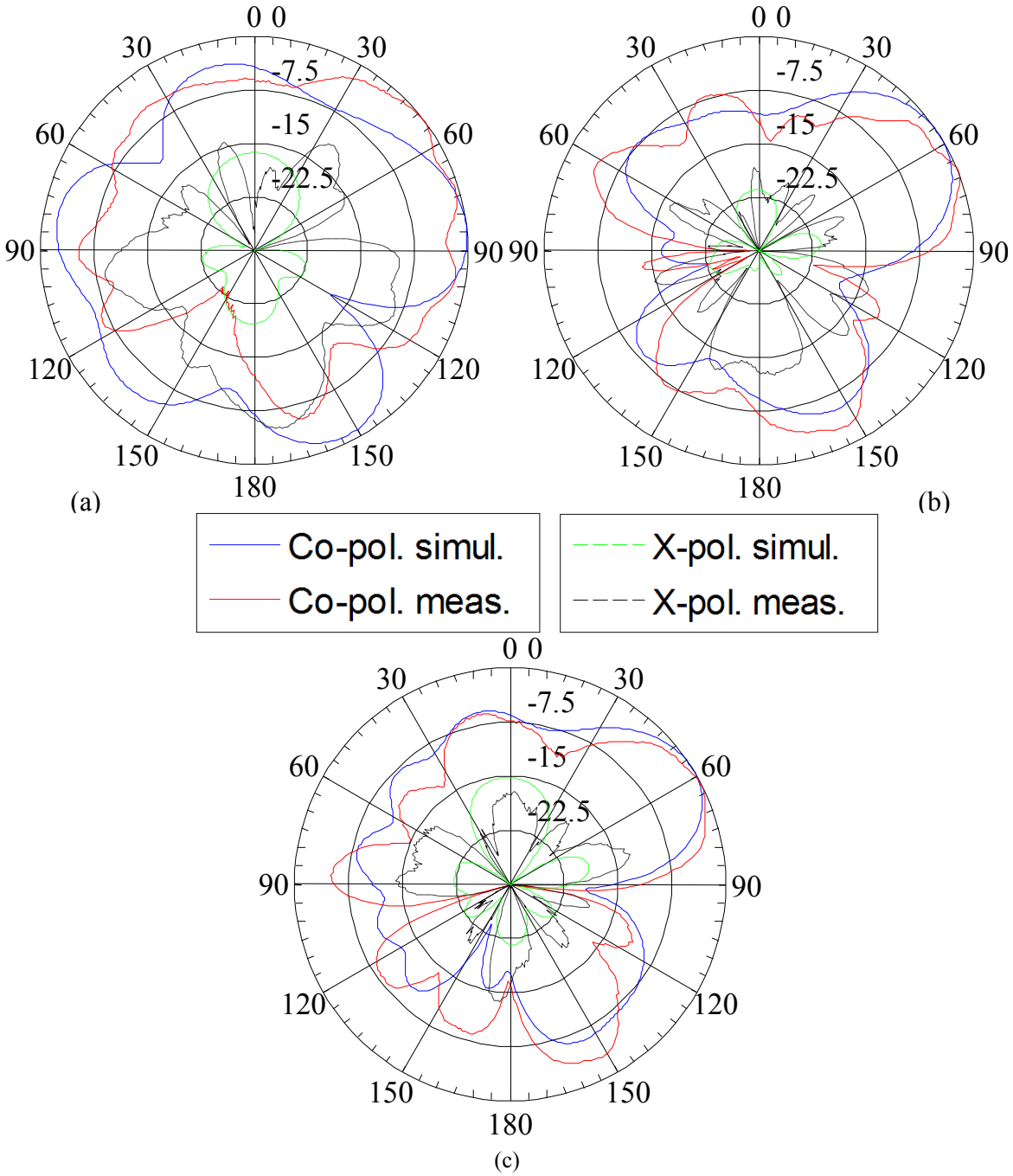

Figure 6.25: Radiation pattern (H-plane) of single port flower vivaldi with switch combination 3at (a) 3.5 GHz, (b) 4.75 GHz, and (c) 6 GHz

The E-plane simulated and measured radiation pattern for switch combination 3 is shown in figure 6.26. The measured results have lower side and back lobes as compared to the simulated results, which leads to better antenna interference rejection in these lobes.

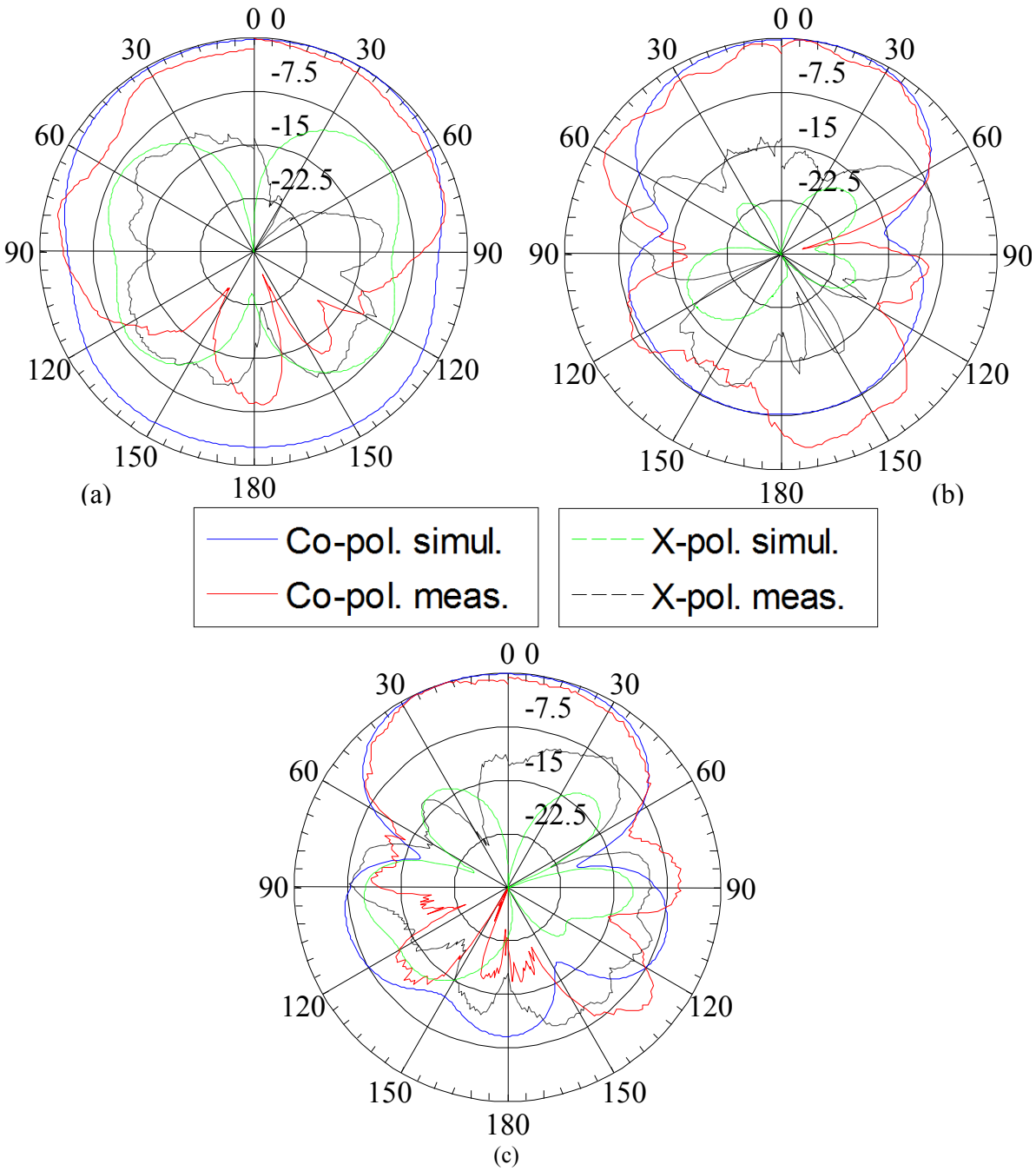

Figure 6.26: Radiation pattern (E-plane) of single port flower vivaldi with switch combination 3at (a) 3.5 GHz, (b) 4.75 GHz, and (c) 6 GHz

Figure 6.27 shows the H-plane radiation pattern for the single port flower Vivaldi for all switch combinations. Four different directions are obtained for all the frequencies measured and this proposed antenna thus holds promise as a pattern reconfigurable device in a number of applications. The side lobes power density is high in some cases and this situation can be improved by introducing more isolation between the respective tapered slots. One way to reduce side lobes is to use RF-MEMS, as they form a physical connection to block current very efficiently from entering the unwanted tapered slots. This is proposed as future work.

The gain of the four switch configurations of the antenna was measured and is shown in figure 6.28. A maximum gain of 9.42, 9.55, 6.65, and 5.95 dB was achieved at 5.25 GHz for the switch combinations 1, 2, 3 and 4 respectively (as shown in Table 6.1). The simulated gain at 5.25 GHz was equal to 5.05 dB, 5.05 dB, 7.16 dB and 7.16 dB for the 4 switch combinations. The measured gain is higher as compared to simulation for switch combinations 1 and 2, but is lower for switch combinations 3 and 4. Over the entire operating bandwidth good gain characteristics are obtained except from 5.75 GHz to 6 GHz.

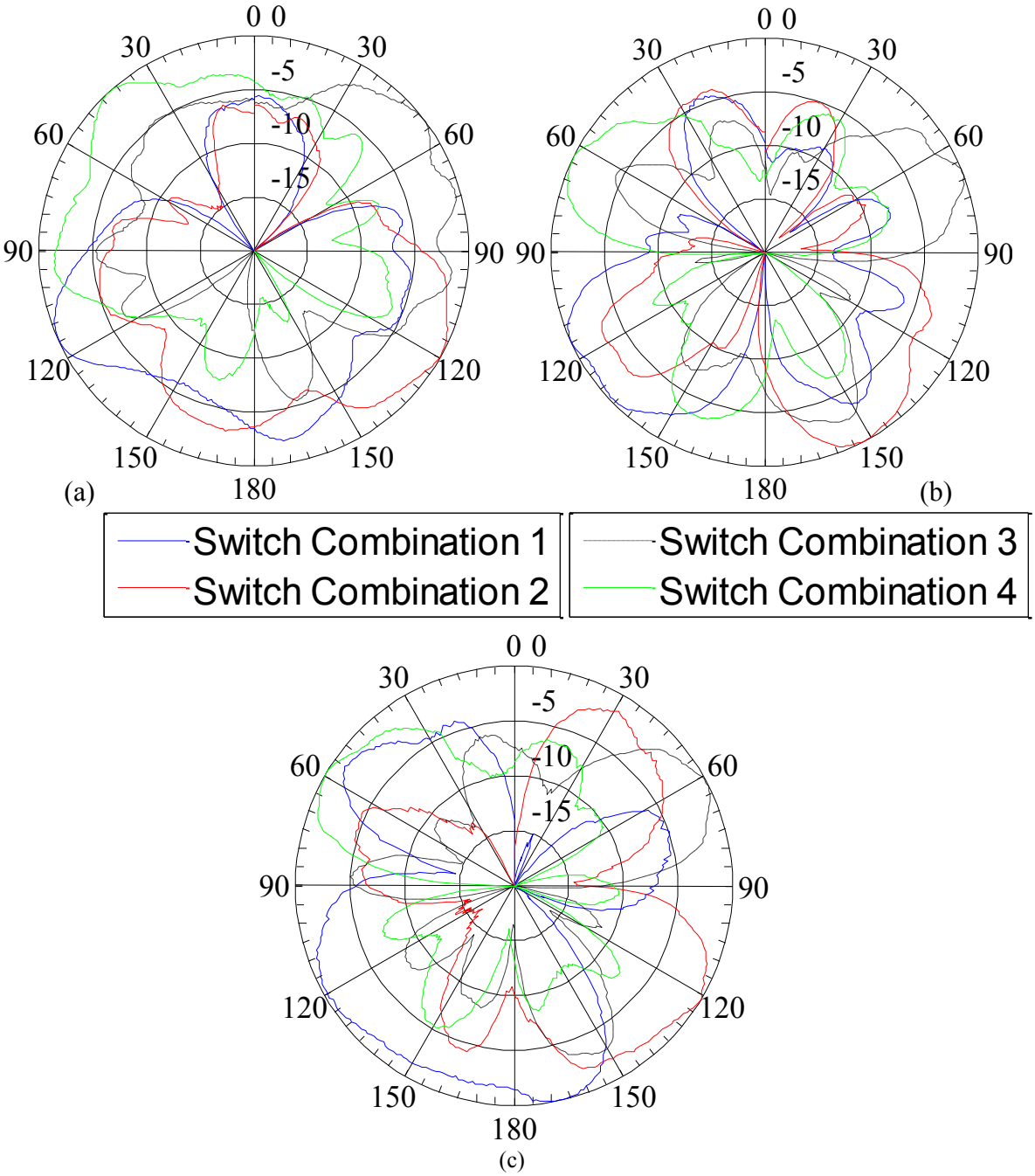

Figure 6.27: Radiation pattern (H-plane) of single port flower vivaldi with all switch combinations at (a) 3.5 GHz, (b) 4.75 GHz, and (c) 6 GHz

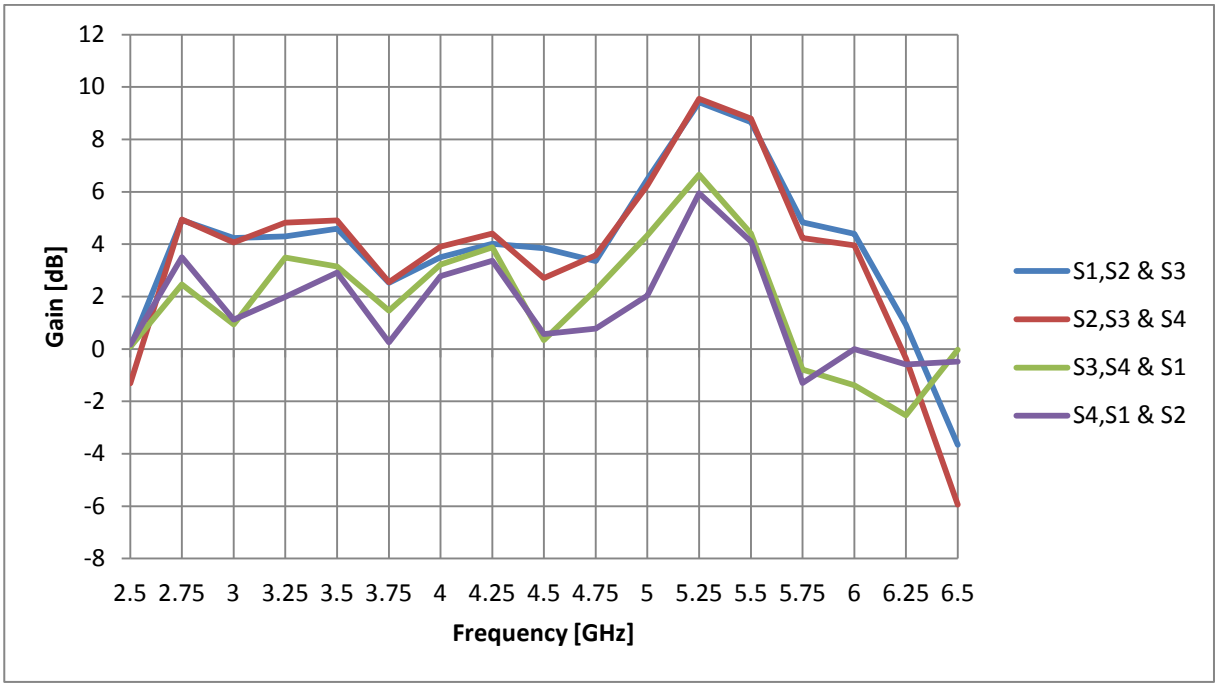

Figure 6.28: Gain of ideal switch flower Vivaldi for all switch combinations

6.3 Vital Signs Monitoring using single port flower Vivaldi antenna

The antenna designed in this chapter was used to measure the heart and breathing rate of a person. This was done to establish whether a system consisting of one antenna would be able to detect the heart rate in all possible directions (360^0) around a single antenna by using different switch combinations to ensure that the person's chest is present in the direction of maximum antenna gain. The system can be programmed to try different switch combinations and detect a returned signal with a certain frequency range (Heart and Breathing Frequency Range) in it or movement artefacts akin to a person. In this way the direction of the person can be determined and the antenna beam is directed appropriately. The system may also operate by possessing a separate motion detector to locate the targeted person and then direct antenna beam in that direction for heart and breathing rate monitoring. Ideal antennas with copper as switches were used to detect the vital signs as the antenna with actual switches contained long DC wires that caused degradation of the radiation pattern and in turn the

accuracy of the vital signs measurement decreases. These limitations caused by radiation pattern degradation can be overcome by using the coin battery [10] and integrated chips techniques [11].

The heart rate was measured with the subject in many directions with respect to the max gain direction of the antenna as shown in the Fig. 6.29. This figure contains the following 5 different configurations in which experiments were performed:

1) Person directly in front of max antenna gain.
2) Person at a 45^0 angle from max antenna gain.
3) Person in the direction of max antenna gain but with transmitted signal passing directly through the receiving antenna.
4) Person at 90^0 from maximum antenna gain.
5) Person at 180^0 from maximum antenna gain.

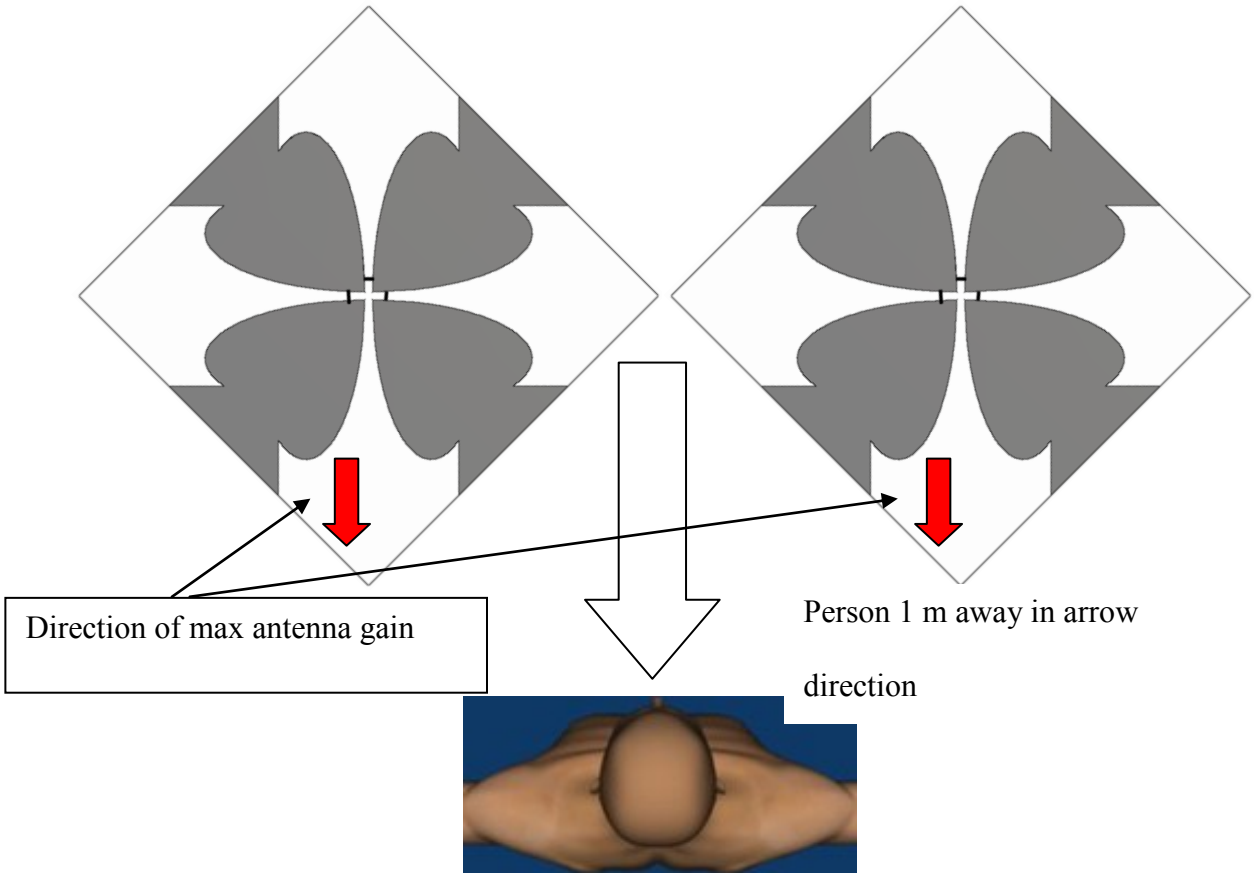

(a)

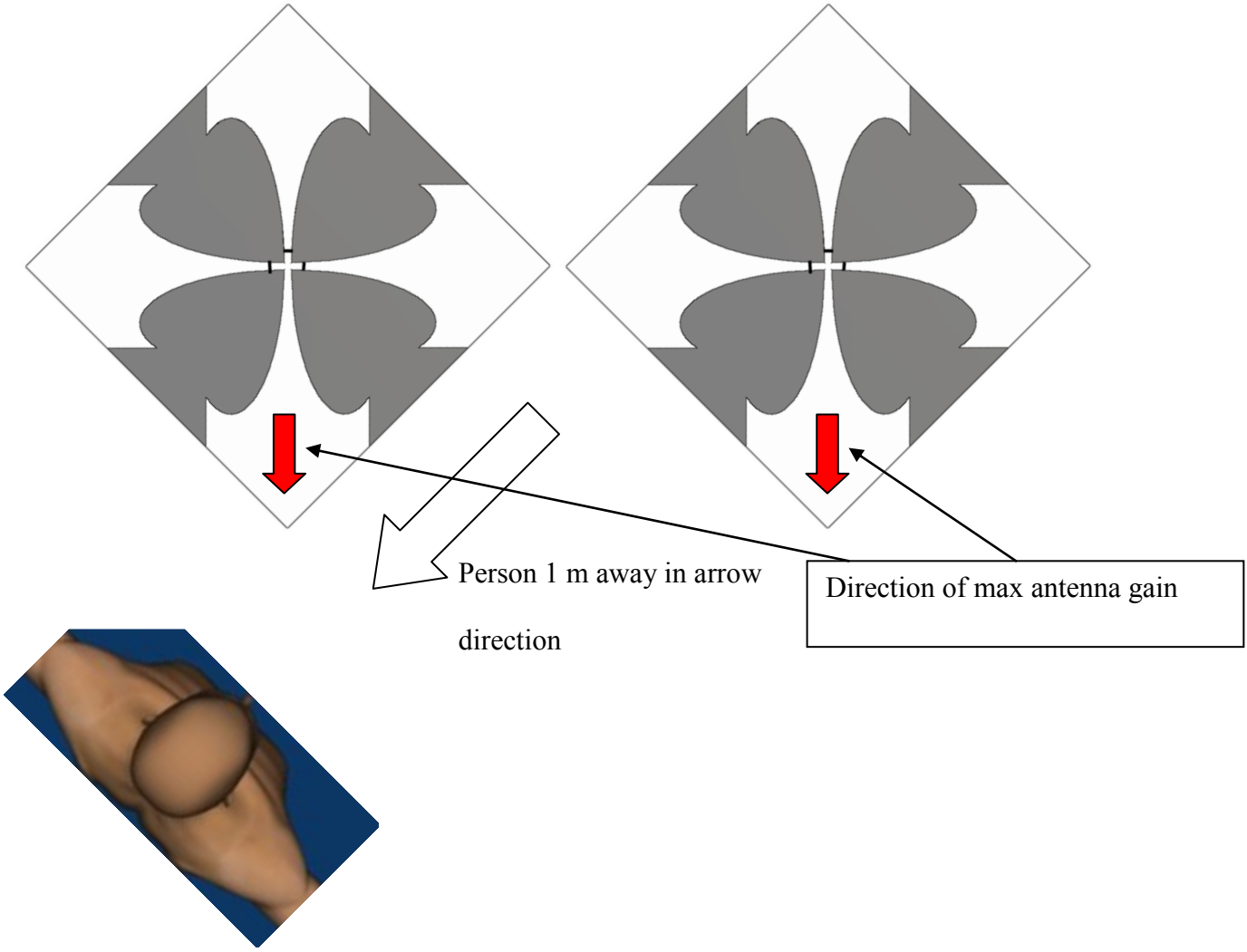
Person 1 m away in arrow
direction
Direction of max antenna gain

(b)

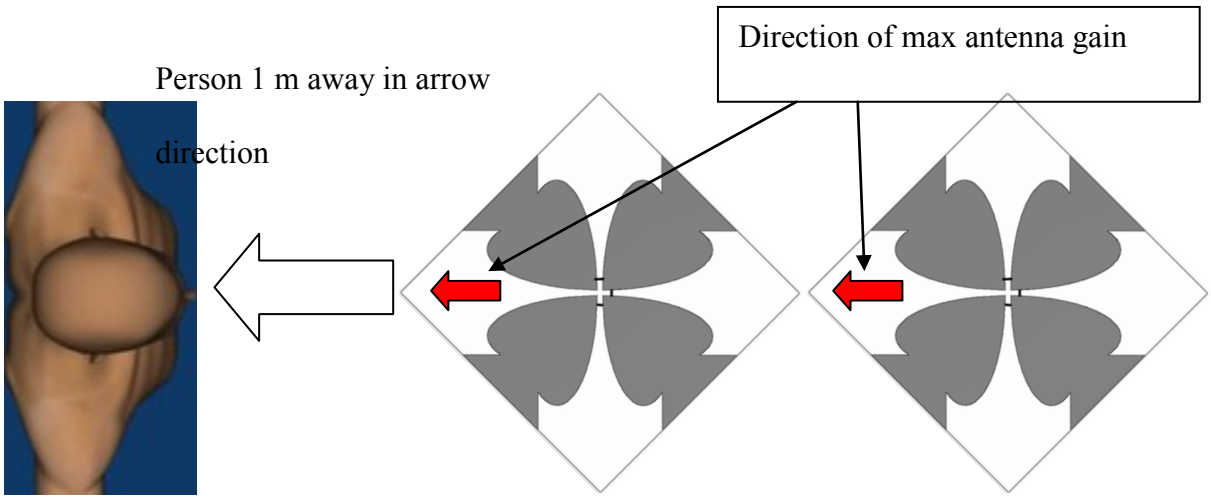
Direction of max antenna gain
Person 1 m away in arrow
direction

(c)

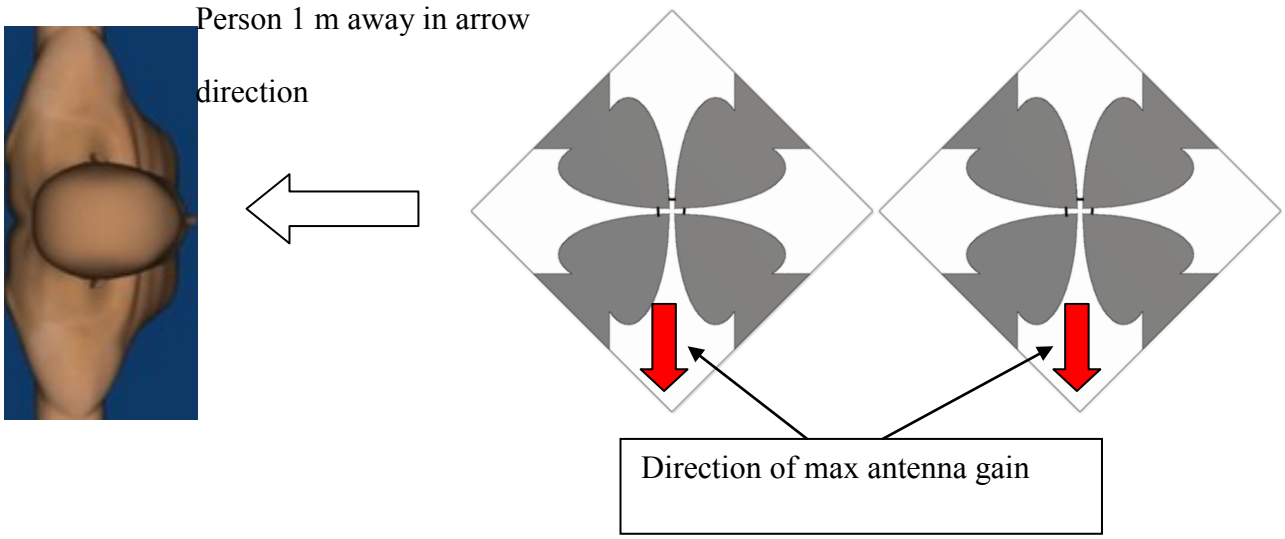

(d)

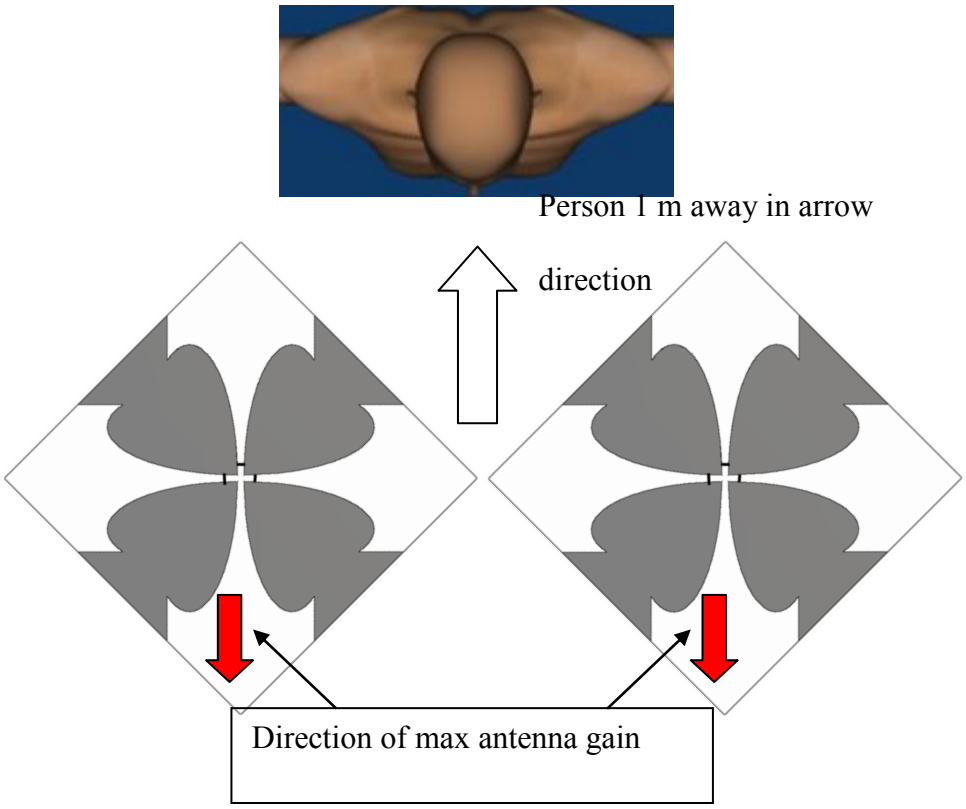

(e)

Figure 6.29: Experimental Configurations: (a) Person directly in front of max antenna gain, (b) Person at a 45^0 angle from max antenna gain, (c) Person in the direction of max antenna gain but with transmitted signal passing directly through the receiving antenna, (d) Person at 90^0 from maximum antenna gain, (e) Person at 180^0 from maximum antenna gain.

The experimental setup is as described in section 3.4.1 with the 4-way ideal switch flower Vivaldi antenna (from section 6.2.1) as the transmitting and receiving antenna. Five minute measurements were recorded for each configuration. The subject used was person 1 from section 4.3.3 and carrier wave frequency was 7 GHz. It was discussed in section 3.5 that as frequency increased up to 9 GHz, the detection accuracy increased. For the 4-way ideal switch flower Vivaldi antenna the highest frequency of correct operation was 7 GHz, so it was chosen for experimentation. Table 6.3 shows the statistical analysis of the results obtained from the ECG module and Doppler radar for the various configurations described in Fig. 6.29. The analysis includes SNR, Bland-Altman analysis (as defined in section 3.4.3) and the accuracy of Doppler radar measurements within 1,2,3,4 and 5 BPM of the ECG reference module. It can be seen that when the person is directly in front of the antenna as in the case of configuration 1, the accuracy within 3 BPM is 91.4% showing the accuracy of the antenna in measuring the vital signs in the correct configuration. When the person is at the angle of 45^0 from the direction of maximum antenna gain as in configuration 2 we see that the accuracy within 3 BPM drops to 76.7 %. The accuracy within 3 BPM of the antenna in configuration 3 when the transmitted signal passes directly over the receiving antenna is 78.4%. In the case of configurations 4 and 5 with the person 90^0 and 180^0 away from the direction of maximum gain the accuracy within 3 BPM has expectedly dropped to 16.3% and 25.6%.

Table 6.3: Statistical Analysis of heart rate from ECG and Doppler Radar for different experimental considerations (from fig. 6.29). All BA results are in BPM.

Configuration from fig. 6.29.	**1**	**2**	**3**	**4**	**5**
SNR	1.2614	0.7917	0.7795	0.4874	0.4007
Accuracy (%) (within 1 BPM)	63.1	44.9	48.2	5.6	10.6
Accuracy (%) (within 2 BPM)	89.4	67.4	68.8	12.6	20.3
Accuracy (%) (within 3 BPM)	91.4	76.7	78.4	16.3	25.6
Accuracy (%) (within 4 BPM)	92.7	78	84.4	19.3	31.6
Accuracy (%) (within 5 BPM)	93.4	79.7	87.7	20.9	36.2
ECG Heart Rate(BPM)	93.5	92.8	85.3	90.8	88.1
Doppler Heart Rate (BPM)	93.2	92	84.9	99	94.6
Mean Diff (BA)	0.3075	0.8522	0.4361	-8.1419	-6.4453
Standard Deviation (BA)	3.1092	6.2645	4.0629	16.0715	14.4563
d +1.96 s_d (BA)	6.4016	13.1307	8.3994	23.3582	21.8891
d -1.96 s_d (BA)	-5.7866	-11.426	-7.5272	-39.6420	-34.7797

Figure 6.30 shows the Bland-Altman plots for the various configurations and it can be clearly seen that the difference between the Doppler radar results and the reference ECG module is near the zero line for the first three configurations and deteriorates rapidly for the last two configurations.

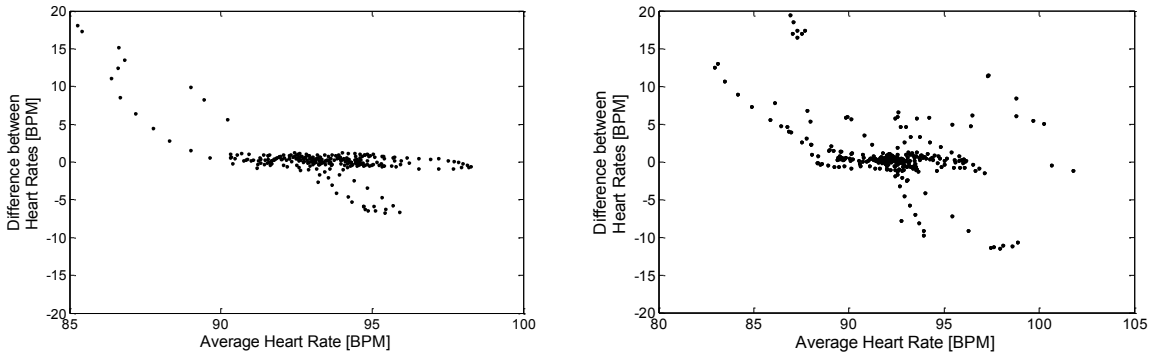

(a) (b)

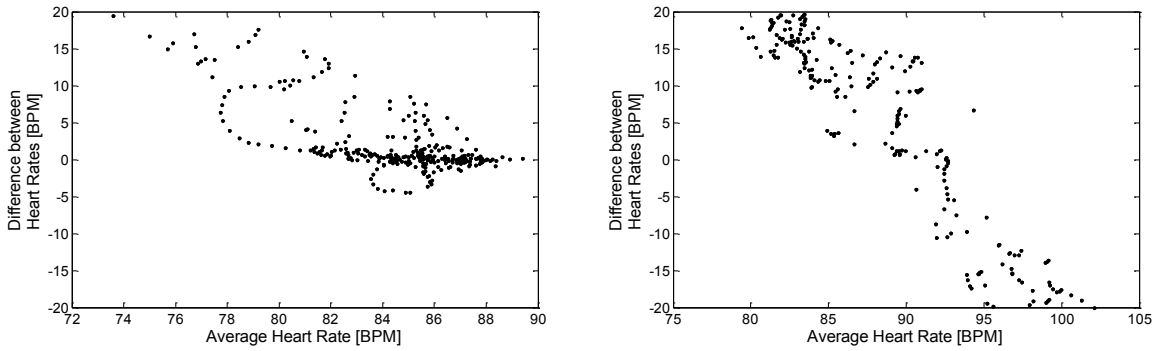

(c)

(d)

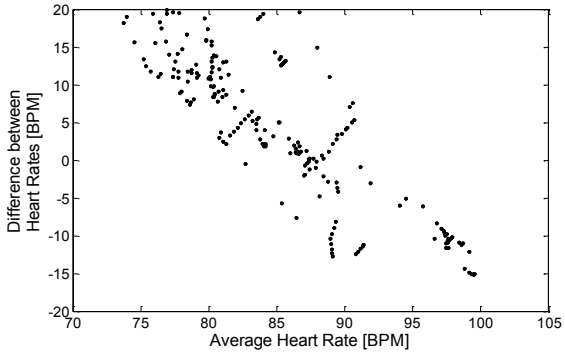

(e)

Figure 6.30: Bland-Altman plots for heart rate calculated using ECG device and Doppler radar for experimental configurations from fig 6.29. (a) 1st configuration, (b) 2nd configuration, (c) 3rd configuration, (d) 4th configuration and (e) 5th configuration.

Figure 6.31 shows the ECG graphs versus the corresponding filtered Doppler radar graphs for the different configurations. Clear heart beat peaks for the Doppler radar graphs with good matches to corresponding ECG graphs are observed for first three configurations while the last two configurations have very weak, erroneous and noisy peaks. Figure 6.32 shows the beats per minute (BPM) versus time graph for both the ECG module and Doppler radar for the different configurations. The first three configurations show a good agreement between the reference and the Doppler radar BPM graphs, while for configurations 4 and 5 the Doppler radar BPM are not following the reference ECG signal's BPM graph.

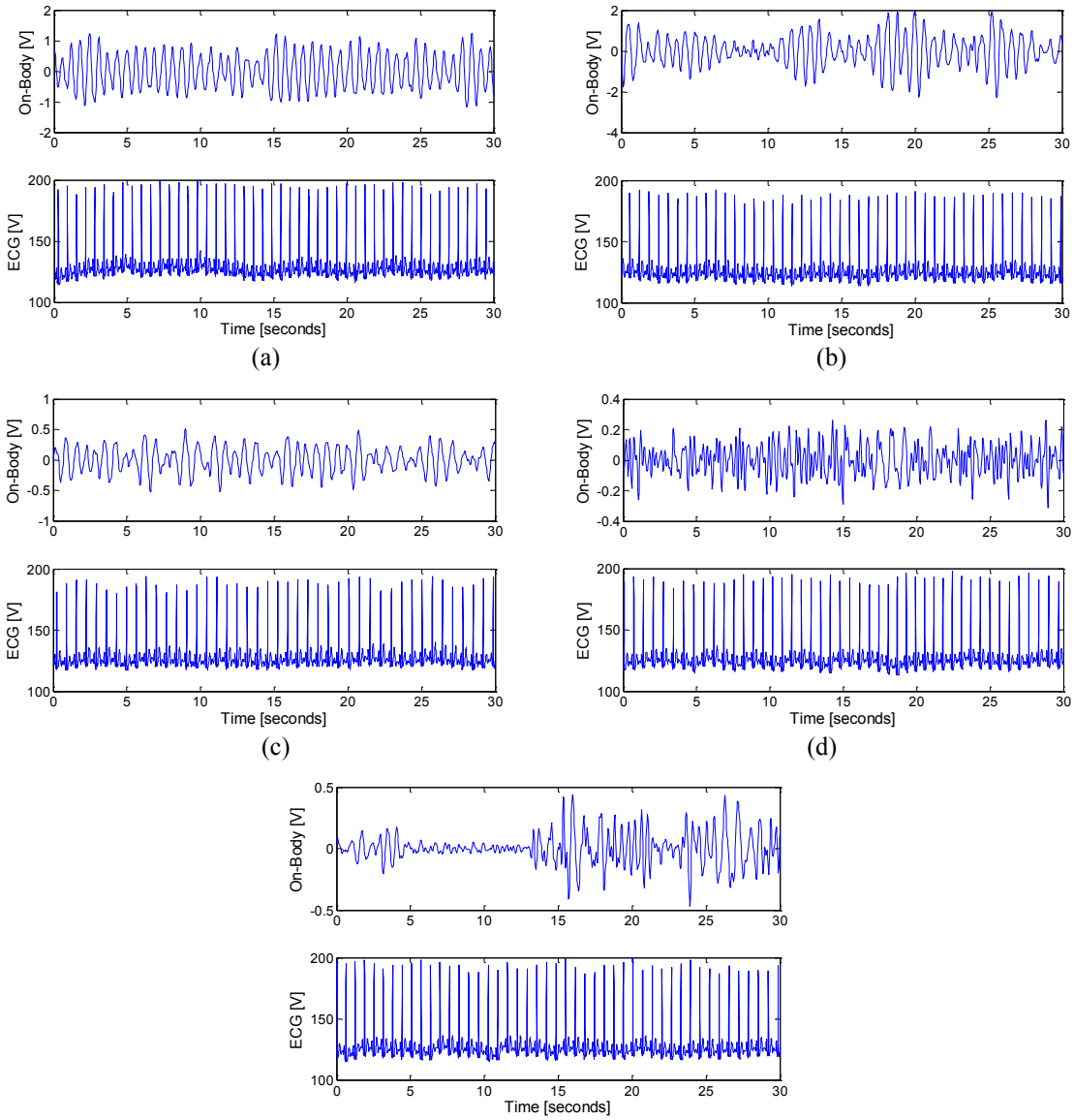

Figure 6.31: ECG signal and filtered Doppler Radar heart rate plots for experimental configurations from fig 6.29. (a) 1st configuration, (b) 2nd configuration, (c) 3rd configuration, (d) 4th configuration and (e) 5th configuration.

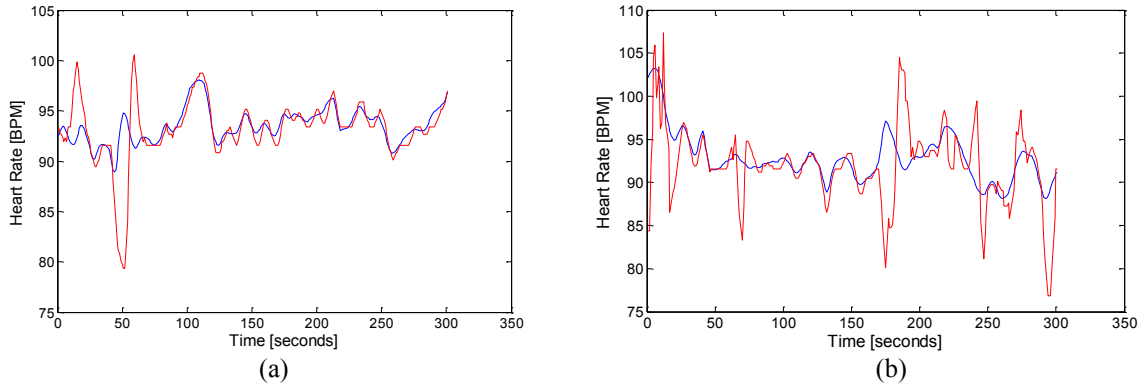

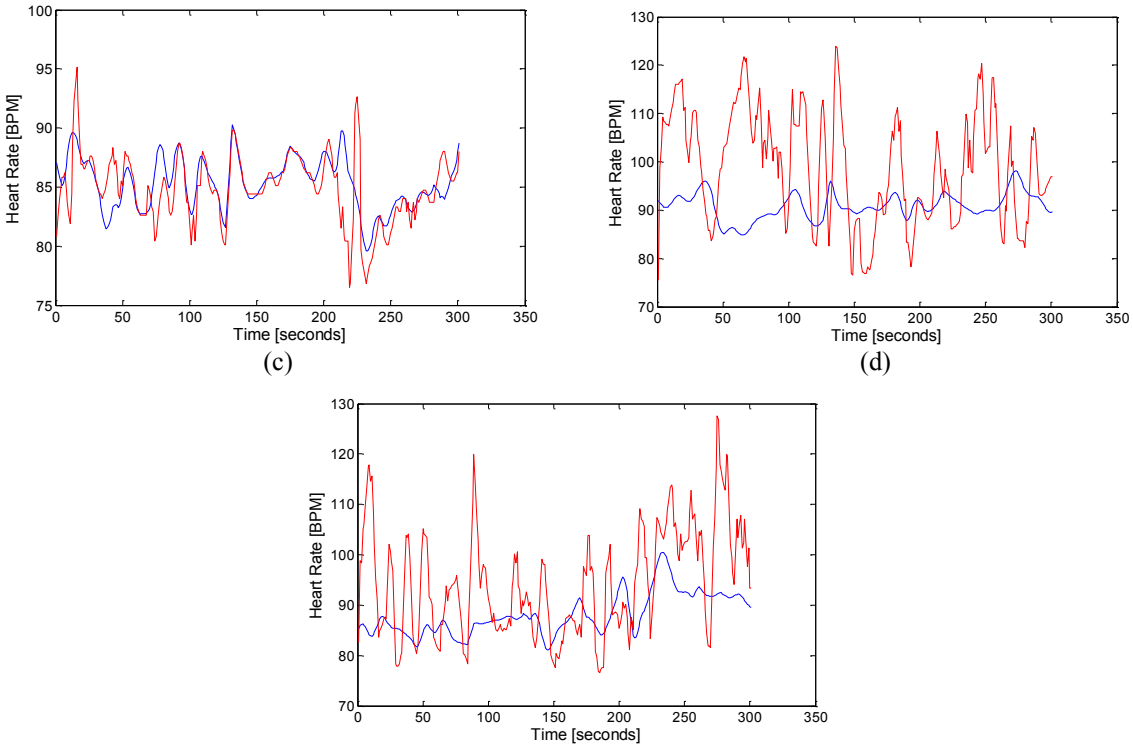

Figure 6.32: Heart rate [BPM] vs. Time for the ECG signal (blue) and Doppler radar (red) for experimental configurations from fig 6.29. (a) 1st configuration, (b) 2nd configuration, (c) 3rd configuration, (d) 4th configuration and (e) 5th configuration.

In case of the first configuration as the person is in the direction of maximum gain of the antenna best results are expected. At 45^0 from the maximum gain a drop off of accuracy happens as that region has slightly less gain. The case of configuration 3 involves the transmitted signal crossing the receiving antenna which results in much more coupling between the antennas as compared with the first case. This unwanted coupling reduces the Doppler radar accuracy. For configurations 4 and 5 it is obvious that being 90^0 and 180^0 away from the maximum gain point has a negative effect on the accuracy. This results from the fact that the side and back lobes of the designed flower Vivaldi antenna are much weaker as compared with the main lobe, which reduces antenna accuracy in those directions. -45 and 270 degrees were not tested due to symmetry.

The results in this section showed that this antenna can detect the heart rate when its beam is directed towards the chest or is at an angle of 45^0 from the chest. It cannot detect it in other regions which include side and back lobes. Hence, theoretically it can be used to find the direction of the person within a certain distance, based on which the heart rate can be monitored. In this way this antenna can effectively be used for vital signs monitoring 360^0 around it.

6.3.1 Respiration

Table 6.4 shows statistical analysis results for the breathing rates extracted using the Doppler radar monitoring method and MLT1132 chest belt for different configurations as shown in fig. 6.29. The statistical analyses include the accuracy, average Doppler radar and chest belt breathing rates, and the Bland-Altman measures (mean difference, standard deviation and the 95 % confidence intervals). It is observed that for configuration 1 (when the person is in line with max antenna gain) the breathing rate is very easily detectable with 95% accuracy (within 1 breath). Excellent accuracy (within 1 breath) of 80.3% is also obtained for configuration 3 (in which the transmitted signal passes through the receiving antenna but the maximum antenna gain is in line with the person). The accuracy for configuration 3 is lower than that for configuration 1 because of more coupling between antennas for configuration 3. For configuration 2 (45^0 between max antenna gain direction and person) less accuracy of 41.7% (within 1 breath) and 84.2 % (within 3 breaths) is achieved again because of lower gain at that angle. While for configuration 4 (90^0 between max antenna gain direction and person) and configuration 5 (180^0 between max antenna gain direction and person), as expected low accuracies (within 1 breath) of 15.8% and 25.5% are obtained. This is again due to the low side and back lobes of the flower Vivaldi antenna.

Table 6.4: Statistical analysis of breathing rate from MLT1132 chest belt and Doppler Radar for different experimental configurations (from fig. 6.29). All BA results are in breaths per minute.

Configuration from fig. 6.29	**1**	**2**	**3**	**4**	**5**
Accuracy (%) (within 1)	95	41.7	80.3	15.8	25.5
Accuracy (%) (within 2)	96.9	68.3	90	32.4	47.9
Accuracy (%) (within 3)	97.7	84.2	95.3	49.4	66
Accuracy (%) (within 4)	100	91.5	98.8	61.8	87.6
Accuracy (%) (within 5)	100	95	100	74.5	98
MLT1132 Belt Breathing Rate	12.6	13.8	12	12.4	12.4
Doppler Breathing Rate	12.4	14.5	11.6	15.3	10.7
Mean Diff (BA)	0.1602	-0.6960	0.3656	-2.8267	1.6337
Standard Deviation (BA)	0.6955	2.1740	1.0687	3.2360	2.1208
d +1.96 s_d (BA)	1.5234	3.5650	2.4603	3.5159	5.7904
d -1.96 s_d (BA)	-1.2029	-4.9570	-1.7291	-9.1692	-2.5231

Figure 6.33 (a), (b) and (c) show the Breathing rate in breaths per minute from the Doppler Radar and the MLT1132 chest Belt for configuration 1, 3 and 5 (from Fig. 6.29). Figure 6.33 (d),(e) and (f) show a 50 sec breathing signal from the Doppler Radar and the MLT1132 chest Belt for configuration 1, 3 and 5 (from Fig. 6.29). Configuration 1 shows almost perfect agreement between MLT1132 belt and Doppler radar results. For configuration 2 graphs, we see that coupling has a slight negative effect on the detection results. While for configuration 3, a very clear degradation of results is observed. The results show that this antenna can detect the breathing rate when its beam is directed towards the chest. It cannot detect it in other regions. Hence, theoretically it can be used to find the direction of the person within a certain

distance, based on which the breathing can be monitored. In this way this antenna can effectively be used for breathing rate monitoring 360^0 around it.

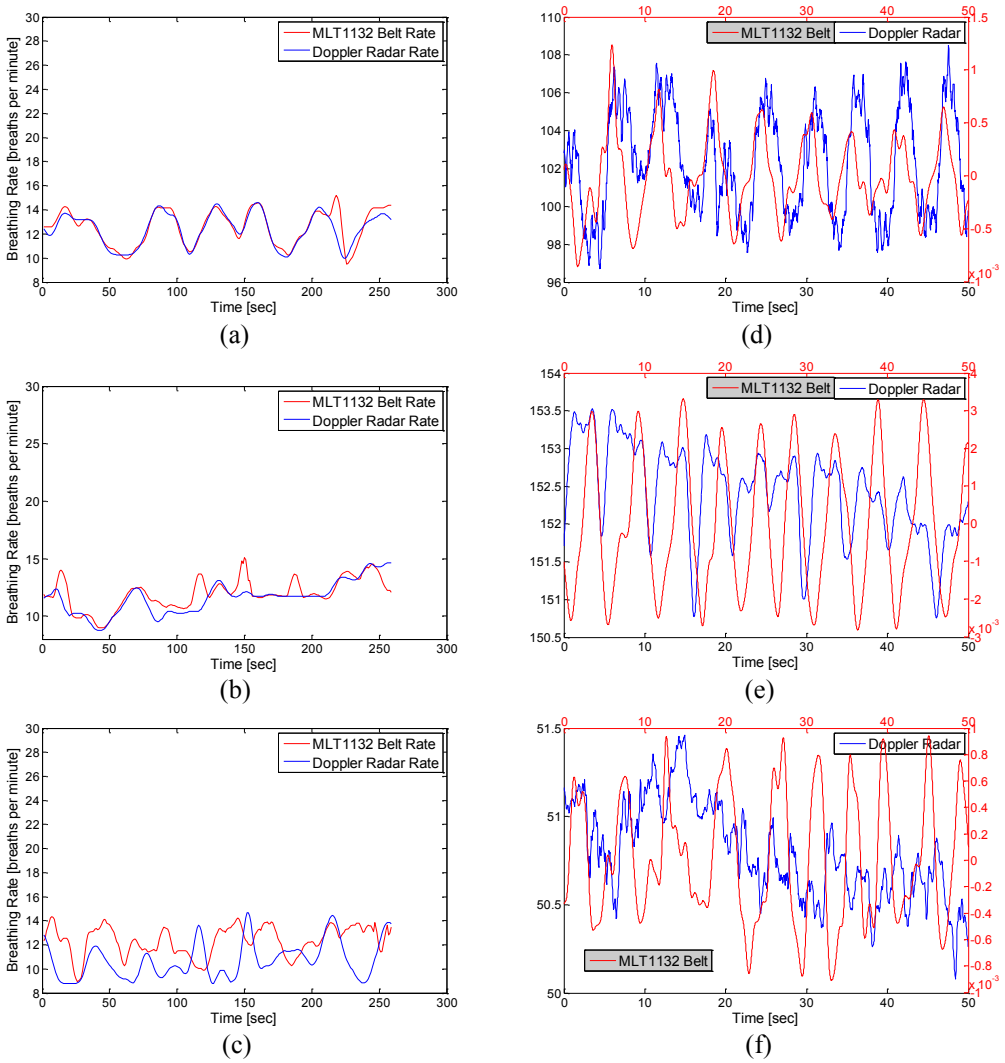

Figure 6.33: Breathing rate [Breaths per minute] vs. Time for the ECG signal and Doppler radar monitor configuration (a) 1, (b) 3 and (c) 5. Breathing signal from Doppler radar and filtered MLT1132 Chest Belt for configuration (d) 1, (e) 3 and (f) 5. These configurations can be found in Fig. 6.29.

6.4 Conclusions

A novel single port four directional flower Vivaldi antenna is proposed which operates by guiding the current to appropriate tapered slots using switches. The antenna can over a wideband provide pattern diversity for a large number of applications. Feed line along with a balun is specifically designed to obtain a wide bandwidth. It has to be noted that there is a

significant tradeoff between the achievable bandwidth and optimal radiation characteristics. Considerable work was needed to obtain a reasonable tradeoff. The proposed single port flower Vivaldi was fabricated with both ideal copper strips for switches and actual diode switches with a biasing circuit. Excellent agreement was achieved for the measured and simulated reflection coefficients of the tested antennas. For the single port flower Vivaldi with actual diode switches extra notches were observed which can be attributed to fabrication errors, RF components, biasing circuit and biasing wires. Radiation patterns were measured and simulated and it was observed that the wires cause a significant increase in the cross polarization but overall excellent similarity is obtained for the co-polarization results.

Methods to improve the cross polarization increase caused due to wires have already been discussed in section 5.4.

Future work involves the use of RF-MEMS. It is expected that RF-MEMS will improve the results significantly as they provide an actual physical contact as compared to the one produced by diode switches.

The 4-way ideal switch flower Vivaldi antenna was used to measure the vital signs. It was shown that this antenna can monitor the vital signs well when the maximum gain of the antenna was in line with the person. In other regions it was not able to detect vital signs. Hence, theoretically it can be used to find the direction of the person within a certain distance, based on which the vital signs can be monitored. In this way this antenna can effectively be used for vital signs monitoring 360^0 around it.

6.5 References

[1] Symeon Nikolaou; Bairavasubramanian, R.; Lugo, C., Jr.; Carrasquillo, I.; Thompson, D.C.; Ponchak, G.E.; Papapolymerou, J.; Tentzeris, M.M.; , "Pattern and frequency

reconfigurable annular slot antenna using PIN diodes," *Antennas and Propagation, IEEE Transactions on* , vol.54, no.2, pp. 439- 448, Feb. 2006

[2] Sung-Jung Wu; Tzyh-Ghuang Ma; , "A Wideband Slotted Bow-Tie Antenna With Reconfigurable CPW-to-Slotline Transition for Pattern Diversity," *Antennas and Propagation, IEEE Transactions on* , vol.56, no.2, pp.327-334, Feb. 2008

[3] Wang, Z.P.; Hall, P.S.; Kelly, J.; Gardner, P.; , "TEM horn circular array for wide band pattern notch reconfigurable antenna system," *Antennas and Propagation Conference (LAPC), 2010 Loughborough* , vol., no., pp.365-368, 8-9 Nov. 2010

[4] Sarrazin, J.; Mahe, Y.; Avrillon, S.; Toutain, S.; , "Pattern Reconfigurable Cubic Antenna," *Antennas and Propagation, IEEE Transactions on* , vol.57, no.2, pp.310-317, Feb. 2009

[5] Pal, A.; Mehta, A.; Mirshekar-Syahkal, D.; Massey, P.J.; , "Doughnut and Tilted Beam Generation Using a Single Printed Star Antenna," *Antennas and Propagation, IEEE Transactions on* , vol.57, no.10, pp.3413-3418, Oct. 2009

[6] Chang won Jung; Ming-jer Lee; Li, G.P.; De Flaviis, F.; , "Reconfigurable scan-beam single-arm spiral antenna integrated with RF-MEMS switches," *Antennas and Propagation, IEEE Transactions on* , vol.54, no.2, pp. 455- 463, Feb. 2006

[7] Kang, W.S.; Park, J.A.; Yoon, Y.J.; , "Simple reconfigurable antenna with radiation pattern," *Electronics Letters* , vol.44, no.3, pp.182-183, January 31 2008

[8] Dong Jiawei; Li Yongxiang; Zhang Biao; , "A Survey on Radiation Pattern Reconfigurable Antennas," *Wireless Communications, Networking and Mobile Computing (WiCOM), 2011 7th International Conference on* , vol., no., pp.1-4, 23-25 Sept. 2011

[9] Matthew J. Slater, Helen K. Pan, and Jennifer T. Bernhard: 'Preliminary results in the development of a compound reconfigurable antenna' *IEEE Antennas and Propagation Society International Symposium*, 2008. AP-S 2008. pp.1-4

Chapter 7

Conclusion and Future Work

Through experimental studies, Doppler radar and On-Body Antennas have been shown to be viable alternatives to already present commercial heart and breathing rate monitors for certain applications.

Doppler Radar

For the Doppler radar, a parametric study was performed considering the frequency, power and distance between the radar and person. It was discovered that as the frequency increases the Doppler radar becomes more sensitive to heart beat movements which has a positive effect on detection accuracy. But beyond a certain frequency the harmonic and inter-modulation interference start to have a significant destructive effect on the heart signal and in turn the accuracy. It was thus established that there is a certain ideal frequency at which the Doppler radar measures the heart rate most accurately which for the system used was 9 GHz. The connectors, cables, antennas and VNA all placed this limit as beyond 9 GHz the performance of this equipment was unreliable and noisy. It was also established that only up to a distance of 1m reliable heart rate monitoring was possible, even though up to 2m decent accuracy was achieved in some cases. Power as low as -20 dBm was enough for reliable monitoring and this fact can be used to create low power devices which is a very desirable commercial feature.

For respiration rate monitoring using Doppler radar it was discovered that all frequencies tested (1-17 GHz) were suitable. At low frequencies the radar was sensitive enough to respiration chest movements to enable detection. At high frequencies the inter-modulation and harmonic interference with the heart rate did not have any effect as the respiration signal was the dominant signal. Even up to a distance of 3m and a power of -45 dBm the respiration rate was detectable.

An experimental study has been performed on 6 people using an optimised horn antenna operating at 9 GHz, -10 dB power and located 1m from the person. Both heart and breathing rate were monitored and the feasibility of Doppler radar heart and breathing rate monitoring was proven. Doppler radar vital signs monitoring was found to be suitable in monitoring the heart rate of a person accurately within 5 BPM. This shows its suitability for determining whether the person's heart beat is normal or abnormal. With the system and signal processing used it was not suitable for monitoring heart rate within 1 BPM accuracy which is required for emergency and triage situations. For respiration rate monitoring Doppler radar was found to be extremely accurate even up to 3m away from the person. This makes Doppler radar an excellent alternative to currently present respiration devices. Current devices require considerable effort and change the natural breathing rate of the person using these devices (which include piezo-resistive belts, capnographs or spirometery devices). Based on the best determined parameters, a Doppler radar prototype can be designed which is non-invasive, cost-effective, small, portable, accurate and comfortable.

On-Body Antenna

The principle of On-Body vital signs monitoring was first studied using CST microwave studio simulation environment. A model of the chest considering skin, fat, muscles, lungs and heart was created. The effect of the movement of this chest model on the antenna reflection

coefficient demonstrated that the chest movement relative to the antenna was the major cause of modulation of heart beating and breathing information on the reflection coefficient phase of the antenna. The simulation study also confirmed that antennas with smaller ground planes were more sensitive to chest movements in the near field of that antenna. Similarly it was proven that as the distance between the chest and the antenna increased the effect of chest movement on the reflection coefficient phase of the antenna decreased.

An extensive parametric study has been conducted to determine the best parameters for accurate vital signs monitoring using On-Body Antenna connected parallel to the chest.

The lower frequencies of the UWB range proved to be best for heart rate detection as at higher frequency harmonic and inter-modulation interferences increased between the heart and breathing rate frequencies. At higher frequencies the antenna was also more susceptible to environmental noise and non-uniform or unwanted motion of the chest and other parts of the body. For the respiration rate detection, all frequencies tested (1-9 GHz) were found to be suitable as it is the dominant signal.

Antennas with small ground planes, radiation pattern towards the chest and polarization along the body were found to be the best heart rate detectors. These antennas included loop antennas, Co-planar waveguide (CPW) planar monopoles, patch antennas and inverted F antennas (IFAs). Most of the antennas tested in this thesis were primarily used for on-body communications; these antennas successfully measured the vital signs as well. This opens up the possibility for having an on-body system with a single antenna that can be used for both communications and vital signs monitoring purposes.

As the antenna is attached to clothes parallel to the chest for On-Body monitoring, power as low as -30 dBm was found to be sufficient for accurate heart rate detection. For respiration

even power as low as -45 dBm proved to be sufficient for accurate breathing rate detection. Both these power results point to the creation of a low power accurate vital signs monitor.

The On-Body antenna was placed at several locations on the chest, abdomen and back. The front left chest area directly in front of the heart was found to be the best location for most accurate heart rate monitoring operation, because at this location the chest moved the most due to heart beats. For the breathing rate monitoring it was observed that most areas of the chest and back were able to monitor breathing rate except for the abdomen area. As the abdomen area contained loosened skin and moved non-uniformly, this caused unreliable modulation of breathing movement on the antenna reflection coefficient phase which resulted in reduced accuracy.

If the distance between the antenna and the chest was increased it was observed that the accuracy reduced because the sensitivity of the antenna reflection coefficient phase to the chest movement reduced with increased distance. When the antenna was directly in contact with the skin the accuracy was reduced because of the unpredictable nature of the extra current paths created (due to direct contact with skin). This problem could be removed by introducing a non-conducting material between the skin and the antenna. These experiments also confirmed that the relative motion of the antenna with respect to the chest or the relative motion of the chest with respect to the antenna was the reason for the heart and breathing signal modulation on the reflection coefficient phase of the antenna. The breathing rate was detectable at all distances between antenna and chest and even when antenna is directly connected to the skin as the respiration movement produces a very powerful signal.

The principle and the feasibility of On-Body vital signs monitoring was validated by performing experiments on 13 people in the sitting position and 10 people in the supine position. The heart rate was detectable with an accuracy (within 2 BPM) of 86% and 87.4% in

the sitting and supine position. The accuracy (within 5 BPM) was 96.4% and 94.8% respectively. This shows that in both the sitting and supine position the On-Body monitor was able to detect heart rate accurately. Thus it can not only be used to monitor whether a person's heart rate is normal or abnormal but also in non-critical home healthcare applications. It can also be used by athletes or trainers as a low profile comfortable vital signs monitor. Continuous monitoring of soldiers, first responders or astronauts is also a potential application. The accuracy (within 1 BPM) is 70.9% and 74.5% for the sitting and supine position which is not suitable for critical situations or situations that require accuracy within 1 BPM. As the heart beats were much more pronounced in the supine position and the breathing signal was slightly weaker this resulted in better heart SNR in the supine position compared to the sitting position. A correlation between high BMI, chest circumference and waist circumference leading to low accuracy in the supine position was also discovered. Since no such correlation in the sitting position was discovered and the population of the study was only 13, a bigger population study is required to confirm the correlation between body type and detection accuracy.

The breathing was detectable with considerable accuracy for most people. It was discovered that the chest belt was not sensitive enough to detect chest movements from all people while the On-Body Monitor was. So not only was the On-Body monitor found to be accurate in monitoring the respiration rate it was also found to be more sensitive. These properties can allow the On-Body antenna monitor to replace current commercial devices (which include piezo-resistive belts, capnographs or spirometery devices) that require considerable effort and change the natural breathing rate of the person. Based on best parameters, an On-Body antenna prototype can be designed which is non-invasive, cost-effective, small, portable, comfortable and accurate in monitoring both the respiration and heart rate.

Heart Rate Variability

Heart Rate Variability (HRV), a very promising diagnostic technique for the future, is measured for people in the sitting and supine position. The supine position is discovered to be suitable for accurate HRV detection due to less movement and more pronounced heart beat peaks in this position. This makes On-Body HRV monitoring a promising alternative to present ECG based uncomfortable HRV monitors especially for long term applications such as during sleep.

Signal Processing

A signal processing study considering various algorithms, filters, window sizes, etc. was conducted. This led to the use of Butterworth filters and Fourier transform for separating and detecting the fundamental frequencies of the breathing and heart signals. A 10 second window was used for heart rate detection and a 15 sec window for breathing rate detection. Wavelet transform was shown to provide unmatched time and frequency resolution properties. This led to unique insight into the properties and accuracy of the signals from On-Body antennas, ECG, and MLT1132 chest belts.

Frequency Reconfigurable Antennas

Novel frequency reconfigurable antennas are designed by integrating band-pass and band-stop filters with wide band antennas. A novel CPW varactor achieved a wide tuning range utilizing $\lambda_g/4$ and $3\lambda_g/4$ resonators and varactors. This filter when integrated with a wide-band antenna provided a continuous narrow-band mode and a wide-band mode. A CPW switch filter was designed which utilized $\lambda_g/4$ resonators and switches to achieve reconfigurability. This filter when integrated with a wide-band CPW antenna provided narrow-band modes, stop-band modes and a wide-band mode. These designed reconfigurable antennas can replace the need for having several antennas for different frequency operations. They take less space, are cost

effective, and simple to design. The frequency agile antennas designed can also scan the spectrum in a wideband mode and choose an available narrow band mode or block a certain frequency. This is especially useful for software defined and cognitive radios.

Pattern Reconfigurable Antennas

A novel single port radiation pattern reconfigurable flower Vivaldi antenna is designed and tested. This antenna can radiate in all four quadrants depending on where the current is directed using switches. It is wideband and can be used for a number of applications which require pattern diversity. It is envisioned that such an antenna can scan the four quadrants and determine the persons location, based on which it can monitor the vital signs. It is used here to monitor the heart rate of a person in all four quadrants.

Future Work

Based on the best parameters obtained from the parametric studies, the obvious future work involves creation of prototypes for both the Doppler radar and On-Body antenna monitor. A larger population study (20-80) should be performed for these prototypes to determine whether feasibility across such a wide population is achieved or not. Also correlation between body types and accuracy can be investigated with such a study. One major stumbling block was the effect of unwanted movement (movement other than chest such as arm or leg movements) or presence of several people during both Doppler radar and On-Body monitoring. This caused sudden spikes and extra noise in the acquired signals. In some cases multiple unwanted signals (from other people or unwanted motion from the tested person) were also added to the desired signal. All this significantly increased errors. One way to remove these errors is by using multiple transceivers with MIMO signal processing. This can open these devices up to a host of new applications such as monitoring people who are

continuously moving , as currently it can only work for applications which require the subject to be almost at rest. It will also open these devices for use around other people or moving objects. Advanced signal processing such as adaptive filtering and better removal of noise from weak bio signals can immensely improve the accuracy of these devices and even remove unwanted motion artifacts. Better fundamental frequency estimation techniques can also significantly improve the overall performance of these systems and make it suitable for use in critical situations. Wavelet transform has the unique property that different mother wavelets can be chosen based on which similarity comparisons are done and coefficients calculated. A possible future work can be creating a mother wavelet which resembles the shape of heart beat from the Doppler radar or On-Body antenna monitor. This should improve wavelet frequency estimation results. Further improvement can be obtained if this mother wavelet is created separately for each person and situation. Based on the antenna study of section 4.5, novel antenna structures considering no ground, along the body polarization and radiation pattern towards the body can be designed that can improve detection accuracy of On-Body vital signs monitoring.

Future work should also involve designing and testing an antenna system which can be used both for communication and vital signs monitoring purposes.

For the frequency and pattern reconfigurable antenna design RF-MEMS should be utilized in the future as they form an actual physical when a high voltage is applied to them. MEMS eliminate the need for constant bias voltage and improve the radiation pattern results as an actual physical contact diverts or blocks current paths as desired.

Long DC bias wires caused degradation in the radiation pattern of the antennas. Coin batteries and chips should be used to provide DC bias voltage to diode switches as this will reduce the number and length of wires required.

Appendix B

B. Signal Processing

In this section the different signal processing techniques that were used to analyse the collected On-Body antenna data will be discussed and compared. These include:

(i) Fast Fourier Transform

(ii) Autocorrelation Function and

(iii) Wavelet Transform

Other methods including Cepstrum analysis, peak detection, etc. were used as well but did not produce any useful results. Peak detection was useful only when the heart signal was without noise and motion artefacts, which was seldom the case. Several de-noising techniques including Wavelet de-noising, threshold de-noising, etc. and filters including Kalman, Kaiser, savitzky-golay , median ,etc. were also studied. These filters and de-noising techniques were not consistent enough to be used reliably and hence were avoided.

For the feasibility analysis of the different signal processing techniques utilized in this thesis two 30 sec On-Body signals from subject 2 and subject 12 of section 4.3.3 were chosen, and are shown in Fig. B.1. The filtered versions of these two signals are shown in Fig. B.2. Subjects 2 and 12 will be denoted as subjects A and B, respectively throughout this section. The following combination of filters was chosen in the final design:

(i) Butterworth high pass filter with 5 Hz cut off and order 12 and

(ii) Butterworth low pass filter with 0.7 Hz cut off and order 8

These filters were chosen after careful analysis of different filters, considering the accuracy and reliability of the final results.

The ECG signal corresponding to the collected On-Body signal, had an average of 71 Beats per Minute [BPM] and 86.7 BPM for subject A and subject B, respectively.

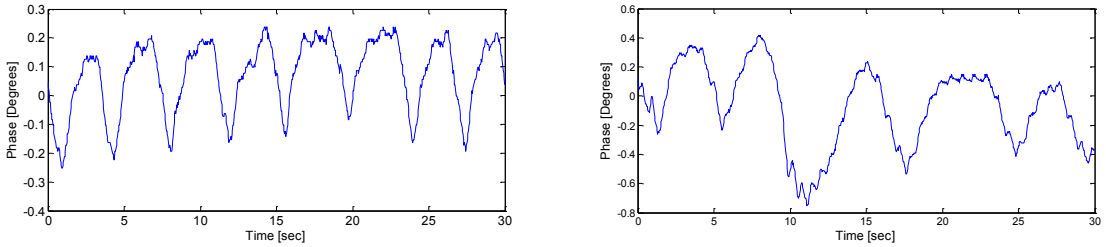

(a) (b)

Figure B.151: On-Body Vital Signs signal from (a) subject A, and (b) subject B.

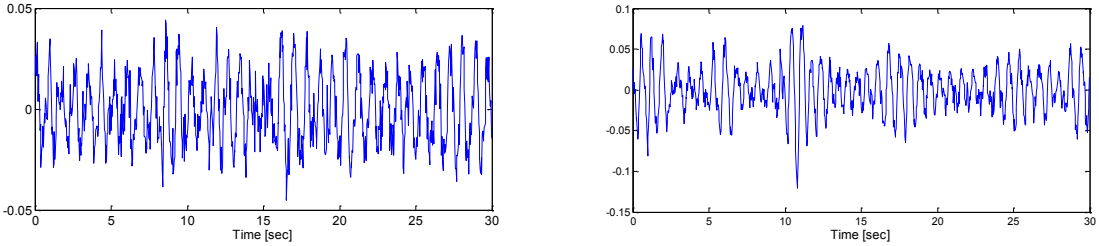

(a) (b)

Figure B.2: Filtered versions of signals in Fig.B.1 showing the heart beats for (a) subject A, and (b) subject B

B.1 Fast Fourier Transform (FFT)

Fourier Transform is a very popular technique which determines the spectral content of a signal. Discrete Fourier Transform (DFT) is used for sampled signals. It provides a frequency domain representation of an N length time domain signal by dividing it into N equal frequency bins. FFT is an algorithm which is widely used to calculate the DFT and will be employed here. Figure B.3(a) shows the result of application of FFT on the signal shown in Fig. B.1 (a). Several frequency peaks are observed of which two frequency peaks are in the desired sections. The desired sections include 0.1-0.6 Hz for the breathing rate and 0.7-2.2 Hz for the heart rate. One peak at 0.2694 Hz (0.2694 * 60 = 16.2 Breath per minute) is the breathing rate and the second peak at 1.167 Hz (1.167 * 60 = 70.02 BPM) is the heart rate. Figure B.3 (b) shows the result of application of FFT on Fig. B.1 (b). Again we see two peaks

in the desired sections. Figure B.4 shows the application of FFT on the filtered On-Body Heart signals of Fig. B.2. Similar heart rate peaks for the FFT spectrum of the unfiltered signals and the filtered signals are observed. The FFT calculated results for subject A and B are 70 and 84.42 BPM respectively, which are close to the ECG results of 71 and 86.7 BPM.

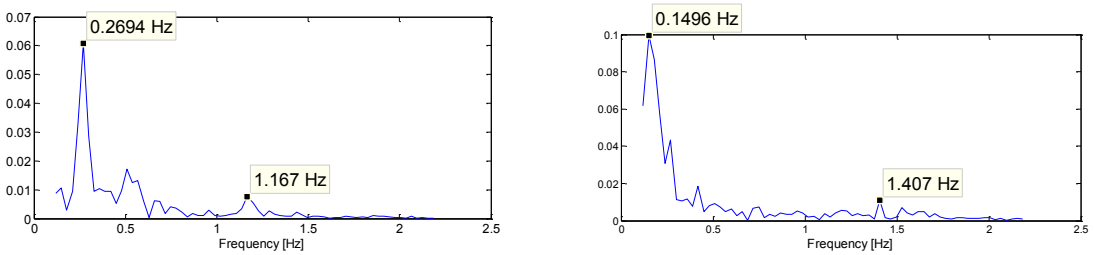

Figure B.3: Spectral domain representation of the unfiltered time domain signals (from Fig. B.1) for subject (a) A and (b) B using FFT.

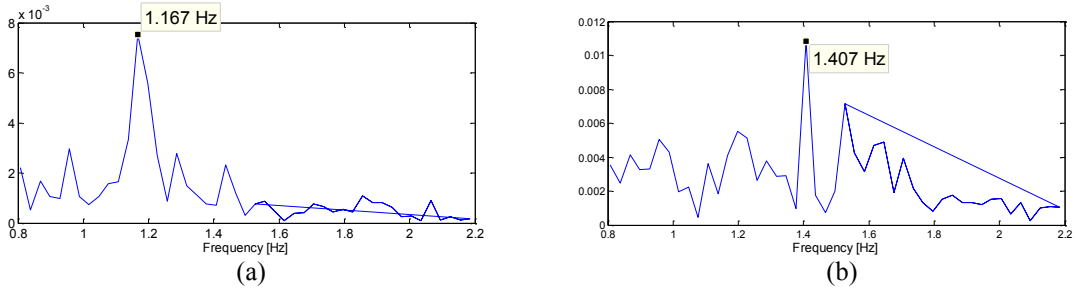

Figure B.4: Spectral domain representation of the filtered time domain signals (from Fig. B.2) for subject (a) A and (b) B using FFT.

B.2 Autocorrelation

Autocorrelation function is used to find repeating patterns in a signal. It can detect a periodic signal which is buried under noise and determine the fundamental frequency of that signal. It does this by multiplying a time delayed version of a signal by itself and then summing up the resulting signal. This process is done for all time delays which results in peaks at the fundamental frequencies and harmonics. The auto-correlation function was unable to detect the heart rate when it was applied to the original unfiltered signals of Fig. B.1. Figure B.5 shows the autocorrelation function time delay graphs of the filtered signals in Fig. B.2. The

calculated BPM from these graphs were 68 and 83. These are less than the ECG values of 71 BPM and 86.7 BPM. After careful testing, it was observed that lower sampling rate resulted in inaccurate performance of the autocorrelation function. This was verified in simulation (using MATLAB) and results from other sources [1] which had a sampling rate of about 100 samples per second. The simulation results showed that auto-correlation function can be useful for calculating the fundamental frequency of heart signals at sampling rates of above 80 approximately. For the lower sampling frequency of 30 samples per second as used in this case, it was found to be unsuitable and inaccurate.

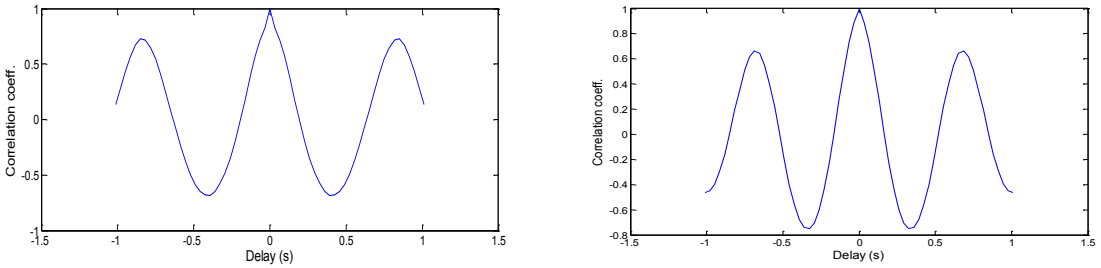

(a) (b)

Figure B.5: Autocorrelation time delay graph of the filtered time domain signals (from Fig. B.2) for subject (a) A and (b) B

B.3 Wavelet Transform

B.3.1 Theory

Wavelet Transform is being increasingly utilized in various signal processing applications because of its unique properties. Continuous wavelet transform (CWT) provides a time-frequency representation of a signal with excellent time and frequency localization. It is specifically designed to work with non-stationary signals. It has been applied for data compression [2], image processing [3] and electrocardiogram signals [4], etc. It was also

employed in [5] to process a chemical oscillating system leading to a better understanding of the overall system. Detailed information about wavelet transform can be found in [6].

In this section, we propose to employ wavelet transform for the first time to study and identify the heart rate from a phase modulated On-Body antenna signal. The Wavelet Transform has got advantages over Fourier transform in analyzing signals that are non-stationary [6] and have discontinuities and sharp peaks like the heart rate signal obtained from an On-Body antenna. Utilizing the time and frequency retention property of wavelet transform new coefficients will be described and employed to study the fine properties of the heart rate signal obtained from On-Body antennas.

The Wavelet Transform $Wf(a,b)$ is given by:

$$Wf(a,b) = \frac{1}{\sqrt{a}} \int_{-\infty}^{+\infty} f(t)\psi^* \left(\frac{t-b}{a}\right) dt \qquad (B.1)$$

where a and b are the scale and translation factors respectively, $f(t)$ is the original time series signal and ψ^* is the complex conjugate of ψ which is the mother wavelet. A mother wavelet is a prototype function which is used to analyse data. A chosen mother wavelet can be scaled depending on a and translated depending on b. The translated and shifted versions of the mother wavelet are passed over the original signal $f(t)$ and the resemblance of this scaled and shifted mother wavelet to the original signal is calculated and stored in the coefficients of $Wf(a,b)$. With some modifications spectral information can be obtained from these wavelet coefficients. The sum of the translation coefficients on every individual scale gives rise to a new set of coefficients:

$$Wf(a) = \sum_{t_1}^{t_2} |Wf(a,t)| \qquad (B.2)$$

where t_1 and t_2 form a time span. Scale can be converted into frequency by using the following equation:

$$Frequency = \frac{Centerfrequency\ of\ Mother\ Wavelet}{sampling\ rate * scale} \qquad (B.3)$$

This is called the wavelet frequency spectrum (WFS) [5]. WFS has frequency (converted form scale using eq. B.3) on the x-axis and energy contained in that frequency on the y-axis. Considering that wavelets retain time information, a new set of coefficients can be devised to gain the benefits of this property. The absolute maximum value of the wavelet coefficients for every transition is stored providing the energy concentration at every transition. This is called the Time Frequency Spectrum (TFS) [42]. It is given by:

$$Tf(t) = \max of\ |Wf(a,t)| \qquad for\ all\ a \qquad (B.4)$$

where t=1 to n(length of the time signal)

The mother wavelet chosen for analysis was morlet. It was chosen because its shape resembled the heart beat signal from the On-Body antenna. Also experimentation with different wavelets revealed it gave the most accurate and robust performance.

WFS and TFS provided an analysis of the On-Body antenna signal which was not possible with other usually employed techniques. The results of these analyses will be discussed in the next section.

B.3.2 Results and Discussions

Figure B.6 shows the 3d plots of the continuous wavelet coefficients of the 30 second On-Body signals in Fig. B.1 for subject A and B. In Fig B.6 (a) three peak regions are observed (around the 97, 41 and 25 scale mark). The 97 (0.2257 Hz) and 24 (1.0334 Hz) peak areas correspond to the breathing rate and the heart rate respectively. The 41 (0.6049 Hz) peak area is the result of harmonics. For Fig. B.6 (b) the peaks are not very clear.

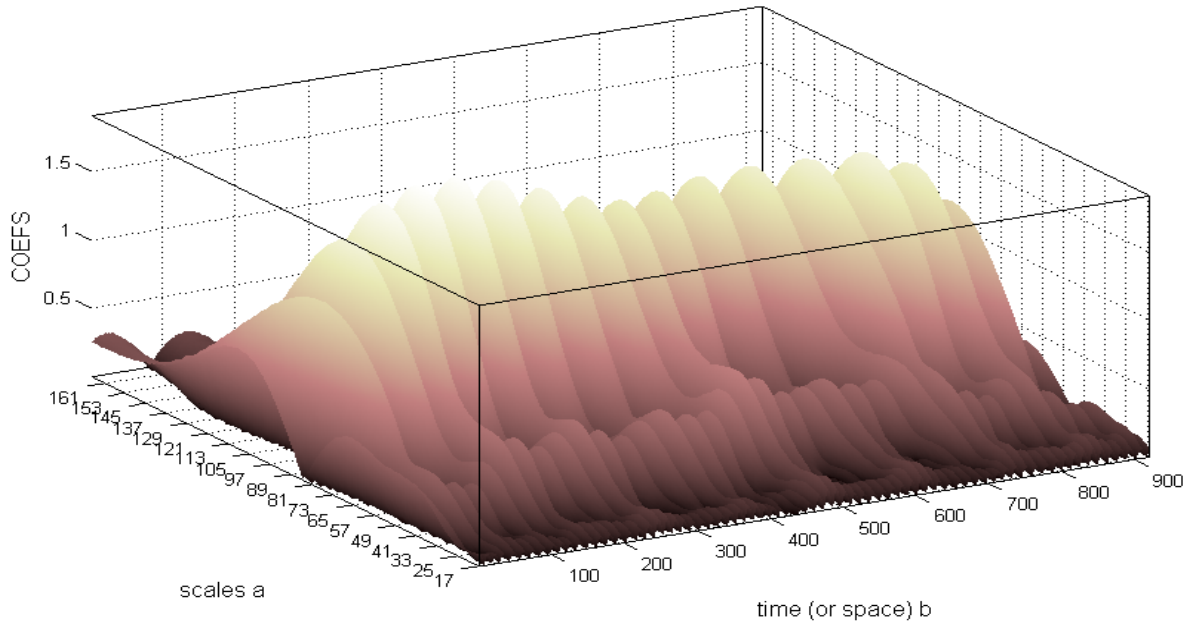

(a)

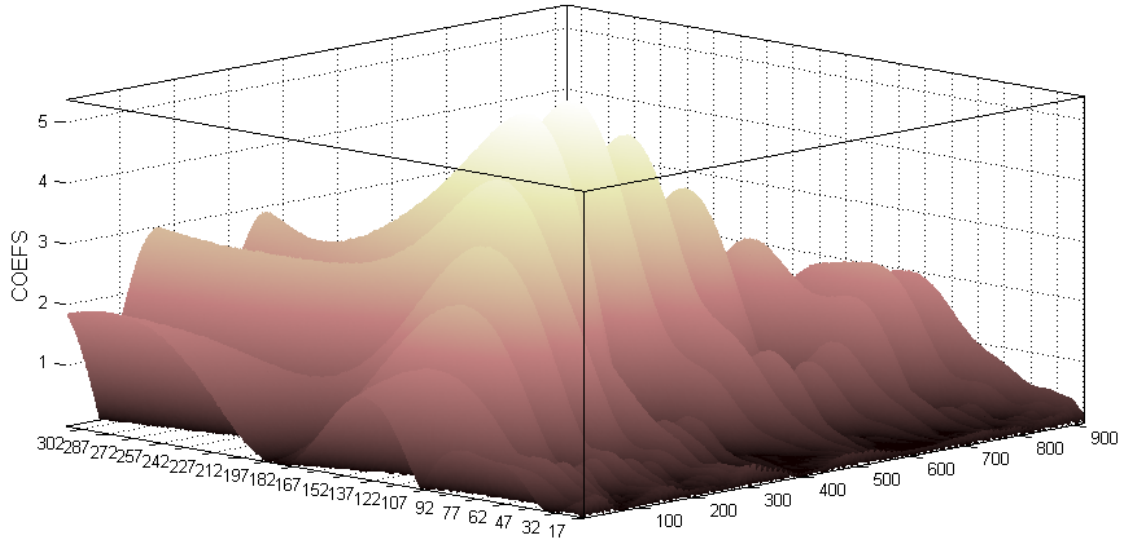

(b)

Figure B.6: 3d plot of wavelet coefficients for the unfiltered time domain On-Body signals (in Fig. B.1) for subject (a) A and (b) B.

Wavelet scalograms convey the time frequency localization property of the CWT. In the scalogram each coefficient is plotted and the intensity of the colour corresponds to the magnitude of the coefficient. The wavelet scalograms for the unfiltered signals of subject A and B (from Fig. B.1) are shown in Fig. B.7. The breathing rates of 0.26775 and 0.1706 Hz

for subject A and B respectively are clearly observable on these scalograms but the heart rate cannot be detected. These rates were calculated by summing translation coefficients on every individual frequency (or scale) and finding the frequency at which the calculated sum is maximum. Fig. B.8 shows the scalograms for the unfiltered signals of subject A and B, but only considering frequencies in the heart rate region (0.9-1.9 Hz). We observe heart rates of 1.1857 and 1.4647 Hz for these scalograms. This shows that even without filtering heart rates are detectable over a 30 sec window using wavelet scalograms.

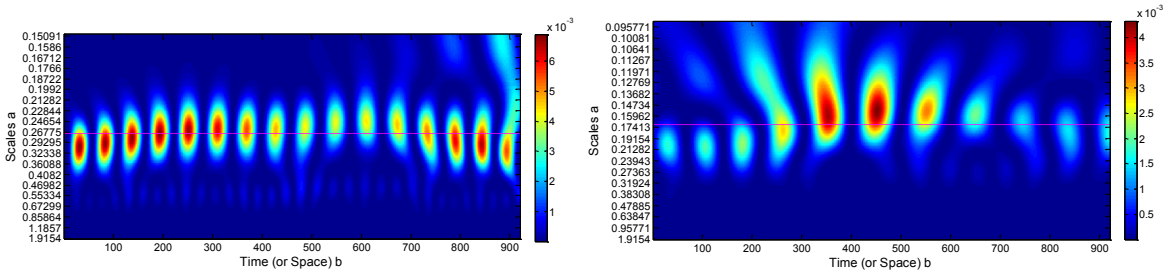

(a) (b)

Figure B.7: Scalogram for the unfiltered time domain On-Body signals (from Fig. B.1) for subject (a) A and (b) B, dashed lines represent the average breathing rate.

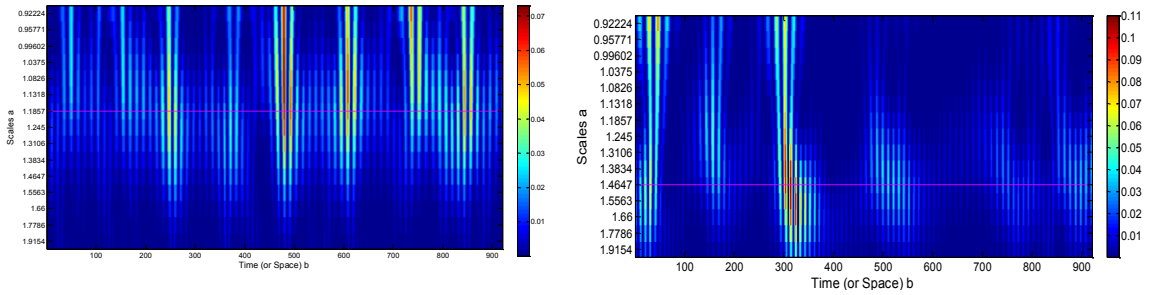

(a) (b)

Figure B.8: Scalogram concentrating on the heart region (0.9-1.9 Hz) for the unfiltered time domain On-Body signals (from Fig. B.1) for subject (a) A and (b) B, dashed lines represent the average heart rate.

The WFS (as described in equation B.2) for the unfiltered modulated On-Body signals of subject A and B are shown in Fig. B.9. Both cases have two peaks, one (higher frequency one) represents the heart rate and the other one represents the breathing rate. The heart rate

average of 71.2 and 87.9 agrees well with the reference device average of 71 and 86.7 respectively.

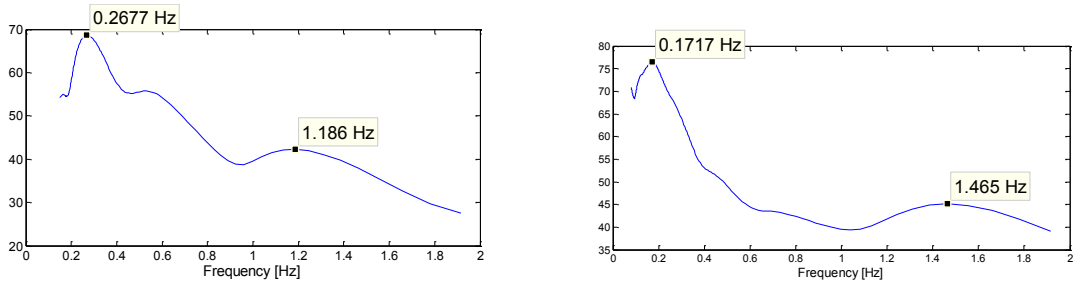

(a) (b)

Figure B.10: Wavelet Frequency Spectrum for the unfiltered time domain On-Body signals (from Fig. B.1) for subject (a) A and (b) B.

Fig. B.10 shows the 3d plot of the cwt for the filtered signals in Fig. B.2 for subject A and B. It is clear that all scales except the heart rate scale areas are filtered out. This is also evident in Fig. B.11 which is the WFS of the filtered On-Body signals for subject A and B. The heart rate according to the WFS for the filtered and unfiltered On-Body signals is same for the subject A but changes from 1.465 Hz to 1.383 Hz for subject B.

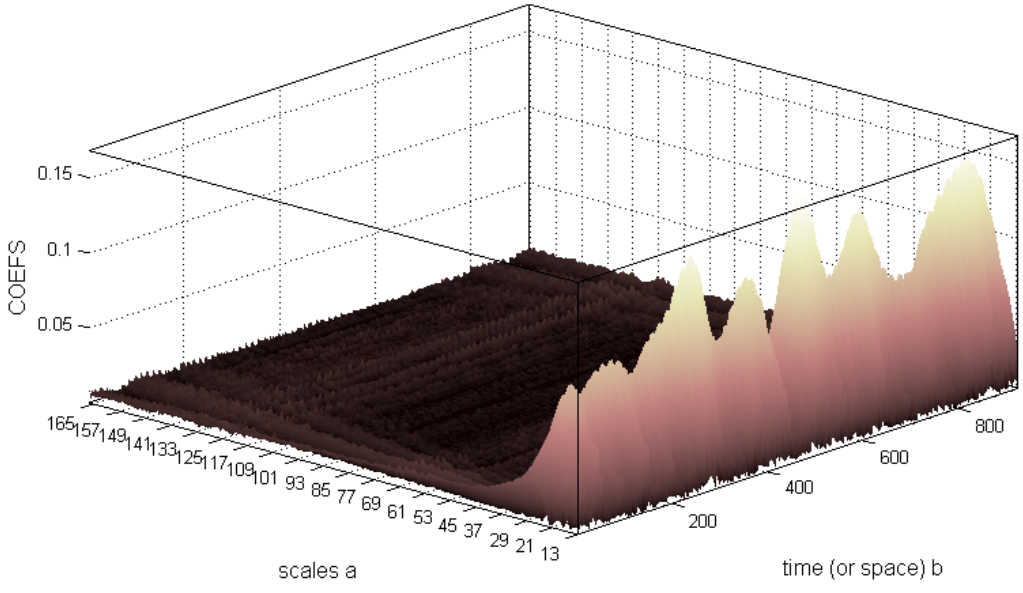

(a)

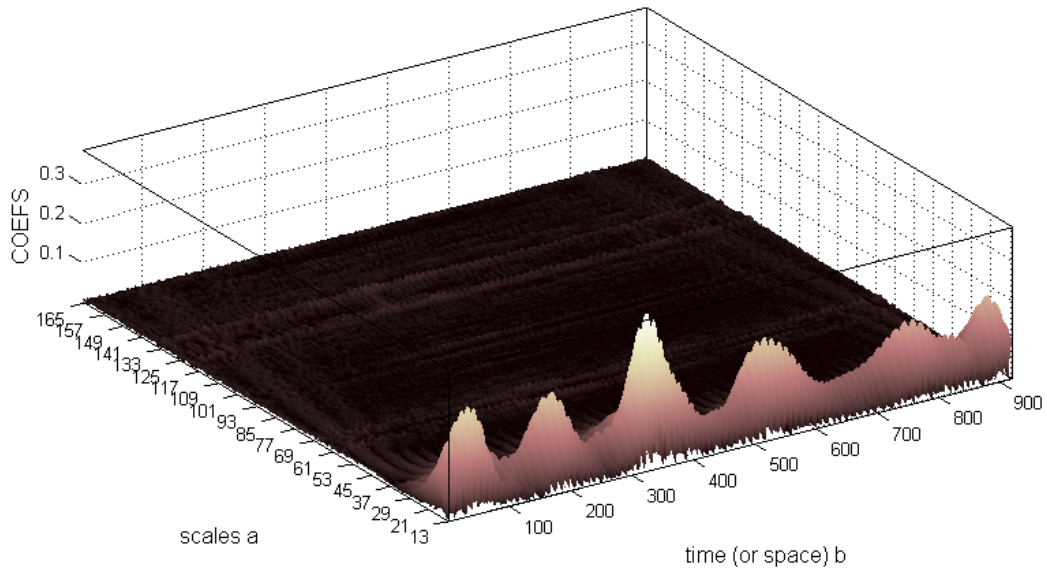

(b)

Figure B.52: 3d plot of wavelet coefficients for the filtered time domain On-Body signals (from Fig. B.2) for subject (a) A and (b) B.

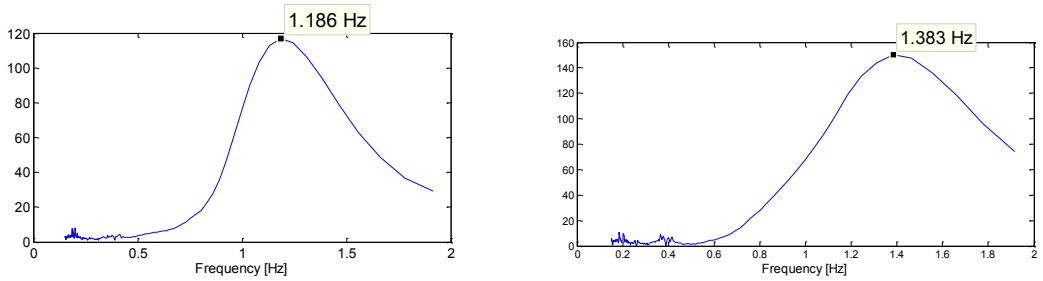

(a) (b)

Figure B.11: Wavelet Frequency Spectrum of the filtered time domain On-Body signals (from Fig. B.2) for subject (a) A and (b) B.

The wavelet scalogram for the filtered On-Body signals of subject A and B are shown in Fig. B.12. This figure also shows the TFS graphs (as described in section B.3.1) for the aforementioned signals. The property of wavelet transform for providing frequency and time resolution can be clearly seen. The red continuously varying line is the TFS (calculated as described in section B.3.1) with averaging over 1 sec worth of samples (30) to get a single point. The TFS shows gradual and rapid changes in heartbeat throughout the 30 seconds and

this can be useful in certain medical studies [4]. The dashed pink line shows the average heart rate for the 30 sec period which is 1.1857 Hz and 1.3771 Hz for subject A and B respectively.

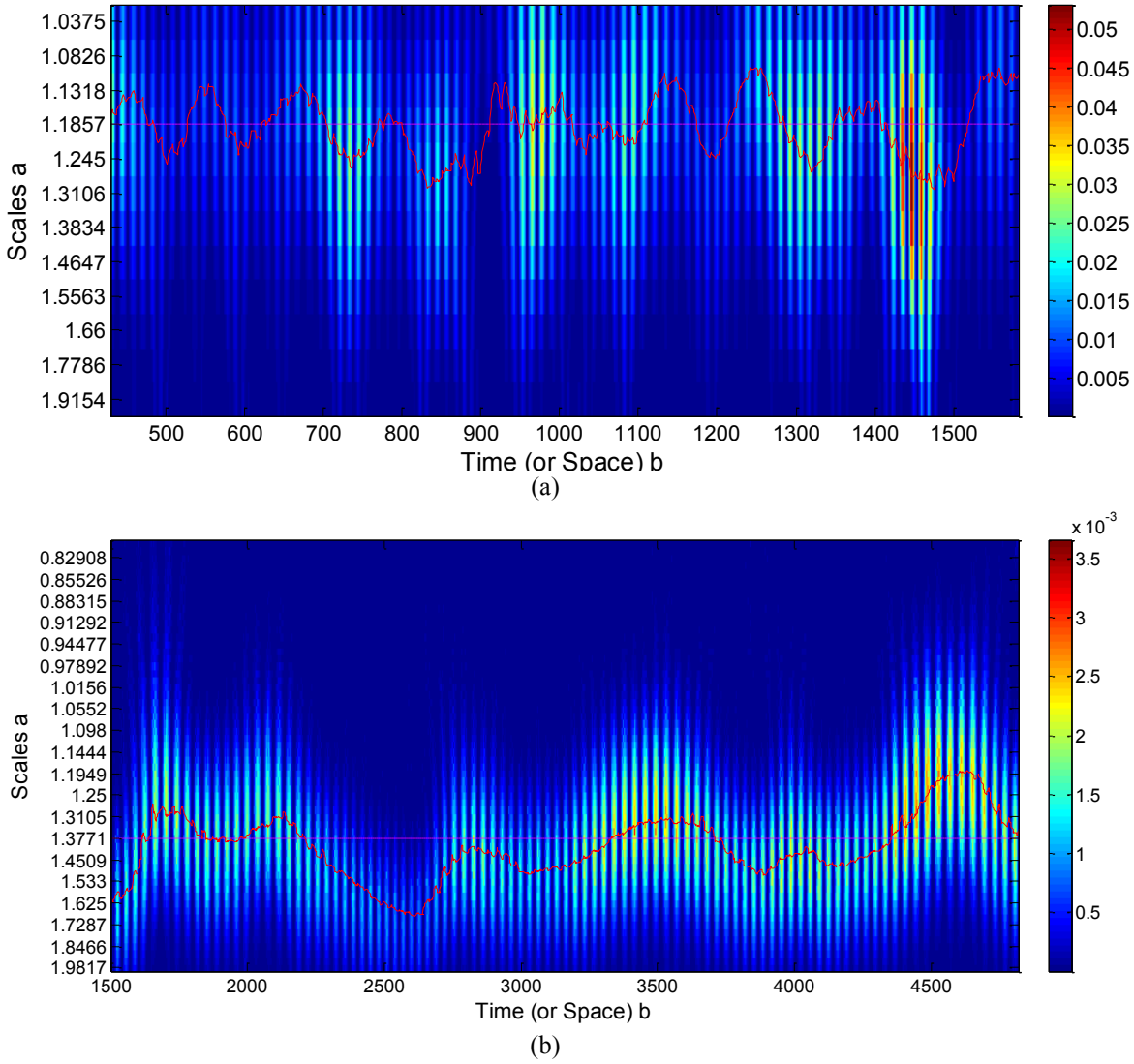

Figure B.12: Scalogram for the filtered time domain On-Body signals (from Fig. B.2) for subject (a) A and (b) B, dashed pink line represents the average Heart Rate and solid continuously moving red line represents the TFS.

Figure 4.63 shows the corresponding ECG wavelet scalograms and TFS graphs for the same periods as the filtered On-Body signals in Fig. 4.52. Average heart rates of 1.1775 and 1.3834 Hz are observed using the ECG which are very close to the On-Body averages of 1.1857 Hz and 1.3771 Hz.

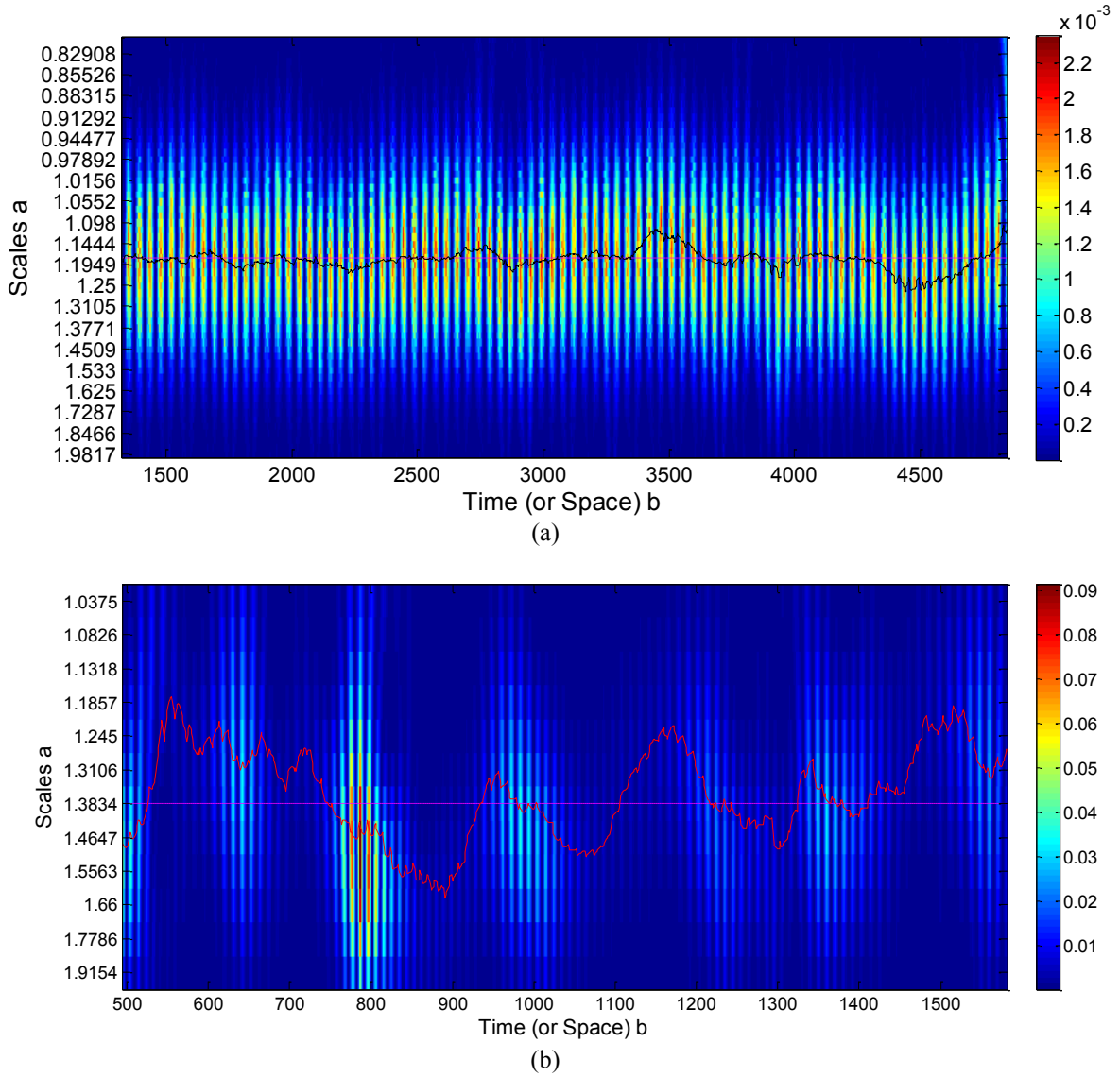

Figure B.13: Scalogram of corresponding ECG signal to the filtered time domain On-Body signals (from Fig. B.2) for subject (a) A and (b) B, dashed pink line represents the average Heart Rate and solid continuously moving red line (black for B.13 (a)) represents the TFS.

Fig. B.14 (a) and (b) shows the TFS of the heart beat waveform obtained from the ECG (in black) and TFS of the heart beat waveform obtained from the On-Body antenna (in red) for both subject A and B respectively. As can be clearly seen the two TFS plots of Fig. B.14 (b) follow for the most part a similar pattern and overlap well with each other. This gives an indication about the accuracy of the On-Body monitoring technique. The TFS plots in Fig.

B.14 (a) follow each other less accurately but the pattern is still similar. The difference in the number of samples is because of the different sampling rates of the ECG device and the VNA.

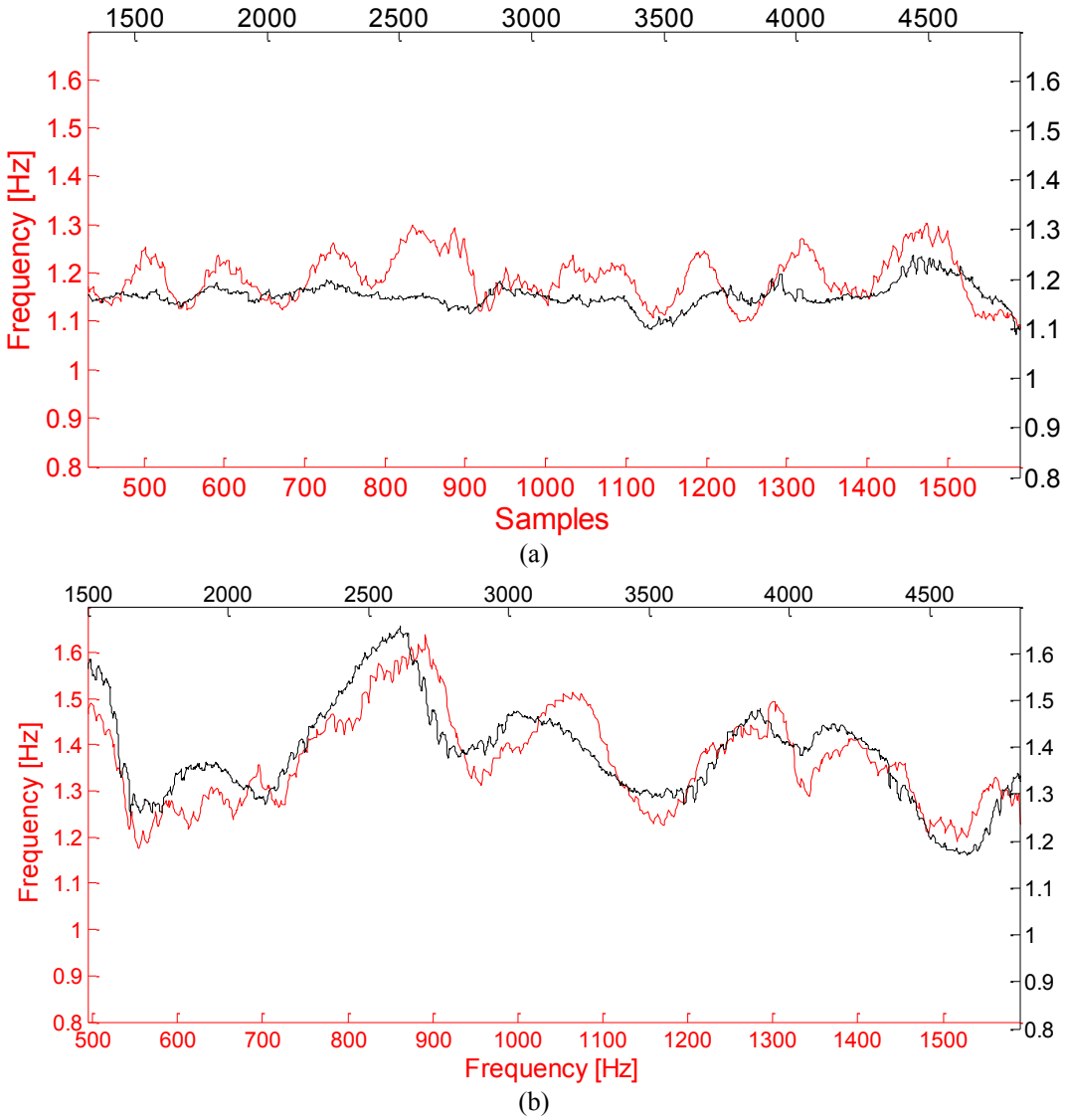

Figure B.14: TFS of Reference ECG (black line) vs On-Body antenna modulated phase signal (red line) for subject (a) A, and (b) B

The application of wavelet transform to the heart rate signals from the ECG and the On-Body antenna provides unique insight into the properties of the signal acquired and accuracy of the On-Body monitoring technique which was not possible with usually employed spectral analysis techniques. This provides Wavelet Transform with a unique advantage over FFT and

autocorrelation function in analysing the Heart beat signal from the On-Body Antenna and ECG device.

B.4 Comparison of various signal processing techniques

In this section the Autocorrelation function, FFT and Wavelet Transform calculated results will be compared based on Bland-Altman analysis (from section 4.3.5) and the accuracy of results obtained from On-Body antennas within 1,2,3,4 and 5 BPM of the reference ECG device. All the results (from all the subjects) collected for the human body experiments of section 4.10 will be utilized here to perform the comparison. In order to determine the heart rate the 5 min acquired heart signals from the On-Body Monitor were divided into windows of specific lengths (in seconds) and above mentioned signal processing techniques were applied to them to find out the heart rate in each window. These windows were then moved forward by 1 second and this process was continued until the end of the 5 minutes. The results obtained due to different durations of window length which are 5,8,10 and 15 seconds long will also be compared here. Table B.1 shows the results of all these above mentioned comparisons.

The bolded numbers represent the best result in that column for the particular window length. For the 5 second window the Wavelet transform and Fourier transform have quite similar results. But overall especially for window size of above 5 seconds the Fourier transform is the clear winner. Also the 10 second window has got the highest accuracy for the Fourier transform results with accuracy within 5 BPM of 93.1 %. The 10 second window not only provides good accuracy but also is small enough to ensure that features of the heart beat that change rapidly are not lost.

Appendix A has been removed from the electronic copy of this thesis due to copyright restrictions

Table B.1: Statistical comparison of different signal processing techniques and different window lengths.

Method Type	**Bland Altman (BPM)**		**Accuracy (%) within**				
	Mean Difference	Limits of agreement	1 BPM	2 BPM	3 BPM	4 BPM	5 BPM
Autocorrelation, 5-second window	1.2148	**1.2148 ± 4.736**	37.9	55.4	66.3	74.4	83
Wavelet Transform, 5-second window	0.7493	0.7493 ± 8.4446	**49.4**	68.1	**75.2**	79.3	82.8
Fast Fourier Transform. 5-second window	**0.1514**	0.1514 ± 6.4684	48.8	**68.3**	75	**79.7**	**83.3**
Autocorrelation, 8-second window	1.1204	1.1204 ± 4.6526	39.2	55.8	66	75.3	83.8
Wavelet Transform, 8-second window	0.9371	0.9371 ± 6.895	53.1	70.6	77.4	81.5	85.1
Fast Fourier Transform. 8-second window	**0.4836**	**0.4836 ± 4.2804**	**53.9**	**74.6**	**81.4**	**86.8**	**89.7**
Autocorrelation, 10-second window	1.0202	1.0202 ± 4.3788	39.6	56.3	66.9	75.7	84.1
Wavelet Transform, 10-second window	0.7615	0.7615 ± 5.3178	54.5	73.2	81.1	85.5	88.9
Fast Fourier Transform. 10-second window	**0.1785**	**0.1785 ± 3.7882**	**62.6**	**78.2**	**85.3**	**89.5**	**93.1**
Autocorrelation, 15-second window	0.5403	0.5403 ± 4.1742	38.5	58	69.6	78.5	87.6
Wavelet Transform, 15-second window	1.0088	1.0088 ± 5.0554	55.6	72.9	79.5	84.3	87.6
Fast Fourier Transform. 15-second window	**0.3473**	**0.3473 ± 3.9936**	**62.2**	**75.8**	**83.7**	**89.4**	**92.7**

Figures B.15 (a) and (b) show the Heart rate [BPM] vs Time [second] graph of subject A and subject B respectively for the ECG device, Fast Fourier transform, autocorrelation and wavelet transform calculated results. As can be seen all of these signal processing techniques follow the ECG device results well, but the Fast Fourier transform follows the results most closely. FFT is the technique that overshoots the most as well. This is something which will be improved in future work.

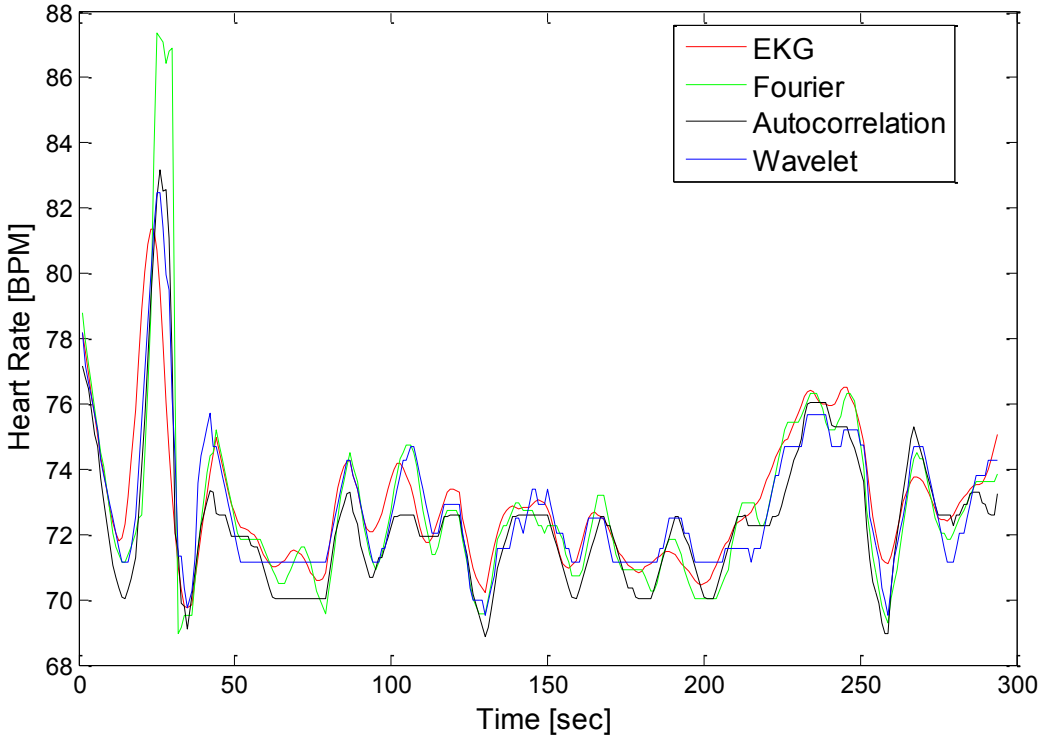

(a)

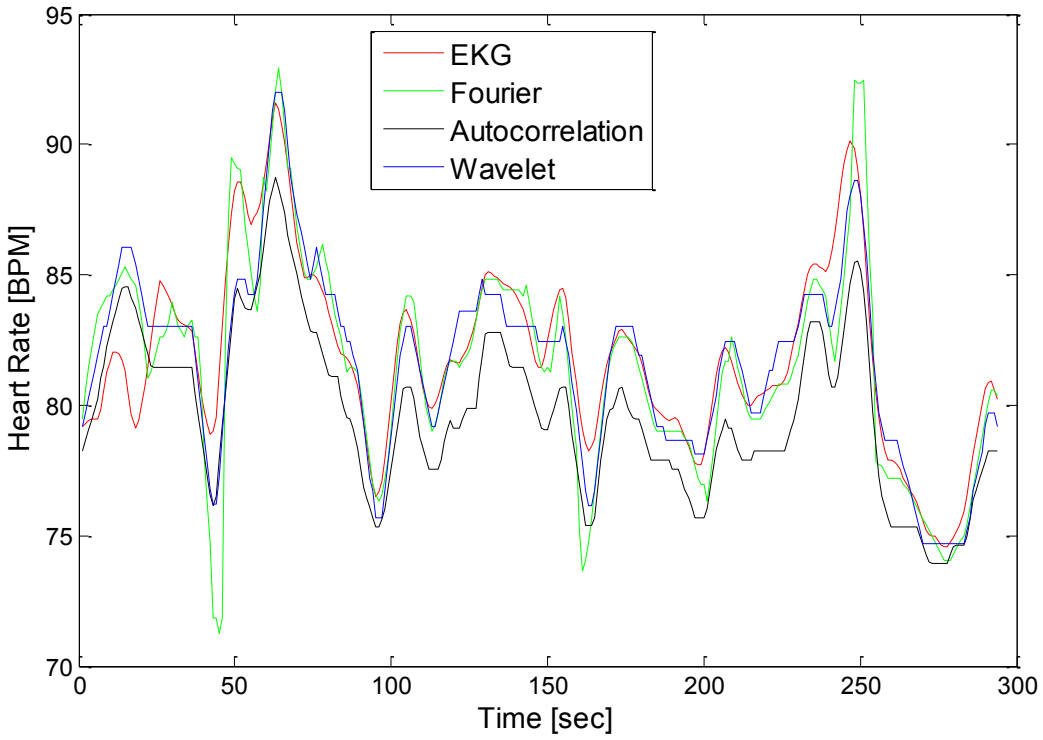

(b)

Figure B.15: Heart rate [BPM] vs Time [sec] graphs of subject (a) A and (b) B for ECG device; Fast fourier transform, autocorrelation and wavelet transform calculated results

As a result of this comparison FFT with a 10 second window was the algorithm of choice. The wavelet transform provides better time and frequency resolution and provides unique insight into the signal. It is especially useful in monitoring changes in heart rate over very short intervals of time. It can be utilized in situations where these features are desired.

B.5 References

[1] Droitcour, A.D.; Boric-Lubecke, O.; Kovacs, G.T.A.; , "Signal-to-Noise Ratio in Doppler Radar System for Heart and Respiratory Rate Measurements," *Microwave Theory and Techniques, IEEE Transactions on* , vol.57, no.10, pp.2498-2507, Oct. 2009

[2] Federal Communications Commission homepage [Online]. Available: http://hraunfoss.fcc.gov/edocs_public/attachmatch/FCC-02-48A1.pdf Zhigang Gao, Y.F. Zheng, "Quality Constrained Compression Using DWT-Based Image Quality Metric," *IEEE Transactions on Circuits and Systems for Video Technology*, vol.18, no.7, pp.910-922, July 2008.

[3] D. Gleich, M. Datcu, "Wavelet-Based Despeckling of SAR Images Using Gauss–Markov Random Fields," *IEEE Transactions on Geoscience and Remote Sensing*, vol.45, no.12, pp.4127-4143, Dec. 2007.

[4] Tan Yun-fu, Du Lei, "Study on Wavelet Transform in the Processing for ECG Signals," *WRI World Congress on Software Engineering, 2009. WCSE '09*, vol.4, pp.515-518, 19-21 May 2009.

[5] Xiaoquan Lu, Hongde Liu, Jingwan Kang, Jin Cheng, "Wavelet frequency spectrum and its application in analyzing an oscillating chemical system," *Analytica Chimica Acta*, Vol. 484, Issue 2, pp 201-210, 19 May 2003.

[6] S. Mallat, *A Wavelet Tour of Signal Processing*, Academic Press, NY, 1998.